Phase Equilibria Measurement and Modelling of Petroleum Reservoir Fluids Containing Gas Hydrate Inhibitors and Water

Michael Wise

Submitted for the degree of Doctor of Philosophy in

Petroleum Engineering

Heriot-Watt University

Energy, Geoscience, Infrastructure and Society

Institute of Petroleum Engineering

July 2016

ABSTRACT

Understanding gas hydrate inhibitor distribution in hydrocarbon phases is essential for the economic design of process equipment. In order to build a clear image of the inhibitor's distribution in various phases, three experimental investigations were devised; solubility in liquid and vapour phase as well as saturation pressure measurements. These data will contribute significantly to the understanding of the partitioning of these components as the data in the open literature are fairly limited.

Aiming at filling the experimental gap found in the literature, the solubility of methane in pure methanol and ethanol as well as 70 and 50 wt% aqueous solutions at 238.15 – 298.15 K and 0.3 – 47 MPa were measured. The data from the ethanol/solution solubility measurements were used to optimise the methane-ethanol Binary Interaction Parameters (BIPs) of the CPA-SRK72 Equation of State (EoS). The model calculations showed an absolute average deviation of 5.3% over the full pure data range. To improve the CPA-SRK72 EoS predictions for aqueous solutions, new methane-ethanol BIPs were regressed showing significant improvement for both solubility and quaternary bubble point predictions. In order to determine the inhibitor loss to the vapour phase, the inhibitor content of methane was measured using Gas Chromatography (GC) between 0.7 – 62 MPa and 273.15 – 298.15 K.

Additionally, a number of bubble point measurements were conducted for binary, ternary and quaternary systems containing methane, a liquid hydrocarbon phase (C7 – C12), methanol/ethanol and water. This was to investigate the effect of the inhibitor phase in the ternary, and the dominant excess water phase in the quaternary system, on the bubble point pressure as well as evaluating the CPA-SRK72 predictions. The saturation pressures were measured at 253.15 – 313.15 K.

The solubility of CO_2 in Mono-ethylene glycol (MEG), Di-ethylene glycol (DEG) and Tri-ethylene glycol (TEG) and their aqueous solutions (90, 60 and 40 wt%), at pressures and temperatures ranging from 0.2 – 43.4 MPa and 263 – 343 K, were measured.

The solubility of CO_2 in pure MEG, DEG and TEG were predicted using the CPA-SRK72 EoS, using a single binary interaction parameter, showing an absolute average deviation of 5.13%, 9.51% and 2.55% respectively. Correlations for the solubility of CO_2 in MEG, DEG and TEG aqueous solutions, using aqueous solution regressed BIPs, showed an overall absolute average deviation of 17.5%, 18.2% and 25.16% respectively, a significant improvement from the non-aqueous solution BIP optimised predictions.

I would like to dedicate this thesis to my parents and little sister

I will always appreciate your support and sacrifice

ACKNOWLEDGEMENT

After an intensive period of 3 years, 7 months and 12 days, I can finally complete my PhD thesis with this note of thanks to all who made it possible. This PhD has had a big impact on me and it has been a period of intense learning that would have only been possible in such a place. I find myself leaving this institute wiser than when I entered it. I would like to reflect on the people who have supported and helped me so much throughout this period.

Firstly I would like to thank my supervisors Dr. Antonin Chapoy and Prof. Bahman Tohidi for providing me with the opportunity to conduct my PhD at the Institute of Petroleum Engineering (for now part of school of EGIS). I am particularly grateful to Antonin for his guidance, resolute dedication, saint like patience and most importantly his unwavering loyalty. I would also like to express my sincerest gratitude to Dr. Rod Burgass for his guidance, absolute dedication and helpfulness throughout my PhD, without which this work would not have been possible. I would also like to thank Dr. Jinhai Yang for his thought provoking discussions and his guidance throughout various aspects of my research and life in general. I am also grateful to the research team's technician, Mr. Jim Allison, for his assistance as well as general guidance. Furthermore I would like to thank Miss. SJ Hill for her unwavering support and help.

This work was conducted within two projects funded through Joint Industrial Projects being conducted jointly at the Institute of Petroleum Engineering, Heriot-Watt University and the CTP laboratory of MINES ParisTech. The JIPs were supported by Chevron, GALP Energia, GDF, Linde AG Engineering Division, OMV, Petrobras, Petroleum Expert, Statoil, TOTAL and National Grid Carbon Ltd, which is gratefully acknowledged. The participation of National Grid Carbon in one of the JIPs was funded by the European Commission's European Energy Programme for Recovery. I would also like to thank the members of the steering committee for their fruitful comments and discussions. Finally the author would like to thank EPSRC for their support through the Heriot Watt University's DTA.

ACADEMIC REGISTRY

Research Thesis Submission

Name*:*	Michael Wise		
School/PGI:	IPE, EGIS		
Version: *(i.e. First, Resubmission, Final)*	Final	Degree Sought (Award **and** Subject area)	PhD

Declaration

In accordance with the appropriate regulations I hereby submit my thesis and I declare that:

1) the thesis embodies the results of my own work and has been composed by myself
2) where appropriate, I have made acknowledgement of the work of others and have made reference to work carried out in collaboration with other persons
3) the thesis is the correct version of the thesis for submission and is the same version as any electronic versions submitted*.
4) my thesis for the award referred to, deposited in the Heriot-Watt University Library, should be made available for loan or photocopying and be available via the Institutional Repository, subject to such conditions as the Librarian may require
5) I understand that as a student of the University I am required to abide by the Regulations of the University and to conform to its discipline.

* *Please note that it is the responsibility of the candidate to ensure that the correct version of the thesis is submitted.*

Signature of Candidate*:*		Date:	

Submission

Submitted By *(name in capitals):*	MICHAEL WISE
Signature of Individual Submitting:	
Date Submitted:	

For Completion in the Student Service Centre (SSC)

Received in the SSC by *(name in capitals):*			
Method of Submission *(Handed in to SSC; posted through internal/external mail):*			
E-thesis Submitted (mandatory for final theses)			
Signature:		Date:	

TABLE OF CONTENTS

LISTS OF TABLES

LISTS OF FIGURES

PUBLICATIONS BY THE CANDIDATE

M. Wise, A. Chapoy, Carbon dioxide solubility in Triethylene Glycol and aqueous solutions, Fluid Phase Equilib. 419 (2016) 39–49. doi:10.1016/j.fluid.2016.03.007.
[used in Chapter 3]

M.H. Kapateh, A. Chapoy, R. Burgass, B. Tohidi, Experimental Measurement and Modeling of the Solubility of Methane in Methanol and Ethanol, J. Chem. Eng. Data. (2015) acs.jced.5b00793. doi:10.1021/acs.jced.5b00793.
[Used in Chapter 4]

M. Wise, A. Chapoy, R. Burgass, Solubility Measurement and Modeling of Methane in Methanol and Ethanol Aqueous Solutions, J. Chem. Eng. Data. (2016).
[Accepted – 23/05/2016]

A. Chapoy, M. Nazeri, *M. Kapateh*, R. Burgass, C. Coquelet, B. Tohidi, Effect of impurities on thermophysical properties and phase behaviour of a CO2-rich system in CCS, Int. J. Greenh. Gas Control. 19 (2013) 92–100. doi:10.1016/j.ijggc.2013.08.019.
[Used in Chapter 4]

A. Chapoy, M. Nazeri, *M. Kapateh*, R. Burgass, B. Tohidi, C. Coquelet, Thermophysical properties and phase behavior of a CO2-rich natural gas, in: GPA Annu. Conv. Proc., Gas Processors Association, 2014: pp. 601–628.

M. Kapateh, A. Chapoy, B. Tohidi, Effect of Impurities in Sour Gas Transportation, in: 6th GERG Acad. Netw., 2014. doi:10.13140/RG.2.1.2353.6729.

M. Kapateh, A. Chapoy, B. Tohidi, Effect of Impurities in CCS Transportation, in: UKCCSRC Autumn Biannu. Meet. 2014, 2014. doi:10.13140/RG.2.1.3926.5363.

M. Kapateh, Thermodynamic Measurement and Modelling of Reservoir Fluids and Sour Gases, in: 1st Young North Sea CCS Res. Meet., 2014. doi:10.13140/RG.2.1.4591.7047.

M. Kapateh, A. Chapoy, The effect of impurities on the thermophysical properties and dehydration requirements in CCS, in: 9th Heriot Watt Postgrad. Res. Conf., 2014. doi:10.13140/RG.2.1.2877.9608.

Luís Manuel Cravo Pereira, *M. Kapateh*, A. Chapoy, Impact of impurities on thermophysical properties and dehydration requirements of CO 2 -rich systems in CCS, in: UKCCSRC Biannu. Meeting Cambridge Univ., 2014. doi:10.13140/RG.2.1.1174.0248.

M. Kapateh, Frozen Assets, Chem. Eng. (2013) 42.

Note: The author published under two different names during his PhD

NOMENCLATURE

μ	Chemical potential
A	Constant in the binary interaction parameter
a	activity parameter of the equation of state
α	Kihara hard-core radius
$\alpha(T_r)$	Temperature dependent function of EoS
a_0	Constant part in the energy parameter of the EoS
AAD	Absolute Average Deviation
APACT	Associated Perturbed Anisotropic Chain Theory
B	Constant in the binary interaction parameter
b	Co-volume parameter of the equation of state
β	Association volume in the CPA-SRK72 EoS
BIP	Binary Interaction Parameter
C	Constant in the binary interaction parameter
c	Parameter of the equation of state
C_1	Methane
C_{10}	Decane
C_{11}	Undecane
C_{12}	Dodecane
C_{16}	Hexadecane
C_2	Ethane
C_3	Propane
C_7	Heptane
C_9	Nonane
CPA-SRK72	Cubic Plus Association - Soave Redlich Kwong Equation of State 1972
DEG	Diethylene glycol
ε	Association energy in the CPA-SRK72 EoS
EoS	Equation of State
EtOH	Ethanol
F	Parameter of the equation of state/Molar fraction of phase/Correction factor
f	fugacity
ϕ	Fugacity Coefficient
G	Gibbs free energy
g	Radial distribution function in the CPA-SRK72 EoS
Γ	Potential energy interaction
γ	Activity coefficient
K	Equilibrium ratio
k	Binary Interaction Parameter for the classical mixing rules/Boltzmann's constant
κ	Interaction volume in the potential energy

L	Liquid
L_1	Aqueous Phase
L_2	Rich hydrocarbon phase
LLE	Liquid-liquid equilibrium
M	Molecular Weight
MEG	Monoethylene glycol
MeOH	Methanol
Mol	Mole
n	Number of Moles
N	Number of Components
P	Pressure
π	Number of phases
PC	Computer
PRT	Platinum Resistance Thermometer
R	Universal Gas Constant
ρ	Density
$\triangle H_{fus}$	Molar enthalpy of fusion
σ	Collision diameter
SAFT	Statistical Associated Fluid Theory
SRK	Soave Redlich Kwong Equation of State
T	Temperature
TEG	Triethylene Glycol
V	Volume
v	Molar volume
VLE	Vapour Liquid Equilibrium
Ω	Parameter in the EoS
ω	Acentric factor
wt%	weight percent
X	Mole fraction of molecules that are not-bonded to the site
x_i	Liquid mole fraction (component i)
y_i	Vapour mole fraction
Z	Compressibility factor

Chapter 1 – INTRODUCTION

1.1 Gas Hydrates

The oil and gas industry has undergone dramatic changes over the last few decades. Oil and gas companies have been moving their exploration towards more challenging reservoirs with a variety of flow assurance challenges.

Natural gas is typically composed of a high concentration of methane with varying amounts of ethane, propane and carbon dioxide before processing. This composition will differ between reservoirs, with some extreme cases containing significantly higher volumes of acid gases than methane. One of these major challenges is the formation of clathrates or gas hydrates. This issue can affect production, transportation and even natural gas processing and storage.

Natural gas hydrates are crystalline solids composed of gas molecules (guests/formers) trapped in water cages (host). In the presence of water many of the natural gas components can form hydrates at production, processing and transportation conditions. The formers stabilise the hydrate structure by van der Waals forces. Guest molecules in hydrate structures are free to rotate inside the host structure cage as there are no covalent bonding between the guest and host molecules, thus gas hydrates may be referred to as solid solutions. [1] Natural gas hydrates form when the following conditions are met:

- Temperature and pressure within the hydrate stability region
- Availability of hydrate former molecule
- Availability of water (not necessarily only free water)

The temperature and pressure at which hydrates form depends on the composition of the gas, the gas to water ratio and water chemistry. In order to prevent hydrate formation, it is only necessary to eliminate one of the conditions stated above. As hydrate formers are the desirable product, it is not possible to eliminate them. The reduction of transportation pressure as well as flashing of the oil are common methods used for hydrate prevention. These methods entail significant costs due to capacity reduction, thus the focus is placed on the other conditions.

There are a number of conditions that enhance hydrate formation. One of these conditions is turbulent flow. This is observed in choke valves, where significant temperature drops are observed due to the Joule-Thomson effect as well as process vessels, heat exchangers and other such process units. Another condition that enhances hydrate formation is the availability of nucleation sites. These can be provided by

imperfections such as weld spots or simple pipe fittings such as elbows, tees and valves. Furthermore, silt, scale, dirt and sand can also provide a sufficient nucleation site for hydrate formation enhancement. The Nucleation sites increase the gas/liquid contact area increasing the probability of hydrate formation. Furthermore they increase mixing resulting in bubble formation.

Accumulation of these solid hydrates is also an important flow assurance issue to consider. Gas hydrate solids may not agglomerate where they are formed. In multiphase pipelines, hydrates may flow with the liquid and deposit in the liquid. This can lead to blockages and severe damage to pipelines. [2–4]

1.1.1 Structure

There are three known types of hydrate structural arrangements. Structure I and II are commonly seen in the petroleum industry and are dependent on the size of the hydrate formers. The third hydrate structure, H, was discovered in 1987 by Ripmeester et al. [5] larger molecules such as butane and other heavier hydrocarbons form structure H hydrates. This structure is the least common structure found in nature. Figure 1.1 illustrates the various hydrate cage structures. As it is apparent, hydrates are asymmetric, semi-spherical cages formed by the hydrogen bonding between water molecules.

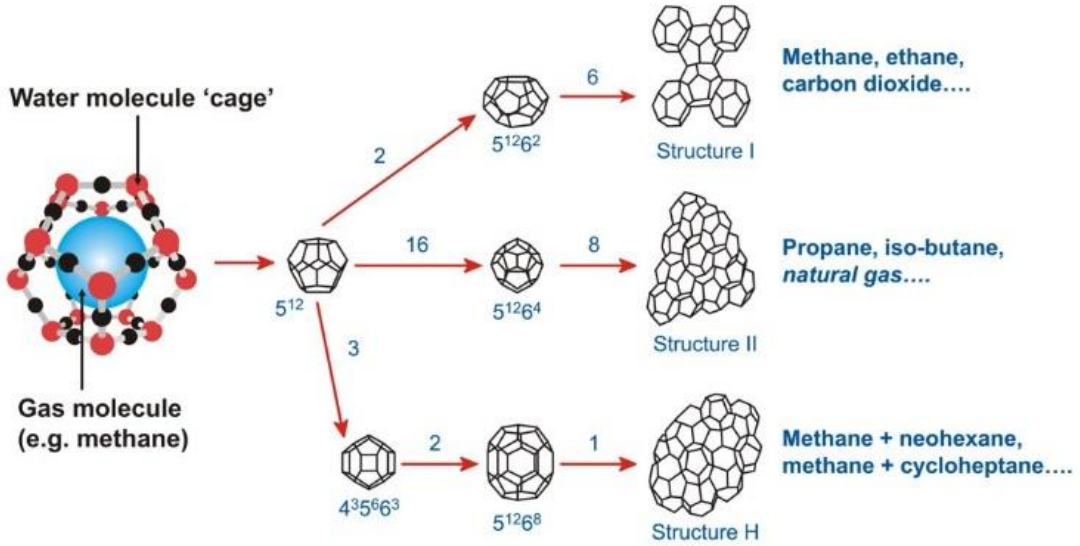

Figure 1.1. Summary of the three hydrate structures and their cages. [2,6]

Structure I is the simplest and most common hydrate structure found in nature. It consists of two types of cage arrangements, dodecahedron and tetrakaidecahedron, where the former are usually smaller than the latter arrangements, thus dodecahedron arrangements are often referred to as 'small cages' and tetrakaidecahedron arrangements are commonly referred to as 'large cages'.

Structure II hydrates are significantly more complicated. These hydrates are similarly formed from two types of structural arrangements, dodecahedron and hexakaidecahedron (16 sided polyhedron with 12 pentagonal and four hexagonal faces), where dodecahedron cages are naturally smaller than hexakaidecahedron cages.

Structure H hydrates are significantly less common than the other two structures described. In order to form this structure hydrates a small molecule, such as methane, together with a type H hydrate former must be present. These hydrates consist of three structural types, dodecahedron, irregular dodecahedron (3 square, 6 pentagonal and 3 hexagonal faces) and irregular icosahedron (12 pentagonal and 8 hexagonal faces). Some of the common structure H formers are 2-methylebutane, 2,2-dimethybutane, 2,3-dimethylbutane, cycloheptane and cyclooctane.

Von Stackelberg made a series of classifications to describe hydrate schemes which are still commonly used. [4,7,8]

The term ‘mixed’ is used to describe hydrates where more than one component occupies the same cage structure type. Hydrates in which each size cage is primarily occupied by a different molecule are commonly referred to as ‘double’ hydrates. Small formers such as nitrogen and methane can enhance hydrate formation for larger components. These hydrates are usually referred to as ‘help gas’. Hydrates with only one guest molecule are referred to as ‘simple’.

1.1.2 Flow Assurance

Hydrates can form in any pipeline which provides the suitable conditions. Oil and gas production has been moving to more extreme conditions, i.e cooler conditions in Siberia and Canada to the deep waters of the Canyon Express system (around 2000 m deep). Higher pressures and lower temperatures in deep water sites are often well within the hydrate stability zone. It is extremely difficult to remove hydrate plugs from pipelines carrying condensed hydrocarbon phases such as gas condensate and crude oil when they are formed.

Hydrate plugs, as well as their dissociation may entail catastrophic economic and safety consequences including major life threatening safety failures. E.g. when dissociating a hydrate plug using heat the outer layer dissociates first, as expected, leading to a pressure build-up behind the plug. The plug may eventually dislodge, and shoot through the pipeline like a torpedo, reaching speeds of 300 km/h. The hydrate will then reach a bend in the pipe and penetrate through causing a rupture in the pipeline with catastrophic

consequences. There are a number of methods used in the industry to prevent hydrate formation in transportation and processing systems. One of the commonly used methods to prevent hydrate formation is heating the system to keep it above the hydrate formation temperature at the specific pressure. Another commonly used method is to remove both free, vaporised and dissolved water from the system through a combination of separation and drying (Triethylene Glycol (TEG) dehydration, solid bed desiccant…).

Thermodynamic inhibitors such as alcohols and glycols are injected at the well head as an indirect method of 'removing' free water, in order for majority of the water to form hydrogen-bonds with the inhibitor, thus 'occupying' the water sites and preventing clathrate formation. This reduces the water activity, hence decreasing and increasing the temperature and pressures, respectively, at which the system allows hydrate formation. Figure 1.2 shows the inhibiting effect of methanol in a methane-water system. The water activity is significantly reduced by the addition of 30 and 50 wt% methanol compared to pure water.

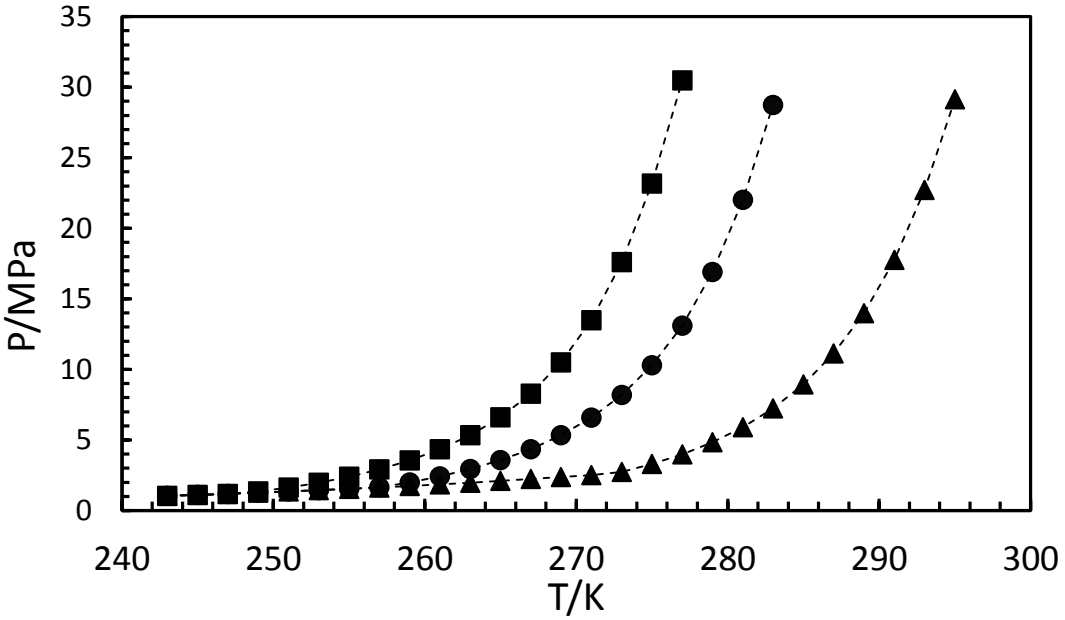

Figure 1.2. CPA-SRK72 model predictions - the inhibiting effect of methanol on the hydrates of methane. Pure water (▲), 30 wt% methanol (●) and 50 wt% methanol (■).

Pipeline operations are designed to prevent hydrate plug formation; however, plugs may form as a result of three abnormal flowline conditions:

1. In scenarios when there is a failure in the inhibition injection such as dehydration unit inefficiency or failure, inhibitor injection pump failure or miscalculation in inhibitor injection quantities required for a particular system.

2. During start-up, following an emergency shut-in, with failure in the inhibitor injection system, such as compressor failure, may result in plug formation.
3. When wet gas flows through a restriction such as a valve resulting in a drop in temperature due to the Joule-Thomson effect, hydrate plugs may form and agglomerate in the flowline. [3,4]

1.1.3 Energy Potential

Significant reserves of natural gas are stored under deep oceans and in permafrost regions throughout the world. The known and postulated location of these potential energy reserves are shown in Figure 1.3. The molar volume of gas stored in the form of gas hydrates is on average equivalent to that of highly compressed gas at 273.15 K and 18 MPa. Despite being lower than LNG, it is sufficiently high to make gas transportation in hydrates an economically viable possibility. With more fuel stored in natural clathrate hydrates than twice the sum of the global fossil fuel reserves, significant investments have been made to exploit this lucrative energy source.

Because the world's gas hydrate reserves reside at the bottom of deep oceans and in deep permafrost layers, production and exploitation is inherently difficult. However, given the current rate of research and development, many scientists believe hydrates will be the primary source of fossil fuel which will meet the world's demand. This will lead to the restructuring of the global energy geopolitics, as many countries with limited access to fossil fuels will gain access to significant gas reserves.

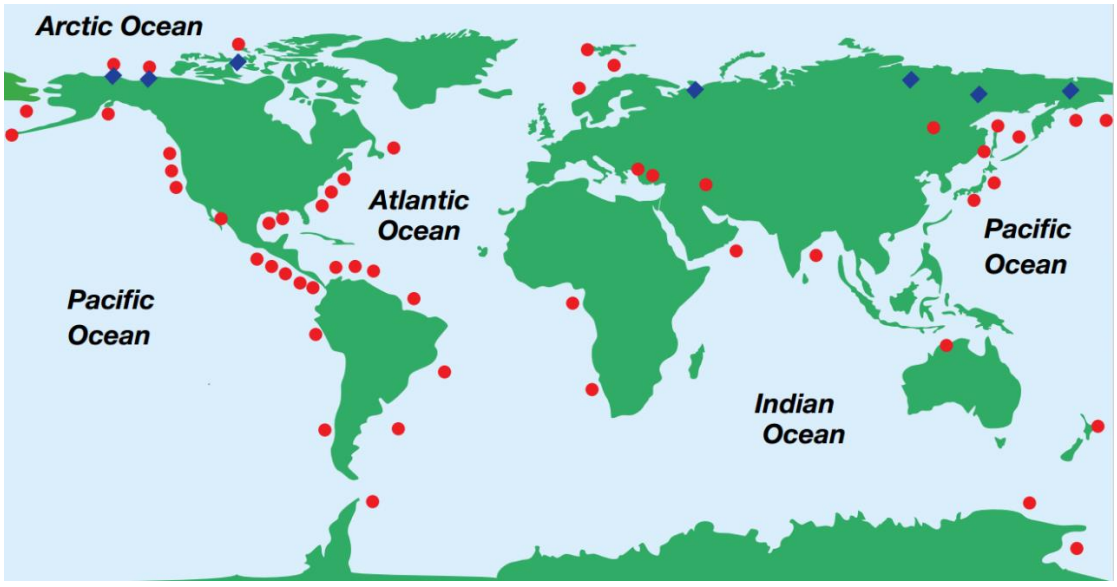

Figure 1.3. Known and inferred natural gas hydrate deposits in permafrost (blue diamonds) and offshore (red dots) adapted from the US Geological Survey [2,9]

While economically viable methods for hydrate extraction do not exist yet, numerous extraction methodologies have been examined. Most of these involve the dissociation of gas hydrates by:

- Increasing the temperature of Gas Hydrate reservoirs above the hydrate stability zone using hot water or steam injection
- Decreasing the reservoir pressure below the hydrate stability region resulting in hydrate dissociation
- The injection of alcohol based inhibitors such as methanol, ethanol and glycols

Japan played host to an exciting and potentially world-changing engineering experiment in March 2013 that saw it successfully extract natural gas from frozen subsea deposits.

Japan Oil, Gas and Metals National Corporation (JOGMEC) estimated that the Nankai trough alone, where the tests were conducted, contains 1.1 tn m^3 of natural gas – equivalent to 11 years of LNG imports for the resource-poor nation. But this is just the tip of the iceberg. The US Department of Energy's Oak Ridge National Laboratory estimates that global reserves of so-called gas hydrates could meet current energy demands for more than 350 - 3500 years. [10]

1.2 Inhibitor Distribution

As it was discussed earlier many operators use thermodynamic inhibitors to prevent hydrate formation. Injection of thermodynamic inhibitors entails huge Capital and Operating Expenditure costs to handle vast quantities of inhibitors. Furthermore, there are numerous environmental limits on the use of such chemicals both upstream and downstream, thus the knowledge of inhibitor distribution is essential for the economic design of upstream, midstream and downstream process and transportation equipment.

Hydrate inhibitors are injected based on calculated/measured hydrate phase boundary, water volumes, highest and lowest probable pressure and temperature conditions and the amount of inhibitor lost. Due to the limitation of the inhibitor distribution data (especially ethanol for natural gas systems), high volumes of inhibitor with large safety margins, are used in the industry to ensure sufficient protection from hydrate formation. It is therefore extremely important to generate experimental data that can be used to determine the inhibitor distribution in various phases.

1.3 Joint industrial Projects

This topic is of great importance to the industry and thus many companies invest in the research in this field. This work was conducted within the framework of two Joint Industrial Projects (JIPs), where 13 companies operating in the oil and gas industry sponsored two JIPs. These include:

- Effect of Impurities on Thermophysical Properties and Phase Behaviour of CO_2 Rich Systems in CCS JIP
- Gas Hydrate Flow Assurance (GHFA) JIP

As part of the Effect of Impurities on Thermophysical Properties and Phase Behaviour of CO_2 Rich Systems in CCS JIP, the research focus was the determination of CO_2 loss in glycols and its aqueous solutions.

CO_2 transportation has become a significant topic of research due to its implications for Carbon Capture and Storage (CCS) as well as Enhanced Oil Recovery (EOR). Glycols are commonly used to prevent hydrate formation; they are also used to remove water from natural gas streams as well as the dehydration of CO_2 for Enhanced Oil Recovery (EOR) and sequestration.

To understand and model the thermodynamic behaviour of CO_2 in glycols, its solubility at various temperature and pressures are required. This understanding and application is an essential part of economic engineering design through the enhancement of EoS calculations in process simulation software.

Under the Gas Hydrate Flow Assurance (GHFA) project, the research focused on the distribution of methanol and ethanol in the liquid and vapour phase, commonly used by the project's sponsors and other operators throughout the world to prevent hydrate formation. In order to build a clear image of these inhibitor's distribution in various phases, 3 experimental investigations were conducted, solubility in liquid and vapour phase as well as saturation pressure measurements.

1.3.1 CO_2 Solubility in Glycols (CCS)

It is important to know the solubility of CO_2 in various glycols and aqueous solutions to develop reliable Equations of State (EoS) which will in turn be used for engineering calculations in various software as mentioned earlier. A thorough literature review showed a number of gaps in the knowledge of CO_2 solubility in glycols and solutions.

This work focused on producing experimental results in a large temperature and pressure range for the CO_2 solubility in Monoethylene glycol (MEG), Diethylene glycol

(DEG) and Triethylene glycol (TEG) and aqueous solutions. These data are important when developing thermodynamic models to predict the phase behaviour of systems containing CO_2, glycols and water.

Classical thermodynamic models have shown to be unreliable for this purpose at high pressures, as these systems contain components that form hydrogen bonds with directional forces (glycols, water, methanol...). Thermodynamic models that account for association (such as CPA-SRK72, SAFT, PC-SAFT…) have shown to produce significantly more reliable predictions. To benefit from the simplicity of classical EoS and the prediction capabilities of Equations of State that consider association, CPA-SRK72, developed by Kontogeorgis et al. [11], was used and optimised in this work. This EoS has been discussed in more detail in Chapter 2. The model correlations in this work were optimised using a single variable Binary Interaction Parameter (BIPs). Due to the scarcity of data in the open literature, the data from this work was used for a number of the BIPs developed. Where this has occurred the reader has been cautioned about using the BIPs without independent validation of the model.

1.3.2 Alcohol Inhibitor Distribution

Alcohols (primarily methanol and ethanol) are commonly used to prevent hydrate formation by many operators throughout the world. Knowledge of methanol and ethanol distribution is extremely important in the industry. There are significant penalties for high concentrations of methanol in sales gas. A number of operators have considered to move to ethanol as a hydrate inhibitor due to the toxicity of methanol based on discussions with the project sponsors. Ethanol is already a popular hydrate inhibitor in South America due to its abundance and relatively low costs.

A number of studies have been conducted to determine the distribution of methanol in liquid and vapour phase. A focus of this work was to create a comprehensive solubility study to fill the gaps in the experimental data required to optimise thermodynamic models. A limited number of methane solubility results in methanol and aqueous solutions are presented in this work. The solubility of methane in ethanol and aqueous solutions were also measured. They were used to verify the reliability of the equipment as well as assist in the optimisation of the CPA-SRK72 EoS. The data from the literature and this work are used to correlate the CPA-SRK72 to the solubility of methane in methanol, ethanol and their solutions using single variable BIPs as described above.

To create a more complete image of methanol and ethanol distribution, the saturation pressure of a number of binary, ternary and quaternary systems were measured. The binary measurements consist of methane and a hydrocarbon phase, the ternary measurements are in the presence of an alcohol inhibitor and quaternary systems contain excess water to determine the effect of water on the saturation pressure. The measurements are compared to the CPA-SRK72 EoS calculations tuned using the BIPs from the solubility measurements in this work and the data from literature.

A very limited number of methanol and ethanol vapour content measurements are also presented to evaluate the CPA-SRK72 vapour content predictions.

The overall conclusion of this work together with future work recommendations are presented in Chapter 5.

1.4 References

[1] K.A. Udachin, J.A. Ripmeester, A complex clathrate hydrate structure showing bimodal guest hydration., Nature. 397 (1999) 420–3. doi:10.1038/17097.

[2] M. Kapateh, Frozen Assets, Chem. Eng. (2013) 42.

[3] J. Carroll, Natural Gas Hydrates: A Guide for Engineers, Elsevier Science, 2014.

[4] E.D. Sloan, Jr., C. Koh, Clathrate Hydrates of Natural Gases, Third Edition, CRC Press, 2007.

[5] J.A. Ripmeester, J.S. Tse, C.I. Ratcliffe, B.M. Powell, A new clathrate hydrate structure, Nature. 325 (1987) 135–136. doi:10.1038/325135a0.

[6] E.D. Sloan, Fundamental principles and applications of natural gas hydrates., Nature. 426 (2003) 353–63. doi:10.1038/nature02135.

[7] M. Von Stackelberg, Feste gashydrate, Naturwissenschaften. 36 (1949) 327–333.

[8] M. von Stackelberg, H.R. Muller, Solid gas hydrates II, Z. Elektrochem. 58 (1954) 25–39.

[9] T. Collett, Natural Gas Hydrates—Vast Resource, Uncertain Future, USGS. (2001).

[10] L. Langley, Methane hydrates, ORNL Report. (2000) 1–3. http://web.ornl.gov/info/reporter/no16/june00.pdf.

[11] G.M. Kontogeorgis, E.C. Voutsas, I. V. Yakoumis, D.P. Tassios, An Equation of State for Associating Fluids, Ind. Eng. Chem. Res. 35 (1996) 4310–4318. doi:10.1021/ie9600203.

Chapter 2 – THERMODYNAMIC MODELLING

2.1 Introduction

An Equation of State (EoS) is an analytical thermodynamic expression relating pressure (P) to temperature (T) and volume (V), thus describing the behaviour of matter under a given set of physical conditions. Equations of State are useful in describing fluid properties, multicomponent mixtures and solids. [1]

It is fundamentally important to be able to describe the PVT behaviour of real multicomponent hydrocarbon fluids in order to safely and economically operate petroleum engineering operations. They are important for simulation software used to design safe and economically viable chemical process and transport equipment.

Numerous EoS have been proposed over the years with either an empirical, semi-empirical or theoretical basis. It is very difficult to determine the suitability of an EoS for multicomponent systems. [2,3] Choosing a suitable EoS requires a degree of experience and predictive and correlative analysis with experimental results. Equations of state have two or more adjustable parameters which can be fitted to experimental results. Classical cubic Equations of State such as Soave-Redlich-Kwong (SRK) [4] and Peng-Robinson (PR) [5] are often highly capable of predicting non-polar and partially polar multicomponent system phase behaviours [6–8]. The prediction capabilities reduce significantly in systems with molecules capable of forming strong associating bonds, such as substances that form numerous hydrogen bonds, particularly when both vapour-liquid equilibria (VLE) and liquid-liquid equilibria (LLE) are required over extended temperature and pressure ranges.

Approaches in applied statistical mechanics have seen significant advancement due to the exponential growth in computing power over the last two decades. This has resulted in these methodologies being more commonly applied in chemical engineering modelling. To simplistically explain this theory, the Helmhotz free energy of fluids may be divided into several contributing parameters, where each parameter correlates to a specific type of interaction within or between the molecules. Numerous Equations of state utilise this theory such as SAFT (Statistic Associating Fluid Theory) employing Wertheim's theory of association, [9] APACT (Associated Perturbed Anistropic Chain Theory), [10] PC-SAFT (Perturbed Chain Statistical Association Theory) [11] and ϒ-SAFT. [12]

Statistical theory based Equations of State account for bond description of the molecular interaction and how these interactions correlate to the macroscopic behaviour of the fluids. When the parameters in these EoS have been adjusted based on the experimental data, they are capable of calculating the phase behaviour of non-ideal fluids, which may be used in numerous processes, pipeline design and flow assurance simulation calculations and software. When experimental data are not available, it is possible to correlate parameters based on similar systems, however it is important to note that this reduces the reliability of the EoS. Statistical models are highly complex and not readily accepted or adopted by the industry. Thus a number of projects have been undertaken to combine the association term from Statistical Association Fluid Theory (SAFT) with a classical cubic EoS. [13,14]. Such an EoS is expected to produce reliable predictions solely on Binary Interaction Parameters (BIPs).

A simplified association based EoS was proposed by Elliott et al. [15] which is known as Elliott-Suresh-Donohue (ESD), combining a semi-empirical equation with Wertheim's Association term, successfully predicting the phase behaviour of alcohol-alkanes and acid-alkanes, [15] water-alkanes and alcohol-alkane [16,17] and water-alcohol-alkanes-gases VLE. [18]

In addition to models based on Wertheim's theory, lattice fluid and chemical theories have been used to model associating systems. Anderko used chemical theory in cubic EoS to predict the phase behaviour of various alcohol-hydrocarbon and cross-associating water-alcohol systems. It was made up of a viral expansion truncated after the fourth coefficient and a closed-form term approximating the higher coefficients. The results showed good agreement with the experimental data. [19,20] An overview together with capabilities and limitations of such Equations of State are discussed in more detail by Kontogeorgis and Coutsikos in a review paper. [21]

This work focused on the optimisation of the CPA-SRK72 EoS, a combination of the EoS proposed by Soave [4] and the association term based on SAFT. It was developed by Kontogeorgis et al. [22] This EoS has shown to predict the phase behaviour of systems containing alkanes, alcohols, glycols and water with high degree of accuracy. [23–26] It is important to note the simplicity and prediction speeds are achieved at the cost of losing the molecular insight observed during Statistical Modelling.

In this work the CPA-SRK72 has been utilised to model the phase behaviour of systems containing associating fluids such as water, alcohols and glycols. The main focus of this work was to produce the experimental data required to optimise Equations of State. The

CPA-SRK72 EoS was optimised using the data from this work and the literature. Many steps were taken to ensure the reliability of the EoS optimisation, however it is important to note, due to the limitation of data in the open literature it is essential to produce independent experimental data to fully validate the reliability of the EoS predictions and calculations in this work.

2.2 CPA Equation of State

Molecules which form hydrogen bonds often demonstrate unexpected behaviours that are not anticipated for systems with similar structures. These strong attractions between molecules results in the formation of molecular clusters. In multicomponent systems, this may occur between molecules of the same species, known as self-association, or between molecules of various species, referred to as solvation or cross-association. Such interactions can greatly affect the thermodynamic behaviour of fluids. Thus it is important to consider chemical equilibria between molecular clusters when thermodynamic models are being developed to increase the reliability of predictions for such systems.

The CPA-SRK72 is briefly described in this chapter. More detailed descriptions can be found published by Kontogeorgis et al. [22,24,27]

The EoS is described in terms of compressibility factors, *Z*.

Eq. 2.1 is the CPA-SRK72 EoS in terms of compressibility factors, where Z^{SRK} is the compressibility factor contribution from SRK and Z^{CPA} is the compressibility contribution form the association term.

$$Z^{CPA} = Z^{SRK} + Z^{Assoc} \tag{2.1}$$

Eq. 2.2 is the Compressibility factor from the Soave-Redlich-Kwong EoS

$$Z^{SRK} = \frac{v}{v-b} - \frac{a}{RT(v+b)} \tag{2.2}$$

Eq. 2.3 is the compressibility factor from the association term

$$Z^{Assoc} = -\frac{1}{2}\left(1+\rho\frac{\partial \ln g}{\partial \rho}\right)\sum_i \sum_{A_i} x_i \left(1-X_{A_i}\right) \tag{2.3}$$

Where v is the molar volume, X_{A_i} is the mole fraction of the molecule i not bonded to site *A* and x_i is the superficial mole fraction of component *i*. The lower case letter *i* denotes molecules and the capital letter *A* denotes the bonding site on the specified molecule.

This EoS accounts for the non-directional interaction contribution between the molecules while the association term describes the specific site-site interaction caused by hydrogen bonding.

2.3 Association Energy and Volume

These hydrogen bonds are strong, short range and demonstrate a high degree of localisation. Figure 2.1 illustrates a rudimentary example of the spheres/spherical segments, which only contain one associating site, A. CPA-SRK72 uses square-well sites to model the association sites. [22] These spheres are only capable of forming an AA-bonded dimer when the optimum distance and orientation is reached. The degree of dimerization has a direct dependency on the AA bond strength.

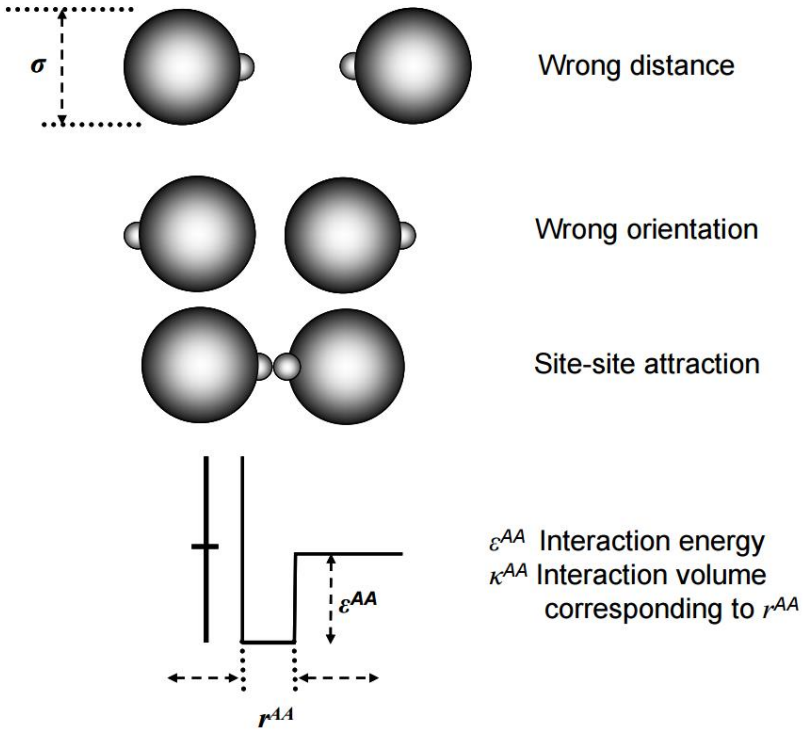

Figure 2.1. Square-well potential model of hard spheres with a single associating site *A* showing a simplified example of molecular association as a result of short range, highly orientation, site-site attraction. [27]

The quantification of the associating bond strength can be achieved with a square-well potential, the centre of which is on the site A. The two characterisation parameters are

- ε^{AA} – Association Energy (well depth)
- k^{AA} – Association volume (well width, r^{AA})

2.4 Fraction of Non-Bonded Associating Molecules, X^A

Mixtures contain a variety of monomers and associated clusters, thus it is required to define mole fractions (X) for the components and their respective monomers. x_i denotes the mole fraction of all of the components, i. The mole fraction of the molecules not bonded at site A is X_{A_i} and hence the mole fraction of the molecules i bonded to site A can be described by $1-X_{A_i}$. This describes both pure and multicomponent self-associated compounds. The CPA EoS may be expressed in terms of pressure with the sum of the SRK EoS and the contribution association term published by Michelsen and Hendriks shown in Eq. 2.4: [28]

$$P=\frac{RT}{V_m-b}-\frac{\alpha(T)}{V_m(V_m+b)}-\frac{1}{2}\left(\frac{RT}{V_m}\right)\left(1+\frac{1}{V_m}\frac{\partial \ln g}{\partial\left(\frac{1}{V_m}\right)}\right)\sum_i x_i\sum_{A_i}\left(1-X_{A_i}\right) \qquad (2.4)$$

Where V_m is the molar volume, X_{A_i} is the fraction of A-sites of molecular i that are not bonded with other active sites and x_i is the mole fraction of the component i.

The term X_{A_i} is calculated by Eq. 2.5.

$$X_{A_i}=\frac{1}{1+(1/V_m)\sum_j x_j\sum_{B_j}X_{B_j}\Delta^{A_iB_j}} \qquad (2.5)$$

Where B_j is the summation over all sites. $\Delta^{A_iB_j}$ is the association (binding) strength between site A on molecule i and site B on molecule j, which can be calculated by Eq. 2.6.

$$\Delta^{A_iB_j}=g(V_m)^{ref}\left[\exp\left(\frac{\varepsilon^{A_iB_j}}{RT}\right)-1\right]b_{ij}\beta^{A_iB_j} \qquad (2.6)$$

Where $\varepsilon^{A_iB_j}$ and $\beta^{A_iB_j}$ are the association energy and volume of interaction between site A of molecule i and site B of molecule j, respectively. $g(V_m)^{ref}$ is the contact value of the radial distribution function for the reference fluid.

The radial distribution function derived from the Carnaham-Starling EoS can be calculated using Eq. 2.7 and 2.8.

$$g(V_m)^{ref}=\frac{1}{1-1.9\eta} \qquad (2.7)$$

The reduced fluid density, η can be calculated using:

$$\eta = \left(\frac{1}{4V_m} \right) b \tag{2.8}$$

Where V_m is the molar volume and b is assumed to be temperature independent.

The energy parameter, α, is calculated using a Soave type temperature dependant equation shown in Eq. 2.9.

$$\alpha(T) = a_0 \left[1 + c_1 \left(1 - \sqrt{T_r} \right) \right]^2 \tag{2.9}$$

Where T_r is the reduced temperature $\frac{T}{T_c}$ and c_1 is the pure component parameter. The CPA-SRK72 constitutes of five pure component parameters. Three of these parameters are assigned to the non-associating components (a_0 , b and c_1) and two additional parameters for associating components ($\varepsilon^{A_iB_j}$ and $\beta^{A_iB_j}$). These parameters are usually obtained by fitting experimental vapour pressure and saturated liquid density data.

For non-associating compounds the a_0 and b are calculated from the critical conditions using Eq. 2.10 – 2.13:

$$a = \frac{\Omega_a R^2 T_c^2}{P_c} \tag{2.10}$$

$$b = \frac{\Omega_b R T_c}{P_c} \tag{2.11}$$

Where:

$$\Omega_a = 0.66121 - 0.76105 Z_c \tag{2.12}$$

and

$$\Omega_b = 0.02207 - 0.20868 Z_c \tag{2.13}$$

Table 2.1. CPA Pure Compound Parameters for Water, Alcohols and Glycols used in this Work.

	a_0 (bar L^2 mol^{-2})	b (L/mol)	c_1	ε (bar L mol^{-1})	β (10^3)	*Reference*
Water	1.228	0.01452	0.6736	166.55	69.2	Kontogeorgis et al. [22]
Methanol	4.053	0.03098	0.4310	245.91	16.1	Kontogeorgis et al. [22]
Ethanol	8.672	0.04908	0.7369	215.32	8.0	Folas et al. [29]
MEG	10.819	0.05140	0.6744	197.52	14.1	Derawi et al. [30]
DEG	26.408	0.0921	0.7991	196.84	6.4	Derawi et al. [30]
TEG	39.126	0.1321	1.1692	143.37	18.8	Derawi et al. [30]

2.5 Association Schemes

The association scheme directly effects the association term of CPA. The association scheme and maximum number of association sites depend on the location of its constituting hydrogen and lone pairs on acceptor atoms. It also depends on whether the molecules form dimers, trimers, oligomers. Furthermore, steric hindrance may be a factor in association scheme selection. [27,31]

Huang and Radosz categorised association into eight different schemes which in turn can be used depending on involved molecules, number and type of associating sites.

Acids are categorised using the one-site (*1A*) scheme, under the condition that the site is able to bond with a lone pair electron, a *H* atom, or a site of the same type. Alcohols and amines are categorised under the two-site (*2B*) or three-site (*3B*) schemes. In the *3B* scheme in the case of alcohols, sites A and B relate to the oxygen lone pairs, whereas site *C* relates to a hydrogen atom.

Highly hydrogen bonded materials such as glycols and water are categorised under the four-site (*4C*) association scheme. Due to the two proton donors and two proton acceptors per molecule, and thus the occurrence of hydrogen bonding between the two hydrogen atoms and the two lone pairs of electrons in oxygen atom of water molecules, this scheme was adopted for the modelling in this work.

Table 2.2 lists the associating schemes described by Huang and Radosz. [31]

Table 2.2. Association schemes based on the Huang and Radosz terminology. [24,31]

Species	Formula	Type	Site fractions (X)
Acids	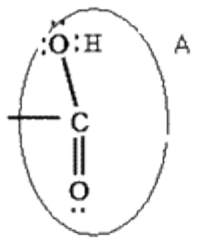	1A	$X_1 = X^A$
Alcohol	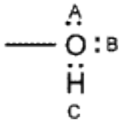	3B	$X^A = X^B; X^C = 2X^A - 1$ $X_1 = X^A X^B X^C$
	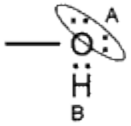	2B	$X^A = X^B$ $X_1 = X^A X^B$
Glycols	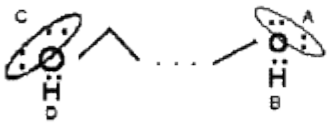	4C	$X^A = X^B = X^C = X^D$ $X_1 = X^A X^B X^C X^D$
Water	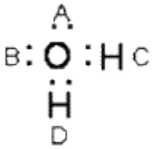	4C	$X^A = X^B = X^C = X^D$ $X_1 = X^A X^B X^C X^D$
	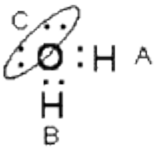	3B	$X^A = X^B; X^C = 2X^A - 1$ $X_1 = X^A X^B X^C$
	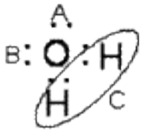	3B	$X^A = X^B; X^C = 2X^A - 1$ $X_1 = X^A X^B X^C$

2.6 Mixing Rules

In order to extend the CPA-SRK72 predictions to multicomponent systems, mixing rules are required. These mixing rules are only needed for the SRK part of the EoS. To achieve this the conventional van der Waals mixing rules for *b* and *a(T)* can be used. The combining rule can be used for the association part to combine $\varepsilon^{A_i B_j}$ and $\beta^{A_i B_j}$. Eq 2.14 and 2.15 show the classical Van der Waals mixing rules:

$$b = \frac{\sum_i n_i \sum_{A_i} n_j b_{ij}}{n^2} \tag{2.14}$$

$$a(T) = \frac{\sum_i n_i \sum_{A_i} n_j a_{ij}(T)}{n^2} \tag{2.15}$$

Where n_i is the number of moles of component *i.*

The classical combining rules are shown by Eq. 2.16 and 2.17:

$$a_{ij} = (1 - k_{ij})\sqrt{a_i a_j} \tag{2.16}$$

$$b_{ij} = \frac{b_i + b_j}{2} \tag{2.17}$$

In order to calculate the association strength, combining rules can be used for the association energy and volume parameters. The arithmetic mean of cross-association energy is directly proportional to the enthalpy and entropy of hydrogen bonding as well as the geometric mean of cross association volume. It has also shown to produce the best overall results for cross-associating systems containing glycols/alcohol and water. [32–34] Eq. 2.18 and 2.19 show the combining rules used to calculate the association energy and volume parameters between the various associating molecules.

$$\varepsilon^{A_i B_j} = \frac{\varepsilon^{A_i B_j} + \varepsilon^{A_i B_j}}{2} \tag{2.18}$$

$$\beta^{A_i B_j} = \sqrt{\beta^{A_i B_j} \beta^{A_i B_j}} \tag{2.19}$$

2.7 CPA EoS - Fugacity Coefficients

Partial derivatives of the Helmholtz function, *A(T,V,n)* can be used to calculate thermodynamic properties. However, it is far less time consuming to use the partial derivatives of the reduced Helmholtz function. Eq. 2.20 is used to calculate the fugacity coefficient of a component in a mixture, Φ_i: [35]

$$RT \ln \Phi_i = \left(\frac{\partial A^r}{\partial n_i} \right)_{T,V,n_j} - RT \ln Z \tag{2.20}$$

The Helmholtz function is calculated by combining the SRK EoS with the association term shown in Eq. 2.21.

$$A^r = A^r SRK + A^r_{Association} \tag{2.21}$$

The fugacity coefficient for the SRK term can be calculated using Eq. 2.22 – 2.29: [35]

$$\frac{\partial}{\partial n_i}\left(\frac{A^r_{SRK}}{RT}\right)_{T,V,n_j} = F_n + F_B B_i + F_D A_i \tag{2.22}$$

Where:

$$F_n = -\ln\left(1-\frac{B}{V}\right) \tag{2.23}$$

$$F_B = -g_B - \frac{A}{T}F_B \tag{2.24}$$

$$F_D = -\frac{f}{T} \tag{2.25}$$

$$f = \frac{\ln\left(1+\frac{B}{V}\right)}{RB} \tag{2.26}$$

$$g_B = -\frac{1}{V-B} \tag{2.27}$$

$$f_B = -\frac{f+Vf_V}{B} \tag{2.28}$$

$$f_v = -\frac{1}{RV\left(V+B\right)} \tag{2.29}$$

Eq. 2.30 and 2.31 show the composition derivatives of the co-volume and the energy term, A_i and B_i respectively:

$$A_i = \frac{\partial}{\partial n_i}\left(n^2 a\right)n_j = 2\sum_j n_j a_{ij} \tag{2.30}$$

$$B_i = \frac{\partial}{\partial n_i}\left(n^2 a\right)n_j = \frac{2\sum_j n_j b_{ij} - B}{n} \tag{2.31}$$

Eq. 2.32, 2.33 and 2.34 show the simplified equation introduced by Michelsen and Hendricks [28] to calculate the association contribution to the chemical potentials.

$$\frac{\partial}{\partial n_i}\left(\frac{A^r_{Association}}{RT}\right) = -\sum_{A_i} \ln X_{A_i} + \frac{h}{2}\frac{\partial \ln g}{\partial n_i} \tag{2.32}$$

$$h = \sum_i n_i \sum_{A_i} \left(1 - X_{A_i}\right) \tag{2.33}$$

$$\frac{\partial \ln g^{simplified}}{\partial n_i} = \frac{0.475B}{V - 0.475B} \tag{2.34}$$

2.8 Binary Interaction Parameters (BIPs)

The Binary Interaction Parameters (BIPs) between the associating and non-associating compounds were adjusted using the solubility data, through a Simplex algorithm utilising the Objective Function, *OF1*, displayed in Equation 2.35.

$$OF1 = \frac{1}{N}\sum_{1}^{N}\left|\frac{x_{\exp} - x_{cal}}{x_{\exp}}\right| \tag{2.35}$$

Where x is the solubility of the gas in alcohol/glycol or aqueous solutions**,** N is the number of data points.

Equation 2.36 shows the Objective Function used for BIPs adjustment between water and alcohol/glycol.

$$OF2 = \frac{1}{N^{BP}}\sum_{1}^{NBP}\left|\frac{P_{\exp} - P_{cal}}{P_{\exp}}\right| + \frac{1}{N^{SLE}}\sum_{1}^{N^{SLE}}\left|\frac{T_{\exp} - T_{cal}}{T_{\exp}}\right| \tag{2.36}$$

2.8.1 Water-non-Associating Component BIPs

Hydrocarbons have a varying degree of solubility in water. Extensive experimental studies have been conducted over the years involving the solubility of hydrocarbons in water within a wide range of pressures and temperatures. A detailed literature review of these data were conducted by Haghighi [36] in his thesis. These data were used to develop the binary interaction parameters between water and the various hydrocarbons.

The water-hydrocarbon BIPs were developed by Haghighi [36] in an earlier work. This was achieved by minimising the Objective Function, OF1 shown in Eq. 2.35, using the solubility of each component in water in the range of 273.15 – 393.15 K, developing temperature dependent k_{ij}, shown in Eq. 2.37.

$$k_{ij} = A + \frac{B}{T} \tag{2.37}$$

Table 2.3 shows the optimised BIPs between water and non-associating compounds used in this work.

Table 2.3. Interaction parameters between water and non-associating components. [36]

Component	A	B
Methane	0.8613	-251.0540
Heptane	0.3926	-121.8260
Nonane	0.0297	-54.4144
Decane	-0.0309	0
undecane	-0.1780	0
dodecane	-0.0846	0
Carbon Dioxide	0.1099	-53.7586

The modelling of the binary CO_2 water system has been fully detailed and validated in a previous publications [37,38]

2.8.2 Alcohol-Hydrocarbon BIPs

As mentioned earlier, methanol is one of the most commonly used gas hydrate inhibitors in the industry. It is also used in gas dehydration, sweetening and liquid recovery. [39] The BIP between methane and pure methanol used in this work was published by Haghighi *et al.* [40]

The solubility data from Wang et al. [41] and this work are used independently to tune concentration dependant BIPs for methanol solutions. The BIPs between methane and ethanol and aqueous solutions are developed using only the data from this work due to the scarcity of data in the open literature. The BIPs generated in this work are reported in Chapter 4.

The BIPs between heavier hydrocarbons used during the experimental work in this study and methanol/ethanol were set to zero.

2.8.3 Methane-Heavy Hydrocarbon BIPs

The BIPs between heavier hydrocarbons used in this work and methane were calculated using the group contribution method introduced and evaluated by Jaubert et al. [42,43]

2.8.4 Alcohol-Water BIPs

The BIPs methanol/ethanol and water used in this work were calculated by Haghighi. [36] The data from the literature listed in Table 2.4 were used to regress the BIPs between methanol and water.

Table 2.4. Vapour-Liquid and Solid-Liquid data for water – methanol binary systems – BP: Bubble Point, DP: Dew Point and FP: Freezing Point

Reference	Type of Data	*T*/K	*P*/ MPa	*N*.pts
Pushin and Glagoleva [44]	FP	177 - 260	0.1	15
Washburn [45]	FP	217 - 266	0.1	7
Feldman and Dahlstrom [46]	FP	233 - 266	0.1	6
Frank et al. [47]	FP	217 - 263	0.1	7
Gristwold and Buford [48]	BP	340.95 - 364.25	0.1	8
Ross [49]	BP	188 - 266	0.1	8
Dalager [50]	BP & DP	337.85 - 373.15	0.1	26
Kato et al. [51]	BP & DP	337.15 - 373.15	0.1	24
Maripuri and Ratcliff [52]	BP & DP	338.8 - 370.0	0.1	16
McGlashan and Williamson [53]	BP	308.15 - 338.15	0.006 - 0.1	39
Ott et al. [54]	FP	157 - 273	0.1	30
Ochi and Kojima [55]	BP	371.15 - 373.15	0.1	20
Green and Venek [56]	BP	291.15	0.1	11
Khalfaoui et al. [57]	BP & DP	337.15 - 373.15	0.1	12
Christensen [58]	BP & DP	333.15 - 373.15	0.02 - 0.04	5
Yao et al. [59]	BP & DP	318.15	0.01-0.04	11

The correlation shown in Eq. 2.38 was proposed by Haghighi [36] to calculate temperature dependant k_{ij} values between methanol-water.

$$k_{ij} = 3.4463\times10^{-6}T^2 - 9.5986\times10^{-4}T - 0.1197 \qquad (2.38)$$

Haghighi [36] evaluated the calculated k_{ij}, which showed good agreement with the experimental data. The data published by Kurihara et al. [60] and Lide [61] were used for independent validation of the BIP calculations.

The data from the literature shown in Table 2.5 were used to calculate BIPs between water and ethanol.

Table 2.5. Vapour-Liquid equilibrium data for water – ethanol binary systems – BP: Bubble Point and FP: Freezing Point

Reference	Type of Data	*T*/K	*P*/ MPa	*N*.pts
Barr-David and Dodge [62]	BP	423.15 - 623.15	0.56 - 19	84
Dalager [50]	BP	351.35 - 373.15	0.1	27
D'Avila and Silva [63]	BP	283.15 - 303.15	0.002 - 0.01	25
Kolbe and Gmehling [63]	BP	363.25 - 423.65	0.1 - 1	114
Ochi and Kojima [55]	BP	370.3 - 373.13	0.1	22
Kurihara et al. [60]	BP	323.15 - 363.15	0.004 - 0.16	202
Lide [61]	FP	228 - 273	0.1	32

The correlation shown in Eq. 2.39 was proposed by Haghighi [36] to calculate temperature dependant k_{ij} values between ethanol-water.

$$k_{ij} = -5.6946\times10^{-7}T^3 + 4.9661\times10^{-4}T^2 - 0.1412\times T - 13.0024 \qquad (2.39)$$

Haghighi [36] evaluated the calculated k_{ij}, which showed good agreement with the experimental data. The data published by Rieder and Thompson [64] and Anderson et al. [65] were used for independent validation of the BIP calculations.

2.8.5 Glycol-Water BIPs

The glycol BIPs used in this work were calculated by Haghighi. [36] The data from the literature listed in Table 2.6 were used to regress the BIPs between MEG and water.

Table 2.6. Vapour-Liquid and Solid – Liquid equilibrium data for the water – MEG binary system (BP: Bubble Point, DP: Dew Point and FP: Freezing Point)

Reference	Type of Data	*T*/K	*P*/ MPa	*N*.pts
Olsen et al. [66]	FP	227 - 270	0.1	9
Washburn [45]	FP	236 - 273	0.1	6
Trimble and Potts [67]	BP	342.15 - 469.15	0.033 - 0.1	79
Conrad et al. [47]	FP	223 - 270	0.1	7
Spangler and Davies [68]	FP	237 - 270	0.1	6
Ross [49]	FP	252 - 270	0.1	10
Mellan [69]	BP	373.15 - 470.5	0.1	41
Nath and Bendert [70]	BP & DP	338.25 - 363.45	0.018 - 0.7	42
Villamanan et al. [71]	BP	333.15	0.0002 - 0.019	24
Lee et al. [72]	BP	383.15 - 457.15	0.1	18
Cordray et al. [73]	FP	217 - 273	0.1	16
Lancia et al. [74]	BP	371.15 - 395.15	0.004 - 0.15	42

The correlation shown in Eq. 2.40 was proposed by Haghighi [36] to calculate temperature dependant k_{ij} values between MEG – water.

$$k_{ij} = 5.6294 \times 10^{-4} T - 0.2313 \qquad (2.40)$$

Haghighi [36] evaluated the calculated k_{ij}, which showed good agreement with the experimental data. The data published by Chiavone-Filho et al. [75] and Lide [61] were used for independent validation of the BIP calculations.

The Binary Interaction Parameters (BIPs) between water and DEG and TEG were adjusted using literature SLE data from Gjertsen et al [76], Burgass et al. [77] and TEG boiling point data from Piemonte et al. [78]

2.8.6 Glycol-CO_2 BIPs

Glycols are commonly used in the petroleum industry to prevent hydrate formation, either as a thermodynamic inhibitor or in dehydration units. Glycols have low vapour pressures and thus do not exhibit the loss issues associated with methanol. However, this low pressure makes the measurement of glycols in the vapour phase extremely difficult, thus the CO_2 solubility in glycols and solutions are used to regress the BIPs. The BIPs for CO_2 in pure MEG and DEG are regressed using the data from Jou et al. [79] and Zheng et al. [80]. The BIP between CO_2 and TEG are calculated using the data from Jou et al. [81] and this work. The solubility of CO_2 in MEG, DEG and TEG solutions from this work are used to regress glycol concentration dependant BIPs. These BIPs are shown in Chapter 3.

2.9 Conclusion

Many attempts have been made over the last 100 years to develop Equations of State which are capable of predicting the behaviour of materials at various *PVT* conditions. Two of the most popular Equations of State used for many engineering designs are SRK and PR. They have been shown to be very reliable when predicting the behaviour of non-associating systems. However, their reliability decreases significantly when predicting the *PVT* properties of systems containing polar components such as water and alcohols. These shortcomings can be partially compensated by using non-density dependant mixing rules.

To improve the predictions further numerous attempts have been made to develop Equations of States utilising the advances in statistical mechanics and computing, resulting in a number of SAFT based EoS. However, these Equations of State are complicated and have proven somewhat unpopular in the industry. CPA-SRK72 has been proposed as a viable option to bridge this gap by utilising the simplicity of SRK and prediction improvements of association theory. This EoS has shown great promise and reliability in predicting the phase behaviour of fluids with associating components.

The main objective of this work has been to produce experimental results which can be used to optimise Equations of State in general. The data have also been used to further optimise the CPA-SRK72 EoS to predict inhibitor distribution in reservoir fluids.

2.10 References

[1] J. Carriere, C.J. Horowitz, J. Piekarewicz, Low-Mass Neutron Stars and the Equation of State of Dense Matter, Astrophys. J. 593 (2003) 463–471. doi:10.1086/376515.

[2] H. Orbey, S.I. Sandler, Modeling Vapor-Liquid Equilibria: Cubic Equations of State and Their Mixing Rules, Volume 1, Cambridge University Press, 1998.

[3] B.E. Poling, J.M. Prausnitz, J.P. O'Connell, The properties of gases and liquids, McGraw-Hill, 2001.

[4] G. Soave, Equilibrium constants from a modified Redlich-Kwong equation of state, Chem. Eng. Sci. 27 (1972) 1197–1203. doi:10.1016/0009-2509(72)80096-4.

[5] D.-Y. Peng, D.B. Robinson, A new two-constant equation of state, Ind. Eng. Chem. Fundam. 15 (1976) 59–64.

[6] M.-J. Huron, G.-N. Dufour, J. Vidal, Vapour-liquid equilibrium and critical locus curve calculations with the soave equation for hydrocarbon systems with carbon dioxide and hydrogen sulphide, Fluid Phase Equilib. 1 (1977) 247–265. doi:10.1016/0378-3812(77)80008-3.

[7] L. Asselineau, G. Bogdanić, J. Vidal, Calculation of thermodynamic properties and vapor-liquid equilibria of refrigerants, Chem. Eng. Sci. 33 (1978) 1269–1276. doi:10.1016/0009-2509(78)85093-3.

[8] M.S. Graboski, T.E. Daubert, A modified Soave equation of state for phase equilibrium calculations. 1. Hydrocarbon systems, Ind. Eng. Chem. Process Des. Dev. 17 (1978) 443–448.

[9] W.G. Chapman, G. Jackson, K.E. Gubbins, Phase equilibria of associating fluids, Mol. Phys. 65 (1988) 1057–1079. doi:10.1080/00268978800101601.

[10] G.D. Ikonomou, M.D. Donohue, Extension of the associated perturbed anisotropic chain theory to mixtures with more than one associating component, Fluid Phase Equilib. 39 (1988) 129–159. doi:10.1016/0378-3812(88)85002-7.

[11] J. Gross, G. Sadowski, Perturbed-Chain SAFT: An Equation of State Based on a Perturbation Theory for Chain Molecules, Ind. Eng. Chem. Res. 40 (2001) 1244–1260. doi:10.1021/ie0003887.

[12] A. Gil-Villegas, A. Galindo, P.J. Whitehead, S.J. Mills, G. Jackson, A.N. Burgess, Statistical associating fluid theory for chain molecules with attractive potentials of variable range, J. Chem. Phys. 106 (1997) 4168. doi:10.1063/1.473101.

[13] P.M. Mathias, H.C. (Air P. and C.I.. A.P. (United S. Klotz, Take a closer look at thermodynamic property models, Chem. Eng. Progress; (United States). 90:6 (1994). http://www.osti.gov/scitech/biblio/7152099 (accessed February 22, 2016).

[14] S. Gupta, J.D. Olson, Industrial Needs in Physical Properties, Ind. Eng. Chem. Res. 42 (2003) 6359–6374. doi:10.1021/ie030170v.

[15] J.R. Elliott, S.J. Suresh, M.D. Donohue, A simple equation of state for non-spherical and associating molecules, Ind. Eng. Chem. Res. 29 (1990) 1476–1485. doi:10.1021/ie00103a057.

[16] S.J. Suresh, J.R. Elliott, Applications of a generalized equation of state for associating mixtures, Ind. Eng. Chem. Res. 30 (1991) 524–532. doi:10.1021/ie00051a013.

[17] S.J. Suresh, J.R. Elliott, Multiphase equilibrium analysis via a generalized equation of state for associating mixtures, Ind. Eng. Chem. Res. 31 (1992) 2783–2794. doi:10.1021/ie00012a025.

[18] A.S. Puhala, J.R. Elliott, Correlation and prediction of binary vapor-liquid equilibrium in systems containing gases, hydrocarbons, alcohols, and water, Ind. Eng. Chem. Res. 32 (1993) 3174–3179. doi:10.1021/ie00024a031.

[19] A. Anderko, A simple equation of state incorporating association, Fluid Phase Equilib. 45 (1989) 39–67. doi:10.1016/0378-3812(89)80166-9.

[20] A. Anderko, Extension of the AEOS model to systems containing any number of associating and inert components, Fluid Phase Equilib. 50 (1989) 21–52. doi:10.1016/0378-3812(89)80282-1.

[21] G.M. Kontogeorgis, P. Coutsikos, Thirty Years with EoS/G E Models—What Have We Learned?, Ind. Eng. Chem. Res. 51 (2012) 4119–4142. doi:10.1021/ie2015119.

[22] G.M. Kontogeorgis, E.C. Voutsas, I. V. Yakoumis, D.P. Tassios, An Equation of State for Associating Fluids, Ind. Eng. Chem. Res. 35 (1996) 4310–4318. doi:10.1021/ie9600203.

[23] G.M. Kontogeorgis, I. V. Yakoumis, H. Meijer, E. Hendriks, T. Moorwood, Multicomponent phase equilibrium calculations for water–methanol–alkane mixtures, Fluid Phase Equilib. 158-160 (1999) 201–209. doi:10.1016/S0378-3812(99)00060-6.

[24] G.M. Kontogeorgis, M.L. Michelsen, G.K. Folas, S. Derawi, N. von Solms, E.H. Stenby, Ten Years with the CPA (Cubic-Plus-Association) Equation of State. Part 1. Pure Compounds and Self-Associating Systems, Ind. Eng. Chem. Res. 45 (2006) 4855–4868. doi:10.1021/ie051305v.

[25] M. Riaz, M.A. Yussuf, G.M. Kontogeorgis, E.H. Stenby, W. Yan, E. Solbraa, Distribution of MEG and methanol in well-defined hydrocarbon and water systems: Experimental measurement and modeling using the CPA EoS, Fluid Phase Equilib. 337 (2013) 298–310. doi:10.1016/j.fluid.2012.09.009.

[26] W. Afzal, M.P. Breil, I. Tsivintzelis, A.H. Mohammadi, G.M. Kontogeorgis, D. Richon, Experimental study and phase equilibrium modeling of systems containing acid gas and glycol, Fluid Phase Equilib. 318 (2012) 40–50. doi:10.1016/j.fluid.2011.12.025.

[27] W.G. Chapman, K.E. Gubbins, G. Jackson, M. Radosz, New reference equation of state for associating liquids, Ind. Eng. Chem. Res. 29 (1990) 1709–1721. doi:10.1021/ie00104a021.

[28] M.L. Michelsen, E.M. Hendriks, Physical properties from association models, Fluid Phase Equilib. 180 (2001) 165–174. doi:10.1016/S0378-3812(01)00344-2.

[29] G.K. Folas, S.O. Derawi, M.L. Michelsen, E.H. Stenby, G.M. Kontogeorgis, Recent applications of the cubic-plus-association (CPA) equation of state to industrially important systems, Fluid Phase Equilib. 228-229 (2005) 121–126. doi:10.1016/j.fluid.2004.08.013.

[30] S.O. Derawi, M.L. Michelsen, G.M. Kontogeorgis, E.H. Stenby, Application of the CPA equation of state to glycol/hydrocarbons liquid–liquid equilibria, Fluid Phase Equilib. 209 (2003) 163–184. doi:10.1016/S0378-3812(03)00056-6.

[31] S.H. Huang, M. Radosz, Equation of state for small, large, polydisperse, and associating molecules, Ind. Eng. Chem. Res. 29 (1990) 2284–2294.

[32] S.O. Derawi, G.M. Kontogeorgis, M.L. Michelsen, E.H. Stenby, Extension of the Cubic-Plus-Association Equation of State to Glycol−Water Cross-Associating Systems, Ind. Eng. Chem. Res. 42 (2003) 1470–1477. doi:10.1021/ie0206103.

[33] Y.-H. Fu, S.I. Sandler, A Simplified SAFT Equation of State for Associating Compounds and Mixtures, Ind. Eng. Chem. Res. 34 (1995) 1897–1909. doi:10.1021/ie00044a042.

[34] E.C. Voutsas, I. V Yakoumis, D.P. Tassios, Prediction of phase equilibria in water/alcohol/alkane systems, Fluid Phase Equilib. 158-160 (1999) 151–163. doi:10.1016/S0378-3812(99)00131-4.

[35] M.L. Michelsen, J.M. Mollerup, Thermodynamic Models: Fundamentals & Computational Aspects, Tie-Line Publications, 2007.

[36] H. Haghighi, PhD Thesis: Phase equilibria modelling of petroleum reservoir fluids containing water, Hydrate Inhibitors and Electrolyte Solutions, (2009).

[37] A. Chapoy, H. Haghighi, R. Burgass, B. Tohidi, On the phase behaviour of the (carbon dioxide+water) systems at low temperatures: Experimental and modelling, J. Chem. Thermodyn. 47 (2012) 6–12. doi:10.1016/j.jct.2011.10.026.

[38] A. Chapoy, R. Burgass, B. Tohidi, I. Alsiyabi, Hydrate and Phase Behavior Modeling in CO 2 -Rich Pipelines, J. Chem. Eng. Data. 60 (2015) 447–453. doi:10.1021/je500834t.

[39] A. Esteban, V. Hernandez, K. Lunsford, Exploit the benefits of methanol, in: 79th GPA Annu. Conv. Atlanta, GA, USA, 2000.

[40] H. Haghighi, A. Chapoy, R. Burgess, S. Mazloum, B. Tohidi, Phase equilibria for petroleum reservoir fluids containing water and aqueous methanol solutions: Experimental measurements and modelling using the CPA equation of state, Fluid Phase Equilib. 278 (2009) 109–116. doi:10.1016/j.fluid.2009.01.009.

[41] L.-K. Wang, G.-J. Chen, G.-H. Han, X.-Q. Guo, T.-M. Guo, Experimental study on the solubility of natural gas components in water with or without hydrate inhibitor, Fluid Phase Equilib. 207 (2003) 143–154. doi:10.1016/S0378-3812(03)00009-8.

[42] J.-N. Jaubert, R. Privat, Relationship between the binary interaction parameters (kij) of the Peng–Robinson and those of the Soave–Redlich–Kwong equations of state: Application to the definition of the PR2SRK model, Fluid Phase Equilib. 295 (2010) 26–37. doi:10.1016/j.fluid.2010.03.037.

[43] J.-N. Jaubert, F. Mutelet, VLE predictions with the Peng–Robinson equation of state and temperature dependent kij calculated through a group contribution method, Fluid Phase Equilib. 224 (2004) 285–304. doi:10.1016/j.fluid.2004.06.059.

[44] N.A. Pushin, A.A. Glagoleva, CCCXXXVII.—The equilibrium in systems composed of water and alcohols: methyl alcohol, pinacone, glycerol, and erythritol, J. Chem. Soc. Trans. 121 (1922) 2813–2822.

[45] E.W. Washburn, International Critical Tables of Numerical Data, Physics, Chemistry and Technology (1st Electronic Edition), Knovel, .

[46] H.B. Feldman, W.G. Dahlstrom, FREEZING POINTS OF THE TERNARY SYSTEM GLYCEROL-METHANOL-WATER, Ind. Eng. Chem. 28 (1936) 1316–1317. doi:10.1021/ie50323a019.

[47] F.H. Conrad, E.F. Hill, E.A. Ballman, Freezing Points of the System Ethylene Glycol–Methanol–Water, Ind. Eng. Chem. 32 (1940) 542–543. doi:10.1021/ie50364a023.

[48] J. Griswold, C.B. Buford, Separation of Synthesis Mixtures Vapor-Liquid Equilibria of Acetone-Methanol-Water, Ind. Eng. Chem. 41 (1949) 2347–2351. doi:10.1021/ie50478a062.

[49] H.K. Ross, Cryoscopic Studies - Concentrated Solutions of Hydroxy Compounds", Ind. Eng. Chem. 46 (1954) 601–610. doi:10.1021/ie50531a054.

[50] P. Dalager, Vapor-liquid equilibriums of binary systems of water with methanol and ethanol at extreme dilution of the alcohols, J. Chem. Eng. Data. 14 (1969) 298–301. doi:10.1021/je60042a022.

[51] M. KATO, H. KONISHI, T. SATO, M. HIRATA, MEASUREMENT OF VAPOR-LIQUID EQUILIBRIA BY DEW-BUBBLE POINT METHOD AND BUBBLE-CONDENSATION POINT METHOD, J. Chem. Eng. Japan. 4 (1971) 6–10. doi:10.1252/jcej.4.6.

[52] V.O. Maripuri, G.A. Ratcliff, Measurement of isothermal vapor-liquid equilibriums for acetone-n-heptane mixtures using modified Gillespie still, J. Chem. Eng. Data. 17 (1972) 366–369. doi:10.1021/je60054a031.

[53] M.L. McGlashan, A.G. Williamson, Isothermal liquid-vapor equilibriums for system methanol-water, J. Chem. Eng. Data. 21 (1976) 196–199. doi:10.1021/je60069a019.

[54] J. Bevan Ott, J. Rex Goates, B.A. Waite, (Solid + liquid) phase equilibria and solid-hydrate formation in water + methyl, + ethyl, + isopropyl, and + tertiary butyl alcohols, J. Chem. Thermodyn. 11 (1979) 739–746. doi:10.1016/0021-9614(79)90005-3.

[55] K. OCHI, K. KOJIMA, A measurement of vapor-liquid equilibria at extreme dilution., J. Chem. Eng. Japan. 20 (1987) 6–10. doi:10.1252/jcej.20.6.

[56] S.J. Green, R.E. Vener, Vapor-Liquid Equilibria of Formaldehyde-Methanol-Water, Ind. Eng. Chem. 47 (1955) 103–109. doi:10.1021/ie50541a037.

[57] B. Khalfaoui, A.H. Meniai, R. Borja, Thermodynamic properties of water + normal alcohols and vapor-liquid equilibria for binary systems of methanol or 2-propanol with water, Fluid Phase Equilib. 127 (1997) 181–190. doi:10.1016/S0378-3812(96)03129-9.

[58] S.P. Christensen, Measurement of dilute mixture vapor–liquid equilibrium data for aqueous solutions of methanol and ethanol with a recirculating still, Fluid Phase Equilib. 150-151 (1998) 763–773. doi:10.1016/S0378-3812(98)00357-4.

[59] J. Yao, H. Li, S. Han, Vapor–liquid equilibrium data for methanol–water–NaCl at 45°C, Fluid Phase Equilib. 162 (1999) 253–260. doi:10.1016/S0378-3812(99)00204-6.

[60] K. Kurihara, T. Minoura, K. Takeda, K. Kojima, Isothermal Vapor-Liquid Equilibria for Methanol + Ethanol + Water, Methanol + Water, and Ethanol + Water, J. Chem. Eng. Data. 40 (1995) 679–684. doi:10.1021/je00019a033.

[61] Lide, CRC Handbook of Chemistry and Physics, 85th Edition, CRC Press, 2004. https://books.google.co.uk/books/about/CRC_Handbook_of_Chemistry_and_Physics_85.html?id=WDll8hA006AC&pgis=1 (accessed March 2, 2016).

[62] F. Barr-David, B.F. Dodge, Vapor-Liquid Equilibrium at High Pressures. The Systems Ethanol-Water and 2-Propanol-Water., J. Chem. Eng. Data. 4 (1959) 107–121. doi:10.1021/je60002a003.

[63] S.G. D'Avila, R.S.F. Silva, Isothermal vapor-liquid equilibrium data by total pressure method. Systems acetaldehyde-ethanol, acetaldehyde-water, and ethanol-water, J. Chem. Eng. Data. 15 (1970) 421–424. doi:10.1021/je60046a010.

[64] R.M. Rieder, A.R. Thompson, Vapor-Liquid Equilibria Measured by a Gillespie Still - Ethyl Alcohol - Water System, Ind. Eng. Chem. 41 (1949) 2905–2908. doi:10.1021/ie50480a060.

[65] R. Anderson, A. Chapoy, H. Haghighi, B. Tohidi, Binary Ethanol−Methane Clathrate Hydrate Formation in the System CH4-C2H5OH-H2O: Phase Equilibria and Compositional Analyses, J. Phys. Chem. C. 113 (2009) 12602–12607. doi:10.1021/jp9021536.

[66] J.C. Olsen, A.S. Brunjes, J.W. Olsen, Freezing and Flow Points for Glycerol, Prestone, Denatured Alcohol, and Methanol, Ind. Eng. Chem. 22 (1930) 1315–1317. doi:10.1021/ie50252a019.

[67] H.M. Trimble, W. Potts, Glycol-Water Mixtures Vapor Pressure-Boiling Point-Composition Relations, Ind. Eng. Chem. 27 (1935) 66–68. doi:10.1021/ie50301a015.

[68] J. Spangler, E. Davies, Freezing Points, Densities, and Refractive Indexes of System Glycerol-Ethylene Glycol-Water, Ind. Eng. Chem. Anal. Ed. 15 (1943) 96–99. doi:10.1021/i560114a004.

[69] E.W. Flick, Industrial Solvents Handbook (5th Edition), William Andrew Publishing/Noyes, 1998. https://app.knovel.com/web/toc.v/cid:kpISHE0009/viewerType:toc/root_slug:industrial-solvents-handbook (accessed March 2, 2016).

[70] A. Nath, E. Bender, Isothermal vapor-liquid equilibriums of binary and ternary mixtures containing alcohol, alkanolamine, and water with a new static device, J. Chem. Eng. Data. 28 (1983) 370–375. doi:10.1021/je00034a007.

[71] M.A. Villamanan, C. Gonzalez, H.C. Van Ness, Excess thermodynamic properties for water/ethylene glycol, J. Chem. Eng. Data. 29 (1984) 427–429. doi:10.1021/je00038a018.

[72] J.I. Lee, A.E. Mather, Solubility of Hydrogen Sulfide in Water, Berichte Der Bunsengesellschaft Für Phys. Chemie. 81 (1977) 1020–1023. doi:10.1002/bbpc.19770811029.

[73] D.R. Cordray, L.R. Kaplan, P.M. Woyciesjes, T.F. Kozak, Solid - liquid phase diagram for ethylene glycol + water, Fluid Phase Equilib. 117 (1996) 146–152. doi:10.1016/0378-3812(95)02947-8.

[74] A. Lancia, D. Musmarra, F. Pepe, Vapor-liquid equilibria for mixtures of ethylene glycol, propylene glycol, and water between 98.DEG. and 122.DEG.C.., J. Chem. Eng. JAPAN. 29 (1996) 449–455. doi:10.1252/jcej.29.449.

[75] O. Chiavone-Filho, P. Proust, P. Rasmussen, Vapor-liquid equilibria for glycol ether + water systems, J. Chem. Eng. Data. 38 (1993) 128–131. doi:10.1021/je00009a031.

[76] L.H. Gjertsen, J.E. Vindstad, I.M. Malvik, A.O. Fredheim, Experimental determination of solid-liquid phase diagrams for glycol/water mixtures - The impact of pressure and hydrocarbon systems, in: Int. Gas Res. Conf., 2001.

[77] R. Burgass, A. Chapoy, B. Tohidi, Solid-Liquid Equilibrium in Water – Glycols Systems: Measurements and Modelling, in: 8th Int. Conf. Gas Hydrates, 8th International Conference on Gas Hydrates, Beijing, 2014.

[78] V. Piemonte, M. Maschietti, F. Gironi, A Triethylene Glycol–Water System: A Study of the TEG Regeneration Processes in Natural Gas Dehydration Plants, Energy

Sources, Part A Recover. Util. Environ. Eff. 34 (2012) 456–464. doi:10.1080/15567031003627930.

[79] F.-Y. Jou, R.D. Deshmukh, F.D. Otto, A.E. Mather, Vapor-Liquid Equilibria of H2S and CO2 and Ethylene Glycol at Elevated Pressures, Chem. Eng. Commun. 87 (1990) 223–231. doi:10.1080/00986449008940694.

[80] D.D.-Q. Zheng, W.W.W.-D. Ma, R. Wei, T.T. Guo, Solubility study of methane, carbon dioxide and nitrogen in ethylene glycol at elevated temperatures and pressures, Fluid Phase Equilib. 155 (1999) 277–286. doi:10.1016/S0378-3812(98)00469-5.

[81] F.-Y. Jou, R.D. Deshmukh, F.D. Otto, A.E. Mather, Vapor-liquid equilibria for acid gases and lower alkanes in triethylene glycol, Fluid Phase Equilib. 36 (1987) 121–140. doi:10.1016/0378-3812(87)85018-5.

Chapter 3 – CO_2 SOLUBILITY IN GLYCOL AND AQUEOUS SOLUTIONS

3.1 Introduction

Over the last few decades the effect of human activities on global warming has become overwhelmingly clear. [1] In addition, the increase in global demand for energy has led energy suppliers to cultivate natural gas reservoirs that were previously deemed un-economical. Carbon dioxide (CO_2) is a common constituent of natural gas, usually accounting for less than 1% of the natural gas stream; however, some reservoirs in Canada and South East Asia contain significantly higher concentrations of CO_2 (>70%), thus economic removal of such constituents is crucial. Natural gas also contains large amounts of water when produced, which can lead to issues such as hydrate formation, as well as the possibility of corrosion.

The research in the last few decades has determined that the CO_2 component of greenhouse gases is one of the major contributors to global warming. The option of storage of CO_2 in underground reservoirs as well as in deep oceans has been researched in depth. [2–4]

Glycols are commonly injected at the well head to prevent hydrate formation; they are also used in glycol dehydration units to remove water from natural gas streams as well as the dehydration of CO_2 for Enhanced Oil Recovery (EOR) systems and sequestration, preventing hydrate formation and corrosion. CO_2 is partially soluble in glycols, resulting in the reduction of efficiency in these dehydration units; therefore knowledge of the phase behaviour of CO_2 in glycols is essential for economic design and operation of process equipment [5]. This study focused on the solubility of CO_2 in Monoethylene Glycol (MEG), Diethylene Glycol (DEG), Triethylene Glycol (TEG) as well as 90, 60 and 40 weight percent (wt%) aqueous solutions of the glycols over a wide temperature and pressure range to ensure its applicability for the modelling requirements of the gas processing industry.

MEG is one of the most commonly used hydrate inhibitors in Europe. The popularity of MEG is due to its low vapour pressure, significantly reducing inhibitor loss through the vapour phase, compared to methanol and ethanol. Occasionally MEG and DEG is used as a hydrate inhibitor as well as for dehydration purposes. TEG is most commonly used in dehydration units; however, in rare circumstances it is also used as a hydrate inhibitor. To mitigate the risk of corrosion and hydrate formation, CO_2 being transported

must undergo a degree of dehydration, thus the knowledge of CO_2-TEG phase behaviour is of utmost importance for the economic design and operation of pure CO_2 and CO_2 rich, multicomponent gas pipelines. Solubility data are essential for developing thermodynamic models capable of predicting phase behaviour in multicomponent systems. The data from this work may be used to develop binary interaction parameters and optimize the classical and statistical models used by operators.

A number of studies have been carried out on the solubility of CO_2 in glycols over the years. Makranczy et al. [6] measured the solubility of CO_2 in the temperature range of 273.15 K – 303.15 K at pressures of up to 4.64 MPa in TEG. Hayduk and Malik reported the solubility of CO_2 in MEG at 298.15 and atmospheric pressure [7]. The solubility of CO_2 in MEG, DEG and TEG were reported by Jou et al. in a series of studies in the temperature range of 298.15 – 403.15 K and pressures from 0.03 – 21 MPa [8–10]. Zheng et al. reported the solubility of CO_2 in MEG at 323.15 –398.15 and 0.2 – 39.6 MPa [11]. Galvão et al. published a number of CO_2 in MEG solubility results in the range of 303.15 – 423.15 K and 0.3 – 6.3 MPa [12]. The solubility of CO_2 in DEG and TEG solutions were also reported by Takashi et al. in the temperature range of 249.26 – 322.04 K and pressure range of 2.5 – 8 MPa [13]. As it is demonstrated the solubility of CO_2 in glycols has been of interest in the past 50 years. However, many of the studies focused on higher temperatures and moderate pressures. The experimental results for the solubility of CO_2 in glycol aqueous solutions are also highly scarce.

3.2 Materials and Method

Table 3.1 shows the materials used during this work together with their suppliers, purities as well as analysis methods used to ensure purity.

Table 3.1. Details of the chemicals, suppliers and purities of the components used in this study.

Chemical Name	Source	Mole % Purity[a]	Certification	Analysis Method[b]
Ethylene Glycol	Fisher Chemicals	99.9	Fisher Chemicals	GC
Diethylene Glycol	Fisher Chemicals	99.9	Fisher Chemicals	GC
Triethylene Glycol	Fisher Chemicals	99.9	Fisher Chemicals	GC
Deionised Water	Pure Lab Elga 2	99	NA	GC
CO_2	BOC	99.995	BOC Certified	GC

[a] No additional purification is carried out for all samples. [b] GC: Gas Chromatography

A schematic of the set-up used for the solubility study is shown in Figure 3.1 and Figure 3.2. Table 3.2 contains the list of keys describing Figure 3.2. The apparatus used in this work was the same as the setup used by Chapoy et al. [14] to measure the saturation pressure of a multicomponent high CO_2 mixture.

A 600 cm^3 (piston) pressure cell was prepared and vacuumed. It was then cooled down to 253.15 K in a freezer for 2 hours. The cylinder was then connected to a main CO_2 cylinder (BOC). All the lines were purged by high pressure CO_2 and the piston cell was loaded with CO_2.

The 350 cm^3 (piston-less) pressure rocking cell was then loaded with 300 cm^3 of glycol/solution via the top keeping the cell horizontal. The pressure rocking cell was then sealed. A vacuum pump was connected to V02, removing the air from the rocking cell, thus minimising the interference of air in the solubility measurements. The 600 cm^3 pressure cell was consequently connected to the rocking cell (V02), the line was purged and CO_2 was injected into the rocking cell. The line was then disconnected from V02. The pneumatic rocking system was used to agitate the mixture until the system demonstrated a steady pressure and temperature on the logger, ensuring equilibrium was reached.

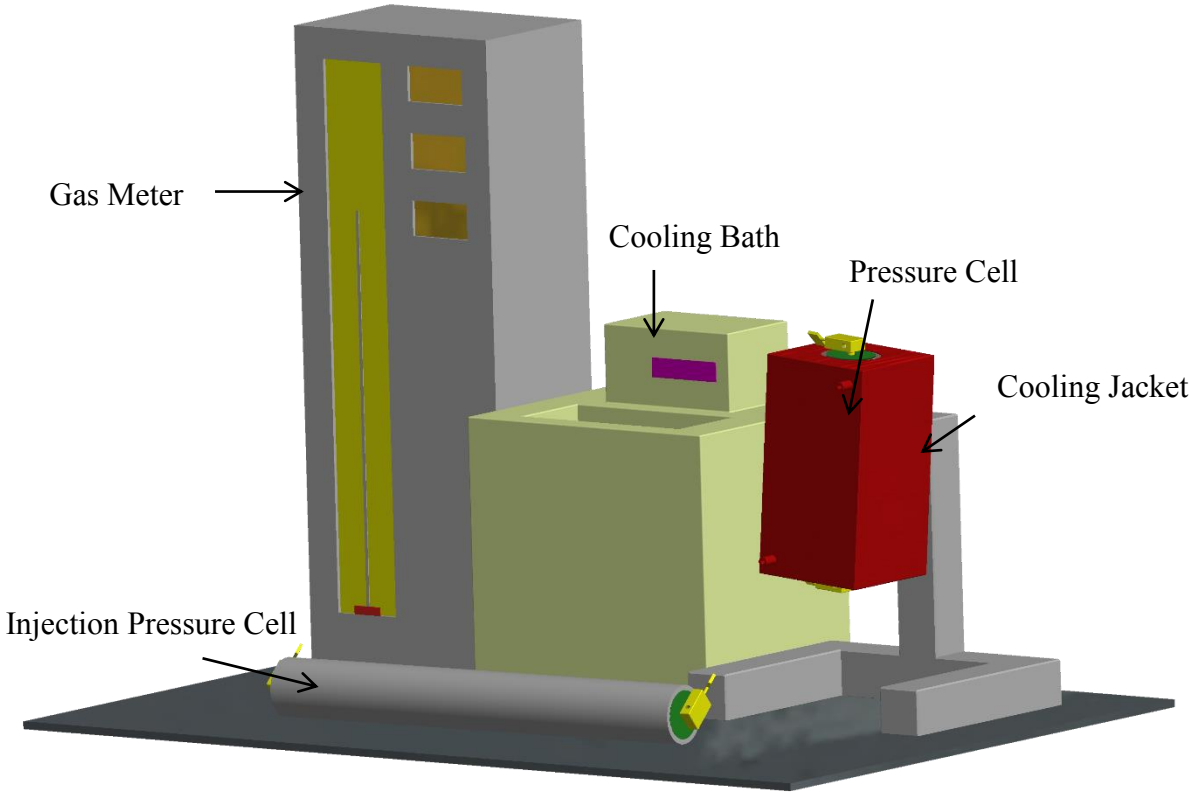

Figure 3.1 3D schematic of the pressure rig used in this work.

A number of steps were required during each solubility measurement. Firstly, the pneumatic rocking system was disabled, and the rocking cell was locked in a vertical position. The CO_2 cylinder was then connected to the rocking cell (V02), the flash tank was connected using V03 and the VINCI Technology manual gas cylinder was connected to the flash tank (V05).

During each measurement the pressure and temperature of the cell, together with the pressure, temperature and initial volume of the gas meter chamber were recorded. The pressure of the cell in the rig was kept constant during sampling by CO_2 injection (V02) from the CO_2 pressure cell. A liquid sample (average of 21 grams per run) was then flashed. The volume of the gas together with the sample weight was then recorded. The density of the CO_2 at each sampling condition (calculated used the Span and Wagner equation of state [15]) was used to determine the mole of CO_2. These were used to calculate the solubility of CO_2 in TEG/solution and standard uncertainty of the measurements as described in Appendix A and B.

The pressure of the cell was increased by CO_2 injection from V01 and V02 and the procedure repeated, producing solubility results at various pressures and at specific temperatures.

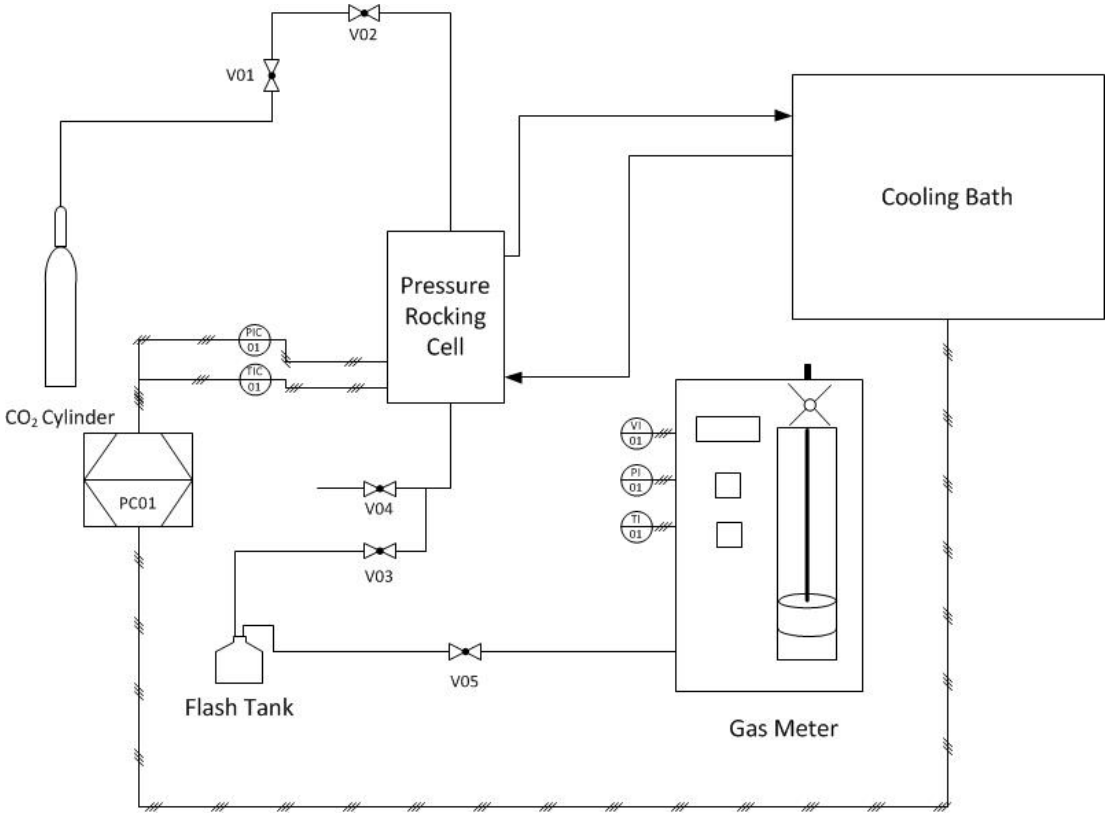

Figure 3.2 showing the rocking cell setup used to measure the solubility of CO_2 in glycol/glycol solutions.

Table 3.2 Key for Figure 3.2.

Key	Description
PI01	Gas Meter Pressure Indicator
PIC01	Equilibrium Cell Pressure Indicator/logger
PC01	Computer Controller/Logger
TI01	Gas Meter Temperature Indicator
TIC01	Equilibrium Cell Temperature Indicator Controller
V01	CO_2 Cylinder Control Valve
V02	Equilibrium Cell Injection Valve
V03	Equilibrium Cell Drain Valve
V04	Equilibrium Cell Drain Valve (Backup)
V05	Gas Meter Inlet Valve
VI01	Gas Meter Volume Indicator

3.3 Results and Discussion

Table 3.3 and Table 3.4 show the solubility of CO_2 in MEG at 7 different isotherms and various pressures where T is temperature in Kelvin, P is the pressure in MPa, x_i is the moles of CO_2 in the aqueous phase and $u_r(x_1)$ is the relative standard uncertainty in moles. These measurements showed a relative standard uncertainty of $u_r(x_1) = 0.026$. The standard uncertainty of the measurements were calculated based on the four main measurement variables combined with the repeatability analysis study published by the author [16]. These variables were the volume of CO_2 measured using the gas meter, the mass of glycol and glycol solution measured using the Toledo (PB3003-S) balance, the standard uncertainty inflicted by the calculation of glycol and water in the atmospheric vapour phase and the mole fraction of CO_2 in the liquid phase using the CPA-SRK72 EoS. The standard uncertainty of the CO_2 density data from NIST was deemed negligible at 0.003%. The apparatus standard uncertainties reported by the manufacturers were then used to calculate the standard uncertainty of each measurement (Appendix A and Appendix B – standard uncertainty equations for CO_2 in glycol and glycol solutions respectively). Figure 3.3 illustrates the solubility of CO_2 in MEG together with CPA-SRK72 model predictions for each isotherm.

Table 3.3. The solubility of CO_2 in MEG (x_1) from T = 263.15 to 298.15, Pressure (P) up to 26 MPa and standard uncertainty $u_r(x_1)$[a].

T/K	*P*/ MPa	x_1 (mol frac)	$u_r(x_1)$	*T*/K	*P*/ MPa	x_1 (mol frac)	$u_r(x_1)$
263.15	0.16	0.0069	0.0001	298.15	0.85	0.0157	0.0002
263.15	0.69	0.0310	0.0003	298.15	0.85	0.0175	0.0002
263.15	0.83	0.0359	0.0002	298.15	1.85	0.0378	0.0003
263.15	2.69	0.1301	0.0006	298.15	1.88	0.0393	0.0003
263.15	3.71	0.1251	0.0006	298.15	0.85	0.0157	0.0002
263.15	8.23	0.1308	0.0006	298.15	0.85	0.0175	0.0002
263.15	12.27	0.1354	0.0006	298.15	1.85	0.0378	0.0003
263.15	24.99	0.1435	0.0006	298.15	1.88	0.0393	0.0003
273.15	0.48	0.0165	0.0001	298.15	2.54	0.0512	0.0003
273.15	1.04	0.0369	0.0002	298.15	3.02	0.0578	0.0003
273.15	1.74	0.0609	0.0003	298.15	3.85	0.0768	0.0004
273.15	3.54	0.1199	0.0006	298.15	3.92	0.0793	0.0004
273.15	7.30	0.1253	0.0006	298.15	5.41	0.1045	0.0005
273.15	11.98	0.1303	0.0006	298.15	6.38	0.1175	0.0006
273.15	17.73	0.1337	0.0006	298.15	6.45	0.1180	0.0006
273.15	25.92	0.1350	0.0006	298.15	6.84	0.1213	0.0006
283.15	0.59	0.0172	0.0001	298.15	7.25	0.1176	0.0006
283.15	1.61	0.0474	0.0003	298.15	7.41	0.1160	0.0006
283.15	3.52	0.0981	0.0005	298.15	8.09	0.1181	0.0006
283.15	4.52	0.1226	0.0006	298.15	10.69	0.1196	0.0006
283.15	16.57	0.1327	0.0006	298.15	11.20	0.1253	0.0006
283.15	20.33	0.1339	0.0006	298.15	13.27	0.1256	0.0006
297.75	0.49	0.0109	0.0002	298.15	13.27	0.1256	0.0006
297.75	1.01	0.0193	0.0001	298.15	14.73	0.1261	0.0006
297.75	6.46	0.1135	0.0005	298.15	14.80	0.1253	0.0006
297.75	10.43	0.1202	0.0006	298.15	19.08	0.1313	0.0006
297.75	17.84	0.1267	0.0006	298.15	19.39	0.1319	0.0006
297.75	21.07	0.1308	0.0006	298.15	23.57	0.1332	0.0006

[a] Standard uncertainties u are at $u_r(x_1) = 0.026$, $u(T) = 0.05$ K and $u(P) = 0.04$MPa

Table 3.4. The solubility of CO_2 in MEG (x_1) from T = 323.15 to 343.15 K, Pressure (P) up to 40 MPa and standard uncertainty $u_r(x_1)$[a].

T/K	P/ MPa	x_1 (mol frac)	$u_r(x_1)$
323.15	0.43	0.0070	0.0001
323.15	0.45	0.0069	0.0001
323.15	1.50	0.0277	0.0002
323.15	1.53	0.0229	0.0001
323.15	2.54	0.0353	0.0002
323.15	3.73	0.0475	0.0003
323.15	3.74	0.0513	0.0003
323.15	10.34	0.1011	0.0005
323.15	10.40	0.0985	0.0005
323.15	15.23	0.1150	0.0005
323.15	15.28	0.1164	0.0005
323.15	23.44	0.1281	0.0006
323.15	23.57	0.1289	0.0006
343.15	0.53	0.0052	0.0001
343.15	1.36	0.0143	0.0001
343.15	1.91	0.0173	0.0001
343.15	3.59	0.0367	0.0002
343.15	7.03	0.0702	0.0004
343.15	8.14	0.0780	0.0004
343.15	12.49	0.1050	0.0005
343.15	18.14	0.1256	0.0006
343.15	26.75	0.1406	0.0006
343.15	36.625	0.1461	0.0007
343.15	40.314	0.1485	0.0007

[a] Standard uncertainties u are at $u_r(x_1) = 0.026$, $u(T) = 0.05$ K and $u(P) = 0.04$MPa

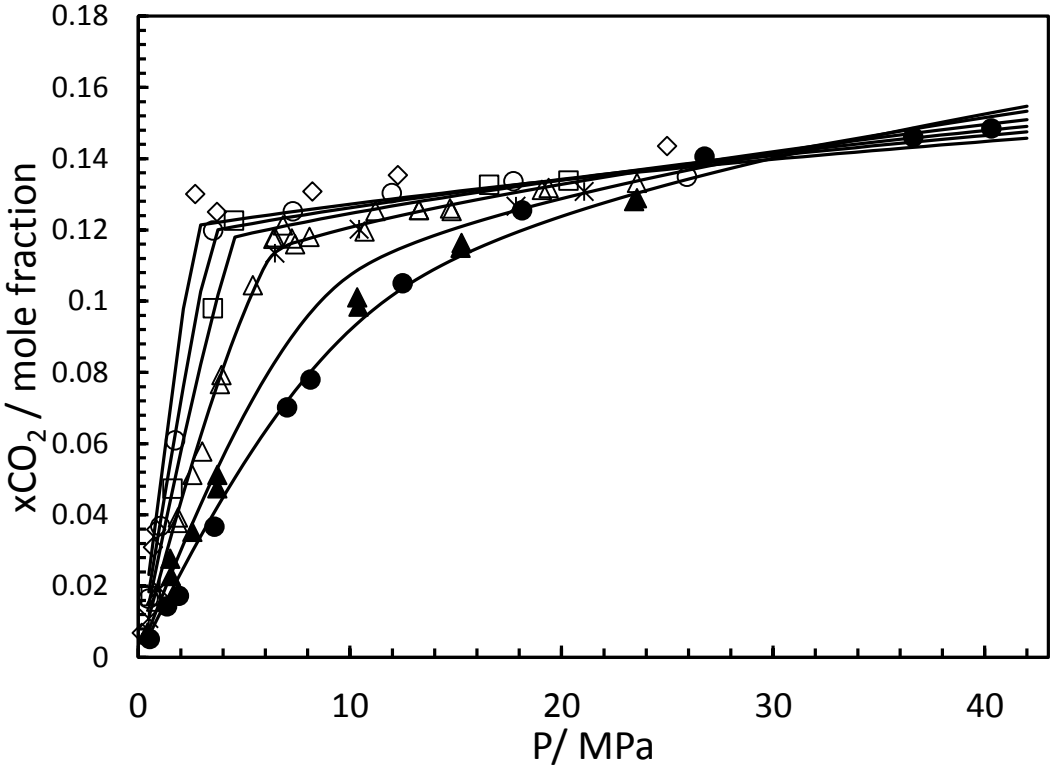

Figure 3.3. CO_2 solubility in pure MEG at 263.15 (◇), 273.15 K (○), 283.15 K (□), 297.75 K (∗), 298.15 K (△), 323.15 K (▲) and 343.15 K (●). Black Lines: CPA-SRK72-model k_{ij} = 0.053.

To verify the reliability of the experimental equipment a number of measurements were carried out using the same temperatures as literature data. Figure 3.4 shows the solubility of CO_2 in MEG from this work and CPA-SRK72 model predictions together with data from Jou et al [9] at 298.15 K. Using cubic spline interpolation trend equations were calculated using Jou et al. [9] data. Using the trend equations, the expected solubility for the same PVT conditions measured in this work were calculated. Comparing the solubility data showed an overall absolute average relative deviation of 5.43% between calculated Jou et al. [9] data and this work in the reported range. Figure 3.5 shows the solubility of CO_2 in MEG at 323.15 K measured in this work and CPA-SRK72 predictions together with data from Jou et al. [9], Galvao et al. [12] and Zheng et al. [11]. Using cubic spline interpolation, the data from this work and the data from Zheng et al. [11] demonstrated an overall absolute average relative deviation of 5.03 %. Figure 3.6 shows the solubility of CO_2 in MEG at 343.15 K measured in this work and CPA-SRK72 predictions together with data from Jou et al. [9]. The data from Jou et al. [9] showed a 4.28% relative overall average deviation from this work, within the reported range, calculated using cubic spline interpolation.

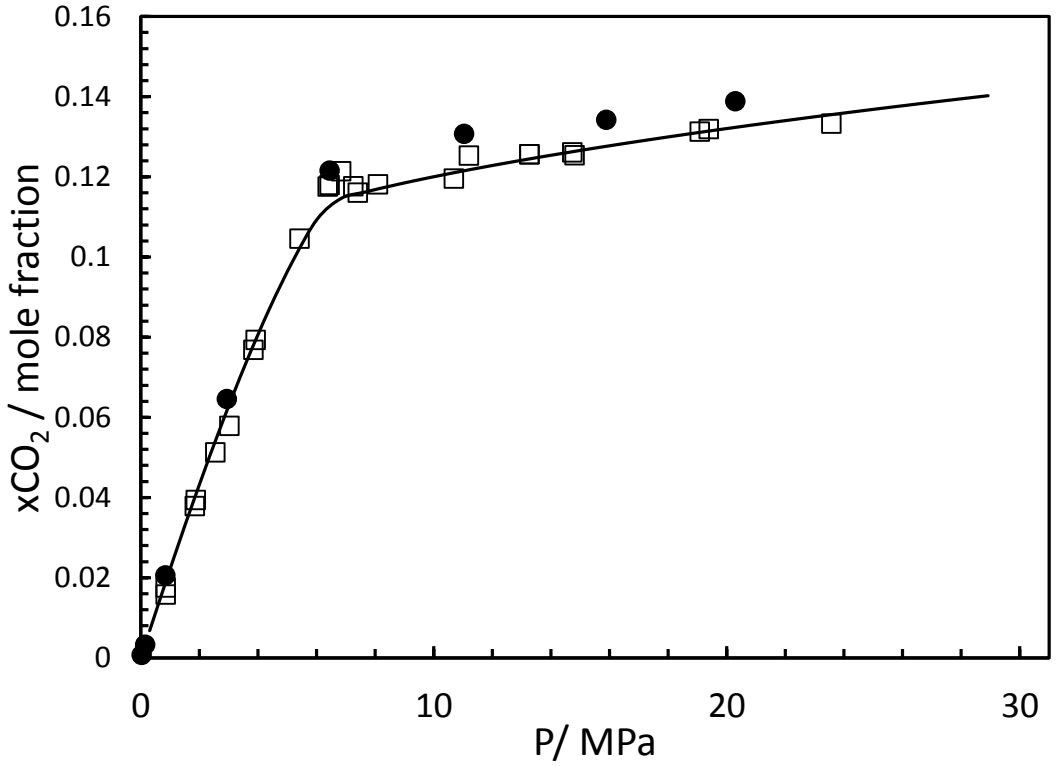

Figure 3.4. Solubility of CO_2 in Pure MEG at 298.15 K from this work (□) together with CPA-SRK72 model predictions (black line) and the data from Jou et al. (●). [9]

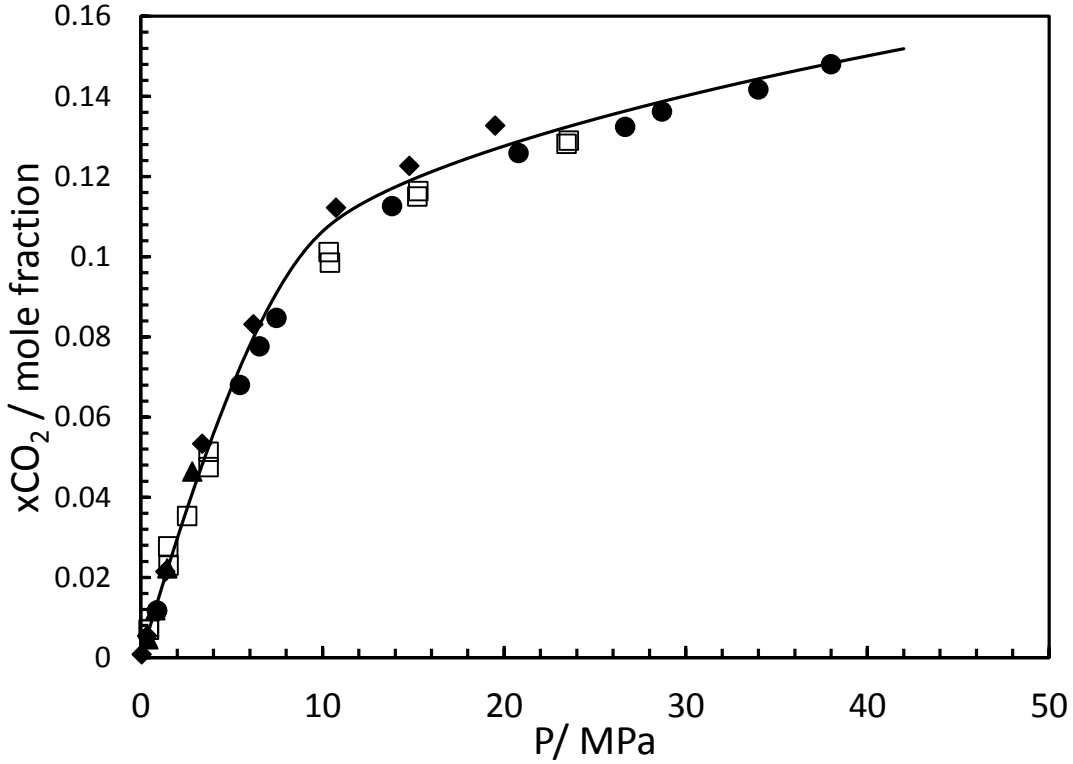

Figure 3.5. Solubility of CO_2 in pure MEG from this work at 323.15 K (□). CPA-SRK72 model (black line), Zheng et al. (●) [11], Jou et al. (◆) [9] and Galvao et al. (▲). [12]

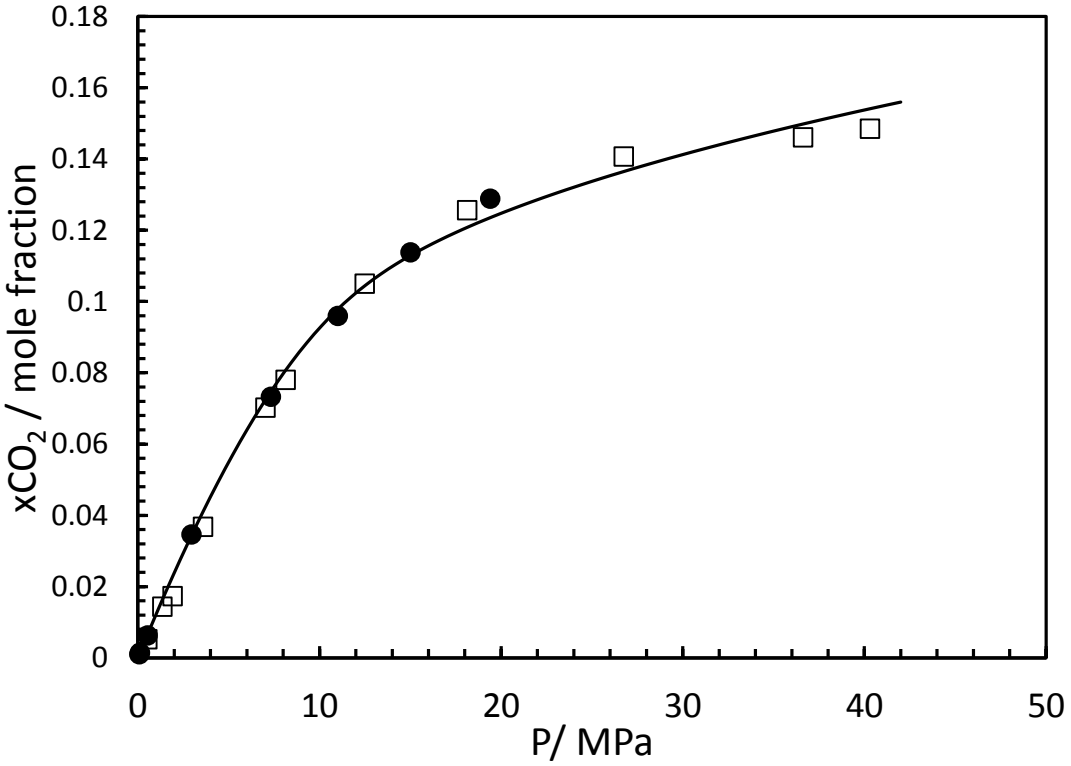

Figure 3.6. Solubility of CO_2 in pure MEG from this work at 343.15 K (□). CPA-SRK72 model (black line) and Jou et al. (●). [9]

Table 3.5 shows the solubility of CO_2 in 90 wt% MEG aqueous solution between 263.15 – 343.15 K and 0.2 – 32 MPa. Figure 3.7 shows the solubility of CO_2 in 90 wt% MEG solution together with optimised calculations (black lines) and non-optimised model predictions (dashed lines). The non-optimised model predictions demonstrated an overall relative absolute average deviation of 33.8% from the experimental work. The CO_2 solubility data in pure MEG were used to tune the BIP (k_{ij}) between MEG-CO_2. The BIP of 0.101 was tuned using the data from this work. Using the new BIP the overall relative average model calculation deviation was reduced to 16.4%.

Table 3.5. The solubility of CO_2 in 90 wt% MEG aqueous solution (x_1) from T = 273.15 to 343.15 K, pressures (P) and standard uncertainty $u_r(x_1)$[a].

T/K	P/ MPa	x_1 (mol frac)	$u_r(x_1)$	T/K	P/ MPa	x_1 (mol frac)	$u_r(x_1)$
273.15	0.41	0.0121	0.0002	298.15	5.59	0.0655	0.0004
273.15	0.62	0.0172	0.0002	298.15	5.64	0.0637	0.0004
273.15	3.51	0.0736	0.0004	298.15	6.90	0.0730	0.0004
273.15	5.69	0.0773	0.0005	298.15	6.94	0.0718	0.0004
273.15	11.69	0.0796	0.0005	298.15	11.18	0.0779	0.0005
273.15	18.38	0.0810	0.0005	298.15	14.56	0.0818	0.0005
273.15	23.48	0.0825	0.0005	298.15	16.64	0.0834	0.0005
283.15	0.27	0.0094	0.0001	298.15	22.97	0.0862	0.0005
283.15	1.31	0.0273	0.0002	343.15	0.80	0.0087	0.0001
283.15	4.50	0.0763	0.0005	343.15	1.61	0.0134	0.0002
283.15	7.34	0.0778	0.0005	343.15	3.95	0.0253	0.0002
283.15	11.57	0.0789	0.0005	343.15	5.20	0.0317	0.0003
283.15	14.88	0.0788	0.0005	343.15	10.38	0.0472	0.0003
283.15	15.21	0.0799	0.0005	343.15	12.29	0.0498	0.0004
283.15	21.70	0.0807	0.0005	343.15	18.68	0.0539	0.0003
298.15	0.61	0.0112	0.0001	343.15	25.04	0.0570	0.0004
298.15	1.51	0.0220	0.0002	343.15	26.50	0.0590	0.0004
298.15	1.51	0.0237	0.0002				

[a] Standard uncertainties u are at $u_r(x_1) = 0.026$, $u(T) = 0.05$ K and $u(P) = 0.04$MPa

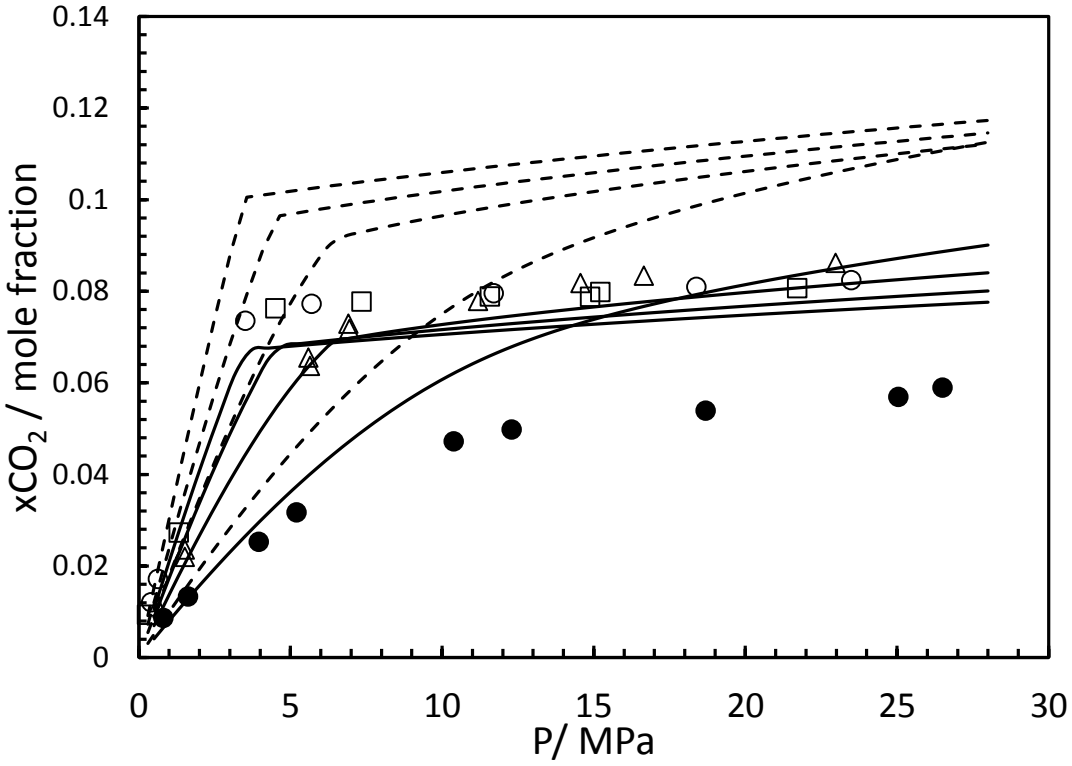

Figure 3.7. CO_2 solubility in 90 wt% MEG aqueous solution at 273.15 K (○), 283.15 K (□), 298.15 K (△) and 343.15 K (●). Black Lines: CPA-SRK72-model – k_{ij} = 0.101. Black Dotted Lines: CPA-SRK72-model – k_{ij} = 0.

Table 3.6 shows the solubility of CO_2 in 60 wt% MEG aqueous solution between 263.15 – 343.15 K and 0.3 – 26 MPa. Figure 3.8 shows the solubility of CO_2 in 60 wt% MEG solution together with optimised calculations and un-optimised model predictions. The un-optimised model predictions demonstrated an overall relative absolute average deviation of 47.8% from the experimental work. The data from this work was used to tune the BIP (k_{ij}) between MEG-CO_2. The BIP of 0.162 was calculated using the data from this work. Using the new BIP the overall relative average model calculation deviation was reduced to 14.2%.

Table 3.6. The solubility of CO_2 in 60 wt% MEG aqueous solution (x_1) from T = 263.15 to 343.15 K, pressures (P) up to 26 MPa and standard uncertainty $u_r(x_1)$[a].

T/K	*P*/ MPa	x_1 (mol frac)	$u_r(x_1)$
263.15	0.34	0.0097	0.0001
263.15	1.54	0.0259	0.0002
263.15	2.69	0.0365	0.0003
263.15	2.85	0.0358	0.0002
263.15	8.43	0.0367	0.0003
263.15	14.35	0.0372	0.0003
273.15	0.54	0.0084	0.0001
273.15	3.58	0.0268	0.0002
273.15	8.22	0.0345	0.0002
273.15	14.84	0.0367	0.0003
273.15	21.60	0.0372	0.0002
298.15	0.68	0.0095	0.0002
298.15	2.04	0.0189	0.0002
298.15	4.94	0.0311	0.0002
298.15	8.16	0.0412	0.0003
298.15	15.18	0.0428	0.0003
298.15	20.06	0.0437	0.0003
298.15	25.16	0.0443	0.0003
343.15	1.30	0.0096	0.0002
343.15	2.49	0.0143	0.0002
343.15	5.62	0.0243	0.0002
343.15	12.45	0.0379	0.0003
343.15	19.15	0.0423	0.0003
343.15	26.30	0.0452	0.0003

[a] Standard uncertainties *u* are at $u_r(x_1) = 0.026$, $u(T) = 0.05$ K and $u(P) = 0.04$MPa

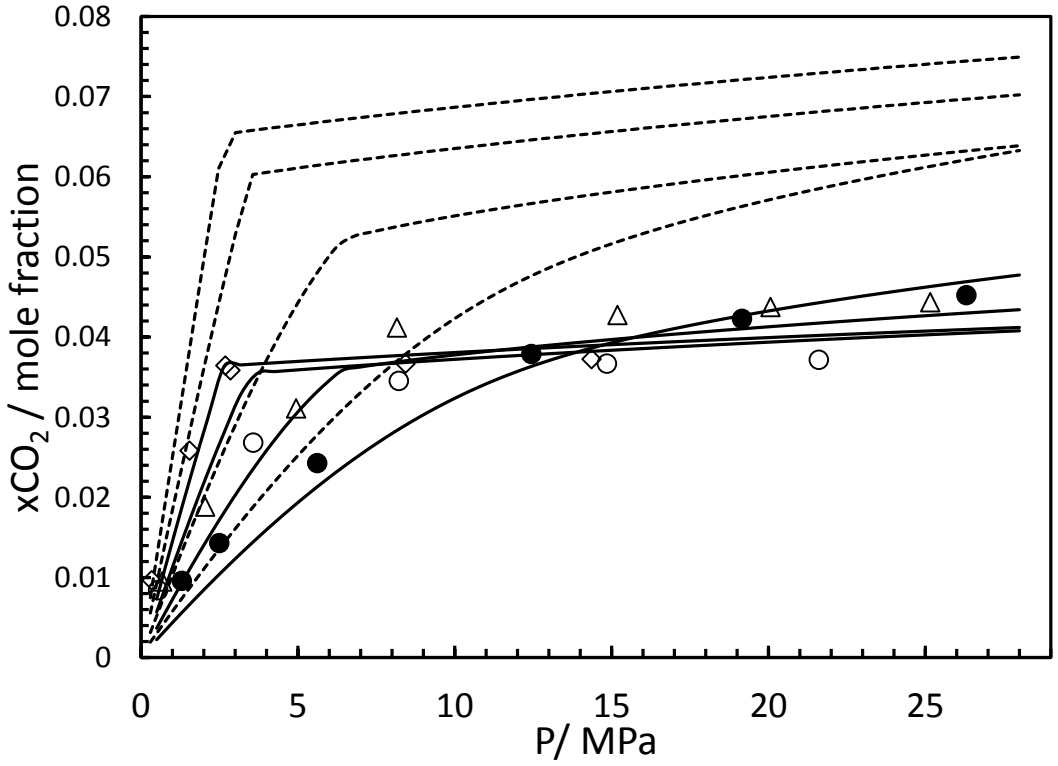

Figure 3.8. CO_2 solubility in 60 wt% MEG aqueous solution at 263.15 (◇), 273.15 K (○), 298.15 K (△) and 343.15 K (●). Black Lines: CPA-SRK72-model – k_{ij} = 0.162. Black Dotted Lines: CPA-SRK72-model – k_{ij} = 0.

Table 3.7 shows the solubility of CO_2 in 40 wt% MEG aqueous solution between 273.15 – 343.15 K and 0.3 – 27 MPa. Figure 3.9 shows the solubility of CO_2 in 40 wt% MEG solution together with optimised calculations and un-optimised model predictions. The un-optimised model predictions demonstrated an overall relative absolute average deviation of 32.5% from the experimental work. The data from this work was used to tune the BIP (k_{ij}) between MEG-CO_2. The BIP of 0.174 was calculated using the data from this work. Using the new BIP the overall relative average model calculation deviation was reduced to 16.7%.

Table 3.7. The solubility of CO_2 in 40 wt% MEG aqueous solution (x_1) from T = 273.15 to 343.15 K, pressures (P) up to 27 MPa and standard uncertainty $u_r(x_1)$[a].

T/K	*P*/ MPa	x_1 (mol frac)	$u_r(x_1)$
273.15	0.31	0.0076	0.0002
273.15	3.59	0.0316	0.0002
273.15	3.65	0.0320	0.0002
273.15	4.93	0.0334	0.0002
273.15	12.00	0.0341	0.0002
273.15	14.32	0.0345	0.0002
298.15	0.37	0.0064	0.0002
298.15	0.78	0.0090	0.0002
298.15	1.79	0.0145	0.0002
298.15	5.21	0.0278	0.0002
298.15	9.29	0.0308	0.0002
298.15	19.97	0.0329	0.0002
298.15	25.70	0.0347	0.0003
343.15	1.14	0.0080	0.0002
343.15	2.08	0.0111	0.0001
343.15	7.69	0.0235	0.0003
343.15	13.93	0.0300	0.0002
343.15	15.84	0.0318	0.0003
343.15	20.08	0.0336	0.0003
343.15	26.74	0.0355	0.0003

[a] Standard uncertainties *u* are at $u_r(x_1) = 0.028$, $u(T) = 0.05$ K and $u(P) = 0.04$MPa

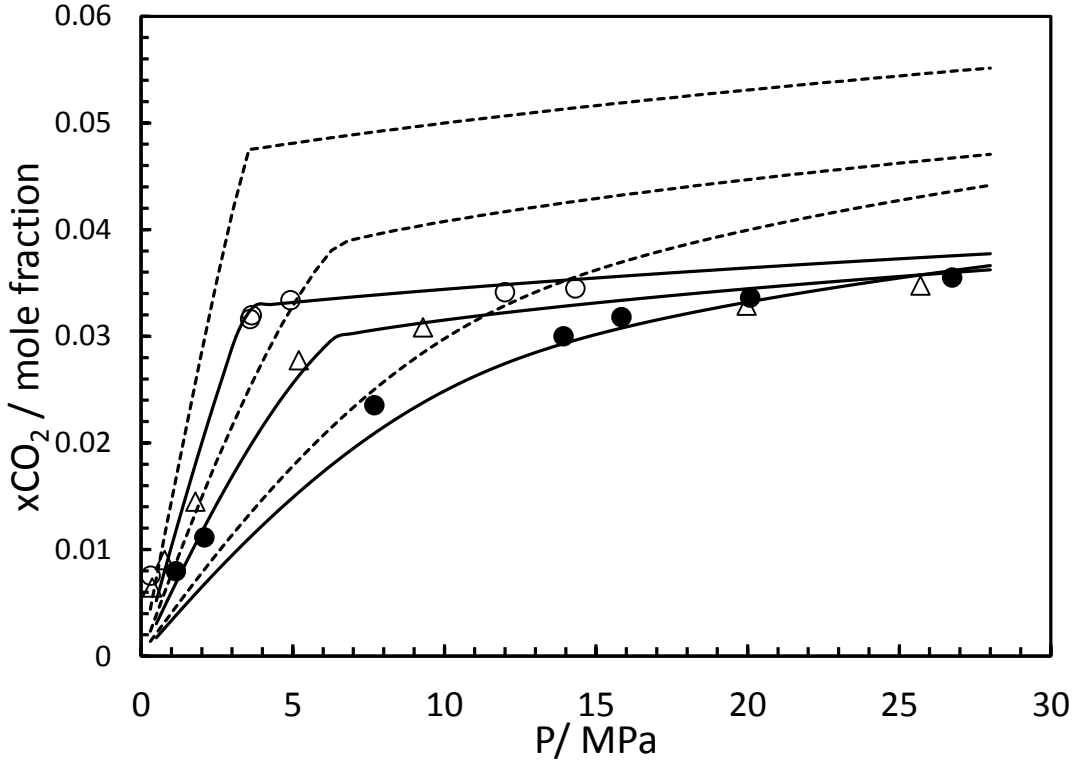

Figure 3.9. CO_2 solubility in 40 wt% MEG aqueous solution at 273.15 K (○), 298.15 K (△) and 343.15 K (●). Black Lines: CPA-SRK72-model – k_{ij} = 0.174. Black Dotted Lines: CPA-SRK72-model – k_{ij} = 0.

Table 3.8 shows the regressed k_{ij} values using this work and in the case of pure MEG, together with data from Jou et al. [9] and Zheng et al. [11]. Figure 3.10 shows the BIPs between MEG and CO_2 regressed using the data from this work. Eq. 3.1 was developed using the data from this work. The correlations may be used to calculate concentration dependant BIPs between MEG and CO_2 for systems containing water.

Table 3.8. Optimised BIPs between CO_2 and MEG for pure and MEG aqueous solutions.

wt% MEG	Mole Fraction	BIPs (k_{ij})	T range (K)
100	1	0.053	263.15 – 398.15 [9,11]
90	0.723	0.101	273.15 -343.15
60	0.303	0.162	273.15 - 343.15
40	0.162	0.174	273.15 - 343.15

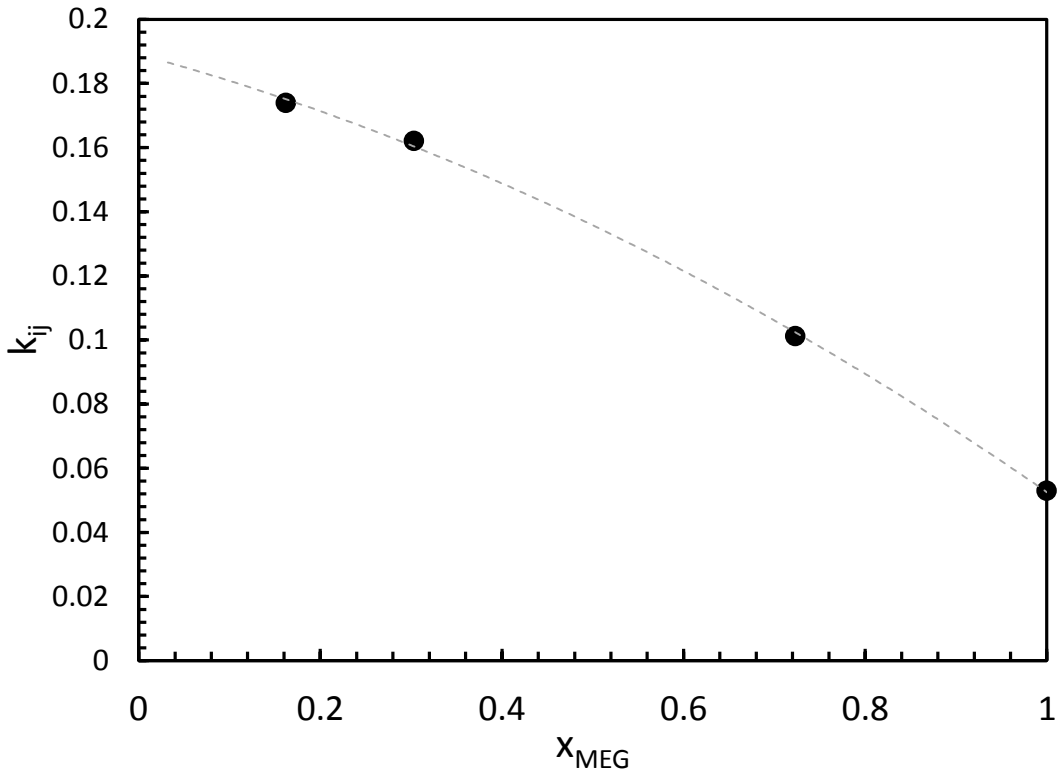

Figure 3.10. Binary Interaction Parameter, k_{ij} between CO_2 and MEG for pure and aqueous solutions.

$$k_{ij} = -0.0599x^2 - 0.0766x + 0.1891 \quad (3.1)$$

Table 3.9 shows the solubility of CO_2 in pure DEG between 263.15 – 343.15 K and 0.3 – 43.4 MPa. Figure 3.11 shows the solubility of CO_2 in pure DEG model predictions. The predictions showed an overall relative average model calculation deviation was reduced to 9.5%.

Table 3.9. The solubility of CO_2 in DEG (x_1) from T = 263.16 to 343.15 K and pressures (P) and standard uncertainty $u_r(x_1)$[a].

T/K	P/ MPa	x_1 (mol frac)	$u_r(x_1)$	T/K	P/ MPa	x_1 (mol frac)	$u_r(x_1)$
263.15	0.71	0.0918	0.0005	283.15	8.78	0.3602	0.0012
263.15	1.51	0.2159	0.0012	283.15	13.87	0.3730	0.0012
263.15	2.72	0.3952	0.0012	283.15	18.82	0.3828	0.0012
263.15	3.22	0.3968	0.0012	298.15	0.54	0.0217	0.0002
263.15	5.20	0.3972	0.0012	298.15	1.10	0.0514	0.0003
263.15	9.34	0.4127	0.0012	298.15	2.31	0.1088	0.0005
263.15	14.65	0.4230	0.0012	298.15	6.67	0.3091	0.0011
263.15	21.13	0.4311	0.0012	298.15	14.21	0.3405	0.0011
273.15	0.58	0.0546	0.0003	298.15	20.33	0.3595	0.0012
273.15	2.63	0.2701	0.0010	298.15	28.01	0.3729	0.0012
273.15	3.69	0.3804	0.0012	298.15	35.00	0.3864	0.0012
273.15	4.56	0.3745	0.0012	343.15	0.53	0.0149	0.0002
273.15	7.32	0.3867	0.0012	343.15	1.10	0.0299	0.0002
273.15	14.63	0.4064	0.0012	343.15	6.00	0.1435	0.0007
273.15	21.67	0.4199	0.0012	343.15	13.56	0.2651	0.0010
283.15	0.28	0.0219	0.0002	343.15	19.53	0.3050	0.0011
283.15	0.59	0.0318	0.0002	343.15	26.35	0.3290	0.0011
283.15	2.79	0.2093	0.0009	343.15	35.58	0.3565	0.0012
283.15	4.55	0.3451	0.0012	343.15	43.40	0.3766	0.0012
283.15	6.26	0.3509	0.0012				

[a] Standard uncertainties u are at $u_r(x_1)$ = 0.025, $u(T)$ = 0.05 K and $u(P)$ = 0.04MPa

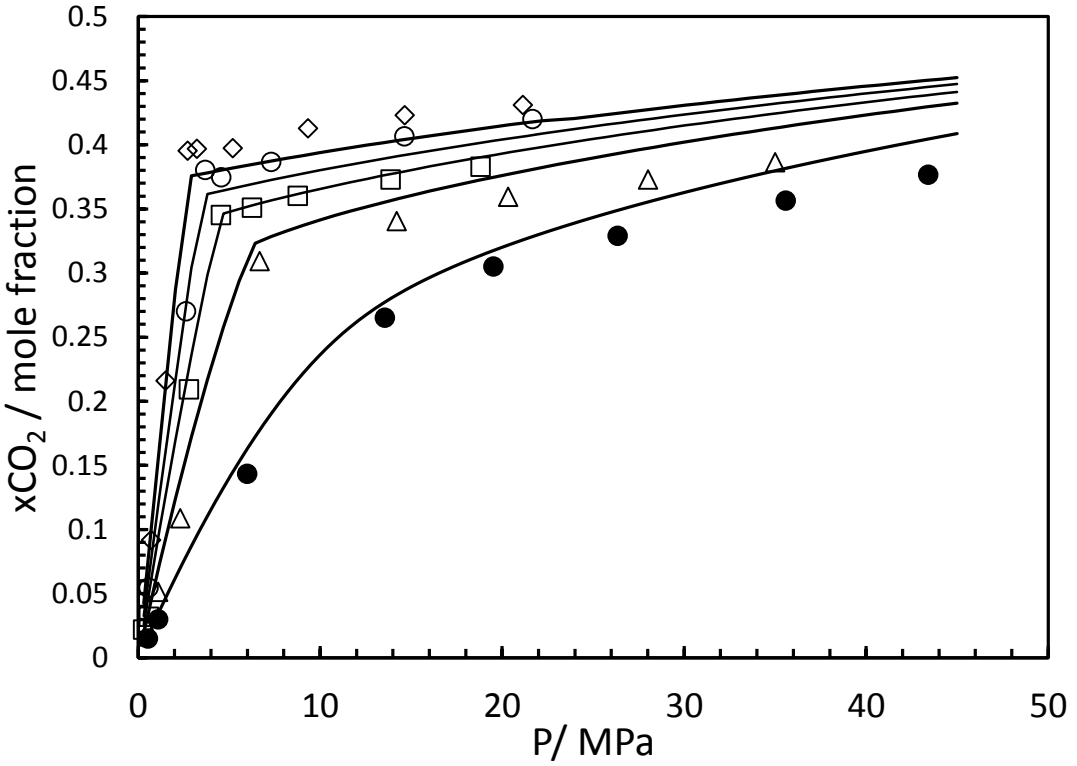

Figure 3.11. CO_2 solubility in pure DEG at 263.15 (◇), 273.15 K (○), 283.15 K (□), 298.15 K (△) and 343.15 K (●). Black Lines: CPA-SRK72-model, k_{ij} = 0.011.

Figure 3.12 shows the solubility of CO_2 in DEG measured in this work at 298.15 K and CPA-SRK72 model predictions together with data from Jou et al. [10]. The data showed good agreement with the measurements in this work.

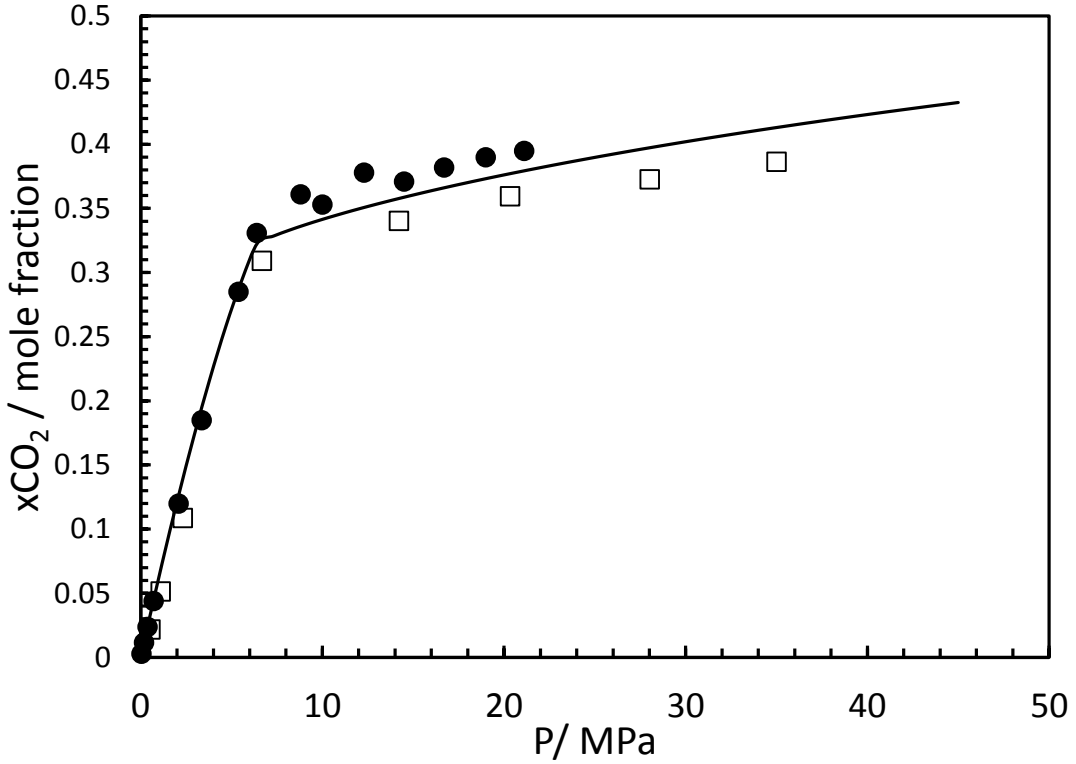

Figure 3.12. Solubility of CO_2 in pure DEG 298.15 K from this work (□), CPA-SRK72 model predictions (black line) and Jou et al. [10] (●).

Table 3.10 shows the solubility of CO_2 in 90 wt% DEG aqueous solution between 273.15 – 343.15 K and 0.3 – 26.5 MPa. Figure 3.13 shows the solubility of CO_2 in 90 wt% DEG solution together with optimised calculations and non-optimised model predictions. The non-optimised model predictions demonstrated an overall relative absolute average deviation of 47.1% from the experimental work. The data from this work was used to tune the BIP (k_{ij}) between MEG-CO_2. The BIP of 0.107 was tuned using the data from this work. Using the new BIP the overall relative average model calculation deviation was reduced to 10.9%.

Table 3.10. The solubility of CO_2 in 90 wt% DEG aqueous solution (x_1) from T = 263.15 to 343.15, pressures (P) up to 32 MPa and standard uncertainty $u_r(x_1)$[a].

T/K	P/ MPa	x_1 (mol frac)	$u_r(x_1)$
263.15	0.19	0.0122	0.0001
263.15	1.71	0.1117	0.0006
263.15	2.32	0.1565	0.0008
263.15	9.29	0.1781	0.0009
263.15	15.64	0.1812	0.0009
298.15	0.39	0.0121	0.0001
298.15	2.59	0.0640	0.0004
298.15	3.59	0.0906	0.0005
298.15	6.74	0.1313	0.0007
298.15	9.85	0.1581	0.0008
298.15	15.67	0.1695	0.0008
298.15	19.93	0.1701	0.0008
298.15	27.39	0.1820	0.0010
343.15	0.37	0.0084	0.0001
343.15	1.05	0.0159	0.0001
343.15	1.06	0.0178	0.0001
343.15	2.22	0.0306	0.0002
343.15	2.32	0.0321	0.0002
343.15	4.45	0.0565	0.0003
343.15	5.06	0.0632	0.0004
343.15	9.89	0.1202	0.0006
343.15	10.74	0.1239	0.0006
343.15	16.76	0.1462	0.0007
343.15	17.54	0.1556	0.0008
343.15	21.32	0.1653	0.0008
343.15	24.63	0.1741	0.0009
343.15	27.25	0.1819	0.0009
343.15	31.61	0.1882	0.0009

[a] Standard uncertainties u are at $u_r(x_1)$ = 0.026, $u(T)$ = 0.05 K and $u(P)$ = 0.04MPa

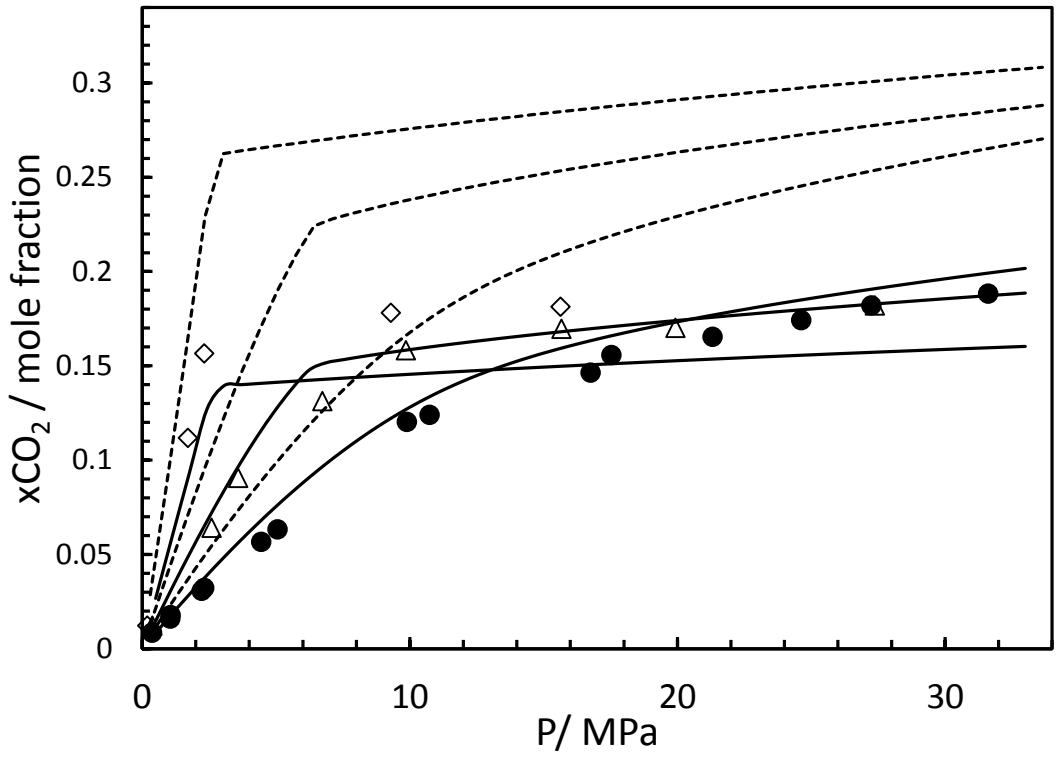

Figure 3.13. CO_2 solubility in 90 wt% DEG aqueous solution at 263.15 (◇), 298.15 K (△) and 343.15 K (●). Black Lines: CPA-SRK72-model – k_{ij} = 0.107. Black Dotted Lines: CPA-SRK72-model – k_{ij} = 0.0106.

Table 3.11 shows the solubility of CO_2 in 60 wt% DEG aqueous solution between 263.15 – 343.15 K and 0.3 – 24.9 MPa. Figure 3.14 shows the solubility of CO_2 in 60 wt% DEG solution together with optimised calculations and non-optimised model predictions. The non-optimised model predictions demonstrated an overall relative absolute average deviation of 91.4% from the experimental work. The data from this work was used to tune the BIP (k_{ij}) between MEG-CO_2. The BIP of 0.204 was tuned using the data from this work. Using the new BIP the overall relative average model calculation deviation was reduced to 11.2%.

Table 3.11. The solubility of CO_2 in 60 wt% DEG aqueous solution (x_1) from T = 263.15 to 343.15 K, pressures (P) and standard uncertainty $u_r(x_1)$[a].

T/K	P/ MPa	x_1 (mol frac)	$u_r(x_1)$
263.15	0.34	0.0104	0.0001
263.15	1.37	0.0221	0.0001
263.15	2.26	0.0379	0.0002
263.15	3.62	0.0406	0.0002
263.15	15.09	0.0451	0.0003
263.15	24.89	0.0453	0.0002
298.15	0.60	0.0091	0.0001
298.15	2.32	0.0211	0.0002
298.15	3.45	0.0278	0.0002
298.15	6.87	0.0441	0.0003
298.15	10.24	0.0448	0.0003
298.15	15.71	0.0458	0.0001
298.15	22.36	0.0471	0.0002
343.15	0.99	0.0100	0.0002
343.15	2.05	0.0148	0.0003
343.15	4.54	0.0252	0.0003
343.15	9.17	0.0399	0.0003
343.15	15.83	0.0509	0.0001
343.15	22.39	0.0551	0.0002

[a] Standard uncertainties u are at $u_r(x_1)$ = 0.026, $u(T)$ = 0.05 K and $u(P)$ = 0.04MPa

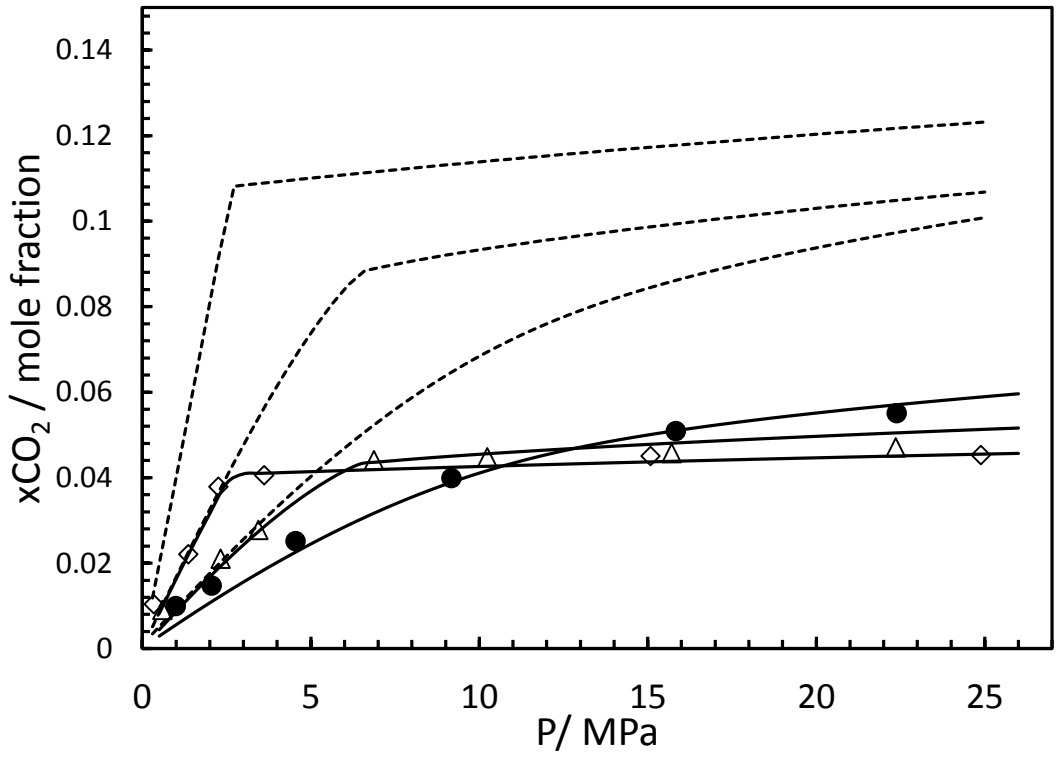

Figure 3.14. CO_2 solubility in 60 wt% DEG aqueous solution at 263.15 (◇), 298.15 K (△) and 343.15 K (●). Black Lines: CPA-SRK72-model – k_{ij} = 0.204. Black Dotted Lines: CPA-SRK72-model – k_{ij} = 0.0106.

Table 3.12 shows the solubility of CO_2 in 40 wt% DEG aqueous solution between 273.15 – 343.15 K and 0.5 – 27.3 MPa. Figure 3.15 shows the solubility of CO_2 in 40 wt% DEG solution together with optimised calculations and un-optimised model predictions. The un-optimised model predictions demonstrated an overall relative absolute average deviation of 55.7% from the experimental work. The data from this work was used to tune the BIP (k_{ij}) between MEG-CO_2. The BIP of 0.223 was regressed using the data from this work. Using the new BIP the overall relative average model calculation deviation was reduced to 15.6%.

Table 3.12. The solubility of CO_2 in 40 wt% DEG aqueous solution (x_1) from T = 273.15 to 343.15 K, pressures (P) up to 27 MPa and standard uncertainty $u_r(x_1)$[a].

T/K	*P*/ MPa	x_1 (mol frac)	$u_r(x_1)$
273.15	0.47	0.0100	0.0001
273.15	2.06	0.0256	0.0001
273.15	3.52	0.0309	0.0002
273.15	10.80	0.0380	0.0002
273.15	17.01	0.0374	0.0003
273.15	27.32	0.0382	0.0002
298.15	0.55	0.0078	0.0002
298.15	1.83	0.0152	0.0002
298.15	6.49	0.0307	0.0002
298.15	9.68	0.0329	0.0002
298.15	14.45	0.0340	0.0002
298.15	19.27	0.0351	0.0001
298.15	22.44	0.0349	0.0002
343.15	0.78	0.0073	0.0002
343.15	2.22	0.0122	0.0004
343.15	7.05	0.0247	0.0002
343.15	16.82	0.0347	0.0004
343.15	21.28	0.0372	0.0001
343.15	24.30	0.0381	0.0002

[a] Standard uncertainties *u* are at $u_r(x_1) = 0.027$, $u(T) = 0.05$ K and $u(P) = 0.04$MPa

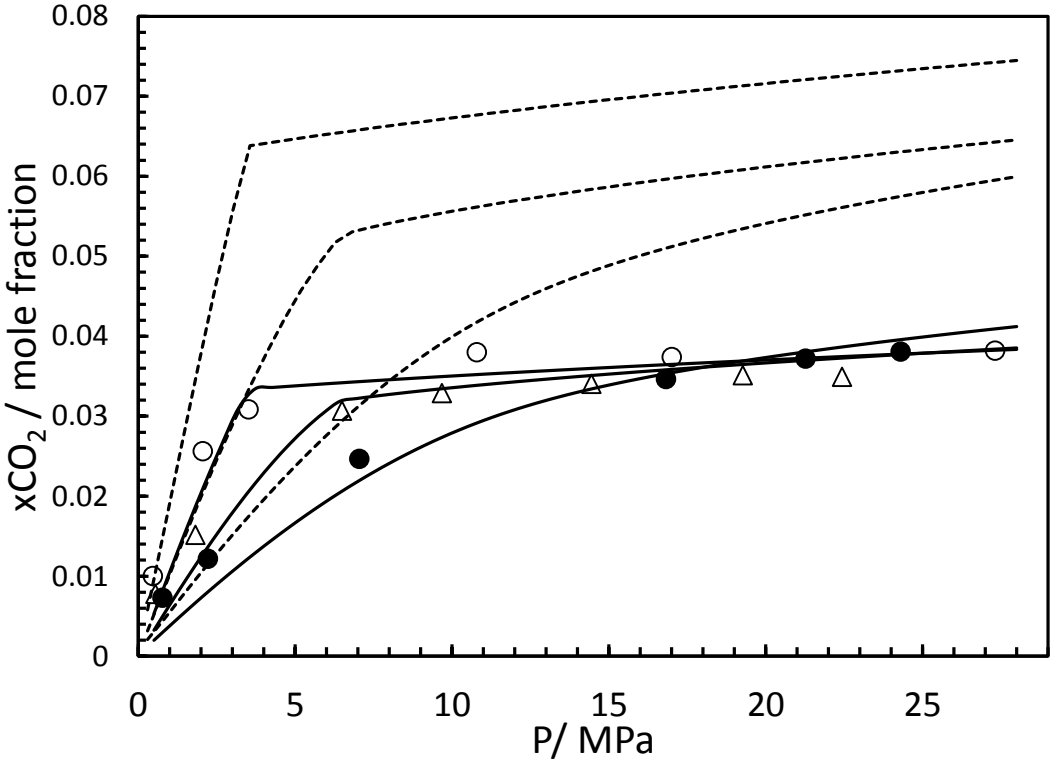

Figure 3.15. CO_2 solubility in 40 wt% DEG aqueous solution at 273.15 K (○), 298.15 K (△) and 343.15 K (●). Black Lines: CPA-SRK72-model – k_{ij} = 0.223. Black Dotted Lines: CPA-SRK72-model – k_{ij} = 0.0106.

Figure 3.16 shows the BIPs between DEG and CO_2 regressed using the data from this work. Eq. 3.2 was developed using the data from this work. The correlations may be used to calculate concentration dependant BIPs between DEG and CO_2 for systems containing water. Table 3.13 shows the regressed k_{ij} values using this work and in the case of pure DEG, together with data from Jou et al. [10].

Table 3.13. Optimised BIPs between CO_2 and DEG for pure and DEG aqueous solutions.

wt% DEG	Mole Fraction	BIPs (k_{ij})	T range (K)
100	1.000	0.0106	263.15 – 398.15 [10]
90	0.604	0.107	263.15 - 343.15
60	0.203	0.204	263.15 - 343.15
40	0.102	0.223	263.15 - 343.15

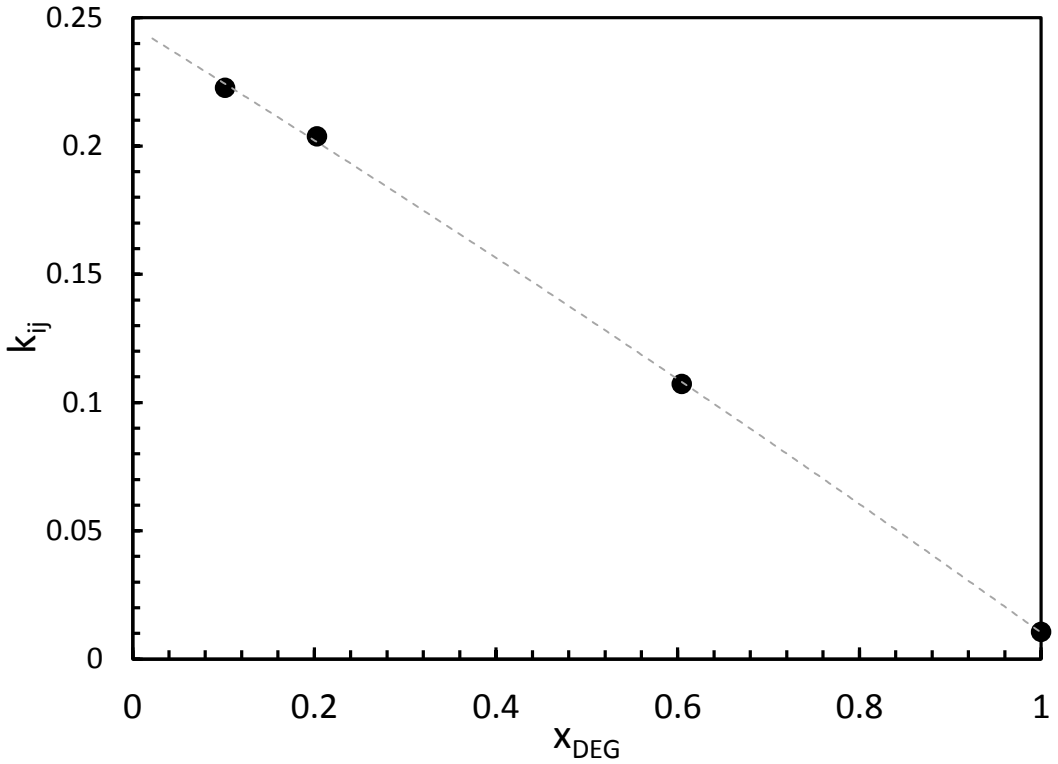

Figure 3.16. Binary Interaction Parameter, k_{ij} between CO_2 and DEG for pure and aqueous solutions.

$$k_{ij} = -0.0178x^2 - 0.2185x + 0.2466 \quad (3.2)$$

Table 3.14 shows the solubility of CO_2 in pure TEG at four different isotherms. Table 3.15 to Table 3.17 demonstrate the solubility of CO_2 in 90, 60 and 40% TEG solutions. These showed an overall standard uncertainty of $u_r(x_1) = 0.029$ for the solubility of CO_2 in pure

TEG and a standard uncertainty $u_r(x_1) = 0.033$ for the solubility of CO_2 in TEG Solutions. Figure 3.17 illustrates the solubility of CO_2 in TEG at 273.15 , 283.15, 298.15 and 343.15 K together with the CPA-SRK72 model predictions for the four isotherms. The model was adjusted using the data from this work showing an absolute average deviation of 2.55% over the measured isotherms. Figure 3.19 shows the solubility of CO_2 in TEG at 298.15 K measured in this work, the literature measurement data from Jou et al. [8] together with the CPA-SRK72 model predictions. The data from Jou et al. [8] was correlated to the measurements in this work using cubic spline interpolation, showing a 4.6% overall absolute deviation within the range. This shows that both works are in good agreement.

Table 3.14 The solubility of CO_2 in TEG (x_1) from T = 273.15 to 343.15 K, pressures (P) up to 37 MPa and standard uncertainty $u_r(x_1)$[a].

T/K	*P*/ MPa	x_1 (mol/mol)	$u_r(x_1)$
273.15	0.58	0.0749	0.0023
273.15	2.63	0.3433	0.0102
273.15	3.69	0.4647	0.0132
273.15	4.56	0.4584	0.0127
273.15	7.32	0.4713	0.0130
273.15	14.63	0.4919	0.0136
273.15	21.67	0.5058	0.0139
283.15	0.42	0.0473	0.0015
283.15	1.24	0.1256	0.0038
283.15	1.81	0.2076	0.0061
283.15	2.57	0.2600	0.0075
283.15	4.52	0.4477	0.0124
283.15	4.96	0.4657	0.0129
283.15	8.49	0.4653	0.0129
283.15	13.70	0.4772	0.0132
283.15	19.71	0.4894	0.0135
298.15	0.60	0.0477	0.0015
298.15	1.59	0.1152	0.0034
298.15	6.49	0.4194	0.0117
298.15	8.83	0.4334	0.0121
298.15	15.15	0.4560	0.0127
298.15	19.91	0.4677	0.0129
343.15	0.62	0.0263	0.0009
343.15	2.95	0.1105	0.0033
343.15	10.07	0.3181	0.0091
343.15	17.55	0.4029	0.0113
343.15	22.39	0.4295	0.0120
343.15	28.85	0.4582	0.0127
343.15	37.40	0.4909	0.0135

[a] Standard uncertainties *u* are at $u_r(x_1) = 0.029$, $u(T) = 0.05$ K and $u(P) = 0.04$MPa

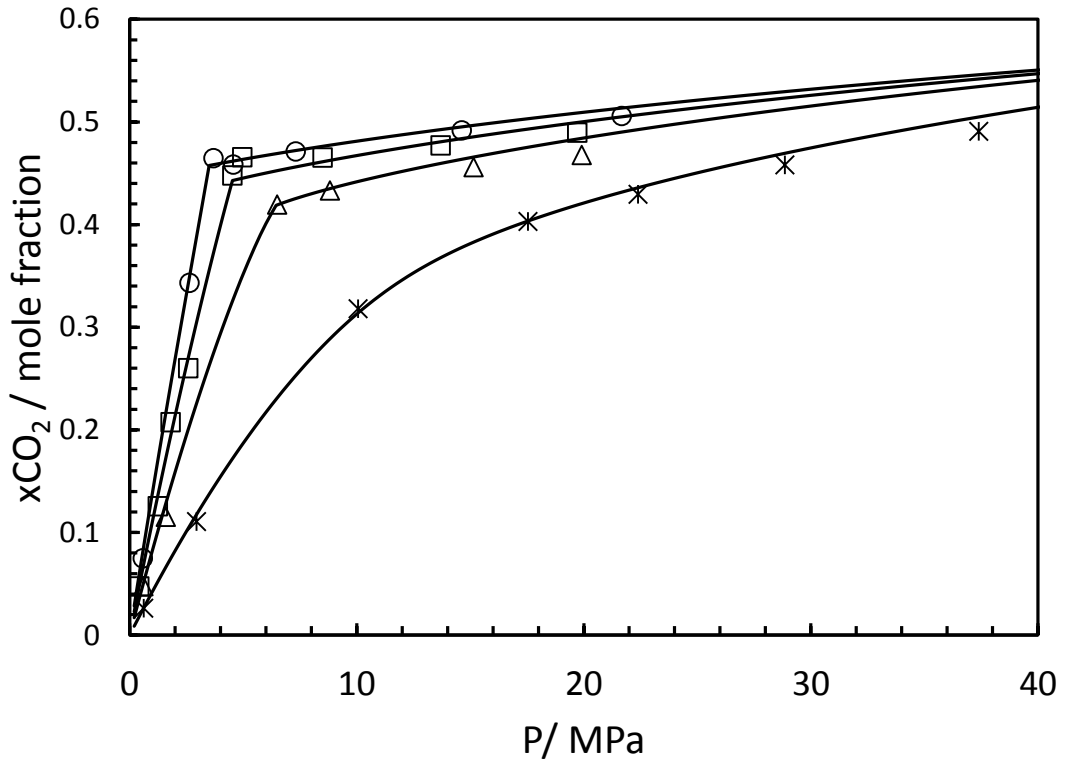

Figure 3.17. CO_2 solubility in pure TEG at 273.15 K. (○), 283.15 K (□), 298.15 K (△) and 343.15 K (∗). Black Lines: CPA-SRK72-model.

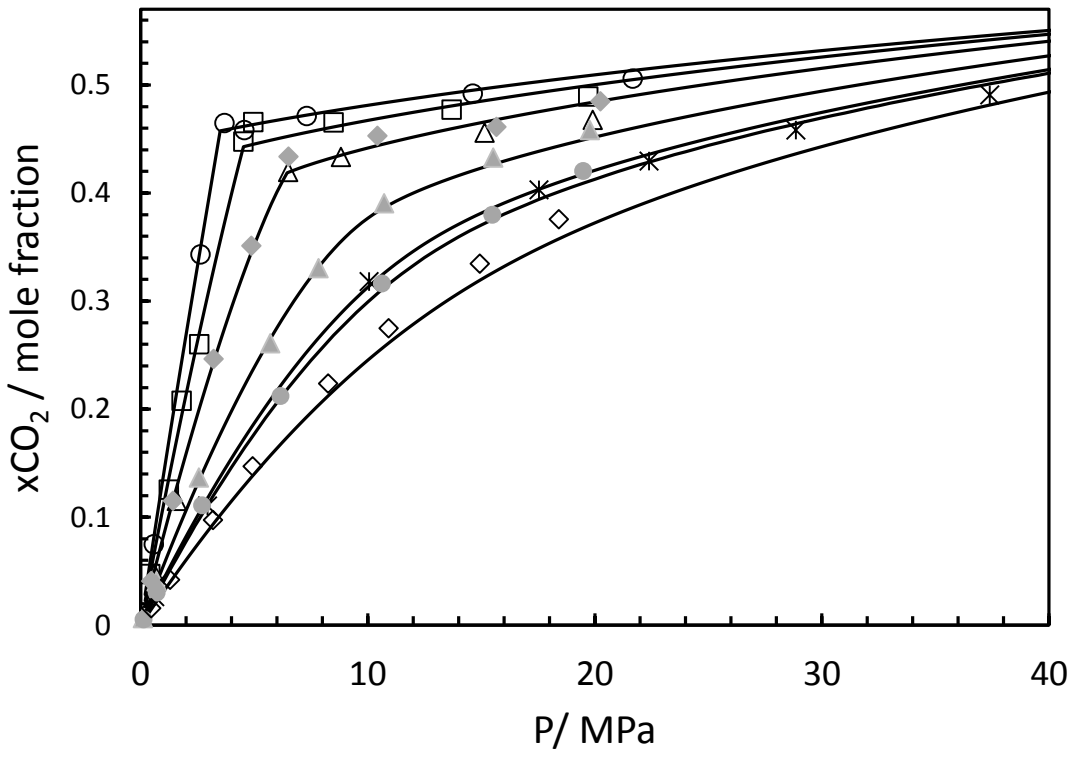

Figure 3.18. CO_2 solubility in pure TEG at 273.15 K. (○), 283.15 K (□), 298.15 K (△), 343.15 K (∗), Jou et al. [8] 298.15 K (◆), Jou et al. [8] 323.15 K (▲), Jou et al. [8] 348.15 K (●) and Jou et al. [8] 373.15 K (◇). Black Lines: CPA-SRK72-model.

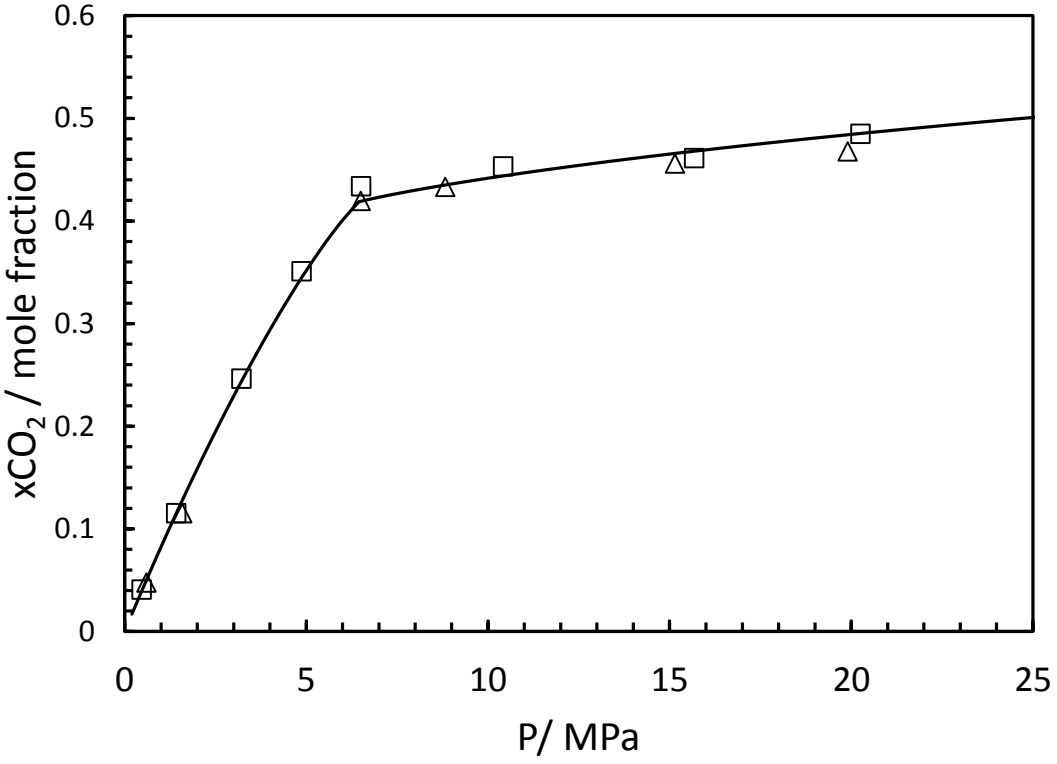

Figure 3.19 showing the solubility of CO_2 in TEG at 298.15K (△), Jou et al. [8] 298.15 K (□). Black Line: CPA-SRK72-model.

Figure 3.20 illustrates the solubility of CO_2 in 90% TEG solution together with CPA-SRK72 model predictions. The solubility of CO_2 in TEG reduces significantly with the addition 3.5 wt% water. This point is demonstrated by the work of Takahashi et al. [13] shown in Figure 3.21 and Figure 3.22 at three different isotherms. The solubility of CO_2 in 96.5 wt% TEG solution was measured between 297.04 to 322.04 and 2.1 to 6.3 MPa shown in Table 3.18 and Figure 3.21. The measurements in this work were not in complete agreement with the work of Takahashi et al. [13] as demonstrated in Figure 3.21. The addition of 3.5 and 7 wt% resulted in a 29% and 60% average drop in the solubility of CO_2 in TEG over the range respectively shown by the work of Takahashi et al. [13]. This is due to the selectivity of TEG to form stronger hydrogen bonds with water, hence occupying more of the surfaces available to CO_2. Figure 3.23 shows the solubility of CO_2 in 60 wt% TEG solution measured at three isotherms, together with CPA-SRK72 predictions. The solubility of CO_2 in 60 wt% TEG solution at 343.15 K surpassed the

solubility of CO_2 in the same solution at 298.15 K at pressures above 10 MPa. This also occurs during the solubility measurements in 40% TEG solution shown in Figure 3.24 together with four different isotherms and CPA-SRK72 predictions.

This effect is seen in the solubility of CO_2 in pure water shown in Figure 3.26. The required pressure for this reduces with increased temperature. The hydrations of polar gases are the sum of two processes:

- The endothermic opening of a clathrate space in the water
- The exothermic positioning of a molecule in that space

At low temperatures in water the endothermic opening of a clathrate space requires a very small amount of energy resulting in easy formation of water clusters. [17] The solubility of CO_2 in water increases with reduction in temperature. As the fit into the water dodecahedral clathrates improves, the enthalpy and entropy of hydration becomes more negative. Thus the solubilisation process is exothermic and is inversely proportional to temperature at lower pressures. At higher pressures and temperatures, the nature of clustering is reduced, resulting in higher energy needs for opening spaces in water. This results in the solubilisation process becoming endothermic, resulting in the solubility going through a minimum before increasing with temperature. [18–20] This phenomenon may feasibly explain the increase in solubility at 343.15 K in 90, 60 and 40% TEG solution. It is not possible to explain this phenomenon fully until the structural behaviour of the system is fully analysed, which is out with the scope of this research project.

Table 3.15 The solubility of CO_2 in 90% TEG Solution (x_1) from T = 263.15 to 343.15 K, pressures (P) up to 25 MPa and standard uncertainty $u_r(x_1)$[a].

T/K	*P*/ MPa	x_1 (mol frac)	$u_r(x_1)$
263.15	0.27	0.0206	0.0007
263.15	1.01	0.0618	0.0019
263.15	2.73	0.1491	0.0044
263.15	2.85	0.2011	0.0059
263.15	7.09	0.2139	0.0063
263.15	13.00	0.2235	0.0066
263.15	16.33	0.2338	0.0069
298.15	0.22	0.0092	0.0003
298.15	0.72	0.0248	0.0008
298.15	1.88	0.0520	0.0016
298.15	6.55	0.1568	0.0047
298.15	8.27	0.1849	0.0055
298.15	14.89	0.2027	0.0060
298.15	20.95	0.2114	0.0062
343.15	0.32	0.0092	0.0003
343.15	0.92	0.0180	0.0006
343.15	1.57	0.0251	0.0008
343.15	2.45	0.0422	0.0013
343.15	4.52	0.0769	0.0023
343.15	7.84	0.1254	0.0038
343.15	10.85	0.1639	0.0049
343.15	14.01	0.1898	0.0056
343.15	19.48	0.2132	0.0063
343.15	24.65	0.2327	0.0068

[a] Standard uncertainties *u* are at $u_r(x_1) = 0.033$, $u(T) = 0.05$ K and $u(P) = 0.04$MPa

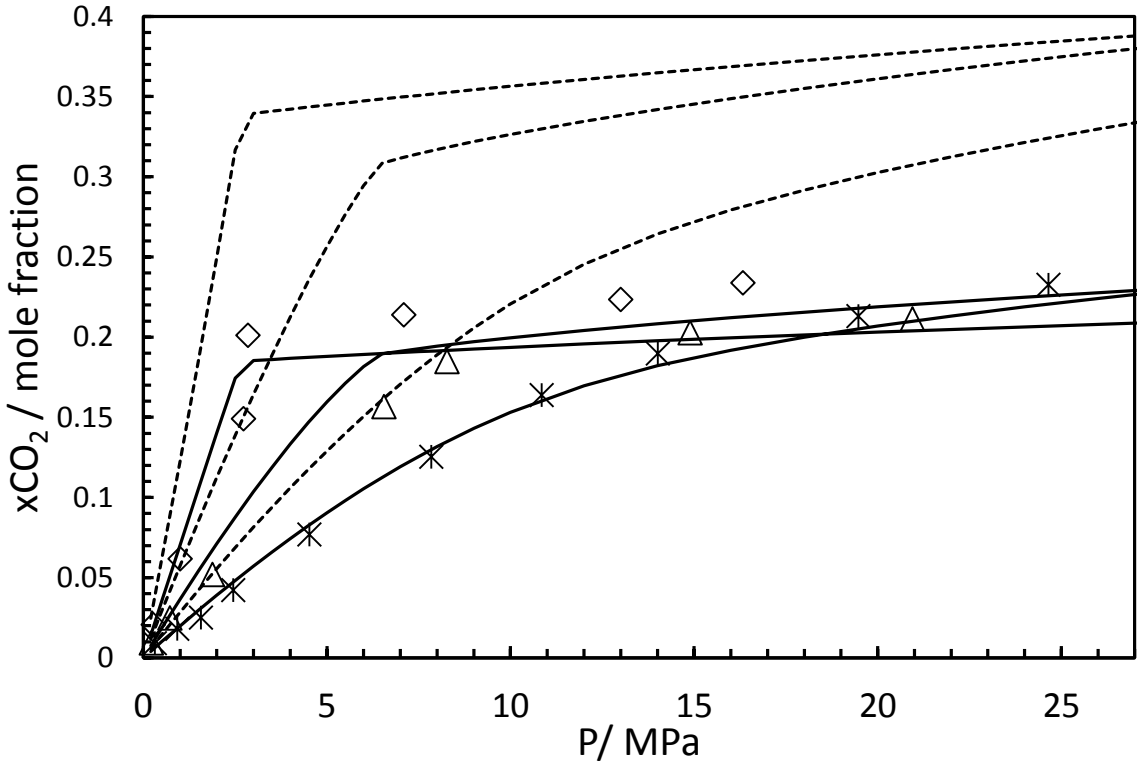

Figure 3.20 showing the solubility of CO_2 in 90% TEG solution at 263.15 K (◇), 298.15 K (△) and 343.15 K (∗). Dotted Black Lines: CPA-SRK72-model with k_{ij} tuned on binary systems. Black Lines: CPA-SRK72-model with specific k_{ij}.

Table 3.16 The solubility of CO_2 in 60% TEG solution (x_1) from T = 263.15 to 343.15 K, pressures (P) up to 30 MPa and standard uncertainty $u_r(x_1)$[a].

T/K	*P*/ MPa	x_1 (mol frac)	$u(x_1)$
263.15	0.57	0.0124	0.0004
263.15	0.97	0.0171	0.0006
263.15	1.59	0.0298	0.0010
263.15	2.71	0.0433	0.0014
263.15	6.85	0.0485	0.0015
263.15	20.80	0.0504	0.0016
263.15	24.37	0.0502	0.0016
298.15	0.60	0.0095	0.0004
298.15	2.29	0.0228	0.0007
298.15	3.92	0.0331	0.0011
298.15	6.51	0.0458	0.0015
298.15	9.89	0.0470	0.0015
298.15	13.13	0.0476	0.0015
298.15	23.19	0.0466	0.0015
343.15	0.77	0.0086	0.0004
343.15	2.11	0.0154	0.0006
343.15	5.24	0.0298	0.0010
343.15	12.88	0.0512	0.0016
343.15	17.79	0.0573	0.0018
343.15	25.10	0.0617	0.0019
343.15	30.13	0.0657	0.0020

[a] Standard uncertainties *u* are at $u_r(x_1) = 0.033$, $u(T) = 0.05$ K and $u(P) = 0.04$MPa

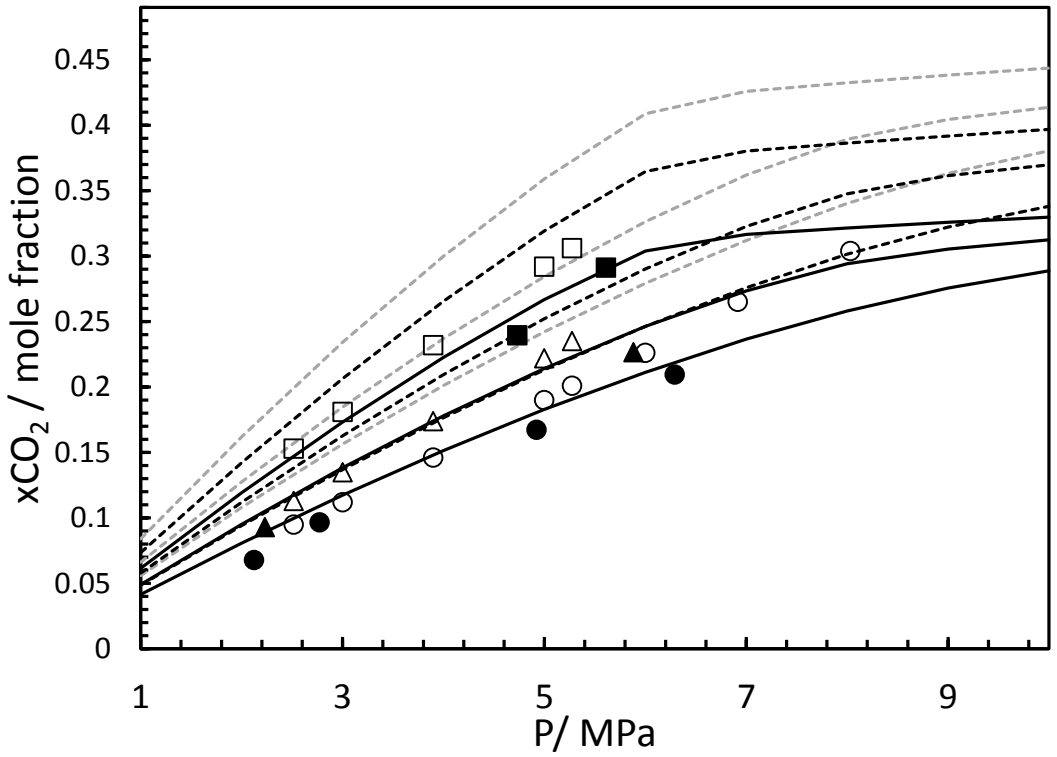

Figure 3.21 illustrates the solubility of CO_2 in 96.5 wt% TEG Solution measured by Takahashi et al. [13] at 297.04 K (□), 310.93 K (△) and 322.04 K (○) and this work at 297.04 K (■), 310.93 K (▲) and 322.04 K (●). Dotted Lines: CPA-SRK72-model predicting the solubility of CO_2 in pure TEG. Black Lines: CPA-SRK72-model at 96.5 wt% solution with extrapolated k_{ij}. Black Dotted Lines: CPA-SRK72-model at 93 wt% Solution with k_{ij} e on binary systems.

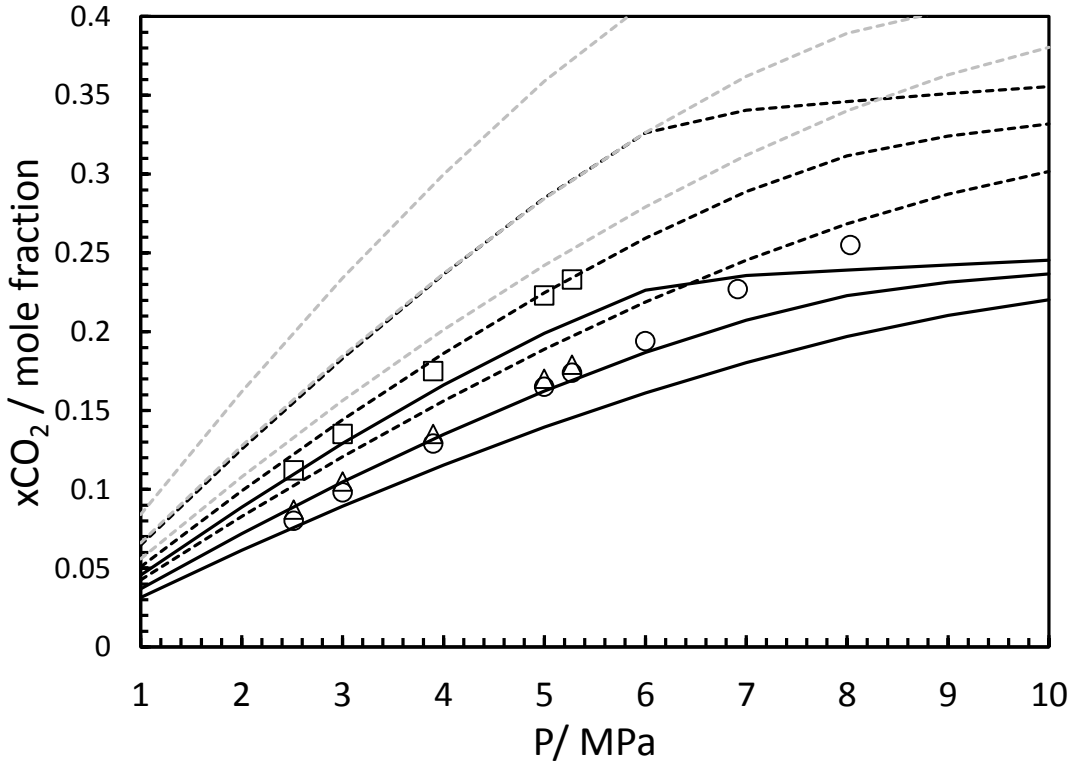

Figure 3.22 illustrates the solubility of CO_2 in 93 wt % TEG Solution measured by Takahashi et al. [13] at 297.04 K (□), 310.93 K (△) and 322.04 K (○). Grey Dotted Lines: CPA-SRK72-model predicting the solubility of CO_2 in pure TEG. Black Lines: CPA-SRK72-model at 93 wt% Solution with extrapolated k_{ij}. Black Dotted Lines: CPA-SRK72-model at 93 wt% solution with k_{ij} tuned on binary systems.

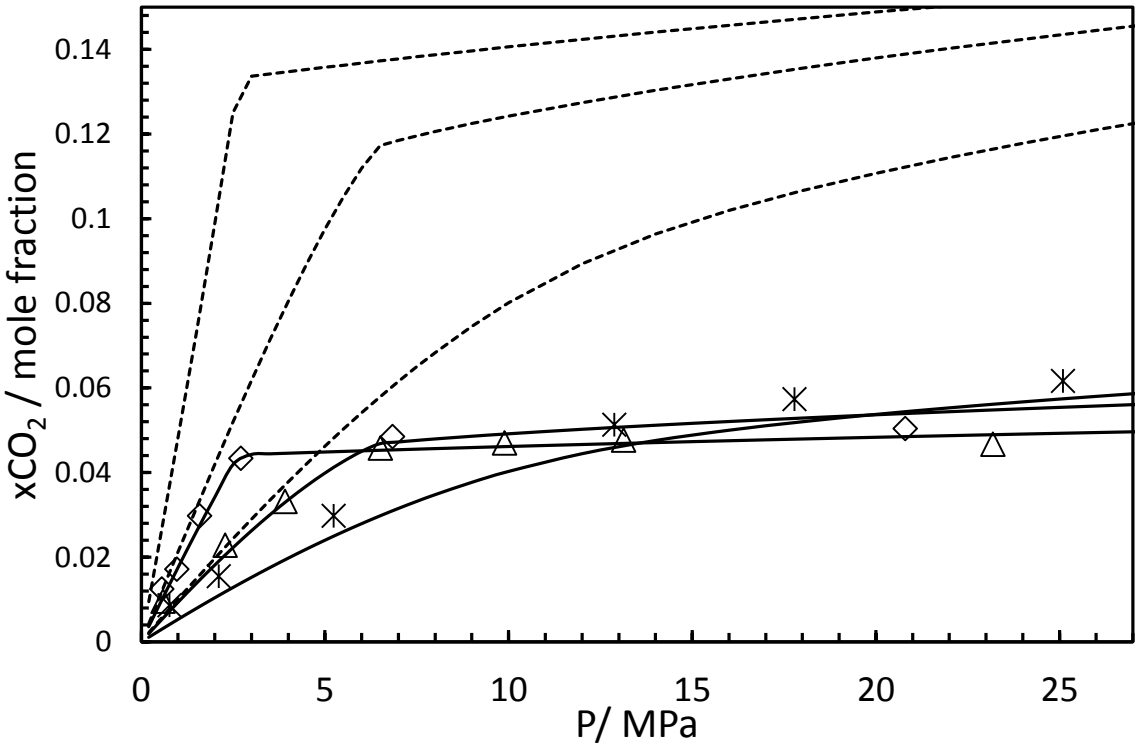

Figure 3.23 showing the solubility of CO2 in 60% TEG solution at 263.15 K (◇), 298.15 K (△) and 343.15 K (∗). Dotted Black Lines: CPA-SRK72-model with k_{ij} tuned on binary systems. Black Lines: CPA-SRK72-model with specific k_{ij}.

Table 3.17 The solubility of CO_2 in 40% TEG solution (x_1) from T = 263.15 to 343.15 K, pressures (P) up to 24 MPa and standard uncertainty $u_r(x_1)$[a].

T/K	P/ MPa	x_1 (mol frac)	$u_r(x_1)$
263.15	0.30	0.0095	0.0004
263.15	0.61	0.0135	0.0005
263.15	2.57	0.0213	0.0007
263.15	4.07	0.0239	0.0008
263.15	12.38	0.0243	0.0008
263.15	18.26	0.0240	0.0008
263.15	23.92	0.0237	0.0008
273.15	0.46	0.0101	0.0004
273.15	1.52	0.0197	0.0007
273.15	2.08	0.0252	0.0008
273.15	3.53	0.0334	0.0011
273.15	6.15	0.0355	0.0011
273.15	11.82	0.0365	0.0012
273.15	16.82	0.0370	0.0012
273.15	23.20	0.0383	0.0012
298.15	0.66	0.0088	0.0003
298.15	2.33	0.0180	0.0006
298.15	6.07	0.0316	0.0011
298.15	10.67	0.0337	0.0011
298.15	16.24	0.0343	0.0011
298.15	21.09	0.0354	0.0011
343.15	0.54	0.0067	0.0003
343.15	1.21	0.0089	0.0004
343.15	3.28	0.0154	0.0006
343.15	9.80	0.0305	0.0010
343.15	15.51	0.0348	0.0011
343.15	20.30	0.0381	0.0011

[a] Standard uncertainties u are at $u_r(x_1)$ = 0.033, $u(T)$ = 0.05 K and $u(P)$ = 0.04MPa

Table 3.18 The solubility of CO_2 in 96.5% TEG solution (x_1) from T = 297.04 to 322.04 K, pressures (P) up to 6 MPa and standard uncertainty $u_r(x_1)$[a].

T/K	P/ MPa	x_1 (mol frac)	u_r (x_1)
297.04	4.73	0.2396	0.0061
297.04	5.61	0.2913	0.0074
310.93	2.23	0.0930	0.0024
310.93	5.88	0.2267	0.0057
322.04	2.12	0.0679	0.0018
322.04	2.77	0.0965	0.0025
322.04	4.92	0.1673	0.0042
322.04	6.29	0.2096	0.0053

[a] Standard uncertainties u are at $u_r(x_1)$ = 0.025, $u(T)$ = 0.05 K and $u(P)$ = 0.04MPa

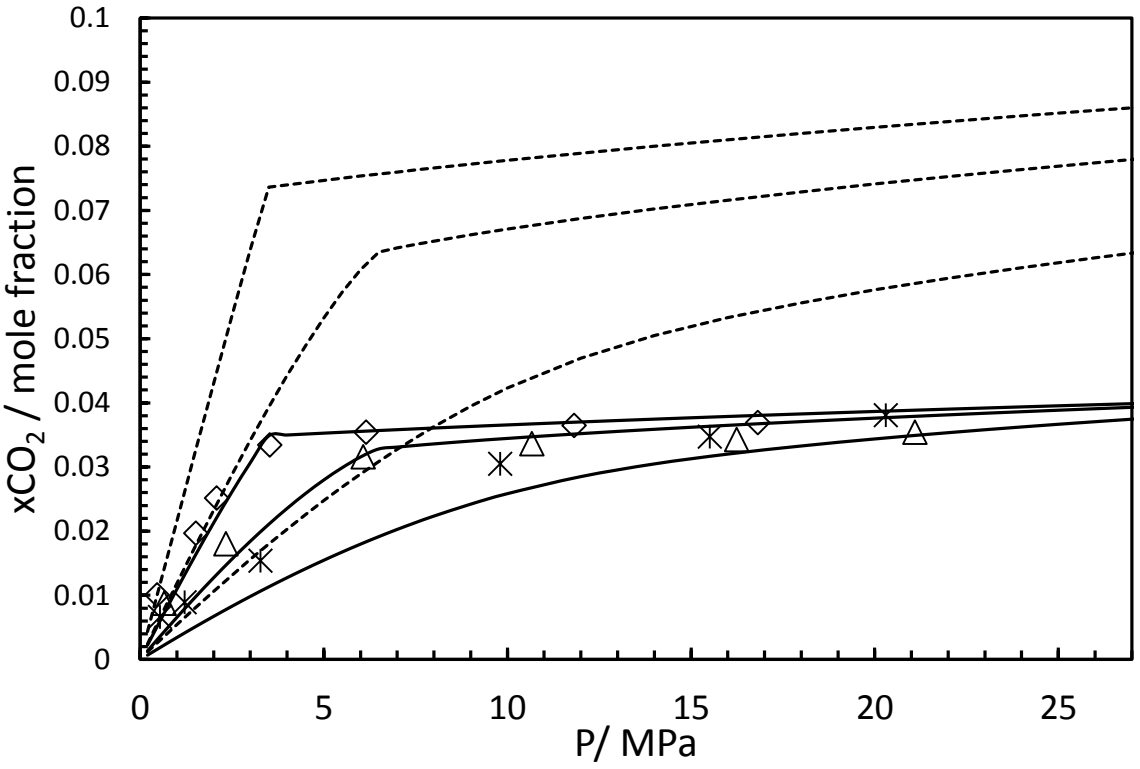

Figure 3.24 showing the solubility of CO_2 in 40% TEG solution at 273.15 K (◇), 298.15 K (△) and 343.15 K (∗). Black lines: CPA-SRK72 model predictions.

Figure 3.25 shows the BIPs between TEG and CO_2 regressed using the data from this work. Eq. 3.3 was developed using the data from this work. The correlations may be used

to calculate concentration dependant BIPs between TEG and CO_2 for systems containing water.

Table 3.19. Optimised BIPs between CO_2 and TEG for pure and TEG aqueous solutions.

wt% DEG	Mole Fraction	BIPs (k_{ij})	T range (K)
100	1.000	0.018	273.15 - 373.15
90	0.519	0.060	263.15 - 343.15
60	0.152	0.092	263.15 - 343.15
40	0.074	0.099	263.15 - 343.15

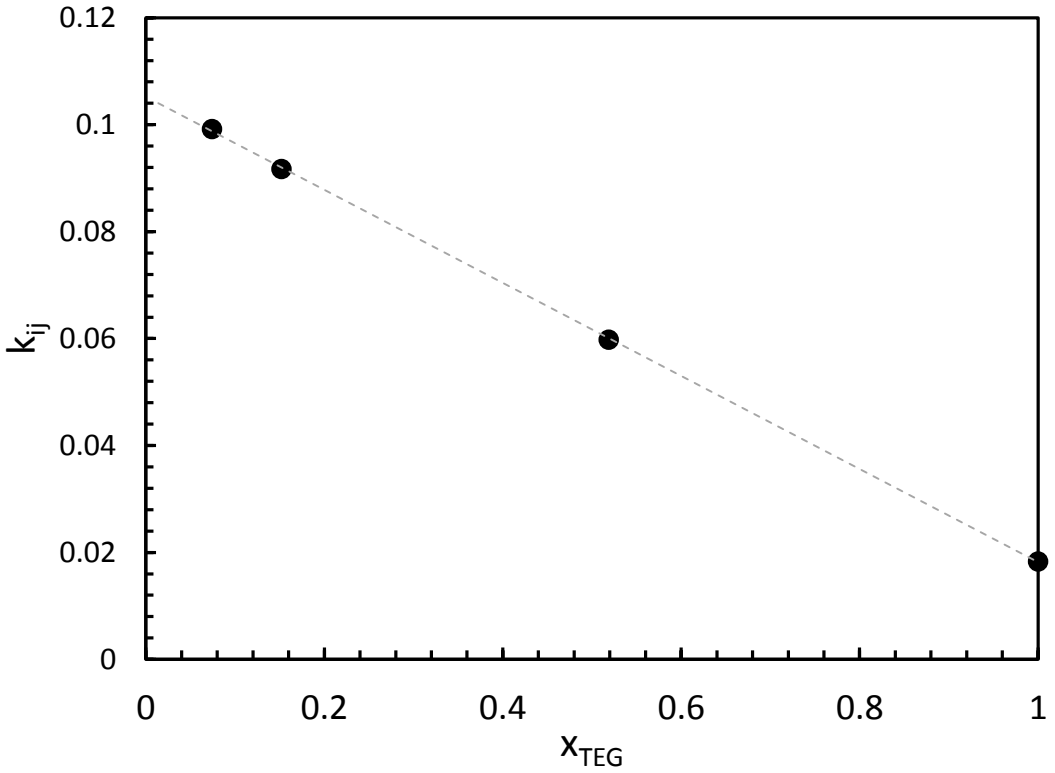

Figure 3.25. Binary Interaction Parameter, k_{ij} between CO_2 and TEG for pure and aqueous solutions.

$$k_{ij} = -0.0871x + 0.1052 \tag{3.3}$$

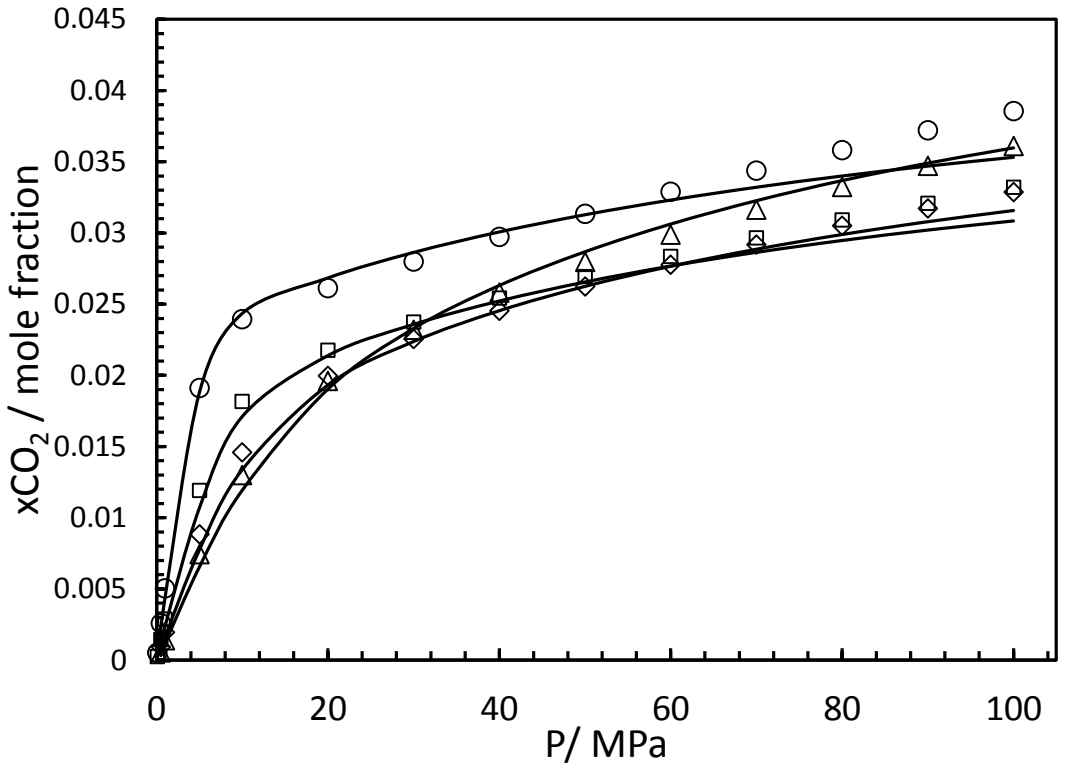

Figure 3.26. Solubility of CO_2 in pure water at 303.15 (○), 333.15 (□), 363.15 (◇), 393.15 (△) and 453.15 (∗) as reported by Duan and Sun [21] together with CPA-SRK72 (black lines) model predictions.

3.4 Conclusion

As the traditional, high methane content natural gas reservoirs are depleted companies have started moving towards exploiting high sour gas content wells. CO_2 transportation issues are a major obstacle in such reservoirs as well as in CCS and EOR projects.

Knowledge of CO_2 solubility in glycols is of paramount importance for the economic design of CO_2 transport pipelines as well as glycol dehydration units.

In this study a number of literature data were collated, showing gaps in solubility measurements for CO_2 in MEG, DEG and TEG and aqueous solutions (90, 60 and 40 wt%) at pressures and temperatures ranging from 0.2 – 43.4 MPa and 263 – 343 K, were measured. These solubility data were used to tune the binary interaction parameters used in predicting inhibitor distribution in multi-component systems.

CPA-SRK72 was used to predict the solubility of CO_2 in MEG, DEG and TEG together with 90, 60 and 40 wt% aqueous solutions at various temperatures and pressures. The predictions were in good agreement with the measurements in this work for pure MEG, DEG and TEG showing an absolute average deviation of 5.13, 9.51 and 2.55% respectively.

The measurements at 298.15 K were in good agreement with the work of Jou et al. [9] demonstrating a relative absolute average deviation of 5.4% from this work within the range published. The solubility measurements for CO_2 in MEG at 323.15 K was compared with the work of Jou et al. [9], Zheng et al. [11] and Galvao et al. [12]. This work showed an overall absolute average deviation of 5.0% from Zheng et al. [11] data. The CO_2 in MEG solubility measurements at 343.15 K demonstrated an absolute average deviation of 4.3%.

The solubility of CO_2 in DEG demonstrated good agreement with the work published by Jou et al. [10] at 298.15 K. The solubility measurements for CO_2 in TEG was compared with the work published by Jou et al. [8] showing an overall absolute average deviation of 4.6%. Thus it may be concluded that CPA-SRK72 results are in good agreement with experimental data for pure glycols.

The solubility of CO_2 in glycols solution decreases significantly with the addition of water as shown by this work and the work conducted by Takahashi et al. [13] The measurements carried out in this work at 96.5 wt% TEG solution did not completely agree with the work of Takahashi et al. [13] and the author recommends further independent measurements of CO_2 solubility in TEG 96.5 and 93 wt% TEG solution.

The BIPs between the glycol and CO_2 were tuned for each of the water concentrations to improve the predictions. This decreased the model prediction deviations significantly; however, it may be concluded that CPA-SRK72 and other classical based EoS are not suitable for predicting the solubility of CO_2 in glycol solution.

3.5 References

[1] C. Rosenzweig, D. Karoly, M. Vicarelli, P. Neofotis, Q. Wu, G. Casassa, et al., Attributing physical and biological impacts to anthropogenic climate change., Nature. 453 (2008) 353–7. doi:10.1038/nature06937.

[2] S. Holloway, An overview of the underground disposal of carbon dioxide, Energy Convers. Manag. 38 (1997) S193–S198. doi:10.1016/S0196-8904(96)00268-3.

[3] C. Marchetti, On geoengineering and the CO2 problem, Clim. Change. 1 (1977) 59–68. doi:10.1007/BF00162777.

[4] M. Myers, L. Stalker, B. Pejcic, A. Ross, Tracers – Past, present and future applications in CO2 geosequestration, Appl. Geochemistry. 30 (2013) 125–135. doi:10.1016/j.apgeochem.2012.06.001.

[5] I. Tsivintzelis, G.M. Kontogeorgis, M.L. Michelsen, E.H. Stenby, Modeling phase equilibria for acid gas mixtures using the CPA equation of state. I. Mixtures with H2S, AIChE J. 56 (2010) 2965–2982. doi:10.1002/aic.12207.

[6] M. J, B. Mohai, S. Papp, L. Rusz, The absorption of Carbon dioxide in Triethylene Glycol and its Aqueous solutions, Gas Absorpt. Stud. XV. 8 (1964) 213–224.

[7] W. Hayduk, V.K. Malik, Density, viscosity, and carbon dioxide solubility and diffusivity in aqueous ethylene glycol solutions, J. Chem. Eng. Data. 16 (1971) 143–146. doi:10.1021/je60049a005.

[8] F.-Y. Jou, R.D. Deshmukh, F.D. Otto, A.E. Mather, Vapor-liquid equilibria for acid gases and lower alkanes in triethylene glycol, Fluid Phase Equilib. 36 (1987) 121–140. doi:10.1016/0378-3812(87)85018-5.

[9] F.-Y. Jou, R.D. Deshmukh, F.D. Otto, A.E. Mather, Vapor-Liquid Equilibria of H2S and CO2 and Ethylene Glycol at Elevated Pressures, Chem. Eng. Commun. 87 (1990) 223–231. doi:10.1080/00986449008940694.

[10] F.-Y. Jou, F.. Otto, A.. Mather, Solubility of H2S and CO2 in diethylene glycol at elevated pressures, Fluid Phase Equilib. 175 (2000) 53–61. doi:10.1016/S0378-3812(00)00440-4.

[11] D.D.-Q. Zheng, W.W.W.-D. Ma, R. Wei, T.T. Guo, Solubility study of methane, carbon dioxide and nitrogen in ethylene glycol at elevated temperatures and pressures, Fluid Phase Equilib. 155 (1999) 277–286. doi:10.1016/S0378-3812(98)00469-5.

[12] A.C. Galvão, A.Z. Francesconi, Solubility of methane and carbon dioxide in ethylene glycol at pressures up to 14MPa and temperatures ranging from (303 to 423)K, J. Chem. Thermodyn. 42 (2010) 684–688. doi:10.1016/j.jct.2009.12.009.

[13] S. Takahashi, K.Y. Song, R. Kobayashi, Experimental vapor-liquid equilibriums in the carbon dioxide-diethylene glycol-water and carbon dioxide-triethylene glycol-water systems at feasible absorption temperatures and pressures, J. Chem. Eng. Data. 29 (1984) 23–28. doi:10.1021/je00035a010.

[14] A. Chapoy, M. Nazeri, M. Kapateh, R. Burgass, C. Coquelet, B. Tohidi, Effect of impurities on thermophysical properties and phase behaviour of a CO2-rich system in CCS, Int. J. Greenh. Gas Control. 19 (2013) 92–100. doi:10.1016/j.ijggc.2013.08.019.

[15] R. Span, W. Wagner, A New Equation of State for Carbon Dioxide Covering the Fluid Region from the Triple-Point Temperature to 1100 K at Pressures up to 800 MPa, J. Phys. Chem. Ref. Data. 25 (1996) 1509. doi:10.1063/1.555991.

[16] M.H. Kapateh, A. Chapoy, R. Burgass, B. Tohidi, Experimental Measurement and Modeling of the Solubility of Methane in Methanol and Ethanol, J. Chem. Eng. Data. (2015) acs.jced.5b00793. doi:10.1021/acs.jced.5b00793.

[17] A. Filipponi, D.T. Bowron, C. Lobban, J.L. Finney, Structural Determination of the Hydrophobic Hydration Shell of Kr, Phys. Rev. Lett. 79 (1997) 1293–1296. doi:10.1103/PhysRevLett.79.1293.

[18] D.T. Bowron, A. Filipponi, M.A. Roberts, J.L. Finney, Hydrophobic Hydration and the Formation of a Clathrate Hydrate, Phys. Rev. Lett. 81 (1998) 4164–4167. doi:10.1103/PhysRevLett.81.4164.

[19] A. Bakk, J.S. Høye, Microscopic argument for the anomalous hydration heat capacity increment upon solvation of apolar substances, Phys. A Stat. Mech. Its Appl. 303 (2002) 286–294. doi:10.1016/S0378-4371(01)00494-0.

[20] N. Muller, Is there a region of highly structured water around a nonpolar solute molecule?, J. Solution Chem. 17 (1988) 661–672. doi:10.1007/BF00645977.

[21] Z. Duan, R. Sun, An improved model calculating CO2 solubility in pure water and aqueous NaCl solutions from 273 to 533 K and from 0 to 2000 bar, Chem. Geol. 193 (2003) 257–271. doi:10.1016/S0009-2541(02)00263-2.

Chapter 4 – ALCOHOL DISTRIBUTION IN THE LIQUID AND GAS PHASE

4.1 Introduction

As the easily accessible oil and gas fields move towards their end of life production, dramatic changes have ensued in the petroleum industry with the advent of deep-water exploration over the past decade. It is thus essential to ensure the un-interrupted production and transport of gas to the processing facilities. One of the major issues faced in such facilities is the production of natural gas hydrates at high pressure and low temperatures, making deep sea facilities a breeding ground for such issues. One of the most commonly used methodologies for hydrate prevention is the utilisation of thermodynamic inhibitors. These are water soluble chemicals, typically alcohols. They reduce the water activity, thus shifting the hydrate phase boundary to lower temperatures and higher pressures. The common industrial practice is to use methanol, ethanol or Mono-ethylene glycol (MEG). Due to the high Capital Expenditure (CAPEX) and Operating Expenditure (OPEX) of hydrate inhibitor injection, it is essential for operators to be able to make accurate calculations using thermodynamic models.

This part of the study focuses on performing measurements that would assist in optimising the CPA-SRK72 EoS to the predict inhibitor distribution in reservoir fluids particularly traditional high CH_4 natural gas compositions. Three experiments were setup to achieve this aim.

- Solubility of CH_4 in methanol, ethanol and ethanol water solutions
- Solubility of methanol and ethanol in CH_4
- Saturation pressure measurements for binary, ternary and quaternary systems containing CH_4, alcohol, water and heavy hydrocarbons.

The solubility of methane (CH_4) in pure methanol and ethanol at numerous isotherms were measured. These data were then used to optimise the binary interaction parameters between methane and the alcohols. Accurate binary interaction parameters are essential in developing thermodynamic models capable of predicting inhibitor distribution in multi-component systems. The model was then used to predict the methanol and ethanol distribution in the methane rich phase (inhibitor loss).

Not only can this data be used for optimising CPA they can be used to develop binary interaction parameters and optimise the numerous classical and statistical models favoured by any operator or modelling software provider.

A number of saturation gas-liquid pressure measurements were conducted for binary, ternary and quaternary systems, with a focus on systems containing gas hydrate inhibitors as well as investigating the effect of water on the saturation pressure. All of the measurements were conducted using methane, the main constituent of natural gas. These were used to test the in-house CPA-SRK72 model as well as determine the phase separation of various hydrocarbon components in the systems.

As part of this section of the work a number of measurements were made determining the vapour content of methane in the presence of methanol and ethanol. These were also used to further optimise the CPA-SRK72 model as well as demonstrate some of its short comings.

Krichevsky et al. measured the solubility of methanol in the CH_4 vapour phase between 0.004 to 71 MPa and 273.15 to 348.15 K. [1] Hemmaplardh et al. measured the vapour content of methane in the presence of methanol between 3.6 to 6.5 MPa and 288.15 to 333.15 K. [2] Lazalde-Crabtree et al. measured the solubility of methanol in methane between 4.1 to 5.7 MPa and 227.15 – 273.15 K. [3] Yarym-agaev et al. conducted a number of solubility measurements for CH_4 and methanol in both vapour and liquid phase at 298.15 to 338.15 K and 2.5 to 12.5 MPa. [4] Brunner et al. completed one the most extensive methanol distribution studies. They measured the solubility of both methane and methanol in vapour and liquid phase at 298.15 – 373.15 K and 3 to 100 MPa. [5] Hong et al. also made a similar contribution to solubility data for methanol and CH_4 in both vapour and liquid phase making measurements between 200 to 330 K and 0.6 to 41.3 MPa. [6] Schneider measured the solubility of CH_4 in methanol in his PhD thesis at 183.15 to 298.15 K and 0.9 to 10.3 MPa. [7] Langhorst made a number of measurements determining the vapour content of methane in the presence of methanol between 2.4 to 9.4 MPa and 242.56 to 282.66 K. [8] Ukai et al. measured CH_4 in methanol solubility at 280.15 K and the pressure ranges of 2.1 to 11.4 MPa. [9] Wang et al. made a number of solubility measurements at 283.2 to 303.2 K and 5 to 40 MPa. [10] Frost et al. also made a number of measurements recently at 298.87 K and 5 to 18 MPa with methane, methanol and water in both vapour and liquid phase. [11]

The literature data for the solubility of CH_4 and ethanol are less common. Suzuki et al. made a limited number of measurements at 313.4 to 333.4 K and 1.8 to 10.5 MPa in both

vapour and liquid phase. [12] Brunner et al. made a number of measurements at 298.15 to 498.15 K and 3.3 to 31.5 MPa for both liquid and vapour phase. [13] Ukai et al. made measurements at 280.15 K and 1.5 to 5.7 MPa in the liquid phase. [9] Friend et al. also made measurements at 323 to 373 K and 2.1 to 2.7 MPa in the liquid phase. [14]

It is apparent from the literature review, the availability of solubility data for CH_4 in ethanol in open literature is limited, particularly at the hydrate inhibition temperatures and pressures. Thus this study's main focus was the measurement and modelling of CH_4 in ethanol at low temperatures and a wide range of pressures. This is of particular importance in the modern petroleum industry where there is a move towards the use of greener, less toxic chemicals. It is also of interest to petroleum companies operating in South America where an abundance of ethanol makes its use far more economically viable than other inhibitors. [15–18]

4.2 Materials and Method

4.2.1 Solubility of Methane in Alcohols and Solutions

The schematics of the set-up used for the solubility study are shown in Figure 4.1 and Figure 4.2. The rig was loaded with an alcohol or solution and the cell was vacuumed to minimise the interference of air on the measurements. A pressurised cylinder containing CH_4 was then used to load the rig to the desired pressure. The details of the material used are shown in Table 4.1.

Table 4.1 Materials, their purity and suppliers used – CH_4 in alcohols.

Material	Source	Mole % Purity[a]	Purity Certification	Analysis method[b]
Methanol	J.T. Baker	99.80	Avantor Materials	GC
Ethanol	J.T. Baker	99.90	Avantor Materials	GC
Methane	BOC	9.995	BOC Certified	GC

[a] No additional purification is carried out for all samples. [b] GC: Gas Chromatography

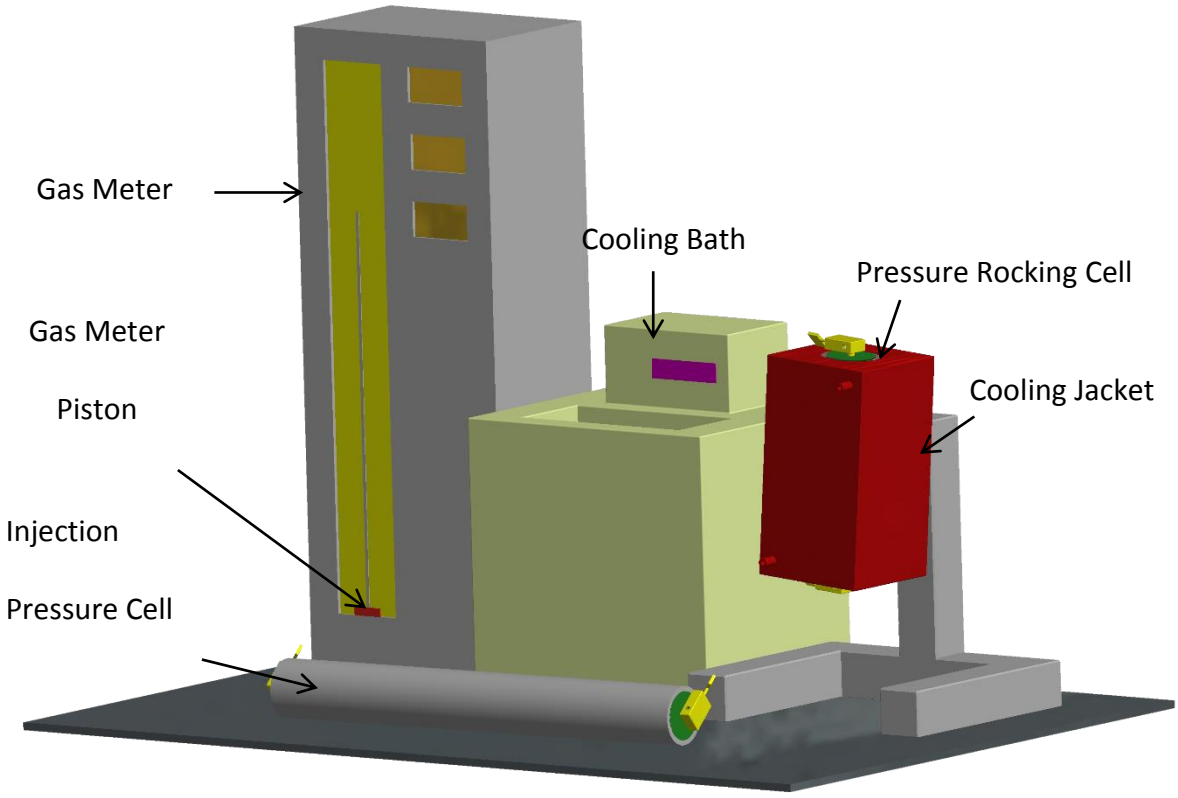

Figure 4.1 3D schematic of the pressure rig used in this work.

The setup used in this work was similar to the rocking cell setup used by Chapoy et al. [19] to determine the saturation pressure of a multicomponent mixture.

The 350 cm^3 (piston-less) pressure rocking cell was loaded with 300 cm^3 of the desired alcohol from the top. The cell was then sealed. The air was vacuumed from the cell top via V02. The gas was injected into the cell from the top via V02. The gas cylinder was then disconnected and the pneumatic rocking cell was initialised, allowing the mixture to equilibrate (steady pressure and temperature on the computer log). To measure the solubility of CH_4 in the solution at the specified pressure and temperature, a flash tank was connected to a VINCI Technology manual gas meter. The gas meter utilized, was capable of retaining a maximum capacity of 4000 cm^3, with a volume and temperature resolution of 0.1 cm^3 and 0.1 °C, respectively and a standard uncertainty of 0.1%.

For each measurement, the pressure and temperature of the cell, together with the pressure, temperature and initial volume of the gas meter chamber were recorded. The pressure of the cell in the rig was kept constant during sampling by CH_4 injection (V02). A liquid sample (average of 10 grams per run) was then passed from the base of the cell (V03), whilst it was held in a vertical position, into the 2-phase separator releasing the gas at atmospheric pressure into the gas meter (V05). By this means the CH_4 was collected

in the gas meter. After all of the CH_4 was collected the volume was adjusted manually to give atmospheric pressure. The final volume at atmospheric pressure, together with temperature was recorded. The mass of the extracted solution was also measured using a Mettler Toledo balance (PB3003-S) with a weighing range of 0.5 – 3100 g, a resolution of 0.01 g and a standard uncertainty of u(m) = 0.01 g. The pressure and temperature of the gas meter were used to obtain the density of CH_4 at each point (relative standard uncertainty $u_r(\rho) = 0.0003$), which were then used to calculate the mole of CH_4 in the vapour phase. See Eq. C.1 in Appendix C for the solubility calculation formula.

The pressure of the cell was increased by CH_4 injection from V01 and V02, and the procedure repeated, producing solubility results at various pressures and at a specific temperature.

The standard uncertainty of the pressure rocking cell transducer $u(P) = 0.04$ MPa and the standard uncertainty for the PRT temperature probe was $u(T) = 0.05$ K, the effects of which was negligible with respect to the overall standard uncertainty of the solubility measurements.

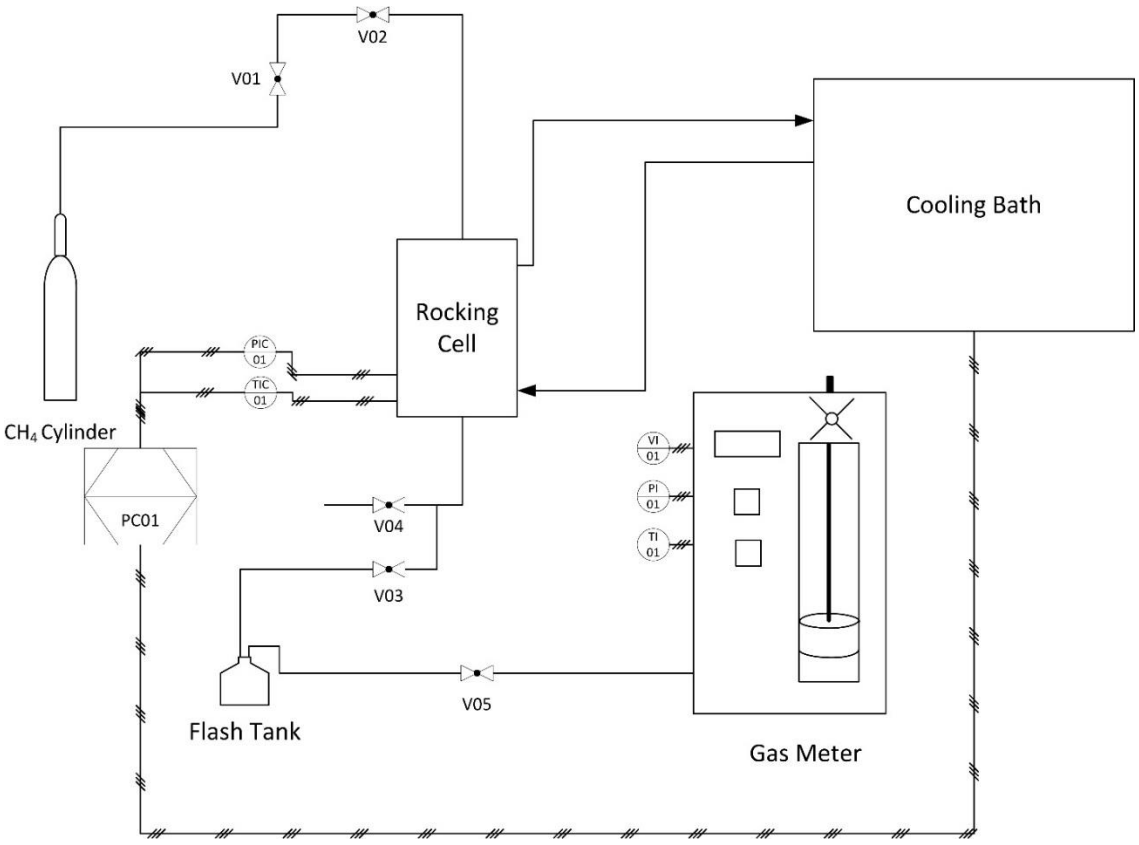

Figure 4.2 Schematic of the rocking cell setup used to measure the solubility of CH_4 in Alcohols. Table 4.2 shows the key for this schematic.

Table 4.2 Key to Figure 4.2.

Key	Description
PI01	Gas Meter Pressure Indicator
PIC01	Equilibrium Cell Pressure Indicator/logger
TI01	Gas Meter Temperature Indicator
TIC01	Equilibrium Cell Temperature Indicator Controller
V01	CH_4 Cylinder Control Valve
V02	Equilibrium Cell Injection Valve
V03	Equilibrium Cell Drain Valve
V04	Equilibrium Cell Drain Valve (Backup)
V05	Gas Meter Inlet Valve
VI01	Gas Meter Volume Indicator

4.2.2 Saturation Pressure of Reservoir Fluids

Table 4.3. Materials, their purity and suppliers used – saturation pressure measurements.

Material	**Source**	**Mole % Purity[a]**	**Purity Certification**	**Analysis Method[b]**
Methane	Air Products Inc	99.995	BOC Certified	GC
Heptane	Rathburn Chemicals	>99	Rathburn Certified	GC
Nonane	Sigma Aldrich Co	>99	Sigma Aldrich Certified	GC
Decane	Sigma Aldrich Co	>99	Sigma Aldrich Certified	GC
Undecane	Sigma Aldrich Co	>99	Sigma Aldrich Certified	GC
Dodecane	Acros Organics	>99	Acros Certified	GC
Toluene	Acros Organics	99.98	Acros Certified	GC
Methanol	Fisher Chemicals	99.8	Fisher Chemical Certified	GC
Ethanol	Fisher Chemicals	99.5	Fisher Chemical Certified	GC

[a] No additional purification is carried out for all samples. [b] GC: Gas Chromatography

Table 4.3 shows the materials used in the saturation pressure measurements together with their purities and suppliers.

The setup used in the saturation pressure measurements was very similar to the rig used for solubility measurements. The schematics of the set-up used for the saturation pressure study is shown in Figure 4.1 and Figure 4.3. The author used this setup for the bubble point measurement published by Chapoy et al. [19].

The setup comprised of an equilibrium cell with a maximum effective volume of 300 cm^3, Julabo F50 cryostat, pneumatic rocking mechanism, as well as temperature and pressure recording equipment controlled by a PC and logged using National Instrument LabView 2012. The equilibrium cell used was a piston-type variable volume titanium cylindrical pressure vessel with a mixing ball, mounted on a horizontal pivot with associated stand for pneumatic controlled rocking through 180 degrees. Rocking of the cell, and the subsequent movement of the mixing ball within it, ensured adequate mixing of the cell fluids.

The rig utilised had a working temperature range of 203 – 323 K, with a maximum operating pressure of 69 MPa. The cell was housed in a metallic jacket, with fluid circulating from the cryostat, at a flow rate of 11 L/min, ensuring stable temperatures. The metallic jacket was further covered using polystyrene insulation foam to prevent fluctuation in temperature. The tubing connected to the cryostat were covered using plastic insulation foam.

The temperature was measured by means of a PRT (Platinum Resistance Thermometer) located within the cooling jacket of the cell with a standard uncertainty of $u(T) = 0.1$ K. A strain gauge pressure transducer, with a standard uncertainty of $u(P) = 0.04$ MPa was used to monitor the rig pressure. Temperatures and Pressures were monitored and recorded by a PC through RS 232 serial ports. The cryostat was monitored and controlled *via* an interface connected to a serial port on the computer.

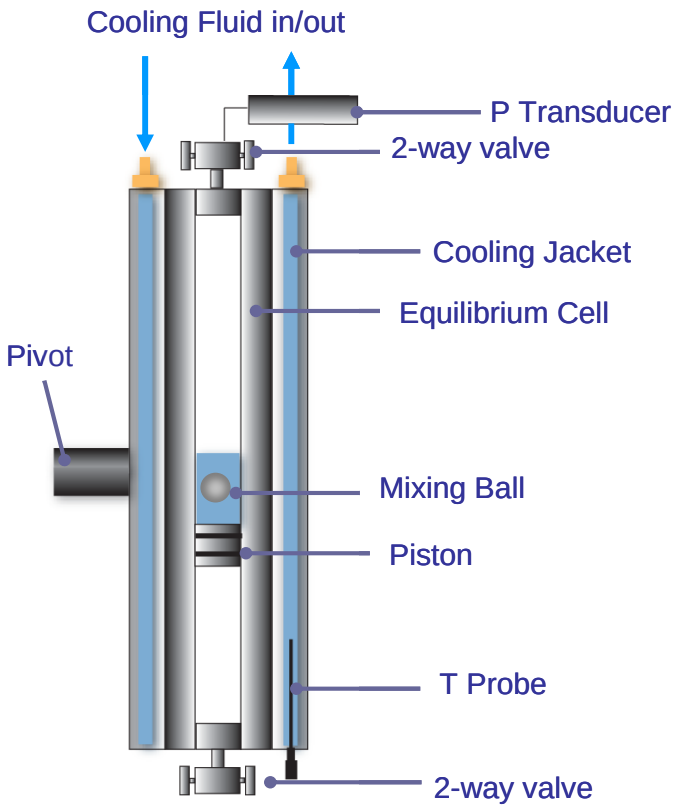

Figure 4.3 Pressure rocking cell used to determine the saturation pressures of various hydrocarbon-aqueous systems in this project.

A 300 cm^3 piston pressure cell was used to prepare the samples. The components were weighed using Mettler Toledo PB3003-S balance with a standard uncertainty of 0.01g. All of the pressure cells used during the preparation and the testing were evacuated using an Edwards IT20 vacuum pump. The prepared sample was pressurised to well above the expected saturation pressure (41 MPa) before being injected into the evacuated rig to ensure uniformity of the system.

Two measurement methods were used while conducting these experiments. The first method was the isothermal method, where the temperatures were kept constant and the volume of the system was decreased gradually, letting the cell content equilibrate for approximately 30 minutes (where no pressure fluctuations were observed). The pressure was then recorded and the procedure repeated until a clear bubble point was observed. To automate the measurements, an isochoric system was setup where the temperature was gradually dropped (45 min was shown to be enough equilibration time) until saturation pressure was achieved. In the first method the equilibrium pressures and change in sample volumes were plotted and the bubble point was indicated by a sharp change in the pressure versus volume plot. An example is shown in Figure 4.4. It also demonstrates that the

bubble point is easily identifiable with a standard uncertainty of 0.05 MPa using the intersection of the straight line equations. The Pressure against Temperature may also be plotted and the same procedure was used to determine the bubble point pressure.

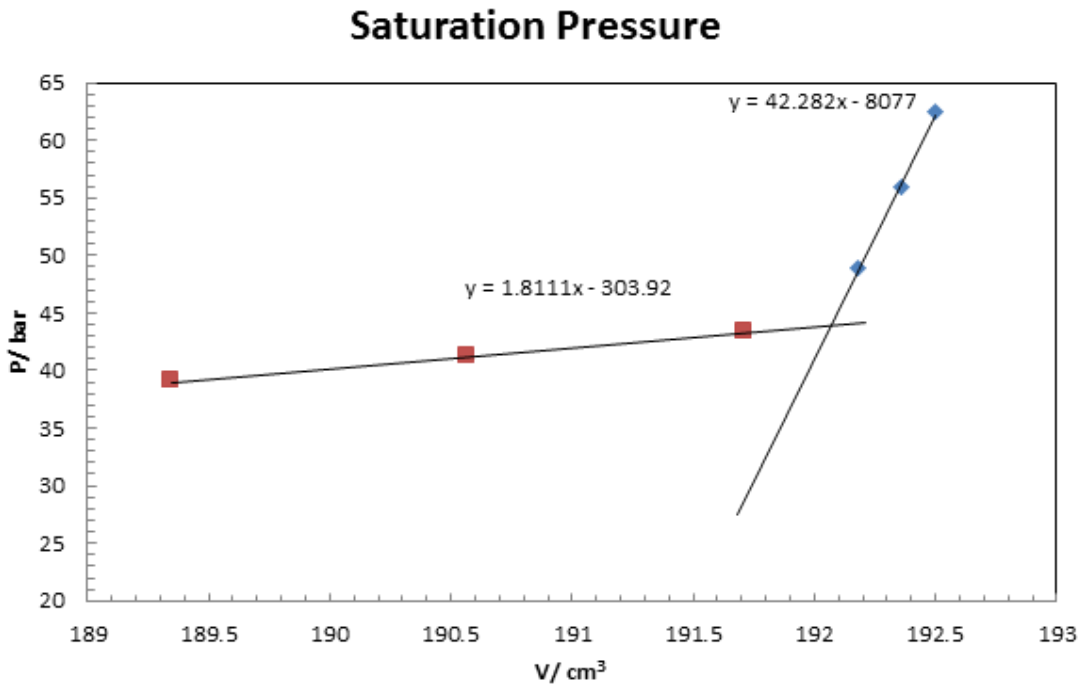

Figure 4.4. Plot showing example of bubble point determination from plot of *P* vs *V*.

For a number of occasions during this work the behaviour of the system was beyond the author's expectation, thus a similar rocking pressure cell with two sapphire windows was used to determine the existence of multiple phases or emulsions. The visual rig comprised of a 100 cm^3 cell with a maximum operating pressure of 50 MPa and a temperature range of 243.15 – 353.15 K. A light source as well as a camera was available to see the phase separation more clearly. The sapphire windows were 40 mm in diameter and the cell was well insulated. The coolant was circulated through the cell's jacket at 15 L/min keeping the temperature of the system constant during each step heating (heating increased with a specific temperature step and allowed to stabilise for a set time period). The bubble point pressure was determined using the isochoric method, however in this case visually.

The mixture being tested was prepared in a separate pressure cell as described earlier. It was then injected into the sapphire pressure cell at a rate of 0.4 MPa/min at a temperature above the expected saturation pressure. The system was then equilibrated in the same manner described earlier. The temperature of the sapphire cell was then reduced one degree (allowing enough time for equilibrium to be reached) at a time until the first

bubble appeared (bubble point). This pressure was recorded and the pressure was reduced further examining the phase separation and noting unusual behaviour.

4.2.3 Vapour Content of Methane in the presence of alcohols

The set-up used to measure the solubility of methanol and ethanol in methane comprised of a HP5890-4 GC fitted with a Poropak-Q column. The GC was fitted with a 6 port external sample injector (type 1/16) contained within an oven set at 373.15 K. Two different cells were used in these measurements. The tests were initially carried out in a 9 litre pressure piston cell with a pressure rating of 27.6 MPa. To conserve gas and increase the pressure range of the measurements a 300 cm^3 piston pressure cell was used.

The 9 litre pressure cell consisted of a stainless steel pressure cylinder with a magnetic stirring motor at the bottom of the cell. The piston was placed on top side of the cell, which was displaced using water injection from a Quizix Q6000 pressure metering pump controlled via a computer interface. The alcohol and gas were injected from a side valve. The stiring motor was allowed to run for 45 minutes before being switched off and the system was allowed to settle for 15 minutes to ensure equilibrium. The pressure was measured using a strain gauge pressure transducer with a standard uncertainty of $u(P)$ = 0.4 MPa. The temperature was measured using a PRT placed inside the cell. A Julabo F70 was used to supply the cooling jacket with the cooling/heating circulating fluid required at a rate of 16 L/min. The cooling jacket was well insulated using foam and radiance limiting reflective aluminium sheets. The tubing connecting the cryostat and the cooling jacket were also well insulated to ensure maximum temperature stability.

The equilibrated gas was transferred from the cell to the GC injector valve via a Winkler heated line maintained at 473.15 K. The 300 cm^3 pressure vessel used in this work was the same as the one described in the CH_4 in alcohol solubility described earlier. To minimise standard uncertainty, 10 samples were taken for each of the pressure points in the isotherm. The mean average of the peak areas were calculated. The calibration formula developed was used to determine the moles of the alcohol and methane.

$$y_i = \frac{y_{CH_3OH}}{y_{CH_4} + y_{CH_3OH}} \times 10^6 \qquad (4.1)$$

Where y_i is the Parts Per Million (ppm) of alcohol in the vapour phase, $y$$CH_3OH$ is the mole of methanol and $y$$CH_4$ is the mole of CH_4. A picture of the heated line,

external sample injector and GC is shown in Figure 4.5.

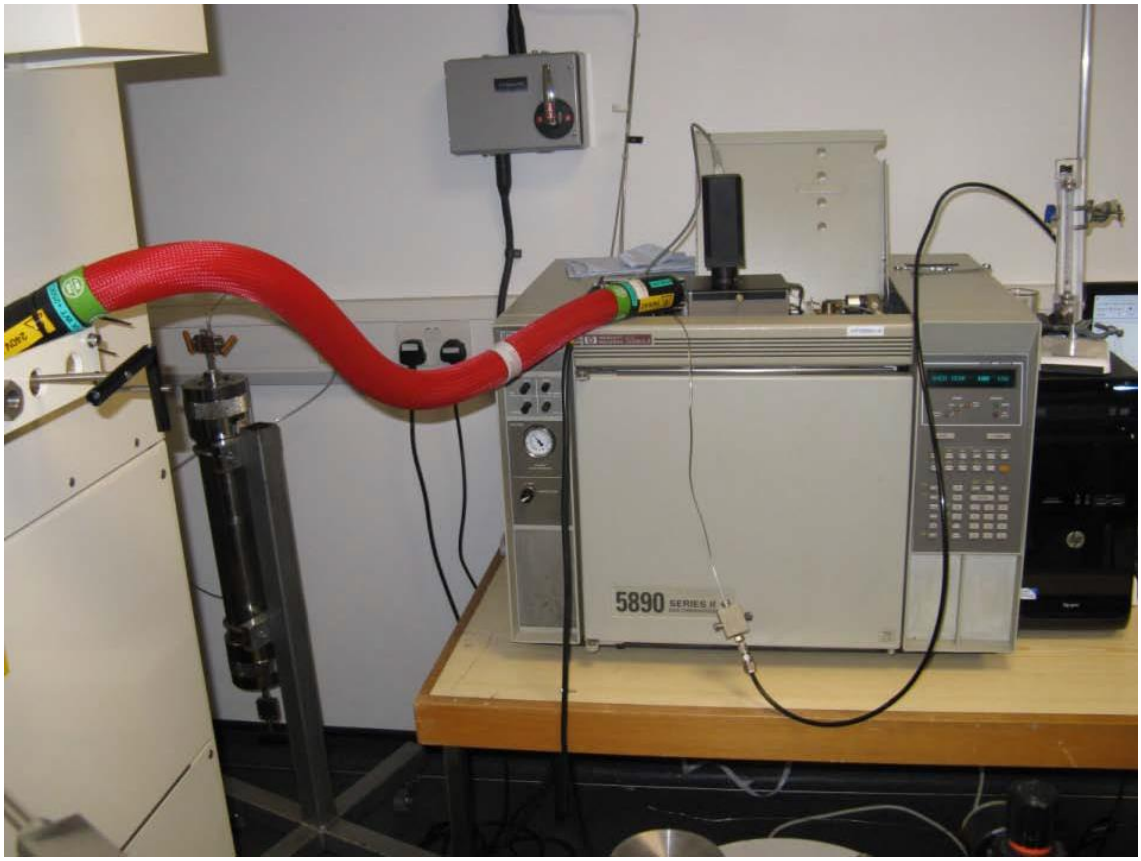

Figure 4.5. Picture showing heated transfer line, heated valve and Hewlett Packard 5890 Series II GC.

4.3 Results and Discussion

4.3.1 Solubility of Methane in Pure Alcohols

Table 4.4 shows the measured solubility of methane in methanol. Table 4.5 and Table 4.6 show the measured solubility of methane in ethanol, where T is temperature in Kelvin, P is the pressure in MPa and x_1 is the mole fraction of CH_4 in the alcohol. Both tables also contain a number of the measurements repeated at the same pressure or in close proximity of the previously measured pressure. Based on the illustrated results the average percentage repeatability was calculated to be within 2.5%. The standard uncertainty of the measurements was calculated based on the four main variables within the measurements, the volume of methane measured using the gas meter, the mass of methanol and ethanol measured using the balance, the error inflicted by the calculation of alcohol in the atmospheric vapour phase, the mole fraction of CH_4 in the liquid phase using the CPA-SRK72 EoS and the repeatability. The standard uncertainty in the density data from NIST was deemed negligible at $u_r(\rho) = 0.0003$. The apparatus measurement standard uncertainties reported by the manufacturers were then used to calculate the uncertainty of each measurement (Appendix A). These showed an overall standard uncertainty of $u_r(x_1) = 0.029$ and $u_r(x_1) = 0.027$ for the solubility of CH_4 in methanol and ethanol respectively.

Table 4.4. The solubility of Methane in Methanol x_1 at $T = 273.15$, Pressure (P) up to 47 MPa and standard uncertainty $u_r(x_1)$ [a].

T/K	P/ MPa	x_1 (mol frac)	$u_r(x_1)$
273.15	1.71	0.0172	0.0005
273.15	3.83	0.0350	0.0010
273.15	6.68	0.0536	0.0015
273.15	8.92	0.0772	0.0021
273.15	10.96	0.0925	0.0025
273.15	14.02	0.1175	0.0034
273.15	17.53	0.1324	0.0037
273.15	22.47	0.1569	0.0043
273.15	38.33	0.2193	0.0059
273.15	46.99	0.2578	0.0071

[a] Standard uncertainties u are at $u_r(x_1) = 0.029$, $u(T) = 0.05$ K and $u(P) = 0.04$ MPa.

Table 4.5 Solubility of Methane in Ethanol x_1 for T = 238.15 to 263.15, Pressure (P) up to 40 MPa and standard uncertainty $u_r(x_1)$ [a].

T/K	P/ MPa	x_1 (mol frac)	$u_r(x_1)$	T/K	P/ MPa	x_1 (mol frac)	$u_r(x_1)$
238.15	1.17	0.0183	0.0006	253.15	19.85	0.2289	0.0059
238.15	0.79	0.0172	0.0005	253.15	27.39	0.2732	0.0070
238.15	1.37	0.0284	0.0008	253.15	27.41	0.2698	0.0069
238.15	1.37	0.0280	0.0008	253.15	34.29	0.3077	0.0079
238.15	2.94	0.0588	0.0016	253.15	34.33	0.3148	0.0081
238.15	2.95	0.0561	0.0015	253.15	39.82	0.3293	0.0085
238.15	5.25	0.0960	0.0025	263.15	0.33	0.0083	0.0003
238.15	5.25	0.0974	0.0025	263.15	0.68	0.0132	0.0004
238.15	8.25	0.1408	0.0036	263.15	0.69	0.0120	0.0004
238.15	8.27	0.1407	0.0036	263.15	2.75	0.0432	0.0012
238.15	16.18	0.2131	0.0055	263.15	2.76	0.0442	0.0012
238.15	16.18	0.2103	0.0054	263.15	6.81	0.0997	0.0026
238.15	24.16	0.2684	0.0069	263.15	6.82	0.0972	0.0025
238.15	24.21	0.2716	0.0070	263.15	11.45	0.1500	0.0039
238.15	31.49	0.3067	0.0079	263.15	11.45	0.1526	0.0039
253.15	0.37	0.0092	0.0003	263.15	13.30	0.1796	0.0046
253.15	0.37	0.0088	0.0003	263.15	13.84	0.1770	0.0046
253.15	1.38	0.0243	0.0007	263.15	19.07	0.2143	0.0055
253.15	1.38	0.0261	0.0008	263.15	19.08	0.2137	0.0055
253.15	8.45	0.1290	0.0033	263.15	25.46	0.2589	0.0066
253.15	8.46	0.1250	0.0032	263.15	25.51	0.2549	0.0065
253.15	13.24	0.1790	0.0046	263.15	32.98	0.3015	0.0077
253.15	13.33	0.1748	0.0045	263.15	33.06	0.3040	0.0078
253.15	19.80	0.2293	0.0059	263.15	39.42	0.3363	0.0087

[a] Standard uncertainties u are at $u_r(x_1)$ = 0.029, $u(T)$ = 0.05 K and $u(P)$ = 0.04 MPa.

Table 4.6. Solubility of Methane in Ethanol x1 for T = 273.15 to 298.15, Pressure (P) up to 42 MPa and standard uncertainty $u_r(x_1)$ [a].

T/K	P/ MPa	x_1 (mol frac)	$u_r(x_1)$	T/K	P/ MPa	x_1 (mol frac)	$u_r(x_1)$
273.15	2.30	0.0332	0.0005	298.15	0.64	0.0116	0.0004
273.15	5.16	0.0714	0.0019	298.15	2.54	0.0234	0.0007
273.15	10.56	0.1244	0.0032	298.15	4.32	0.0530	0.0014
273.15	13.07	0.1501	0.0039	298.15	8.09	0.0927	0.0024
273.15	17.20	0.1944	0.0050	298.15	11.36	0.1268	0.0033
273.15	21.71	0.2352	0.0061	298.15	15.58	0.1674	0.0043
273.15	28.41	0.2715	0.0070	298.15	21.03	0.2191	0.0057
273.15	32.08	0.2958	0.0076	298.15	28.99	0.2707	0.0069
273.15	36.64	0.3256	0.0084	298.15	35.17	0.3229	0.0083
273.15	41.19	0.3490	0.0090	298.15	41.69	0.3535	0.0091

[a] Standard uncertainties u are at $u_r(x_1)$ = 0.029, $u(T)$ = 0.05 K and $u(P)$ = 0.04 MPa.

Figure 4.6 shows the measured solubility of methane in Methanol at 273.15 K from this work along with the solubility measurements performed by Schneider and Hong et al.[6,7] and model calculations demonstrating the model and literature data's agreement with the solubility measurements in this work. As shown in Figure 4.6 the experimental data set is in good agreement, demonstrating the reliability of the methods and equipment used in this work. It also illustrates the model calculations using the CPA-SRK72 EoS. The model was optimized for CH_4 in Methanol during a previous study Haghighi et al. [20] using numerous data points from literature.

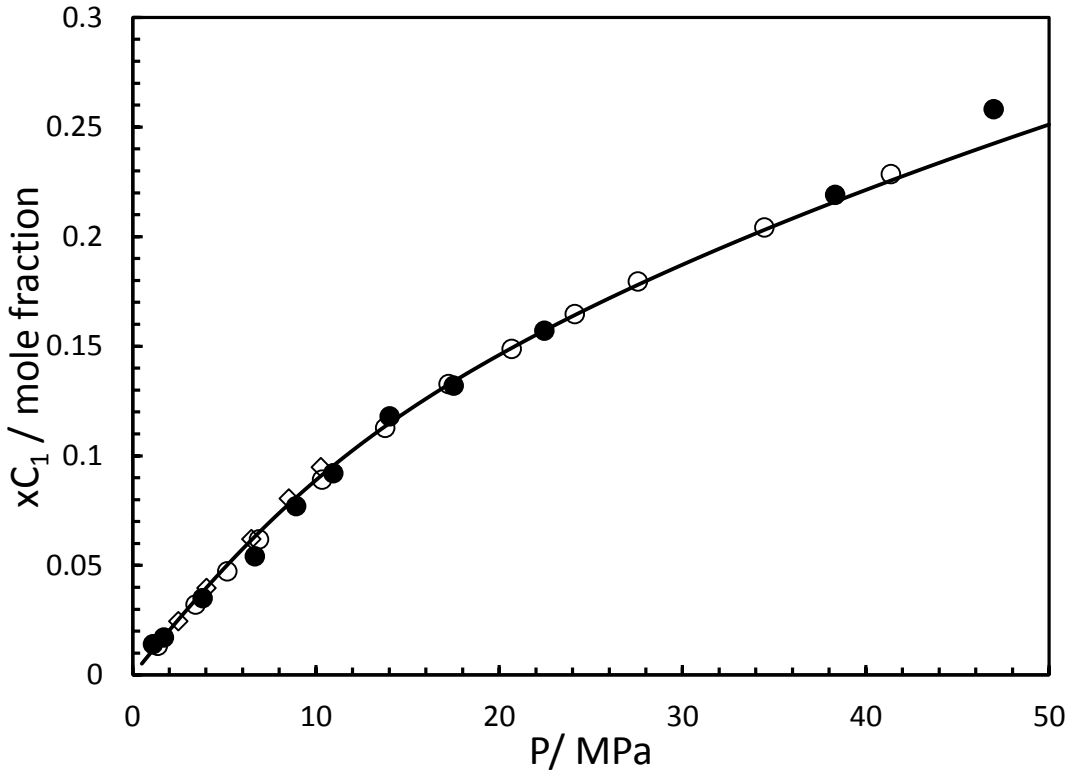

Figure 4.6. Methane Solubility in Methanol at 273.15 K. (●), this work; (◇) data from Schneider, 1978 [7] ; (○) data from Hong et al., 1987 [6]. Black Line: CPA-SRK72-model.

Figure 4.7 shows the solubility of CH_4 in Methanol at 5 different isotherms measured by Hong et al [6] and the CPA-SRK72 model calculations for each isotherm. The model calculations are in good agreement with the experimental results, illustrating the reliability of the CPA-SRK72 EoS in calculating these solubilities. Figure 4.8 shows the CH_4 in methanol solubility measurements by Brunner et al, Schneider and Yarym-Agaev et al. [4,5,7] at 298.15 K in conjunction with the CPA-SRK72 model calculations, showing very good agreement between the calculations and the experimental measurements by the three sets of data. This figure clearly illustrates in more detail the reliability of the EoS for this system.

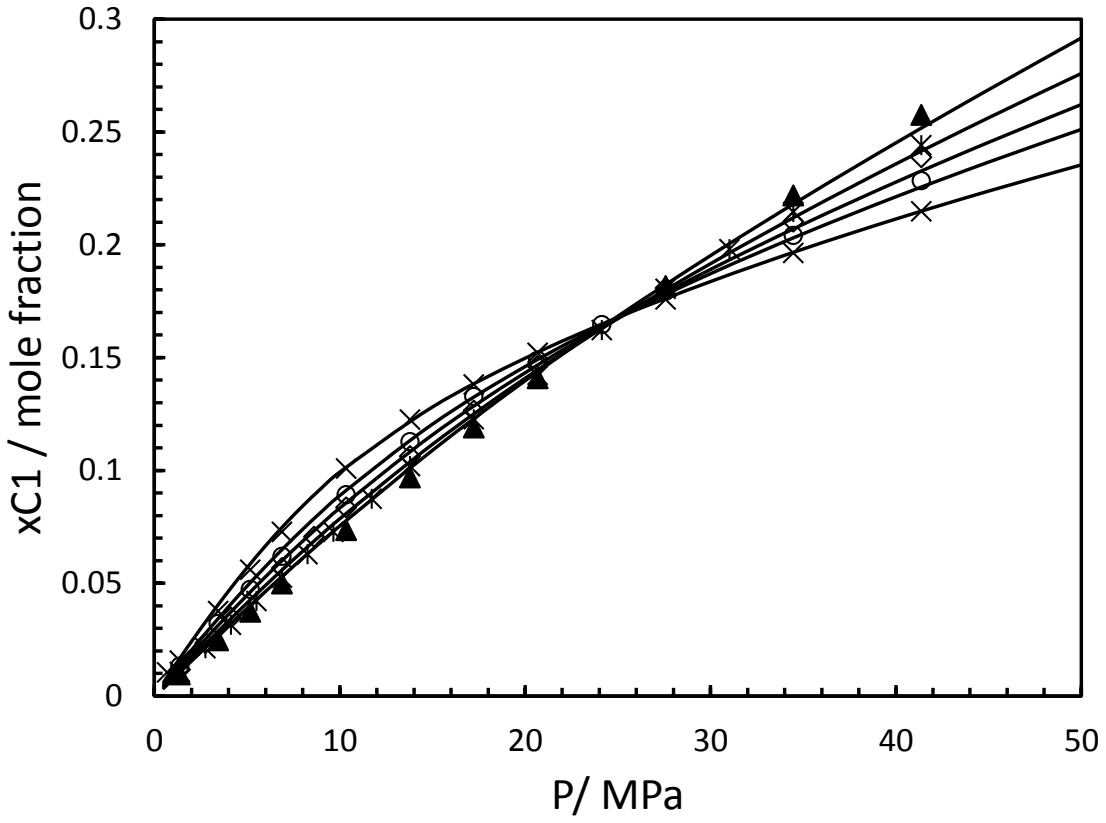

Figure 4.7. Methane Solubility in Methanol at (×) 250 , (○) 273.15 , (◇) 290 , (✱) 310 and (▲) 330 K. data from Hong et al., 1987 [6]. Black Line: CPA-SRK72-model.

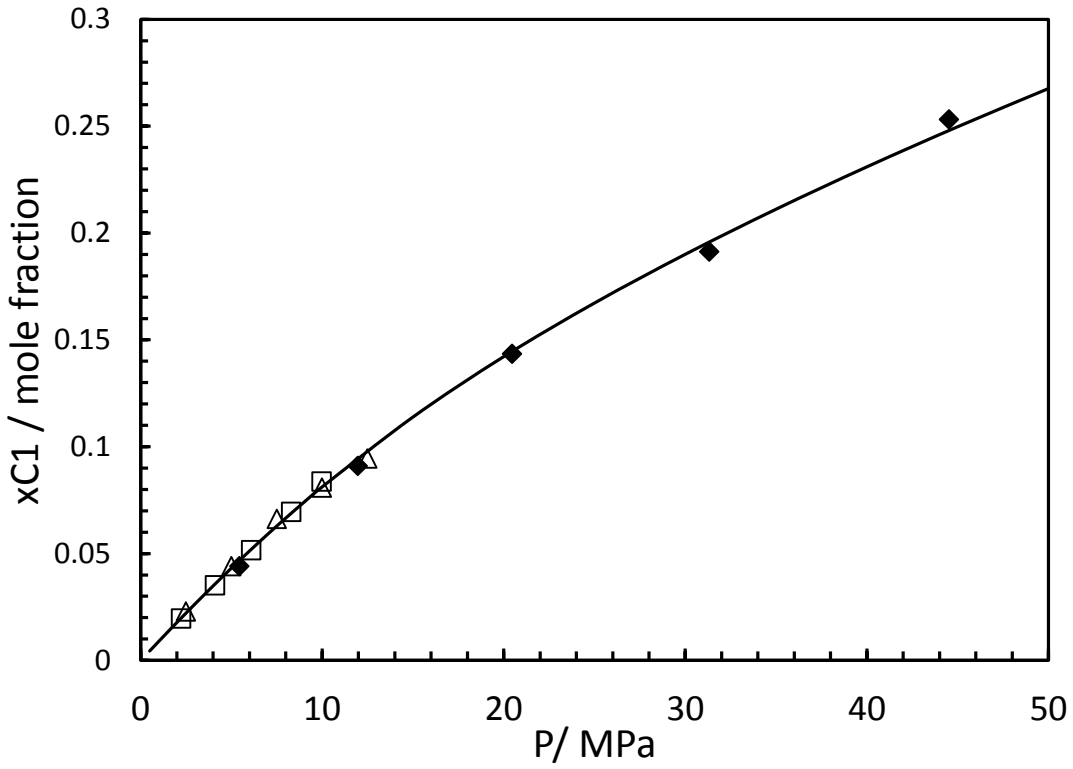

Figure 4.8. Methane Solubility in Methanol at 298.15 K. (◆), Brunner et al., 1987; (□) data from Schneider, 1978 ; (△) data from Yarym-Agaev et al., 1985 [4,5,7]. Black Line: CPA-SRK72-model.

Figure 4.9 and Figure 4.10 show the solubility of methanol in CH_4 vapour phase at 273.15 and 298.15 K measured by Brunner et al., Krichevsky and Koroleva, Yarym-Agaev et al., Hemmaplardh and King and Hong et al [1,2,4–6] together with the CPA-SRK72 model predictions. As demonstrated, the predictions are in good agreement with the experimental results at lower pressures however as the pressure increases the model consistently under predicts the solubility.

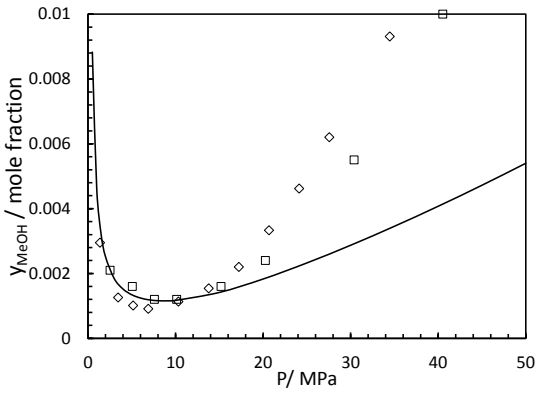

Figure 4.9. Methanol Solubility in Methane at 273.15 K. (□) data from Krichevsky and Koroleva, 1941 [1]; (◇) data from Hong et al. (1987) [6]. Black Line: CPA-SRK72-model.

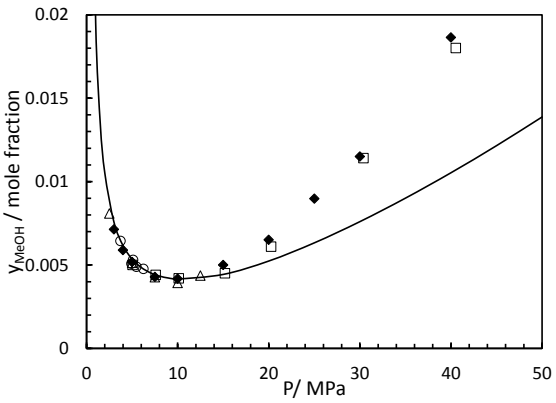

Figure 4.10. Methanol Solubility in Methane 298.15 K. (◆), Brunner et al., 1987; (□) data from Krichevsky and Koroleva, 1941 ; (△) data from Yarym-Agaev et al., 1985 ; (○) data from Hemmaplardh and King (1972); [1,2,4,5]. Black Lines: CPA-SRK72-model.

Figure 4.11 illustrates the solubility of methane in ethanol at 298.15 K measured in this work together with the measurements by Brunner et al [13], and unadjusted and adjusted CPA-SRK72 model predictions. The model's k_{ij} binary interaction parameters were adjusted using the measured experimental results in this work as no major source of solubility data for CH_4 in ethanol could be found. The measurements conducted within this work were also in good agreement with the measurements by Brunner et al. [13]. This was also to further validate the experimental equipment used by comparing the measured data to peer reviewed literature data. Figure 4.12 shows the solubility measurements from this work together with un-adjusted and adjusted CPA-SRK72 model predictions at five different isotherms. The predictions were in good agreement with the measured data after optimisation. The model's Binary Interaction Parameters were tuned on the experimental data from this work due to scarcity of experimental results in the open literature.

The high pressure solubility measurements demonstrated a reversing in trend for both methanol and ethanol when compared to the low pressure measurements seen in Figure 4.7 and Figure 4.12. Figure 4.7 clearly shows a cross over point at 25 MPa where the solubility trend is reversed for methane in methanol. This cross over is visible at 35 MPa in Figure 4.12 for the solubility of methane in ethanol. A similar trend was observed when measuring the solubility of CO_2 in glycols (another series of commonly used

inhibitors). Furthermore, this trend is shown when the solubility of CO_2 is measured in water as shown in Figure 3.26.

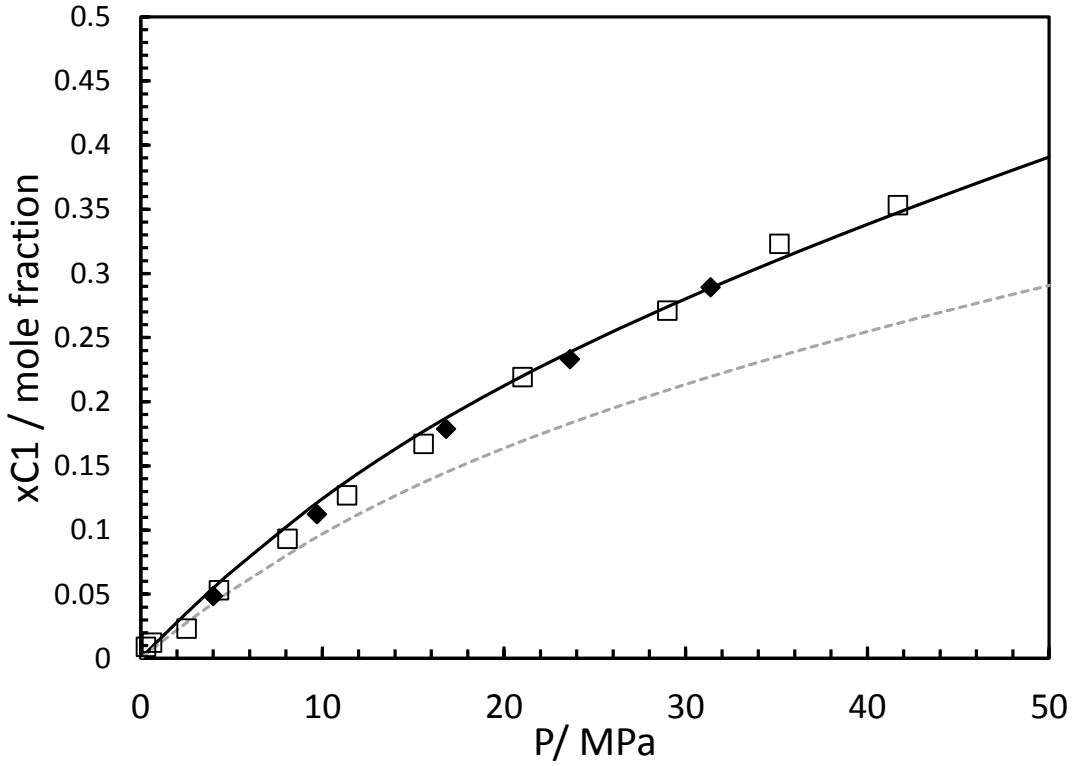

Figure 4.11. Methane Solubility in Ethanol at 298.15 K. (◆), Brunner et al., 1990 [13]; (□) This work. Lines: CPA-SRK72-model - Black lines: adjusted k_{ij} = -0.049; Dotted grey lines: $k_{ij} = 0$.

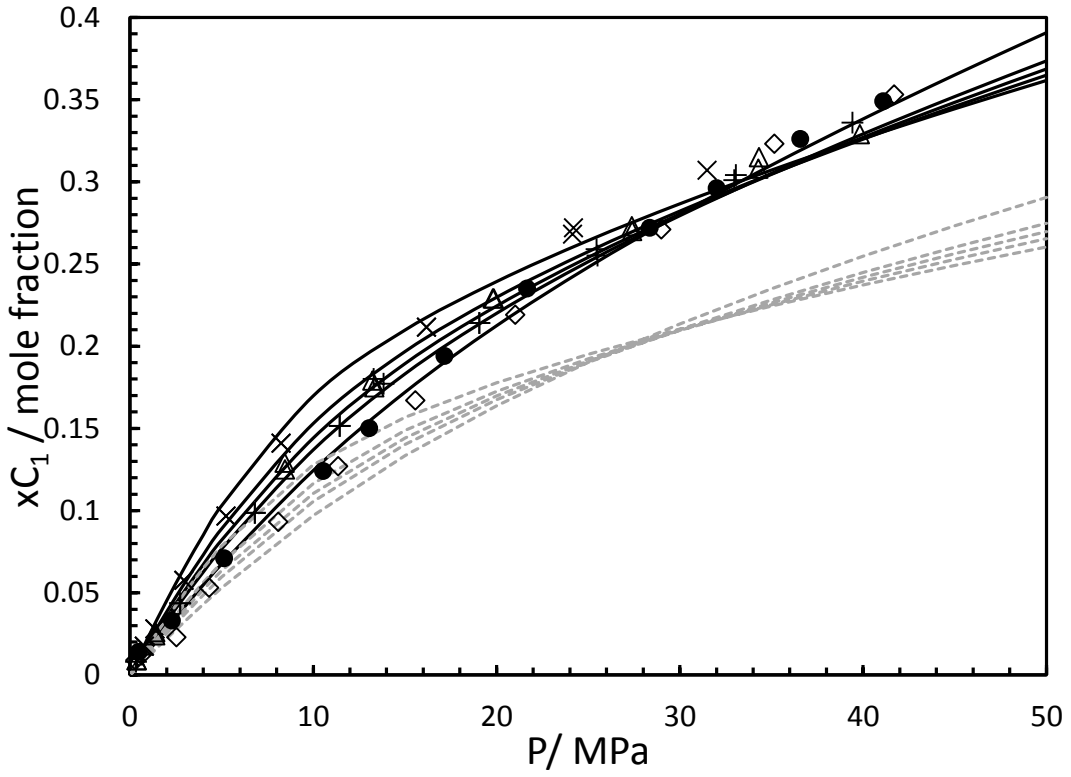

Figure 4.12. Methane Solubility in ethanol at various temperatures. (×), 238.15 K; (△), 253.15 K; (+), 263.15 K; (●), 273.15 K; (◇), 298.15 K. Lines: CPA-SRK72-model - Black lines: adjusted k_{ij} = -0.049; Dotted grey lines: k_{ij} = 0.

4.3.2 Solubility of Methane in Alcohol Solution

Table 4.7 shows the measured solubility of methane in 70 wt% methanol aqueous solution.

Table 4.8 and Table 4.9 show the solubility of methane in 70 and 50 wt% ethanol solutions respectively. Figure 4.13 shows the solubility of methane in 70wt% methanol solution together with model correlations utilizing the BIPs developed based on the binary and tertiary data respectively. The CPA-SRK72 EoS was tuned using a single variable BIP between methane and methanol for the dataset as demonstrated in Table 4.10 and the data presented by Wang et al. [21] shown Table 4.11.

Table 4.12 shows the BIPs between methane and ethanol for pure [22], 70 and 50 wt% ethanol solution. Figure 4.14 and Figure 4.15 show the solubility of methane in 70 and 50 wt% ethanol solution respectively. Figure 4.14 shows the solubility for methane in ethanol at 273.15 and 298.15 K.

The solubility measurements demonstrated in Figure 4.15 for 50 wt% ethanol solutions showed a similar crossover point at 10 MPa, which was not reciprocated by the optimized (k_{ij} = 0.130) CPA-SRK72 model calculations. However, the optimized models demonstrated significant improvement in reducing the correlation deviation especially at higher pressures. This phenomenon has been discussed in details by Wise and Chapoy for systems containing TEG solutions. [23]

Figure 4.16 illustrates the optimised concentration dependent BIPs between methanol and methane tuned using the data presented by Wang et al. [21] and measurements in this work. Figure 4.17 shows the optimised k_{ij} BIPs developed using the experimental measurements from this work at various ethanol concentrations.

Using the data presented by Wang et al. [21] a correlation was developed which can be used to calculate concentration dependent (methanol) BIPs between methane and methanol for systems containing water (eq. 4.2).

A similar correlation was developed using the data from this work which can be utilized to calculate concentration (ethanol) dependent BIPs between methane and ethanol (eq. 4.3). The BIPs can be predicted with a high level of accuracy between 50 – 100 wt% ethanol solutions using eq. 4.3.

Table 4.7. Solubility of Methane in 70 wt% methanol solution, x_1 at T = 273.15 K, Pressure (P) up to 47 MPa and standard uncertainty $u_r(x_1)$ [a].

T/K	P/MPa	x_1 (mol frac)	$u_r(x_1)$
293.15	0.54	0.00227	0.00013
293.15	0.54	0.00205	0.00008
293.15	0.60	0.00283	0.00010
293.15	0.61	0.00270	0.00010
293.15	1.51	0.00487	0.00016
293.15	1.52	0.00463	0.00015
293.15	2.49	0.00671	0.00021
293.15	2.49	0.00705	0.00022
293.15	4.32	0.00996	0.00029
293.15	4.34	0.00990	0.00029
293.15	6.54	0.01343	0.00039
293.15	10.33	0.01876	0.00053
293.15	10.33	0.01924	0.00054
293.15	18.88	0.02652	0.00073
293.15	26.43	0.03204	0.00088
293.15	26.52	0.03222	0.00088
293.15	35.35	0.03633	0.00099

[a] Standard uncertainties u are at $u_r(x_1)$ = 0.032, $u(T)$ = 0.05 K and $u(P)$ = 0.04 MPa.

Table 4.8. Solubility of Methane in 70 wt% ethanol solution, x_1 for T = 273.15 to 298.15 K, Pressure (P) up to 44 MPa and standard uncertainty $u_r(x_1)$ [a].

T/K	P/MPa	x_1 (mol frac)	$u_r(x_1)$	T/K	P/MPa	x_1 (mol frac)	$u_r(x_1)$
273.15	0.97	0.00554	0.00020	298.15	0.46	0.00254	0.00009
273.15	1.00	0.00447	0.00015	298.15	0.49	0.00300	0.00012
273.15	4.56	0.01388	0.00038	298.15	2.85	0.00937	0.00027
273.15	4.61	0.01452	0.00041	298.15	2.88	0.00917	0.00026
273.15	9.34	0.02502	0.00067	298.15	7.15	0.01999	0.00054
273.15	9.36	0.02557	0.00069	298.15	7.16	0.02028	0.00056
273.15	16.43	0.03648	0.00096	298.15	13.02	0.03174	0.00086
273.15	16.44	0.03696	0.00098	298.15	13.04	0.03259	0.00087
273.15	23.65	0.04374	0.00115	298.15	19.08	0.04139	0.00108
273.15	23.67	0.04430	0.00116	298.15	19.09	0.04286	0.00114
273.15	30.73	0.05073	0.00132	298.15	26.71	0.05107	0.00133
273.15	30.76	0.05012	0.00130	298.15	26.73	0.04999	0.00130
273.15	37.31	0.05645	0.00147	298.15	34.53	0.05978	0.00156
273.15	37.34	0.05462	0.00142	298.15	34.54	0.05677	0.00147
273.15	43.95	0.05865	0.00152	298.15	41.85	0.06357	0.00165
273.15	43.97	0.06074	0.00158	298.15	41.88	0.06477	0.00169

[a] Standard uncertainties u are at $u_r(x_1)$ = 0.029, $u(T)$ = 0.05 K and $u(P)$ = 0.04 MPa.

Table 4.9. Solubility of Methane in 50 wt% ethanol solution, x_1 for T = 273.15 to 298.15 K, Pressure (P) up to 34 MPa and standard uncertainty $u_r(x_1)$ [a].

T/K	P/MPa	x_1 (mol frac)	$u_r(x_1)$	T/K	P/MPa	x_1 (mol frac)	$u_r(x_1)$
273.15	0.52	0.001	0.0001	298.15	0.66	0.002	0.0001
273.15	0.53	0.002	0.0001	298.15	0.68	0.002	0.0001
273.15	1.68	0.003	0.0001	298.15	1.48	0.003	0.0001
273.15	1.68	0.003	0.0001	298.15	1.48	0.003	0.0001
273.15	2.63	0.004	0.0001	298.15	3.96	0.005	0.0001
273.15	2.65	0.004	0.0001	298.15	3.96	0.005	0.0002
273.15	4.49	0.005	0.0002	298.15	6.92	0.008	0.0002
273.15	4.52	0.006	0.0002	298.15	13.04	0.012	0.0003
273.15	8.01	0.009	0.0002	298.15	13.06	0.012	0.0003
273.15	8.02	0.008	0.0002	298.15	19.51	0.015	0.0004
273.15	13.96	0.012	0.0003	298.15	19.53	0.015	0.0004
273.15	13.98	0.012	0.0003	298.15	28.04	0.018	0.0005
273.15	20.99	0.014	0.0004	298.15	34.37	0.020	0.0005
273.15	21.01	0.015	0.0004				

[a] Standard uncertainties u are at $u_r(x_1)$ = 0.029, $u(T)$ = 0.05 K and $u(P)$ = 0.04 MPa.

Table 4.10. Optimised BIPs between methane and methanol for pure [20] and methanol aqueous solutions.

wt% methanol	Mole Fraction	BIPs (k_{ij})	T range (K)
70	0.567	0.099	293.15

Table 4.11. Optimised BIPs between methane and methanol for pure and methanol aqueous solutions using the data from Wang et al. [21]

Methanol			
wt%	Mole Fraction	BIPs (k_{ij})	T range (K)
20	0.123	0.273	283.2 - 303.2
40	0.273	0.239	283.2 - 303.2
60	0.457	0.136	283.2 - 303.2
80	0.692	0.058	283.2 - 303.2
100	1	-0.019	283.2 - 303.2

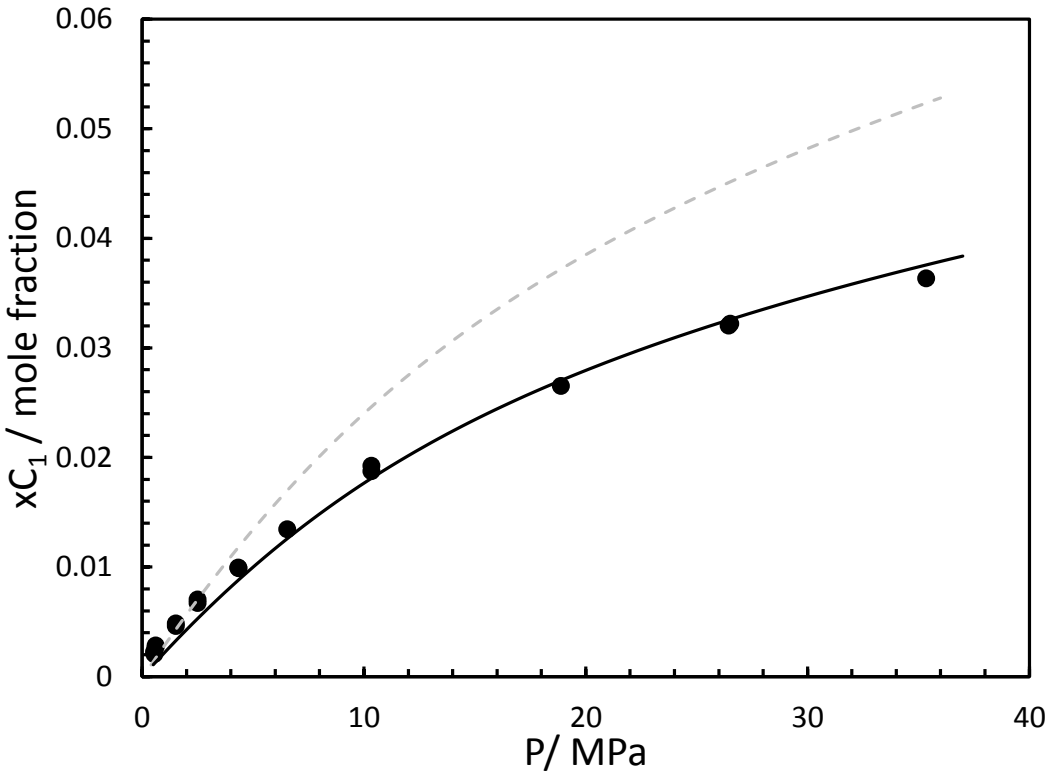

Figure 4.13. Methane Solubility in 70 wt% methanol solution at (●) 293.15. Lines: CPA-SRK72 model prediction. Grey Dashed Line: k_{ij} = 0.049. Black Line: k_{ij} = 0.099.

Table 4.12. Optimised BIPs between methane and ethanol for pure and ethanol aqueous solutions.

Ethanol		BIPs (k_{ij})	T range (K)
wt%	Mole Fraction		
100	1	-0.049	238.15 – 298.15
70	0.477	0.052	273.15 – 298.15
50	0.281	0.130	273.15 – 298.15

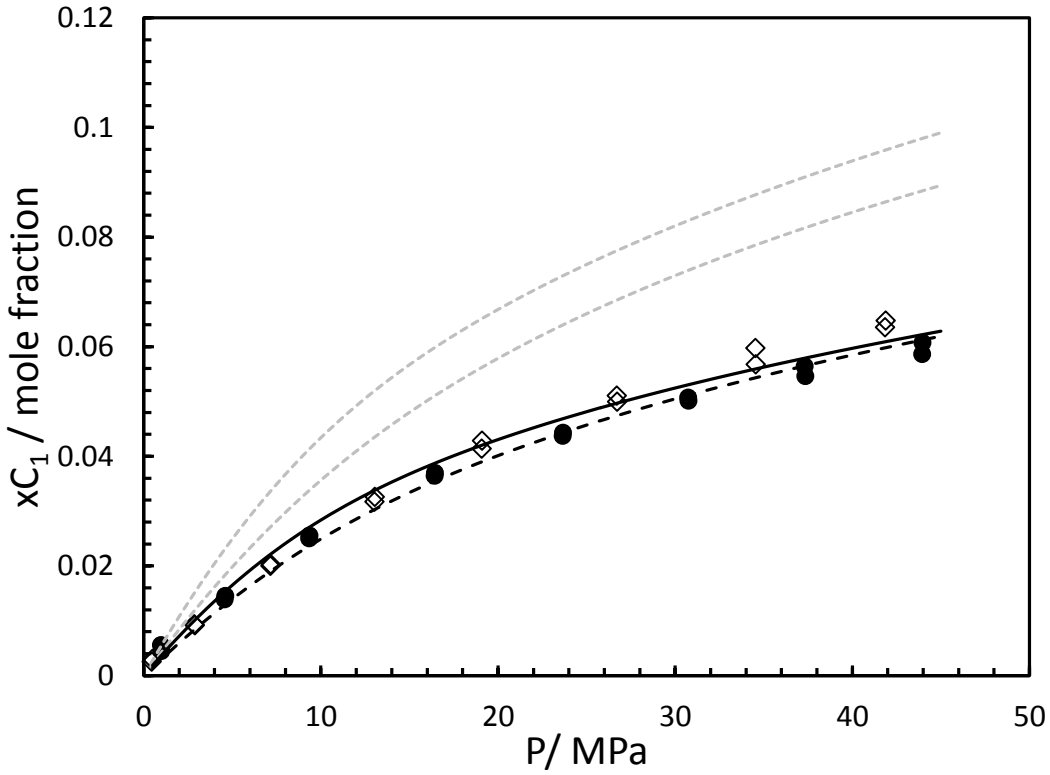

Figure 4.14. Methane Solubility in 70 wt% ethanol solution at (●) 273.15, (◇) 298.15 K. Line: CPA-SRK72 model predictions. Grey Lines: k_{ij} = -0.049. Black Lines: k_{ij} = 0.052 prediction for 273.15 K and 298.15 K (respectively – high to low solubility).

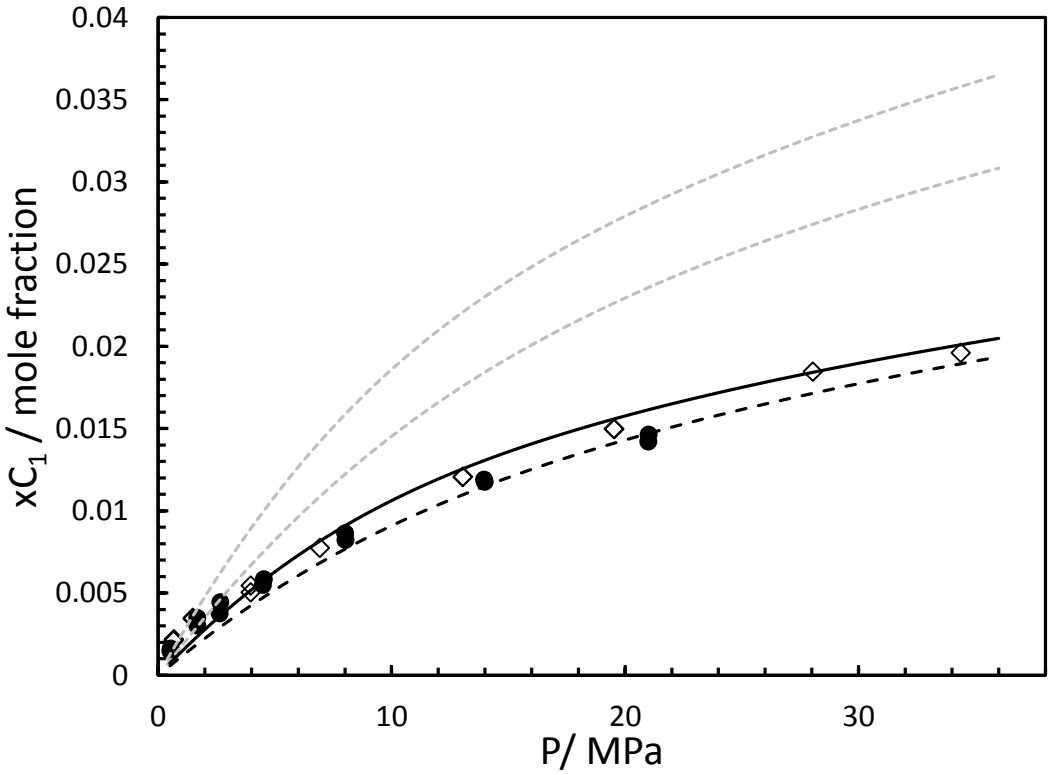

Figure 4.15. Methane Solubility in 50 wt% ethanol solution at (●) 273.15, (◇) 298.15 K. Lines: CPA-SRK72 model predictions. Dashed Grey Lines: k_{ij} = -0.049. Black Line: k_{ij} = 0.130 correlations for 273.15 K. Black Dashed Line: k_{ij} = 0.130 correlations for 298.15 K.

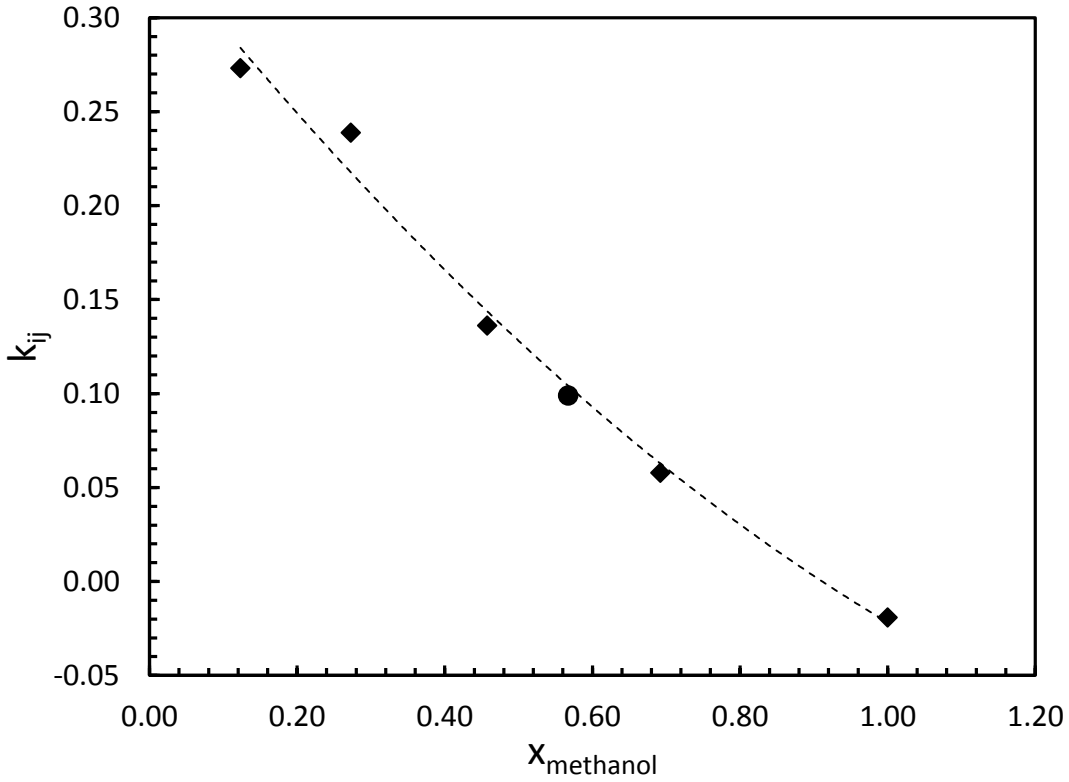

Figure 4.16. Binary Interaction Parameter, k_{ij} between methane and methanol for pure and aqueous solutions using the work of Wang et al. (◆) [21] and this work (●). Correlation corresponds to the Wang et al. data to ensure independence. [21]

$$k_{ij} = 0.13x^2 - 0.4948x + 0.343 \tag{4.2}$$

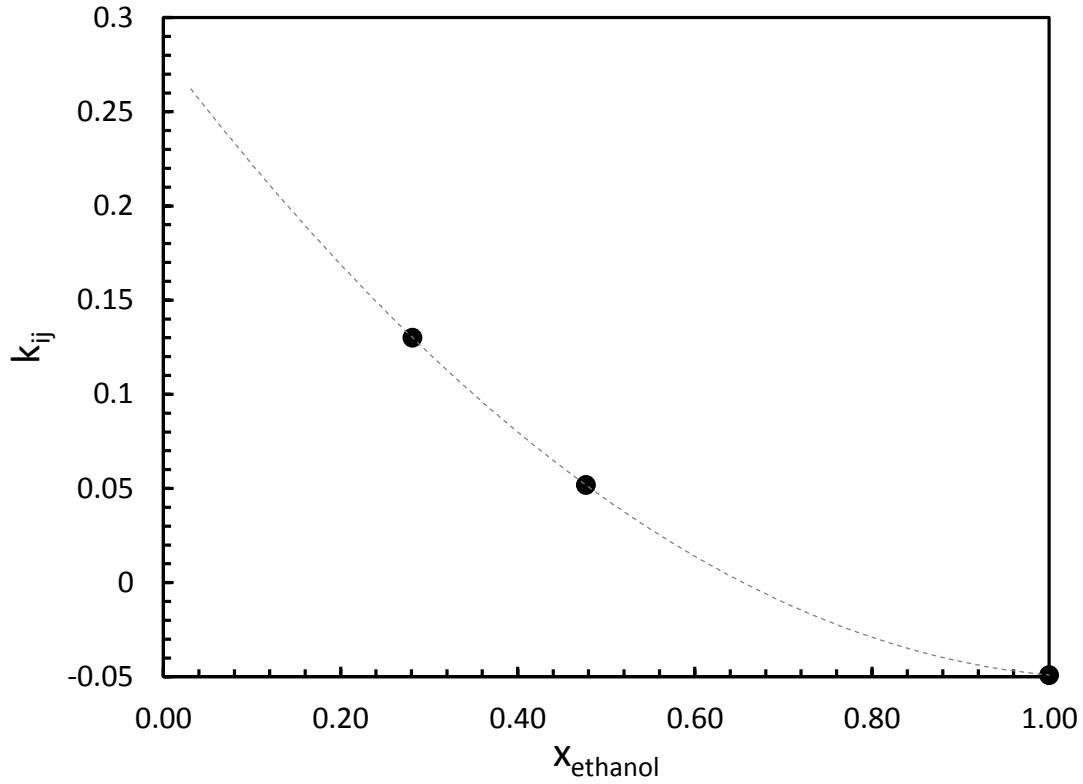

Figure 4.17. Binary Interaction Parameter, k_{ij} between methane and ethanol for pure and aqueous solutions.

$$k_{ij} = 0.2875x^2 - 0.6175x + 0.281 \tag{4.3}$$

4.3.3 Vapour Content of Methane in the presence of alcohols

In order to validate the measurement setup, certified SPECTRASEAL® standards composed of 500, 1000 and 3000 ppmV methanol or ethanol in CH_4 were purchased from BOC Special Gases. Typical scientific practice to validate experimental set up is to obtain significant amounts of consistent data from the literature and repeating those data to validate the experimental setup. There are a number of sources of methanol and ethanol in CH4 data, however there are significant differences between the reported values. The measured values for the methanol standards are shown along with the certified values in Table 4.13, showing good agreement and within the uncertainty of the certified values. BOC reported an expanded uncertainty of $U(y_i) = 0.05$.

As it is clearly apparent from Table 4.13, the GC results for the standards are in very good agreement with the certified values, and within the reported expanded uncertainty of 5%, illustrating the reliability of the setup used for these measurements.

Table 4.13. Comparison of measured and certified values for methanol content in methane of SPECTRASEAL® standards where the expanded uncertainty, $U(y_i)$ is in Parts Per Million in Volume of gas.

Measured methanol content ppmV	Certified methanol content ppmV $U(y_i) = 0.05$	% variance
548	525	+4.3
1015	1008	+0.7
3080	3064	+0.5

Due to issues developing with the equipment, it was required to replace the GC column as well as repeating the calibration using the new column, thus only limited number of measurements were conducted, before the end of the JIP phase was reached.

The methanol in methane vapour content measurements at 273.15 K are shown in Table 4.14. Figure 4.18 shows the methanol vapour content in methane together with measurement published by Krichevsky et al. [1] and Hong et al. [6] and CPA-SRK72 model predictions. The measurements in this work are in very good agreement with measurements made by Hong et al. [6] using a similar experimental setup. Significant deviations are observed at pressures above 14 MPa between the experimental results and the model predictions.

Table 4.14. Experimental measurements of the methanol content of methane in equilibrium with liquid methanol at 273.15 K, where *P* is pressure in MPa and the expanded uncertainty, $U(y_i)$ is in Parts Per Million in Volume of gas.

P/MPa	Methanol Content (ppmV)	$U(y_i)$ (ppmV)
18.20	2651	46.20
25.07	5057	88.14

[a] Standard uncertainties *u* are at $u(S) = 0.019$, $u(T) = 0.05$ K and $u(P) = 0.04$ MPa

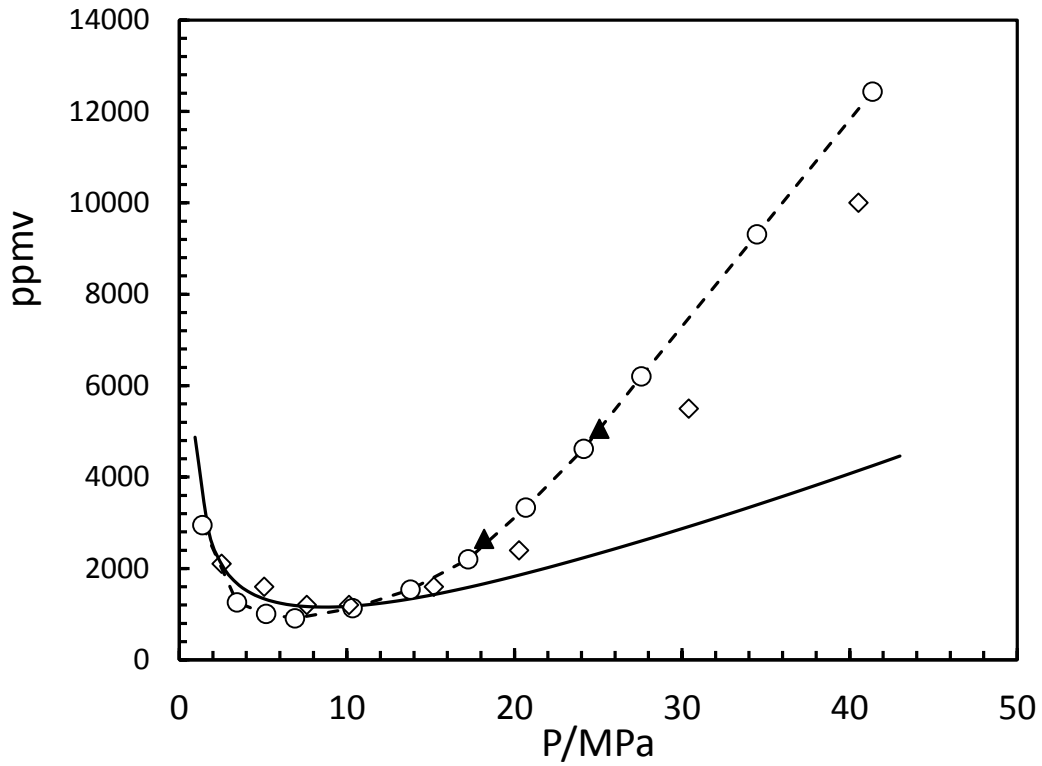

Figure 4.18. Experimental measurements of the methanol content of methane in equilibrium with liquid methanol at 273.15 K (▲) together with Krichevsky et al. (◇) [1] and Hong et al. [6] (○). The dashed line is shows trend in data presented by Hong et al. [6]. Black Line: CPA-SRK72 model predictions.

The initial measurements in this work were carried out using a 9 litre equilibrium cell. The methanol in methane vapour content measurements at 298.15 K are shown in Table 4.15. Figure 4.19 shows the methanol vapour content in methane together with measurement published by Krichevsky et al. [1], Hemmaplardh et al. [2], Yarym-Agaev et al. [4] , Brunner et al. [5] and CPA-SRK72 model predictions. The measurements in this work are in very good agreement with the literature. Good agreement between the experimental results from the two rigs used were observed. Significant deviations are

shown at pressures above 14 MPa between the experimental results and the model predictions once again.

Table 4.15. Experimental measurements for the methanol content of methane in equilibrium with liquid methanol at T = 298.15 K, pressure (P) up to 62 MPa is pressure in MPa and the expanded uncertainty, $U(y_i)$.

Cell Volume	*P*/MPa	Methanol Content (ppmV)	$U(y_i)$ (ppmV)
9 Litre	2.61	7684	133.92
	5.68	4859	84.68
	8.12	4172	72.71
	12.13	4364	76.06
	13.81	4966	86.55
	15.18	5280	92.02
	20.85	6892	120.12
0.3 Litre	2.68	7316	127.51
	5.30	4706	82.02
	10.51	4161	72.52
	14.84	5037	87.79
	20.51	7114	123.99
	40.09	19762	344.42
	62.00	31500	549.00

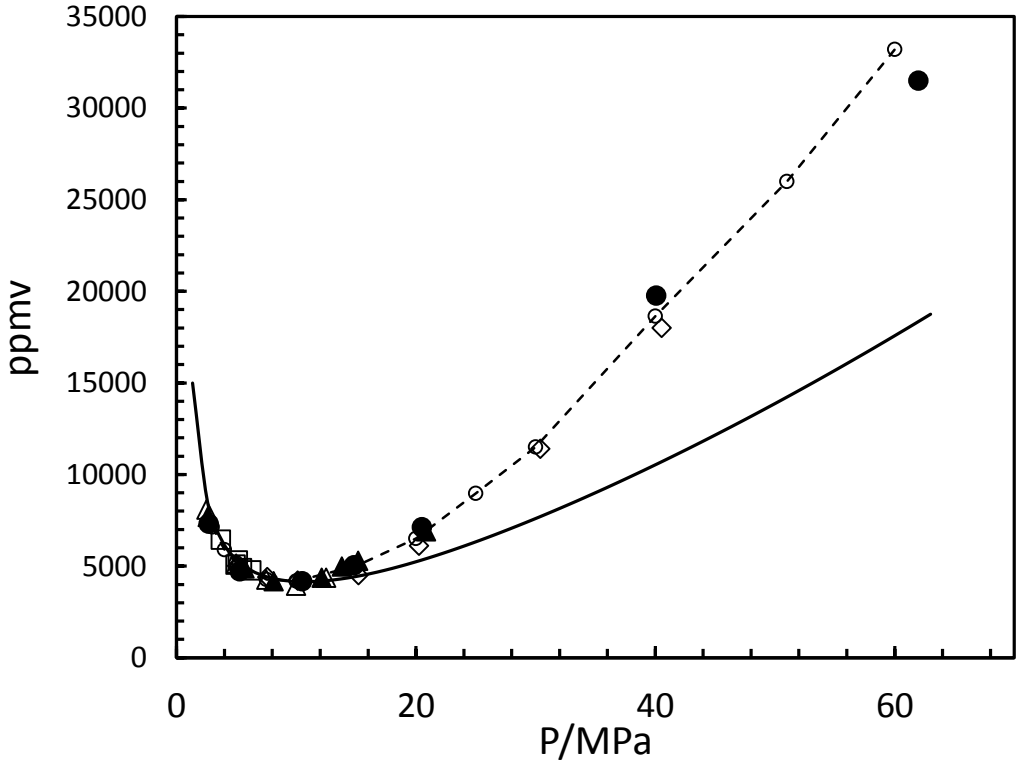

Figure 4.19. Experimental measurements of the methanol content of methane in equilibrium with liquid methanol at 298.15 K measured using the 9 litre (▲) and 0.3 litre (●) pressure rigs together with Krichevsky et al. (◇) [1], Hemmaplardh et al. (□) [2], Yarym-Agaev et al. (△) [4] and Brunner et al. (○ and dotted line) [5]. Black Line: CPA-SRK72 model predictions.

The ethanol in methane vapour content measurements at 273.15 K are shown in Table 4.16. Figure 4.20 shows the ethanol vapour content in methane. Significant deviations are shown at pressures above 20 MPa between the experimental results and the model predictions once again.

Table 4.16. Experimental measurements for the ethanol content of methane in equilibrium with liquid methanol at T = 273.15 K, pressure (P) up to 36 MPa is pressure in MPa and the expanded uncertainty, $U(y_i)$[a].

P/MPa	Ethanol content (ppmV)	$U(y_i)$ (ppmV)
1.00	1867	32.54
2.07	1056	18.40
7.40	630	10.98
13.58	991	17.27
21.37	3165	55.16
28.84	7030	122.52
36.27	12158	211.89

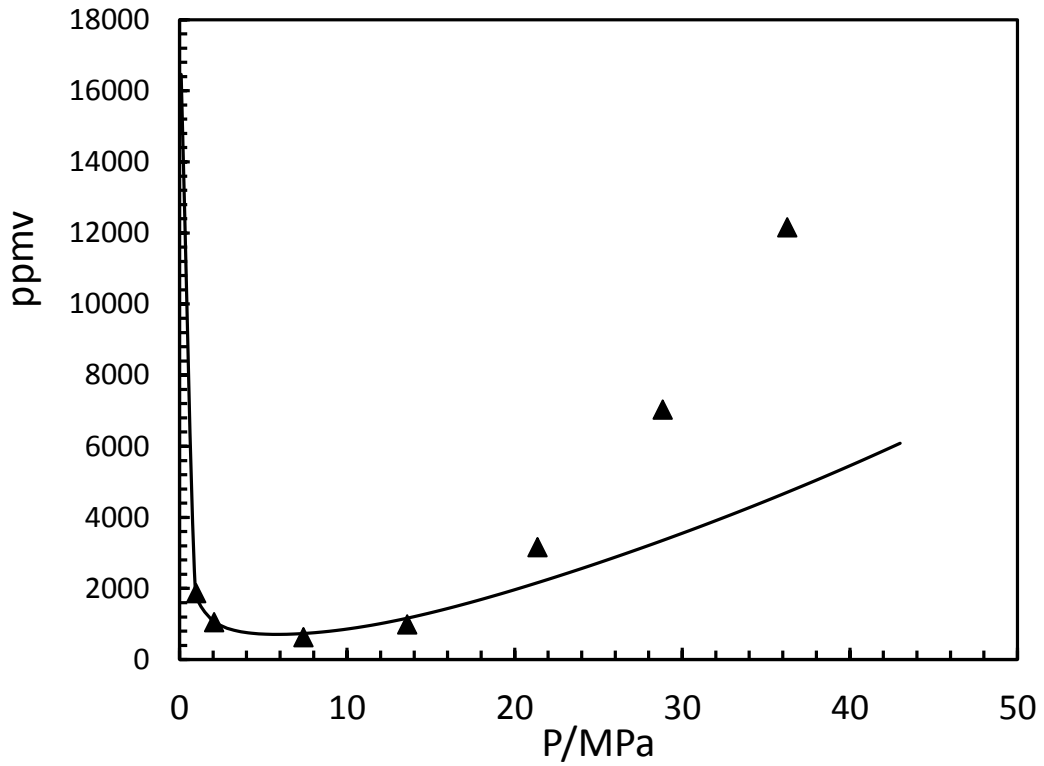

Figure 4.20. Experimental measurements of the ethanol content of methane in equilibrium with liquid ethanol at 273.15 K. Black Line: CPA-SRK72 model predictions.

The methanol in methane vapour content measurements at 298.15 K are shown in Table 4.17. Figure 4.21 shows the methanol vapour content in methane together with measurement published by Krichevsky et al. [1] and CPA-SRK72 model predictions. As it can be seen the measurements in this work are in very good agreement with the

literature. Significant deviations are observed at pressures above 25 MPa between the experimental results and the model predictions.

Table 4.17. Experimental measurements for the ethanol content of methane in equilibrium with liquid methanol at T = 298.15 K, pressure (P) up to 41 MPa is pressure in MPa and the expanded uncertainty, $U(y_i)$[a].

P/MPa	Ethanol Content (ppmV)	$U(y_i)$ (ppmV)
0.70	13035	227.18
1.10	7180	125.14
2.14	3849	67.08
2.60	3697	64.43
5.04	2352	40.99
5.29	2566	44.72
10.44	2359	41.11
11.01	2553	44.49
17.39	3825	66.66
19.77	4665	81.30
25.21	7814	136.19
31.23	12304	214.44
40.63	21201	369.50

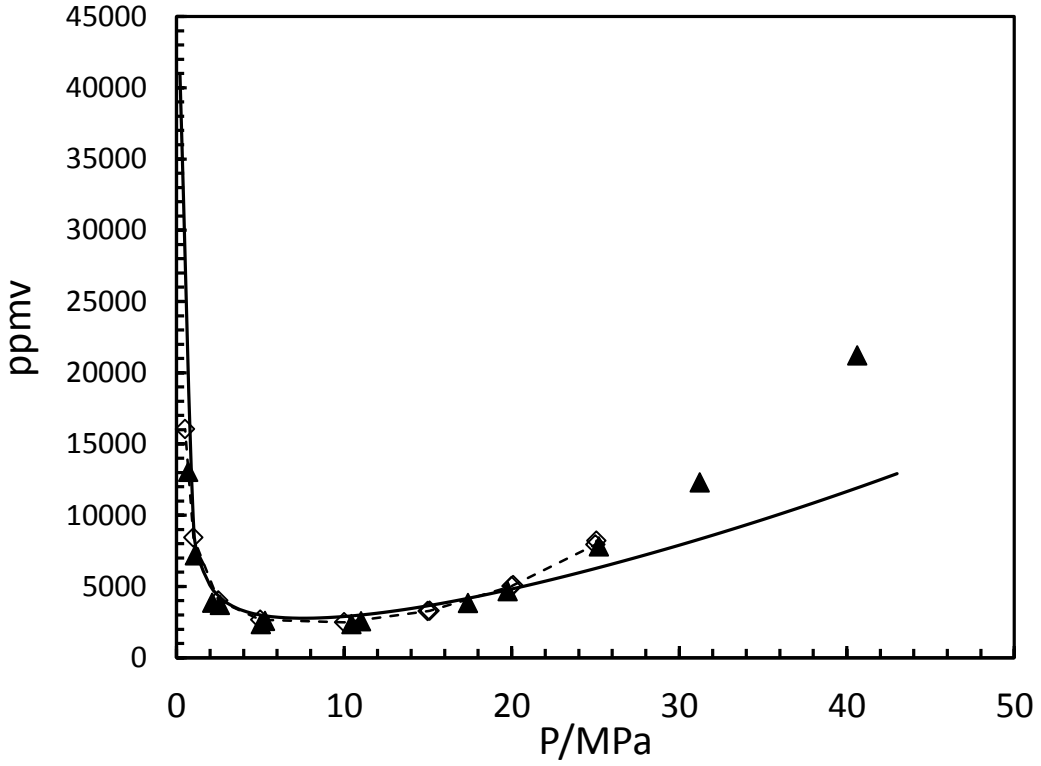

Figure 4.21. Experimental measurements of the ethanol content of methane in equilibrium with liquid ethanol at 298.15 K together with Brunner et al. (◇). [24] Black Line: CPA-SRK72 model predictions.

4.3.4 Saturation Pressure of Reservoir Fluids

Table 4.18 shows the bubble point measurements for a heptane-methane-ethanol ternary system together with CPA-SRK72 model predictions. Due to the linear nature of the measurement equation a standard Pythagorean mean was used to determine the standard uncertainty in the bubble point measurements. This was a combination of the standard uncertainty of the mass and pressure measurements as published by the manufacturers. The standard uncertainty due to temperature was deemed negligible using sensitivity analysis. The measurements showed a combined standard uncertainty of $u(S) = 0.039$. The CPA-SRK72 model was optimised using a variety of data (see chapter 2). The Binary Interaction Parameters between CH_4-ethanol were developed using the solubility from this work. The CPA-SRK72 demonstrated an absolute average deviation of 10% from the experimental results. Figure 4.22 shows the bubble point measurements for the heptane-methane-ethanol system together with the CPA-SRK72 model predictions.

Table 4.18. Bubble point measurement and modelling for a ternary system containing heptane, methane and ethanol.

System Components (Mol %)			*P* (MPa)	*T* (K)	CPA-SRK72 (MPa)	$u(S)$[a] (MPa)	Relative CPA Deviation
C_7H_{16}	CH_4	C_2H_5OH	3.36	263.15	3.02	0.07	-10%
43.8	12.56	43.64	3.67	273.15	3.25	0.04	-11%
			4.06	293.15	3.68	0.12	-9%
			4.38	313.15	4.02	0.08	-8%

[a] Standard uncertainties *u* are at $u(S) = 0.039$, $u(T) = 0.05$ K and $u(P) = 0.04$ MPa.

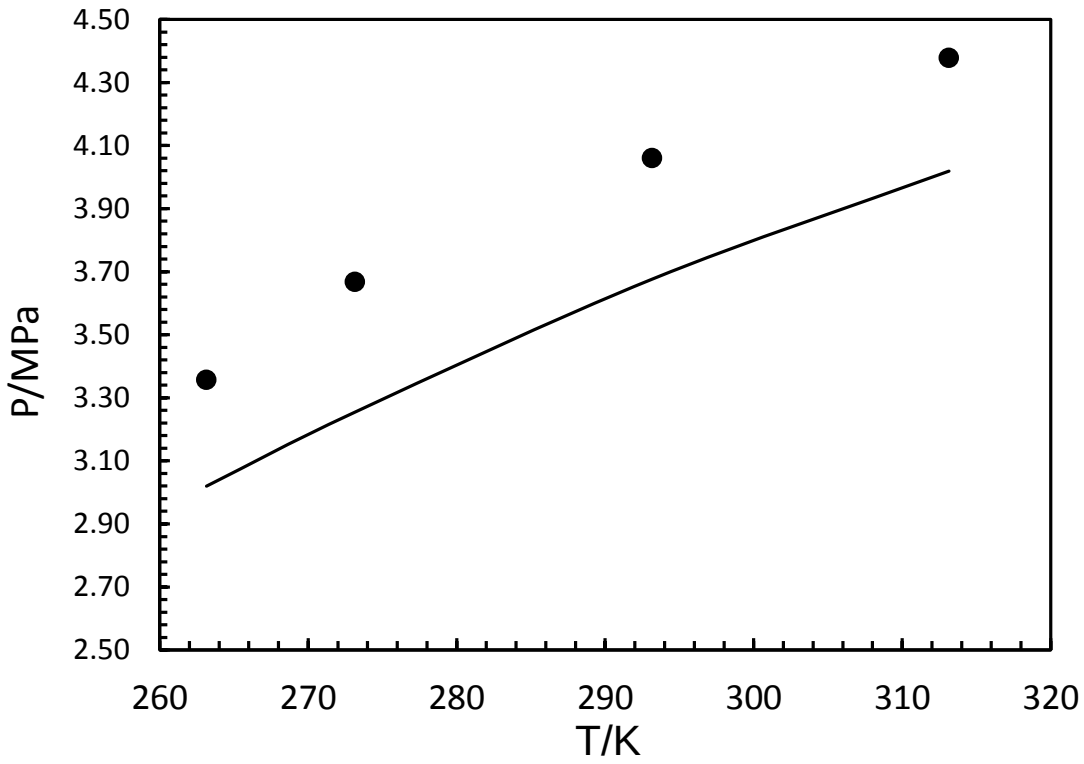

Figure 4.22. Shows the bubble point measurements for a heptane-methane-ethanol system (●) measured in this work together with CPA-SRK72 model predictions (Black line).

Table 4.19 demonstrates the bubble point measurements for a toluene-methane-methanol ternary system together with CPA-SRK72 model predictions. The measurements showed a combined standard uncertainty of $u(S)$ = 0.016. The CPA-SRK72 demonstrated an absolute average deviation of 13% from the experimental results. Figure 4.23 shows the bubble point measurements for the toluene-methane-methanol system together with the CPA-SRK72 model predictions.

Table 4.19. Bubble point measurement and modelling for a ternary system containing toluene, methane and methanol.

System Components (Mol %)			*P* (MPa)	*T* (K)	CPA-SRK72 (MPa)	$u(S)$[a] (MPa)	Relative CPA Deviation
Toluene	CH_4	CH_3OH	5.10	253.46	6.04	0.04	18%
38.25	9.39	51.72	5.40	263.55	6.28	0.04	16%
			5.69	273.21	6.47	0.04	14%
			6.01	285.7	6.69	0.04	11%
			6.61	311.8	6.99	0.04	6%

[a] Standard uncertainties *u* are at $u(S) = 0.016$, $u(T) = 0.05$ K and $u(P) = 0.04$ MPa

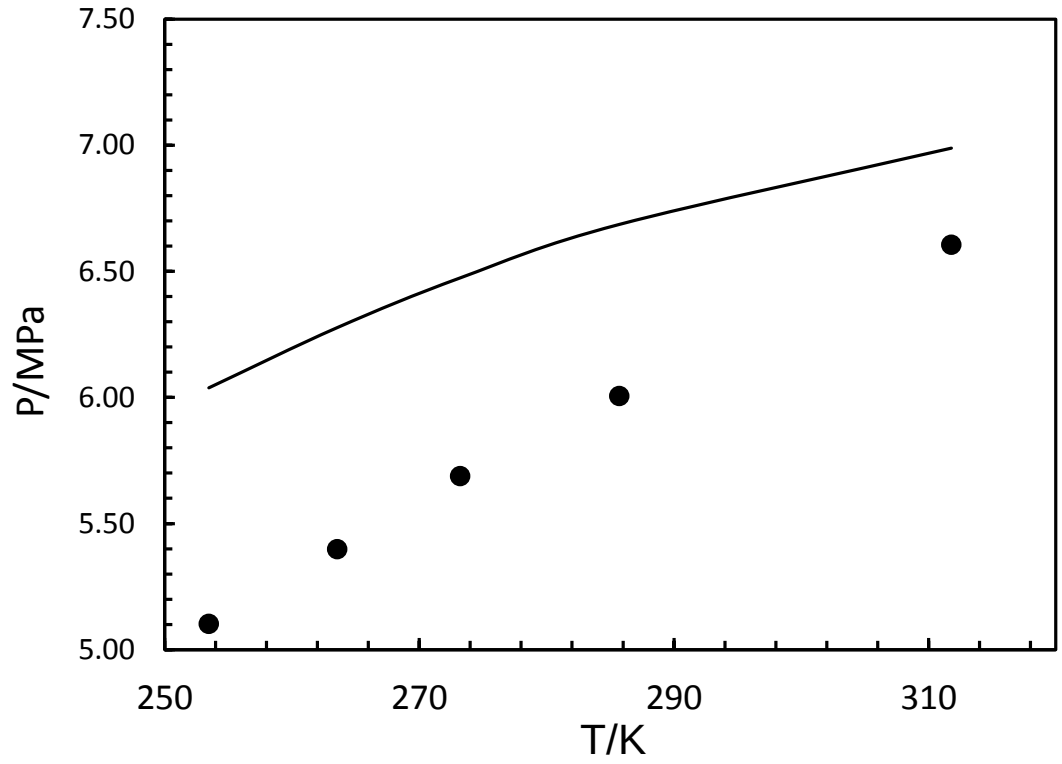

Figure 4.23. Shows the bubble point measurements for a toluene-methane-methanol system (●) measured in this work together with CPA-SRK72 model predictions (Black line).

Table 4.20 shows the bubble point measurements for a toluene-methane-ethanol ternary system together with CPA-SRK72 model predictions. The measurements showed a combined standard uncertainty of $u(S) = 0.015$. The CPA-SRK72 demonstrated an

absolute average deviation of 20% from the experimental results. This deviation is unexpectedly high and maybe due to the interaction of the heavy hydrocarbon phase, toluene, with the aqueous alcohol phase. Although it is possible to improve the predictions by developing new BIPs between the hydrocarbon and alcohol phase. This will require separate calculation for each component making the predictions irrelevant. This is a limit of cubic EoS such as CPA. Figure 4.24 illustrates the bubble point measurements for the toluene-methane-methanol system together with the CPA-SRK72 model predictions.

Table 4.20. Bubble point measurement and modelling for a ternary system containing toluene, methane and ethanol.

System Components (Mol %)			*P* (MPa)	*T* (K)	CPA-SRK72 (MPa)	*u*(*S*)[a] (MPa)	Relative CPA Deviation
Toluene 46.69	CH_4 11.12	C_2H_5OH 42.20	5.47	260.45	4.39	0.04	-20%
			5.79	271.55	4.67	0.04	-19%
			6.09	281.66	4.90	0.04	-20%
			6.34	291.55	5.09	0.04	-20%

[a] Standard uncertainties *u* are at *u*(*S*) = 0.015, *u*(*T*) = 0.05 K and *u*(*P*) = 0.04 MPa

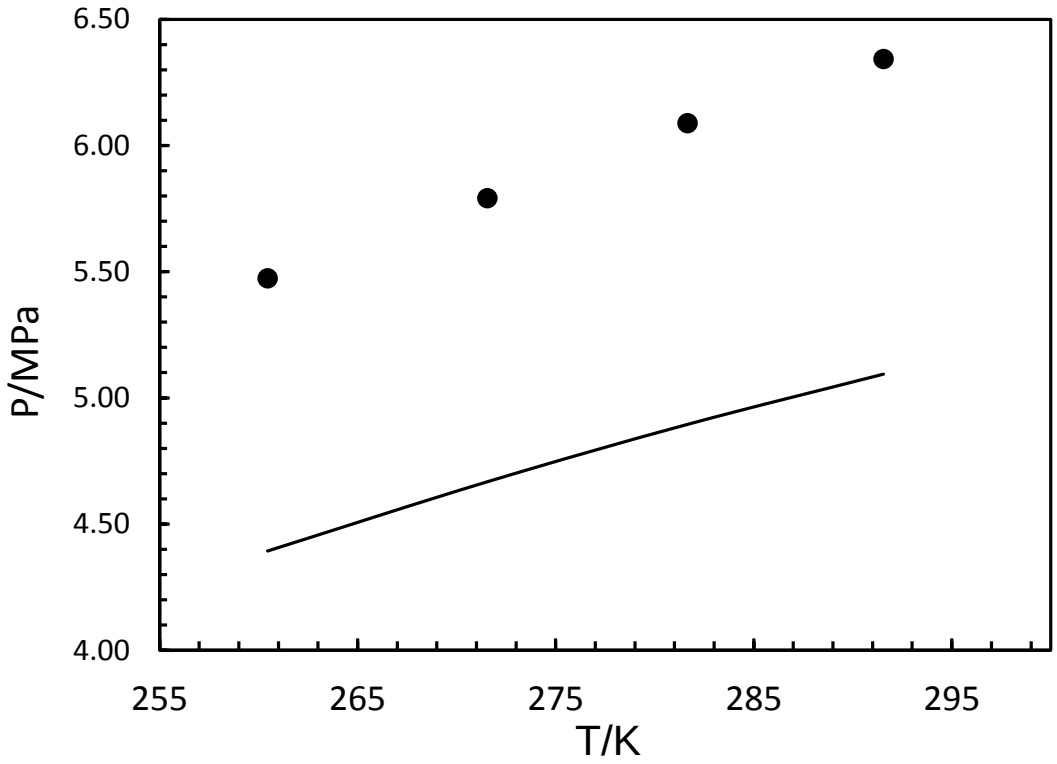

Figure 4.24. Shows the bubble point measurements for a toluene-methane-ethanol system (●) measured in this work together with CPA-SRK72 model predictions (Black line).

Table 4.21 and Table 4.22 demonstrates the bubble point measurements for a toluene-methane-methanol-water quaternary system together with CPA-SRK72 model predictions. The measurements showed a combined standard uncertainty of $u(S) = 0.006$. The CPA-SRK72 demonstrated a deviation of 6% from the experimental result. The singularity of the result in Table 4.21 is due to a failure in the equipment and the necessity to repeat the test by creating a new mixture.

As discussed earlier, to improve the solubility predictions for methane in aqueous methanol and ethanol, new BIPs were regressed. The regression was used to develop cubic equations to correlate new k_{ij} values between methane and various concentrations of methanol and ethanol aqueous solutions based on data from Wang et al. [21] and this work respectively. A k_{ij} of 0.267 was calculated for the interaction between methane and methanol for this system.

Table 4.21. Bubble point measurement and modelling for a quaternary system containing toluene, methane, methanol and water.

System Components (Mol %)				*P* (MPa)	*T* (K)	$u(S)^a$ (MPa)	CPA-SRK72 (MPa)	Relative CPA Deviation
Toluene 11.41	CH_4 2.91	CH_3OH 13.71	H_2O 71.97	7.33	287.61	0.44	7.78	6%

[a] Standard uncertainties *u* are at *u*(*S*) = 0.006, *u*(*T*) = 0.05 K and *u*(*P*) = 0.04 MPa

Table 4.22. Bubble point measurement and modelling for a quaternary system containing toluene, methane, methanol and water.

System Components (Mol %)				*P* (MPa)	*T* (K)	$u(S)^a$ (MPa)	CPA-SRK72 (MPa)	Relative CPA Deviation
Toluene 12.47	CH_4 4.18	CH_3OH 47.31	H_2O 36.05	7.39	253.70	0.44	6.52	-12%
				7.78	263.82	0.46	7.45	-4%
				8.15	273.84	0.47	8.43	3%
				8.50	293.15	0.48	10.00	18%
				8.78	312.51	0.48	10.20	16%

[a] Standard uncertainties *u* are at *u*(*S*) = 0.006, *u*(*T*) = 0.05 K and *u*(*P*) = 0.04 MPa

Table 4.23 demonstrates the bubble point measurements for a toluene-methane-methanol-water quaternary system together with CPA-SRK72 model predictions. . The measurements showed a combined standard uncertainty of *u*(*S*) = 0.008. The CPA-SRK72 demonstrated an absolute average deviation of 7% from the experimental result. The singularity of this result is due to a failure in the equipment and the necessity to repeat the test by creating a new mixture.

Table 4.24 presents the bubble point measurements for a toluene-methane-ethanol-water quaternary system together with CPA-SRK72 model predictions. The measurements showed a combined standard uncertainty of $u(S) = 0.008$. The CPA-SRK72 demonstrated an absolute average deviation of 11% from the experimental result.

Table 4.23. Bubble point measurement and modelling for a quaternary system containing toluene, methane, methanol and water.

System Components (Mol %)				P (MPa)	T (K)	u(S)[a] (MPa)	CPA-SRK72 (MPa)	Relative CPA Deviation
Toluene	CH_4	CH_3OH	H_2O	8.26	285.62	0.47	7.67	-7 %
11.44	2.89	13.96	71.71	8.92	312.49	0.50	8.26	-7%

[a] Standard uncertainties u are at $u(S) = 0.008$, $u(T) = 0.05$ K and $u(P) = 0.04$ MPa

Table 4.24. Bubble point measurement and modelling for a quaternary system containing toluene, methane, ethanol and water.

System Components (Mol %)				*P* (MPa)	*T* (K)	*u*(*S*) (MPa)	CPA-SRK72 (MPa)	Relative CPA Deviation
Toluene	CH_4	C_2H_5OH	H_2O	4.50	251.89	0.39	4.82	7%
12.48	4.18	39.76	43.57	5.30	261.56	0.40	5.62	6%
				5.61	271.59	0.40	6.27	12%
				6.09	291.93	0.42	6.92	14%
				6.36	312.56	0.42	7.33	15%

[a] Standard uncertainties *u* are at *u*(*S*) = 0.008, *u*(*T*) = 0.05 K and *u*(*P*) = 0.04 MPa

Table 4.25 shows the bubble point measurements for a nonane-methane binary system together with CPA-SRK72 model predictions. The measurements showed a combined standard uncertainty of u(S) = 0.014. The CPA-SRK72 demonstrated an absolute average deviation of 3% from the experimental result, demonstrating good agreement with the model predictions. Figure 4.25 illustrates the bubble point measurements for the nonane-methane system together with the CPA-SRK72 model predictions.

Table 4.25. Bubble point measurement and modelling for a binary system containing nonane and methane.

System Components (Mol %)		*P* (MPa)	*T* (K)	*u*(*S*)[a] (MPa)	CPA-SRK72 (MPa)	Relative CPA Deviation
Nonane	CH_4	4.24	251.84	0.04	4.27	-1%
75.02	24.98	5.80	296.39	0.04	5.99	-3%
		6.24	314.44	0.04	6.52	-5%

[a] Standard uncertainties *u* are at *u*(*S*) = 0.014, *u*(*T*) = 0.05 K and *u*(*P*) = 0.04 MPa

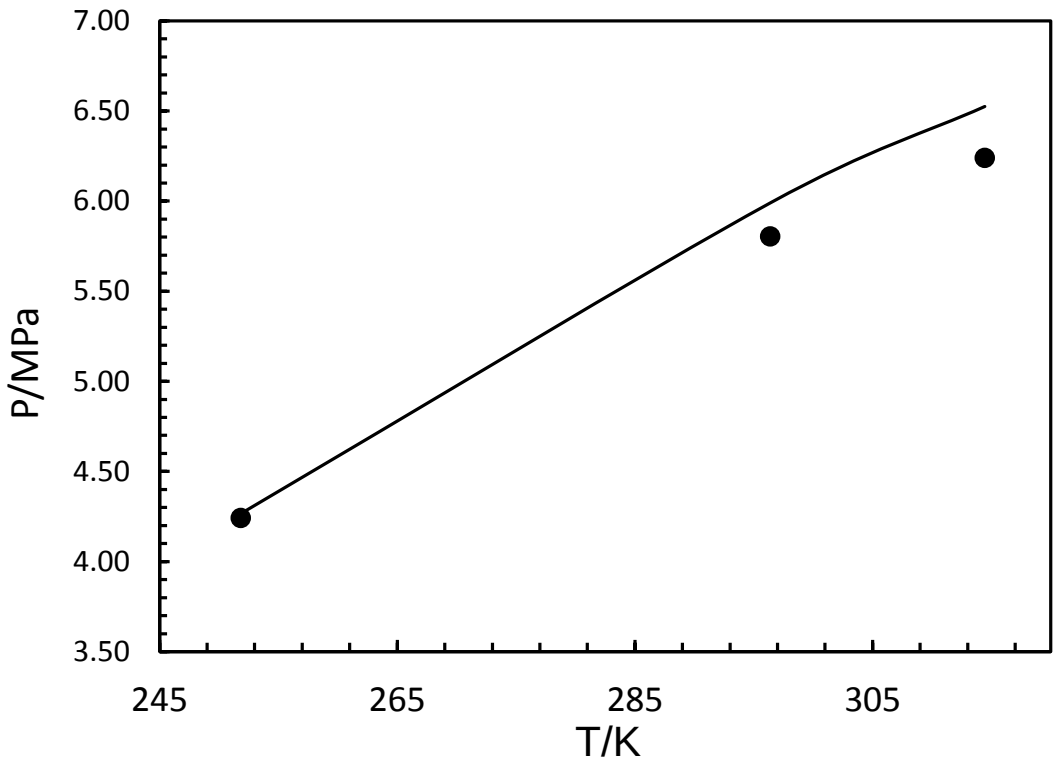

Figure 4.25. Shows the bubble point measurements for a nonane-methane system (●) measured in this work. Black line: CPA-SRK72 model prediction with modified k_{ij}.

Table 4.26 shows the bubble point measurements for a nonane-methane-methanol ternary system together with CPA-SRK72 model predictions. The measurements showed a combined standard uncertainty of u(S) = 0.020. The CPA-SRK72 has an absolute average deviation of 13% from the experimental result, demonstrating the introduction of deviation due to the polar alcohol phase. Figure 4.26 shows the bubble point measurements for the nonane-methane-methanol system together with the CPA-SRK72 model predictions.

Table 4.26. Bubble point measurement and modelling for a quaternary system containing nonane, methane and methanol.

System Components (Mol %)			*P* (MPa)	*T* (K)	CPA-SRK72 (MPa)	$u(S)^a$ (MPa)	Relative CPA Deviation
Nonane	CH_4	CH_3OH	3.80	256.43	3.28	0.39	14%
			4.04	265.53	3.52	0.37	13%
39.47	13.15	47.38	4.28	274.85	3.75	0.39	12%
			4.88	294.43	4.17	0.40	14%
			5.25	314.40	4.52	0.32	14%

[a] Standard uncertainties *u* are at $u(S) = 0.020$, $u(T) = 0.05$ K and $u(P) = 0.04$ MPa

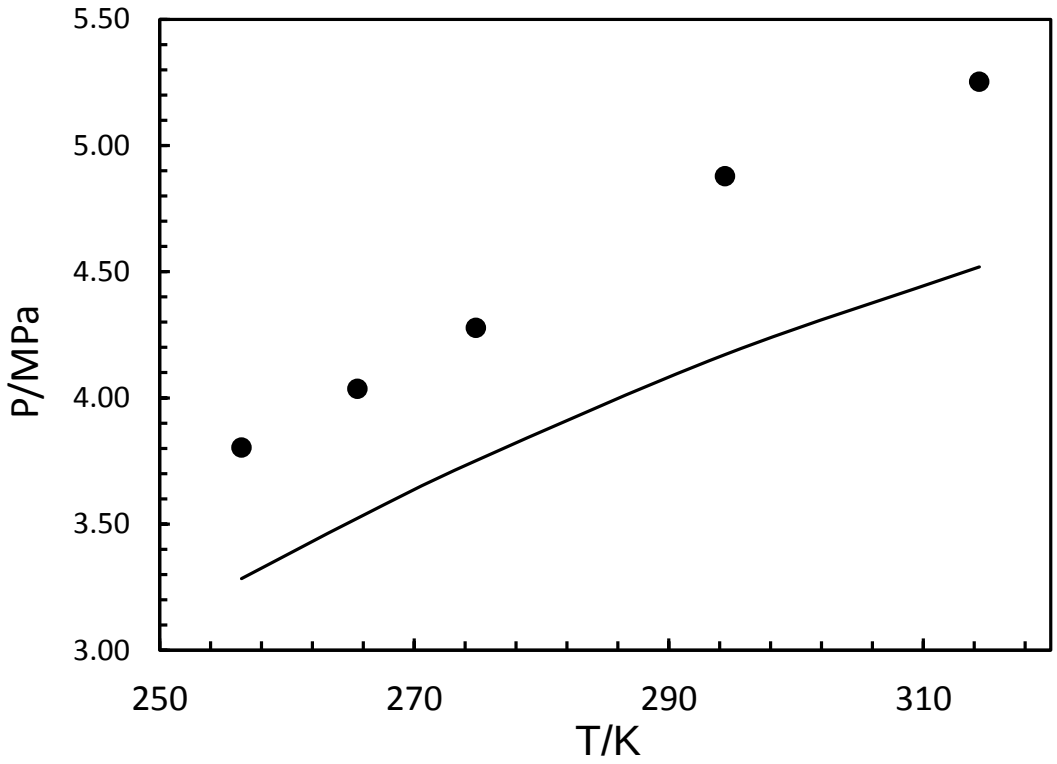

Figure 4.26. Shows the bubble point measurements for a nonane-methane-methanol system (●) measured in this work. Black line: CPA-SRK72 model prediction with modified k_{ij}.

Table 4.27 demonstrates the bubble point measurements for a nonane-methane-methanol-water quaternary system together with CPA-SRK72 model predictions. The correlation developed using the Wang et al. data [21] was used to calculate a new k_{ij} of 0.104. The measurements showed a combined standard uncertainty of $u(S) = 0.018$. The CPA-SRK72 demonstrated an absolute average deviation of 5% from the experimental result, using the correlated methane-methanol k_{ij} in the aqueous solutions. This is a significant improvement from an absolute average deviation of 14% calculated using k_{ij} developed using pure methanol by Haghighi et al. [20]. Figure 4.27 shows the bubble point measurements for the nonane-methane-methanol-water system together with the CPA-SRK72 model predictions.

Table 4.27. Bubble point measurement and modelling for a quaternary system containing nonane, methane, methanol and water.

System Components (Mol %)				*P* (MPa)	*T* (K)	*u*(*S*)[a] (MPa)	CPA-SRK72 (MPa)	Relative CPA Deviation
Nonane	CH_4	CH_3OH	H_2O	3.61	253.57	0.04	3.31	8%
				3.89	263.72	0.04	3.65	6%
12.50	4.16	47.29	36.05	4.65	293.95	0.04	4.49	3%
				5.02	315.23	0.04	4.92	2%

[a] Standard uncertainties *u* are at *u*(*S*) = 0.018, *u*(*T*) = 0.05 K and *u*(*P*) = 0.04 MPa

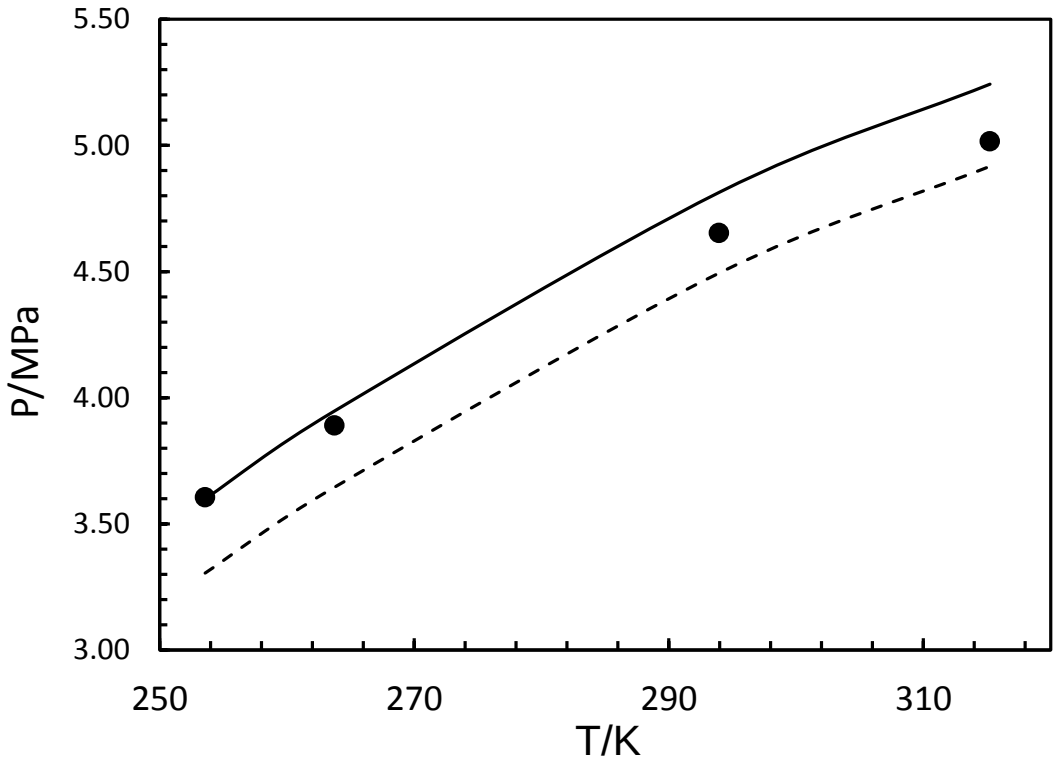

Figure 4.27. Shows the bubble point measurements for a nonane-methane-methanol-water system (●) measured in this work. Black line: CPA-SRK72 model prediction with modified k_{ij}. Dashed line: CPA-SRK72 model prediction with original k_{ij}.

Table 4.28 show the bubble point measurements for a nonane-methane-ethanol- water quaternary system together with CPA-SRK72 model predictions. The correlation developed using this work was used to calculate a new k_{ij} of 0.052. The measurements showed a combined standard uncertainty of u(S) = 0.027. The CPA-SRK72 demonstrated an absolute average deviation of 7% from the experimental result, using the correlated methane-methanol k_{ij} in the aqueous solutions. This is a significant improvement from an absolute average deviation of 9% calculated using k_{ij} developed using pure ethanol from this work. Figure 4.28 shows the bubble point measurements for the nonane-methane-methanol-water system together with the CPA-SRK72 model predictions.

Table 4.28. Bubble point measurement and modelling for a quaternary system containing nonane, methane, ethanol and water.

System Components (Mol %)				*P* (MPa)	*T* (K)	*u*(*S*)[a] (MPa)	CPA-SRK72 (MPa)	Relative CPA Deviation
Nonane	CH_4	C_2H_5OH	H_2O	3.10	253.96	0.04	3.14	-1%
				3.21	261.86	0.04	3.40	-6%
				3.30	262.77	0.04	3.43	-4%
				3.51	272.74	0.04	3.75	-7%
				3.58	274.01	0.04	3.78	-6%
12.53	4.07	39.79	43.61	3.83	290.08	0.04	4.22	-10%
				3.89	293.31	0.04	4.30	-10%
				3.98	293.93	0.04	4.31	-8%
				4.31	311.39	0.04	4.67	-8%
				4.17	312.74	0.04	4.69	-12%

[a] Standard uncertainties *u* are at *u*(*S*) = 0.027, *u*(*T*) = 0.05 K and *u*(*P*) = 0.04 MPa

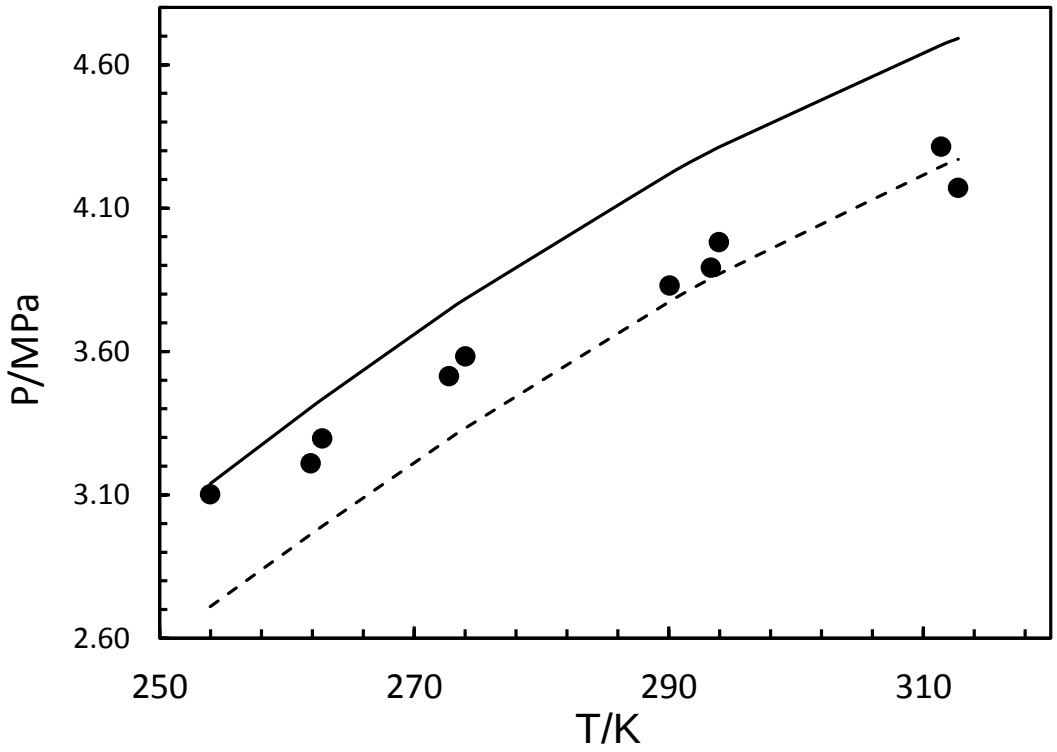

Figure 4.28. Shows the bubble point measurements for a nonane-methane-ethanol-water system (●) measured in this work. Black line: CPA-SRK72 model prediction with modified k_{ij}. Dashed line: CPA-SRK72 model prediction with original k_{ij}.

Table 4.29 demonstrates the bubble point measurements for a decane-methane-methanol ternary system together with CPA-SRK72 model predictions. The measurements showed a combined standard uncertainty of $u(S) = 0.030$. The CPA-SRK72 demonstrated an absolute average deviation of 6% from the experimental result, demonstrating good agreement with the model predictions. Figure 4.29 illustrates the bubble point measurements for the decane-methane-methanol system together with the CPA-SRK72 model predictions.

Table 4.29. Bubble point measurement and modelling for a ternary system containing decane, methane and methanol.

System Components (Mol %)			*P* (MPa)	*T* (K)	CPA-SRK72 (MPa)	$u(S)^a$ (MPa)	Relative CPA Deviation
Decane	CH_4	CH_3OH	5.56	263.15	5.19	0.08	-7%
32.14	15.73	52.13	5.98	273.15	5.59	0.08	-6%
			6.67	293.15	6.30	0.09	-6%
			7.14	313.15	6.86	0.09	-4%

[a] Standard uncertainties u are at $u(S) = 0.030$, $u(T) = 0.05$ K and $u(P) = 0.04$ MPa

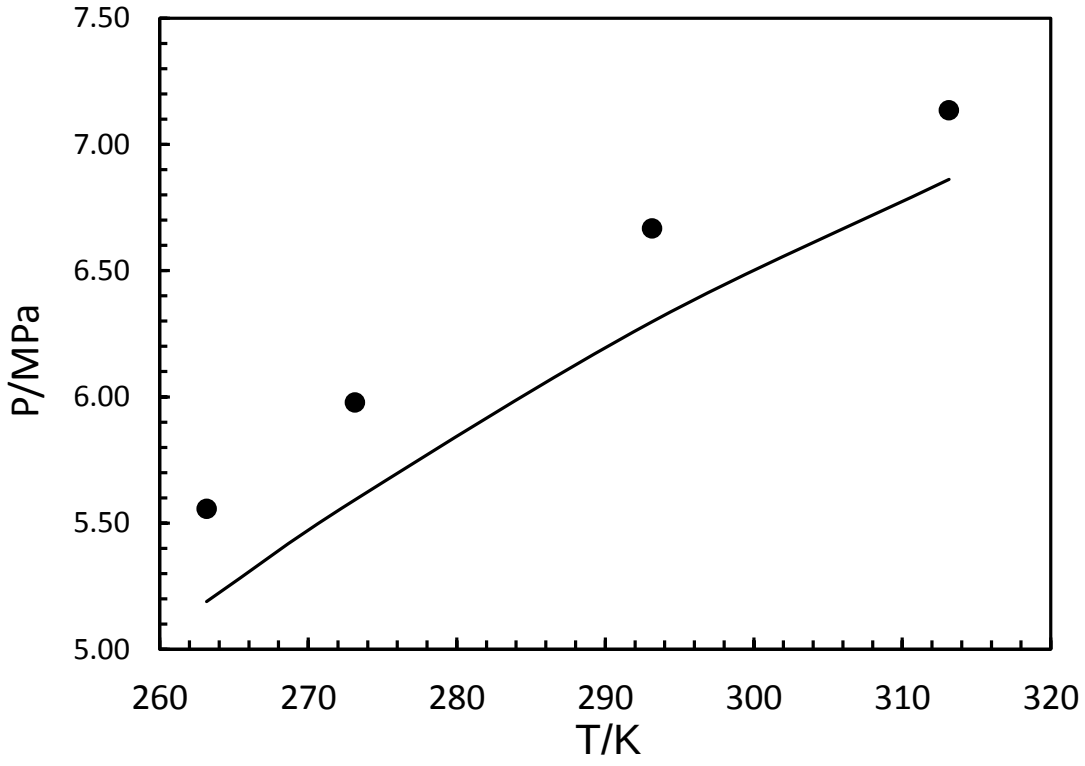

Figure 4.29. Shows the bubble point measurements for a decane-methane-methanol system (●) measured in this work together with CPA-SRK72 model predictions (Black line).

Table 4.30 shows the bubble point measurements for a decane-methane-ethanol ternary system together with CPA-SRK72 model predictions. The measurements demonstrated a combined standard uncertainty of $u(S)$ = 0.029. The CPA-SRK72 demonstrated an absolute average deviation of 17% from the experimental result, demonstrating significant deviation from the experimental results. Figure 4.30 illustrates the bubble point measurements for the decane-methane-methanol system together with the CPA-SRK72 model predictions.

Table 4.30. Bubble point measurement and modelling for a ternary system containing decane, methane and ethanol.

System Components (Mol %)			*P* (MPa)	*T* (K)	CPA-SRK72 (MPa)	$u(S)$[a] (MPa)	Relative CPA Deviation
Decane	CH_4	C_2H_5OH	5.31	263.15	6.78	0.08	28%
38.25	18.50	43.25	5.55	273.15	6.86	0.08	24%
			6.27	293.15	6.97	0.09	11%
			6.62	313.15	6.96	0.09	5%

[a] Standard uncertainties u are at $u_r(S)$ = 0.029, $u(T)$ = 0.05 K and $u(P)$ = 0.04 MPa

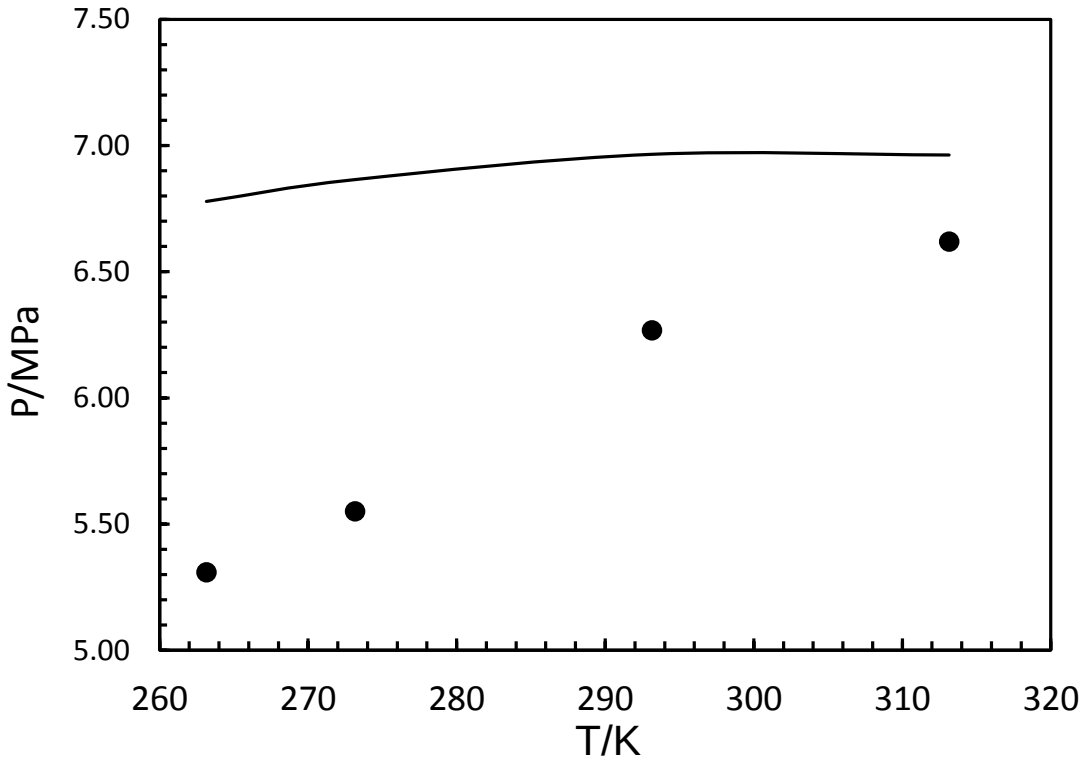

Figure 4.30. Shows the bubble point measurements for a decane-methane-ethanol system (●) measured in this work together with CPA-SRK72 model predictions (Black line).

Table 4.31 demonstrates the bubble point measurements for a decane-methane-methanol- water quaternary system together with CPA-SRK72 model predictions. The correlation developed using Wang et al. [21] data to calculate a new k_{ij} of 0.104 between methane-ethanol. The measurements showed a combined standard uncertainty of $u(S)$ = 0.024. The CPA-SRK72 demonstrated an absolute average deviation of 2% from the experimental result, using the correlated methane-methanol k_{ij} in the aqueous solutions. This is a significant improvement from an absolute average deviation of 9% calculated using k_{ij} developed using pure methanol from this work. Figure 4.31 illustrates the bubble point measurements for the decane-methane-methanol-water system together with the CPA-SRK72 model predictions.

Table 4.31. Bubble point measurement and modelling for a quaternary system containing decane, methane, methanol and water.

System Components (Mol %)				*P* (MPa)	*T* (K)	*u*(*S*)[a] (MPa)	CPA-SRK72 (MPa)	Relative CPA Deviation
Decane	CH_4	CH_3OH	H_2O	3.98	262.64	0.40	3.82	-4%
12.50	4.17	47.29	36.05	4.27	272.93	0.42	4.15	-3%
				4.62	285.67	0.43	4.52	-2%
				4.75	293.24	0.45	4.71	-1%
				5.12	313.02	0.46	5.13	0%

[a] Standard uncertainties *u* are at *u*(*S*) = 0.020, *u*(*T*) = 0.05 K and *u*(*P*) = 0.04 MPa

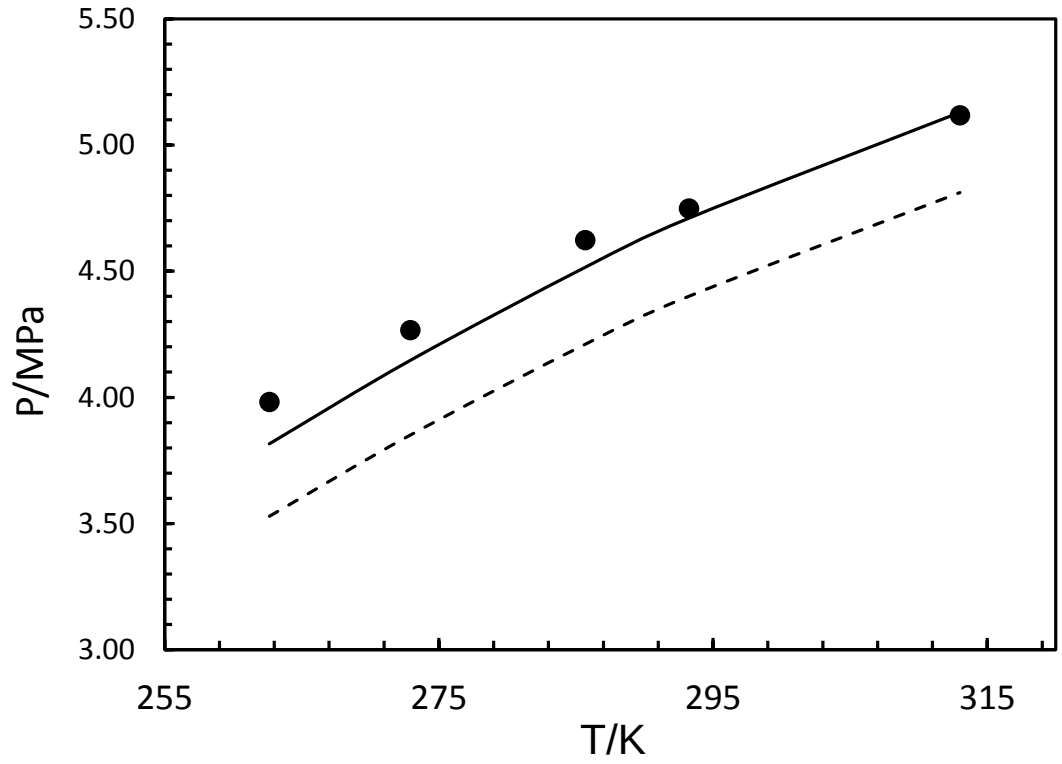

Figure 4.31. Shows the bubble point measurements for a decane-methane-methanol-water system (●) measured in this work. Black line: CPA-SRK72 model prediction with modified k_{ij}. Dashed line: CPA-SRK72 model prediction with original k_{ij}.

Table 4.32 demonstrates the bubble point measurements for a decane-methane-ethanol-water quaternary system together with CPA-SRK72 model predictions. The correlation developed using this work to calculate a new k_{ij} of 0.053 between methane-ethanol. The measurements showed a combined standard uncertainty of $u(S)$ = 0.024. The CPA-SRK72 demonstrated an absolute average deviation of 4% from the experimental result, using the correlated methane-ethanol k_{ij} in the aqueous solutions. This is a significant improvement from an absolute average deviation of 13% calculated using k_{ij} developed using pure ethanol from this work. Figure 4.32 illustrates the bubble point measurements for the decane-methane-ethanol-water system together with the CPA-SRK72 model predictions.

Table 4.32. Bubble point measurement and modelling for a quaternary system containing decane, methane, ethanol and water.

System Components (Mol %)				*P* (MPa)	*T* (K)	$u(S)$[a] (MPa)	CPA-SRK72 (MPa)	Relative CPA Deviation
Decane	CH_4	C_2H_5OH	H_2O	3.38	252.84	0.39	3.11	-8%
12.38	4.13	39.49	44	3.63	262.81	0.40	3.45	-5%
				3.85	272.81	0.40	3.77	-2%
				4.27	291.90	0.42	4.30	1%
				4.54	312.99	0.44	4.75	5%

[a] Standard uncertainties *u* are at $u(S)$ = 0.024, $u(T)$ = 0.05 K and $u(P)$ = 0.04 MPa

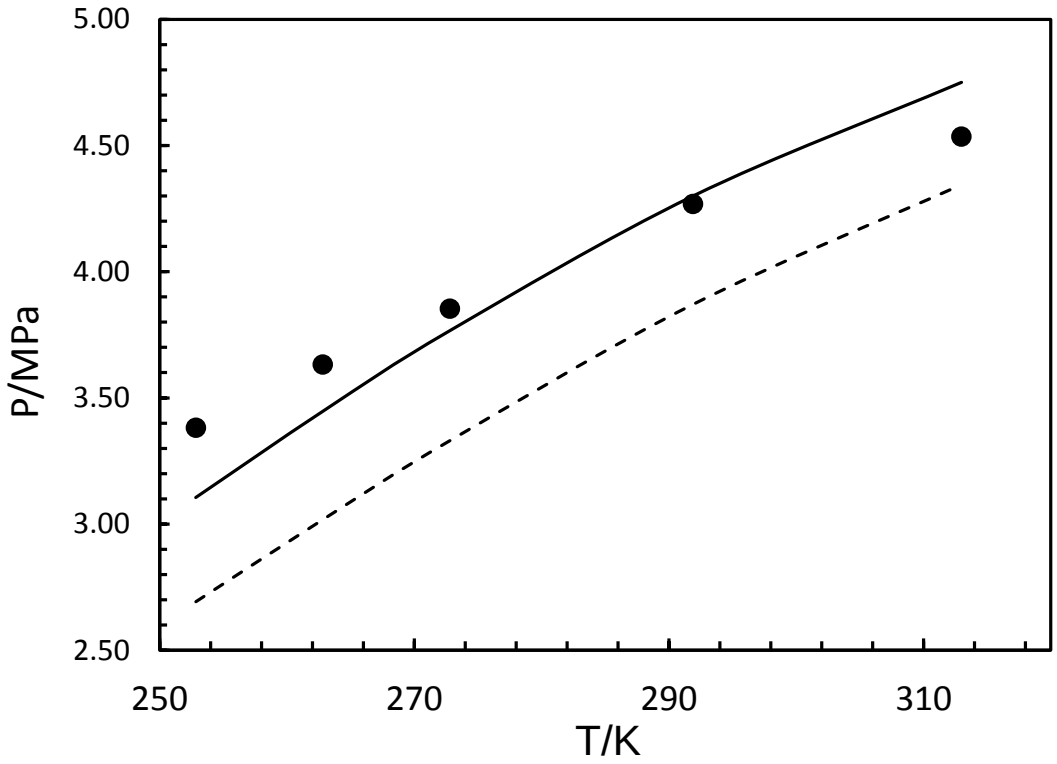

Figure 4.32. Shows the bubble point measurements for a decane-methane-ethanol-water system (●) measured in this work. Black line: CPA-SRK72 model prediction with modified k_{ij}. Dashed line: CPA-SRK72 model prediction with original k_{ij}.

Table 4.33 shows the bubble point measurements for an undecane-methane binary system together with CPA-SRK72 model predictions. The measurements showed a combined standard uncertainty of $u(S)$ = 0.019. The CPA-SRK72 demonstrated an absolute average deviation of 3% from the experimental result, showing good agreement with the model predictions. Figure 4.33 illustrates the bubble point measurements for the undecane-methane system together with the CPA-SRK72 model predictions.

Table 4.33. Bubble point measurement and modelling for a binary system containing undecane and methane.

System Components (Mol %)		*P* (MPa)	*T* (K)	*u*(*S*)[a] (MPa)	CPA-SRK72 (MPa)	Relative CPA Deviation
Undecane	CH_4	4.14	253.66	0.04	3.93	5%
75.05	24.95	4.48	263.49	0.04	4.34	3%
		4.84	273.67	0.04	4.75	2%
		5.51	292.60	0.04	5.45	1%
		6.11	317.00	0.05	6.21	-2%

[a] Standard uncertainties *u* are at *u*(*S*) = 0.019, *u*(*T*) = 0.05 K and *u*(*P*) = 0.04 MPa

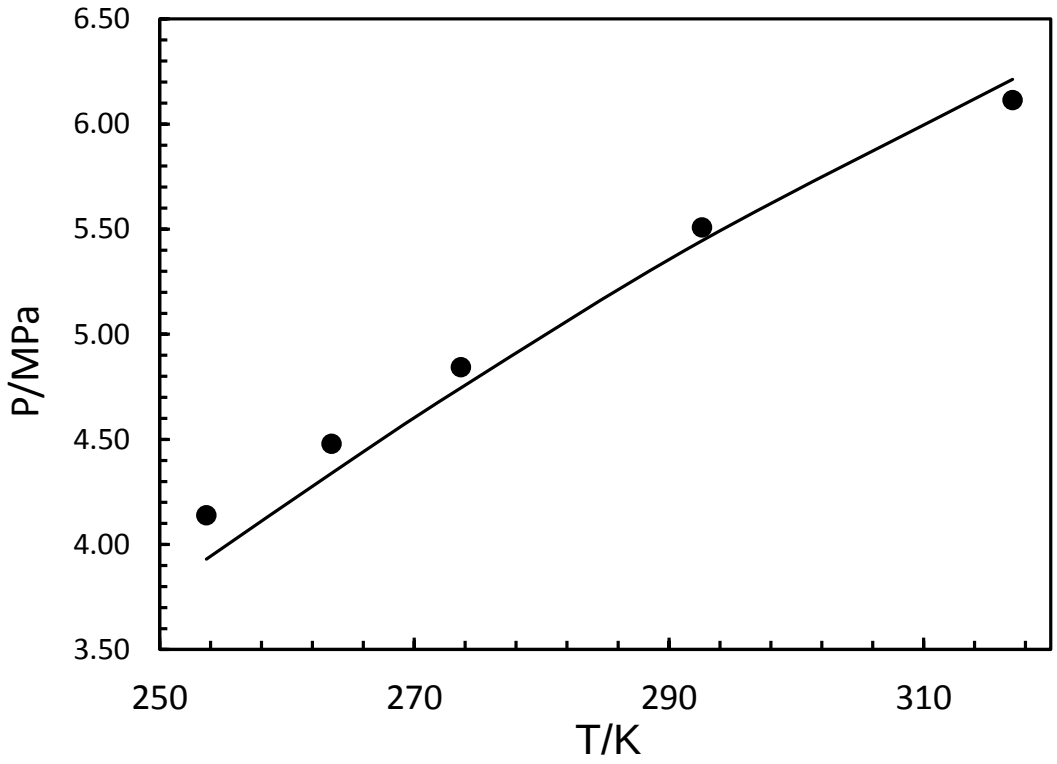

Figure 4.33. Shows the bubble point measurements for a undecane-methane system (●) measured in this work. Black line: CPA-SRK72 model prediction with modified k_{ij}.

Table 4.34 shows the bubble point measurements for an undecane-methane-methanol ternary system together with CPA-SRK72 model predictions. The measurements demonstrated a combined standard uncertainty of $u(S) = 0.021$. The CPA-SRK72 showed an absolute average deviation of 18% from the experimental result, indicating significant deviation from the experimental results. Figure 4.34 illustrates the bubble point measurements for the undecane-methane-methanol system together with the CPA-SRK72 model predictions.

Table 4.34. Bubble point measurement and modelling for a ternary system containing undecane, methane and methanol.

System Components (Mol %)			*P* (MPa)	*T* (K)	CPA-SRK72 (MPa)	$u(S)^a$ (MPa)	Relative CPA Deviation
Undecane	CH_4	CH_3OH	3.86	263.50	3.06	0.39	21%
39.01	12.95	48.04	4.20	276.26	3.39	0.42	19%
			4.61	293.73	3.80	0.46	18%
			4.61	293.77	3.80	0.46	18%
			4.97	314.85	4.23	0.50	15%

[a] Standard uncertainties *u* are at $u(S) = 0.021$, $u(T) = 0.05$ K and $u(P) = 0.04$ MPa

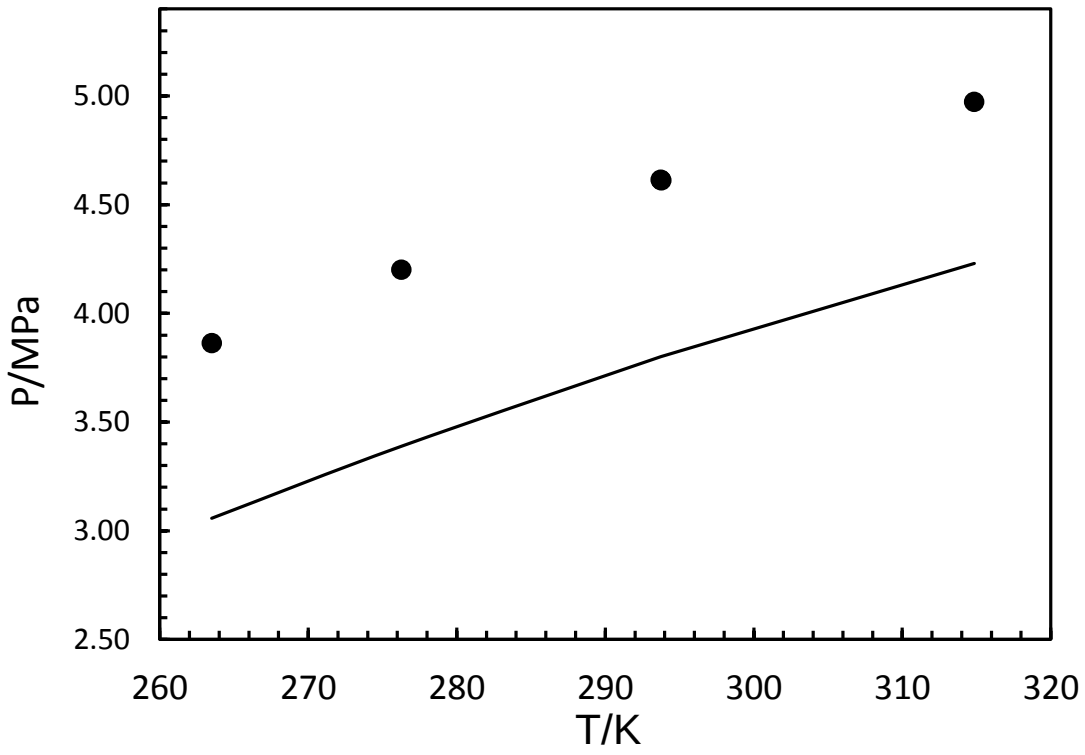

Figure 4.34. Shows the bubble point measurements for a undecane-methane-methanol system (●) measured in this work. Black line: CPA-SRK72 model prediction with modified k_{ij}.

Table 4.35 show the bubble point measurements for an undecane-methane-ethanol ternary system together with CPA-SRK72 model predictions. The measurements demonstrated a combined standard uncertainty of $u(S)$ = 0.023. The CPA-SRK72 demonstrated an absolute average deviation of 3% from the experimental result, demonstrating significant deviation from the experimental results. Figure 4.35 illustrates the bubble point measurements for the undecane-methane-ethanol system together with the CPA-SRK72 model predictions.

Table 4.35. Bubble point measurement and modelling for a ternary system containing Undecane, methane and ethanol.

System Components (Mol %)			*P* (MPa)	*T* (K)	CPA-SRK72 (MPa)	$u(S)$[a] (MPa)	Relative CPA Deviation
Undecane	CH_4	C_2H_5OH	3.50	263.89	3.61	0.04	-3%
39.53	12.94	47.54	3.79	274.63	3.79	0.04	0%
			4.17	294.83	4.06	0.04	3%
			4.55	315.46	4.25	0.04	7%

[a] Standard uncertainties *u* are at $u(S)$ = 0.023, $u(T)$ = 0.05 K and $u(P)$ = 0.04 MPa

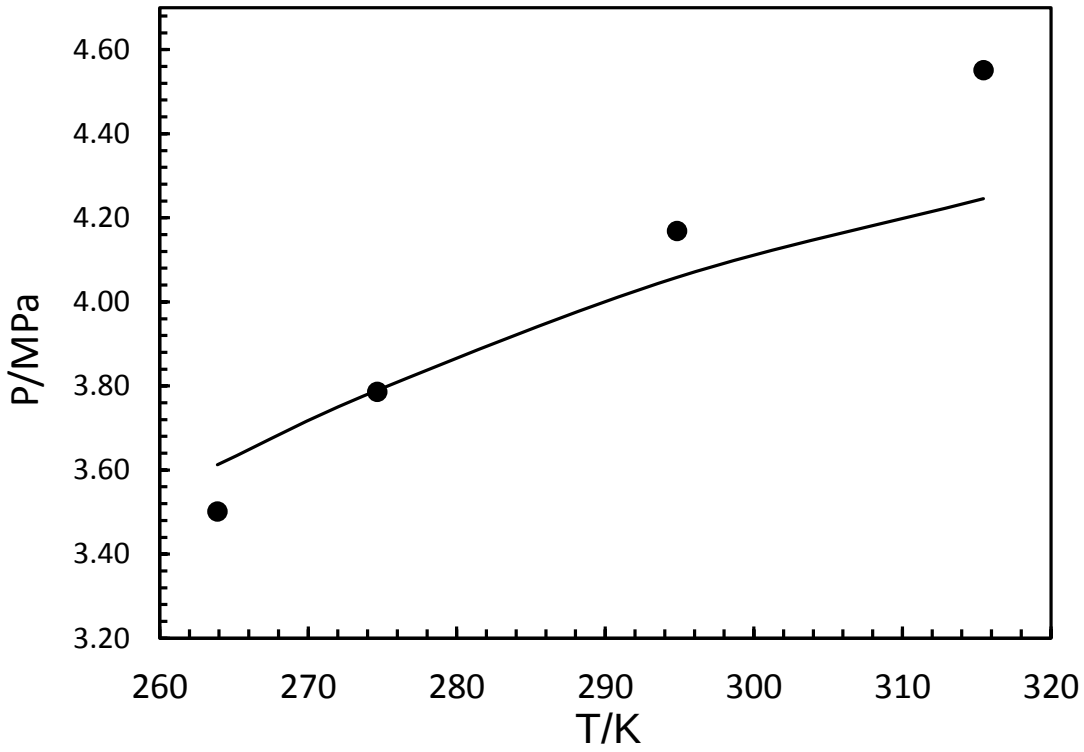

Figure 4.35. Bubble point measurement for a ternary system containing Undecane, methane and ethanol (●). Black line: CPA-SRK72 model prediction with modified k_{ij}.

Table 4.36 demonstrates the bubble point measurements for an undecane-methane-methanol-water quaternary system together with CPA-SRK72 model predictions. The correlation developed using the data from Wang et al. [21] was used to calculate a new k_{ij} of 0.104 between methane-methanol. The measurements showed a combined standard uncertainty of $u(S) = 0.016$. The CPA-SRK72 demonstrated an absolute average deviation of 5% from the experimental result, using the correlated methane-methanol k_{ij} in the aqueous solutions. This is a significant improvement from an absolute average deviation of 11% calculated using k_{ij} developed using pure methanol from Haghighi et al. [20]. Figure 4.36 shows the bubble point measurements for the undecane-methane-methanol-water system together with the CPA-SRK72 model predictions.

Table 4.36. Bubble point measurement and modelling for a quaternary system containing undecane, methane, methanol and water.

System Components (Mol %)				*P* (MPa)	*T* (K)	*u*(*S*)[a] (MPa)	CPA-SRK72 (MPa)	Relative CPA Deviation
Undecane	CH_4	CH_3OH	H_2O	3.91	264.82	0.04	3.66	6%
12.51	4.16	47.29	36.05	4.18	275.03	0.04	3.98	5%
				4.65	293.86	0.04	4.48	4%

[a] Standard uncertainties *u* are at *u*(*S*) = 0.016, *u*(*T*) = 0.05 K and *u*(*P*) = 0.04 MPa

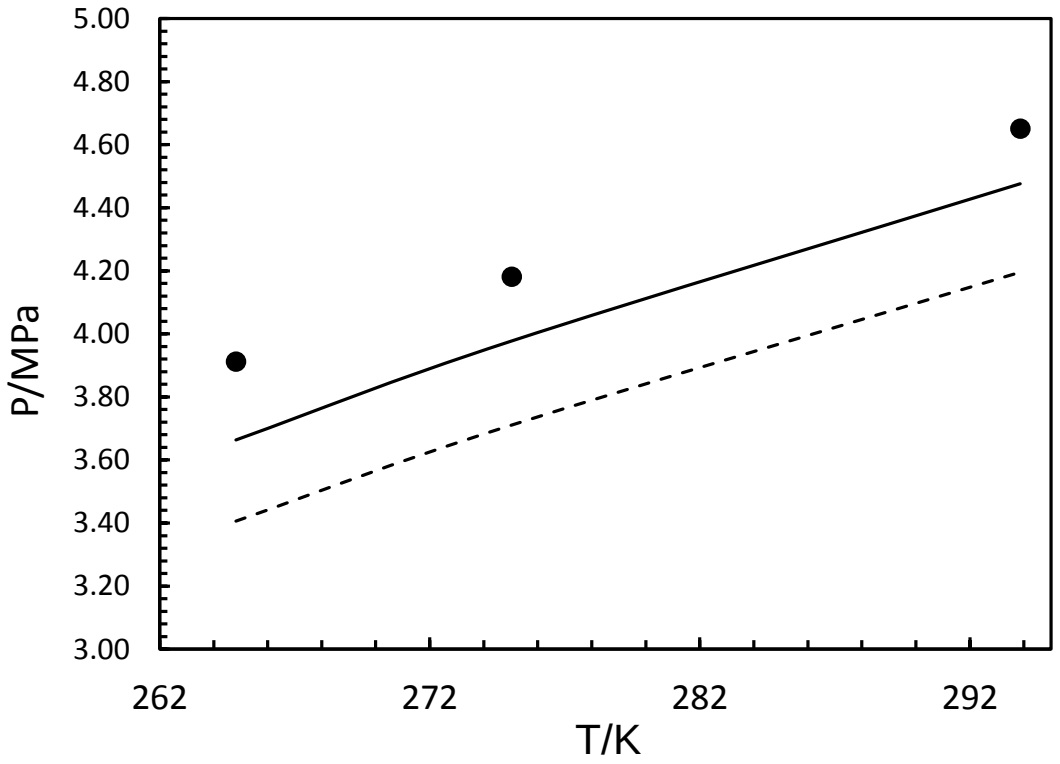

Figure 4.36. Bubble point measurement for a quaternary system containing Undecane, methane, methanol (●). Black line: CPA-SRK72 model prediction with modified k_{ij}.

Table 4.37 demonstrates the bubble point measurements for an undecane-methane-ethanol- water quaternary system together with CPA-SRK72 model predictions. The correlation developed using this work was used to calculate a new k_{ij} of 0.052 between methane and ethanol. The measurements showed a combined standard uncertainty of u(S) = 0.023. The CPA-SRK72 predictions demonstrated an absolute average deviation of 7% from the experimental result, using the correlated methane-ethanol k_{ij} in the aqueous solutions. This is a significant improvement from an absolute average deviation of 16% calculated using k_{ij} developed using pure ethanol from this work. Figure 4.37 shows the bubble point measurements for the undecane-methane-ethanol-water system together with the CPA-SRK72 model predictions.

Table 4.37. Bubble point measurement and modelling for a quaternary system containing Undecane, methane, ethanol and water.

System Components (Mol %)				*P* (MPa)	*T* (K)	*u*(*S*)[a] (MPa)	CPA-SRK72 (MPa)	Relative CPA Deviation
Undecane	CH_4	C_2H_5OH	H_2O	3.40	255.45	0.04	3.00	12%
12.56	4.11	39.76	43.57	3.66	266.32	0.04	3.35	9%
				3.82	274.29	0.04	3.59	6%
				3.82	275.17	0.04	3.62	5%
				4.49	315.52	0.04	4.57	-2%

[a] Standard uncertainties u are at *u*(*S*) = 0.023, *u*(*T*) = 0.05 K and *u*(*P*) = 0.04 MPa

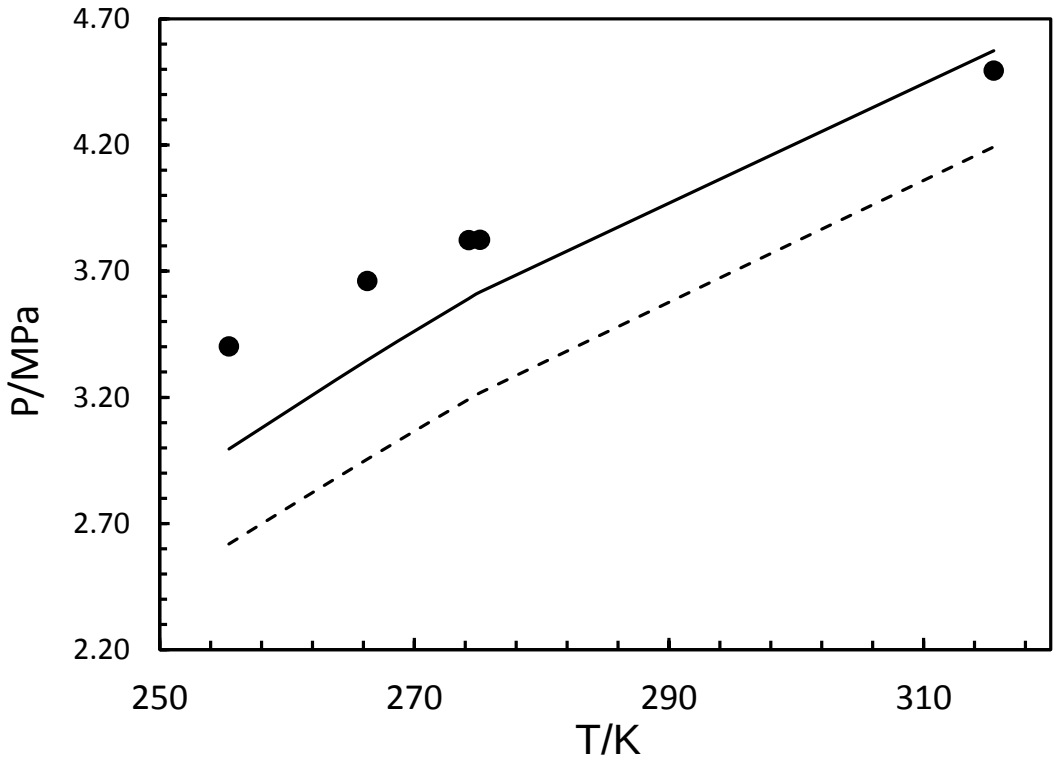

Figure 4.37. Bubble point measurement for a quaternary system containing Undecane, methane, ethanol and water (●). Black line: CPA-SRK72 model prediction with modified k_{ij}.

Table 4.38 shows the bubble point measurements for a dodecane-methane binary system together with CPA-SRK72 model predictions. The measurement showed a combined standard uncertainty of $u(S)$ = 0.010. The CPA-SRK72 demonstrated an absolute average deviation of 3% from the experimental result, showing good agreement with the model predictions. This measurement was carried out to confirm the model's capability in making acceptable predictions for binary systems before moving onto more complex multicomponent systems.

Table 4.38. Bubble point measurement and modelling for a binary system containing dodecane and methane.

System Components (Mol %)		P (MPa)	T (K)	$u(S)$[a] (MPa)	CPA-SRK72 (MPa)	Relative CPA Deviation
Dodecane 68.46	CH_4 31.54	7.42	293.29	0.48	7.17	-3%

[a] Standard uncertainties u are at $u(S)$ = 0.010, $u(T)$ = 0.05 K and $u(P)$ = 0.04 MPa

Table 4.39 demonstrates the bubble point measurements for a dodecane-methane-ethanol ternary system together with CPA-SRK72 model predictions. The measurements demonstrated a combined standard uncertainty of $u(S)$ = 0.015. The CPA-SRK72 demonstrated an absolute average deviation of 12% from the experimental result, demonstrating significant deviation from the experimental results. Figure 4.38 illustrates the bubble point measurements for the dodecane-methane-ethanol system together with the CPA-SRK72 model predictions.

Table 4.39. Bubble point measurement and modelling for a ternary system containing dodecane, methane and ethanol.

System Components (Mol %)			*P* (MPa)	*T* (K)	CPA-SRK72 (MPa)	$u(S)$[a] (MPa)	Relative CPA Deviation
Dodecane 39.68	CH_4 18.28	C_2H_5OH 42.04	4.95	263.15	4.41	0.04	-11%
			5.27	273.15	4.73	0.04	-10%
			5.89	293.15	5.19	0.04	-12%
			6.35	313.35	5.36	0.04	-15%

[a] Standard uncertainties *u* are at $u(S) = 0.015$, $u(T) = 0.05$ K and $u(P) = 0.04$ MPa

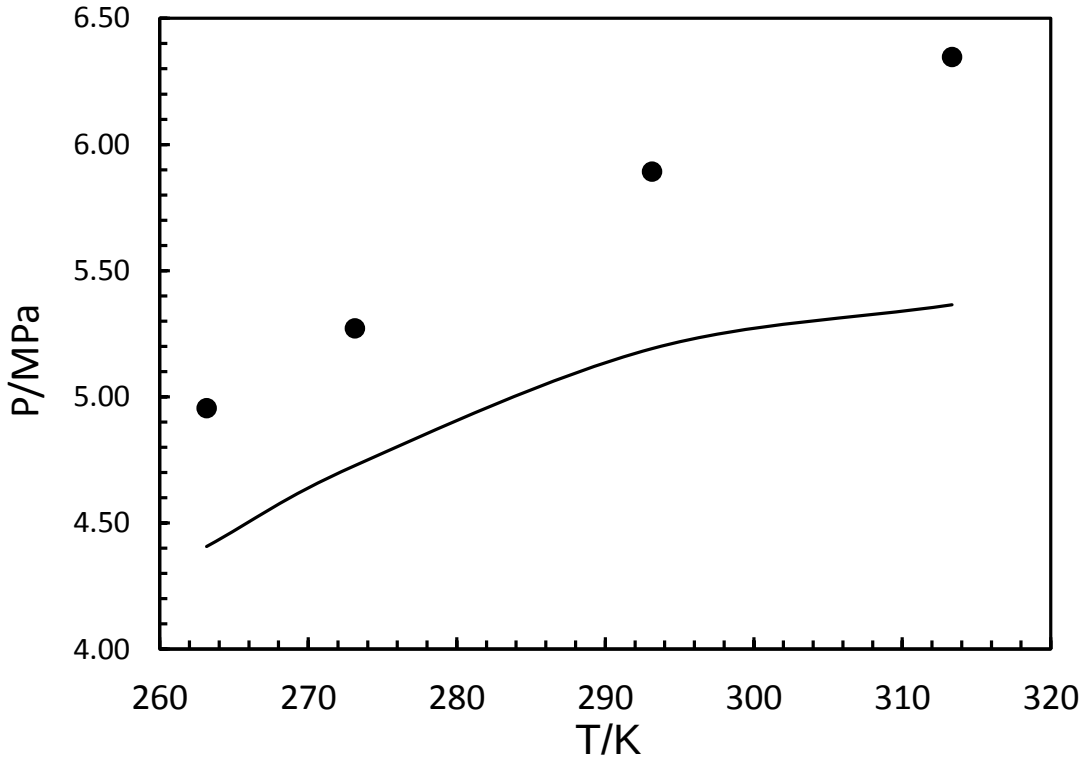

Figure 4.38. Shows the bubble point measurements for a dodecane-methane-ethanol system (●) measured in this work together with CPA-SRK72 model predictions (Black line).

Table 4.40 demonstrates the bubble point measurements for an undecane-methane-methanol- water quaternary system together with CPA-SRK72 model predictions. The correlation developed using the data from Wang et al. [21] was used to calculate a new k_{ij} of 0.104 between methane-methanol. The measurements showed a combined standard uncertainty of $u(S)$ =0.018. The CPA-SRK72 demonstrated an absolute average deviation of 3% from the experimental result, using the correlated methane-methanol k_{ij} in the aqueous solutions. This is a significant improvement from an absolute average deviation of 9% calculated using k_{ij} developed using pure methanol from Haghighi et al. [20]. Figure 4.39 shows the bubble point measurements for the dodecane-methane-methanol-water system together with the CPA-SRK72 model predictions.

Table 4.40. Bubble point measurement and modelling for a quaternary system containing dodecane, methane, methanol and water.

System Components (Mol %)				P (MPa)	T (K)	$u(S)$[a] (MPa)	CPA-SRK72 (MPa)	Relative CPA Deviation
Dodecane	CH_4	CH_3OH	H_2O	4.11	274.43	0.04	3.90	5%
12.5	4.16	47.29	36.05	4.55	295.15	0.04	4.44	2%
				4.91	315.58	0.05	4.84	1%

[a] Standard uncertainties u are at $u(S)$ = 0.018, $u(T)$ = 0.05 K and $u(P)$ = 0.04 MPa

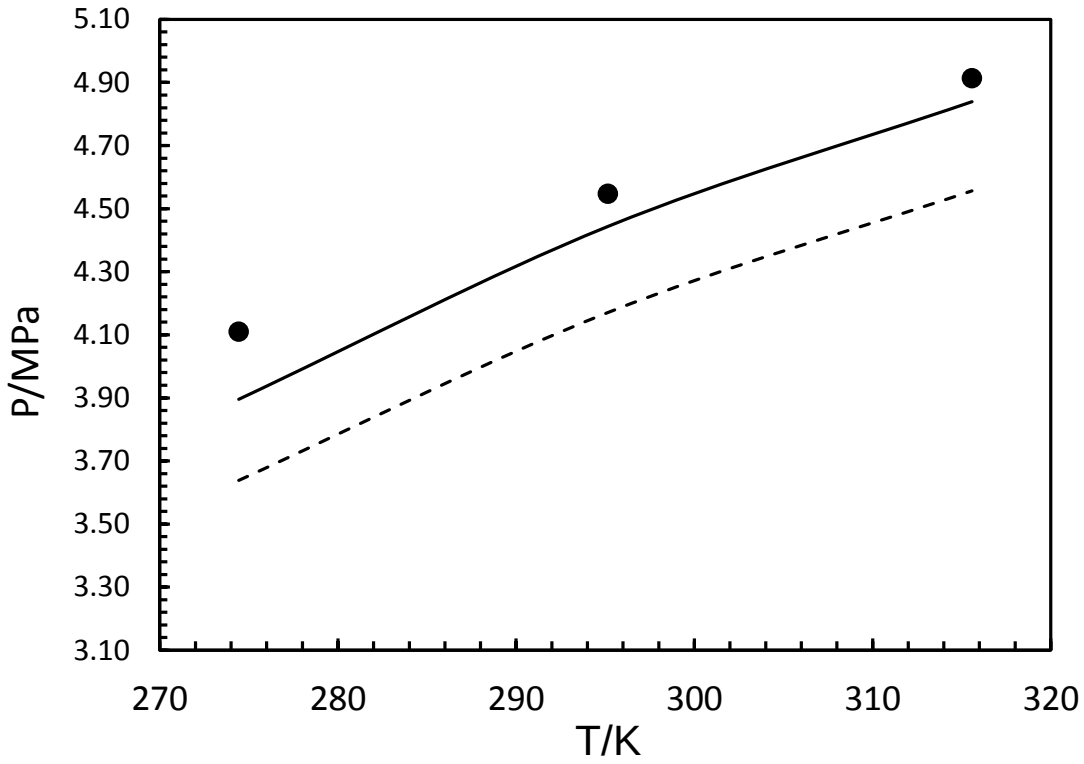

Figure 4.39. Shows the bubble point measurements for a dodecane-methane-methanol-water system (●) measured in this work. Black line: CPA-SRK72 model prediction with modified k_{ij}. Dashed line: CPA-SRK72 model prediction with original k_{ij}.

Table 4.41 shows the bubble point measurements for an undecane-methane-ethanol-water quaternary system together with CPA-SRK72 model predictions. The correlation developed using this work was used to calculate a new k_{ij} of 0.052 between methane and ethanol. The measurements showed a combined standard uncertainty of $u(S) = 0.021$. The CPA-SRK72 predictions demonstrated an absolute average deviation of 8% from the experimental result, using the correlated methane-ethanol k_{ij} in the aqueous solutions. This is a significant improvement from an absolute average deviation of 18% calculated using k_{ij} developed using pure ethanol from this work. Figure 4.40 shows the bubble point measurements for the dodecane-methane-ethanol-water system together with the CPA-SRK72 model predictions. It is important to note that dodecane-methane-ethanol-water form a three phase mixture.

Table 4.41. Bubble point measurement and modelling for a quaternary system containing dodecane, methane, ethanol and water.

System Components (Mol %)				*P* (MPa)	*T* (K)	*u*(*S*)[a] (MPa)	CPA-SRK72 (MPa)	Relative CPA Deviation
Dodecane	CH_4	C_2H_5OH	H_2O	3.62	262.94	0.04	3.21	11%
12.51	4.14	39.77	43.58	3.86	273.63	0.04	3.54	8%
				4.07	283.84	0.04	3.84	6%
				4.43	294.45	0.04	4.12	7%

[a] Standard uncertainties *u* are at *u*(*S*) = 0.021, *u*(*T*) = 0.05 K and *u*(*P*) = 0.04 MPa

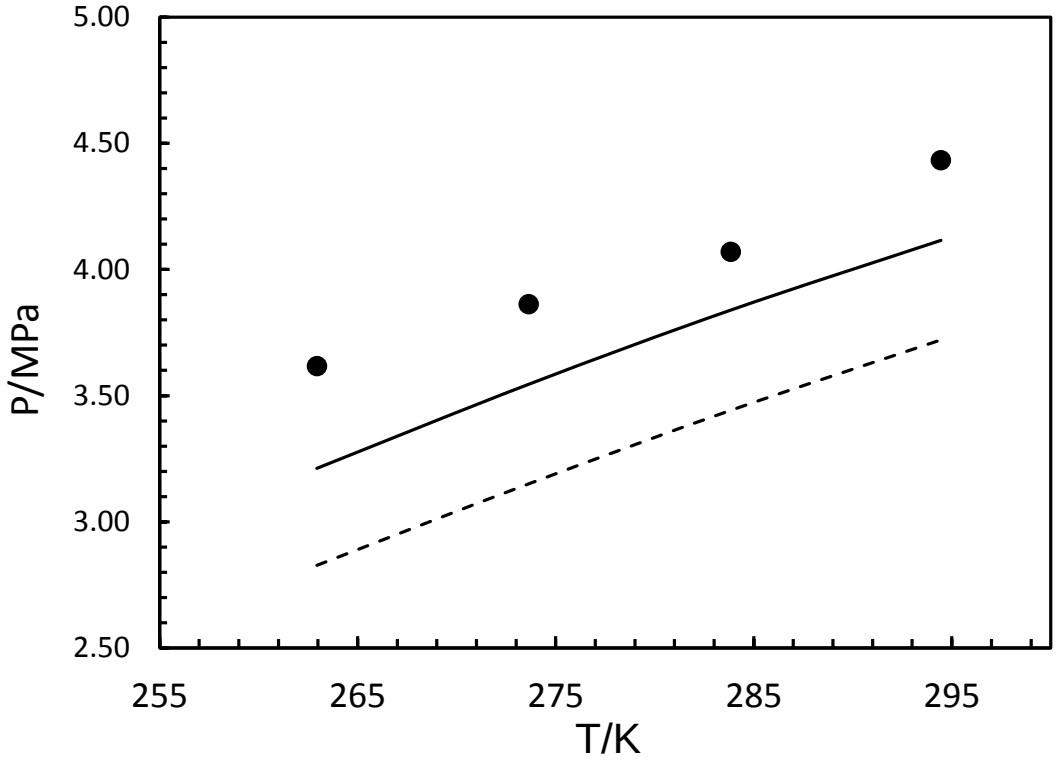

Figure 4.40. Shows the bubble point measurements for a dodecane-methane-ethanol-water system (●) measured in this work. Black line: CPA-SRK72 model prediction with modified k_{ij}. Dashed line: CPA-SRK72 model prediction with original k_{ij}.

An attempt was made to determine the bubble point of hexadecane-methane-methanol using the described set-up. However, the system could not reach equilibrium and was too unstable for a bubble point measurement. After further investigation, using a sapphire

pressure vessel, it was determined that the system formed an emulsion. The system was analysed at temperatures ranging 313.15 – 343.15 K.

4.4 Conclusion

4.4.1 Solubility of CH_4 in Alcohols

Methanol and ethanol are commonly used hydrate inhibitors by a number of oil and gas operators. Due to the lack of data in open literature for the temperature range required in hydrate prevention, the experimental measurements in this work were focused on the solubility of methane in ethanol. The solubility of CH_4 in methanol showed good agreement with the data published in open literature thus demonstrating the reliability of the equipment and methods used in this work. Overall the model predictions showed an absolute average deviation of 5.31% using a single Binary Interaction Parameter (BIP).

The solubility of methane in methanol and ethanol was substantially reduced with the addition of water. This illustrated the affinity of methanol and ethanol molecular surfaces to form hydrogen bonds with the water, thus reducing the available surfaces for CH_4 interaction. This had previously been observed by Wang et al. [21] measuring the solubility of CH4 in methanol solutions.

The model calculations using the BIPs developed for the pure alcohols demonstrated significant deviation from the experimental work, however the model calculations were drastically improved by regressing BIPs between methane and the alcohol using the solubility in aqueous solution results.

It is essential to note that the results from this work were used to optimise the CPA-SRK72 model, due to the limitation of independent data in the open literature. Both modelling and experimental results can be directly used by the industry and research organisations, however it is important to note to ensure reliability of the model, it must be compared to independent literature data.

4.4.2 Vapour Content of Methane in the presence of alcohols

The knowledge of methanol and ethanol loss to the vapour phase is very important due to numerous factors including ensuring sufficient inhibitor is available to prevent hydrate formation as well as to mitigate penalties entailed when the level of inhibitor in the vapour phase exceeds the standards set. The data showed good agreement with the data from literature. Some of the benefits of the CPA-SRK72 EoS are speed, simplicity and precision which were demonstrated by the results.

Due to the extremely limited number of data in the open literature a substantial amount of work was carried out to ensure the reliability of the results. To evaluate the reliability of the calibration, three BOC certified gases were tested, the results showing very good agreement with the measured values.

4.4.3 Saturation Pressure of Reservoir Fluids

A number of measurements were made to determine the bubble point in binary, ternary and quaternary systems containing a heavy hydrocarbon phase (C7 – C12), alcohol phase (methanol and ethanol) and excess water phase respectively. The main objective of these measurements were to evaluate the capabilities of the CPA-SRK72 model in determining the inhibitor distribution in various phases. The data may also be used to optimise thermodynamic models; however the author has not used the saturation pressure measurements for optimisation. The solubility data from this work and literature were used to optimise the model predictions. The model predictions were in good agreement with the binary bubble point measurements, however various levels of deviation were observed in ternary and quaternary systems and each system must be judged individually. Bubble point prediction of binary systems demonstrated the lowest absolute average deviation from the experimental results at an average of 3%. The bubble point predictions for the ternary system demonstrated the largest absolute average deviation range of 3 – 20%. The model predictions for systems containing water were significantly improved by using the calculations from the correlations developed in the solubility measurement section of this work. The CPA-SRK72 predictions for quaternary systems using the correlated k_{ij} showed and absolute average deviation range of 2 – 9%. The CPA-SRK72 EoS may be further evaluated using multicomponent systems containing water to show its capabilities.

4.5 References

[1] I. Krichevsky, M. Koroleva, The solubility of methanol in compressed gases, Acta Physicochim. URSS. 15 (1941) 327–342.

[2] B. Hemmaplardh, A.D. King, Solubility of methanol in compressed nitrogen, argon, methane, ethylene, ethane, carbon dioxide, and nitrous oxide. Evidence for association of carbon dioxide with methanol in the gas phase, J. Phys. Chem. 76 (1972) 2170–2175. doi:10.1021/j100659a018.

[3] H. Lazalde-Crabtree, G.J.F. Breedveld, J.M. Prausnitz, Solvent losses in gas absorption. Solubility of methanol in compressed natural and synthetic gases, AIChE J. 26 (1980) 462–470. doi:10.1002/aic.690260318.

[4] N.. Yarym-agaev, K. Sinyavskaya R.P, фазовые равновесия в бинарных системах вода-метан, метанол-метан при высоких давлениях (Phase equilibria in binary systems of water-methane, methanol-methane at high pressures), ZHurnal Prikladoi Khimii. 58 (1985) 165 –168.

[5] E. Brunner, W. Hültenschmidt, G. Schlichthärle, Fluid mixtures at high pressures IV. Isothermal phase equilibria in binary mixtures consisting of (methanol + hydrogen or nitrogen or methane or carbon monoxide or carbon dioxide), J. Chem. Thermodyn. 19 (1987) 273–291. doi:10.1016/0021-9614(87)90135-2.

[6] J.H. Hong, P. V. Malone, M.D. Jett, R. Kobayashi, The measurement and interpretation of the fluid-phase equilibria of a normal fluid in a hydrogen bonding solvent: the methane - methanol system, Fluid Phase Equilib. 38 (1987) 83–96. doi:10.1016/0378-3812(87)90005-7.

[7] R. Schneider, PhD Thesis: Experimentelle Bestimmung der dynamischen Viskosität von Flüßigkeitsgemischen aus Methanol mit CO2, CH4, C2H6 und C3H8, Technical University of Berlin, 1978.

[8] R. Langhorst, Experimentelle Untersuchung der Dampfphase in weitsiedenden Gemischen sowie Aufbau einer Datenbank für Phasengleichgewichte, Berlin Technical University, 1987.

[9] T. Ukai, D. Kodama, J. Miyazaki, M. Kato, Solubility of Methane in Alcohols and Saturated Density at 280.15 K, J. Chem. Eng. Data. 47 (2002) 1320–1323. doi:10.1021/je020108p.

[10] L.-K. Wang, G.-J. Chen, G.-H. Han, X.-Q. Guo, T.-M. Guo, Experimental study on the solubility of natural gas components in water with or without hydrate

inhibitor, Fluid Phase Equilib. 207 (2003) 143–154. doi:10.1016/S0378-3812(03)00009-8.

[11] M. Frost, E. Karakatsani, N. von Solms, D. Richon, G.M. Kontogeorgis, Vapor–Liquid Equilibrium of Methane with Water and Methanol. Measurements and Modeling, J. Chem. Eng. Data. 59 (2014) 961–967. doi:10.1021/je400684k.

[12] K. Suzuki, H. Sue, M. Itou, R.L. Smith, H. Inomata, K. Arai, et al., Isothermal vapor-liquid equilibrium data for binary systems at high pressures: carbon dioxide-methanol, carbon dioxide-ethanol, carbon dioxide-1-propanol, methane-ethanol, methane-1-propanol, ethane-ethanol, and ethane-1-propanol systems, J. Chem. Eng. Data. 35 (1990) 63–66. doi:10.1021/je00059a020.

[13] E. Brunner, W. Hültenschmidt, Fluid mixtures at high pressures VIII. Isothermal phase equilibria in the binary mixtures: (ethanol + hydrogen or methane or ethane), J. Chem. Thermodyn. 22 (1990) 73–84. doi:10.1016/0021-9614(90)90033-M.

[14] D.G. Friend, D.J. Frurip, E.W. Lemmon, R.E. Morrison, J.D. Olson, L.C. Wilson, Establishing benchmarks for the Second Industrial Fluids Simulation Challenge, Fluid Phase Equilib. 236 (2005) 15–24. doi:10.1016/j.fluid.2005.04.020.

[15] C. Lundstrøm, M.L. Michelsen, G.M. Kontogeorgis, K.S. Pedersen, H. Sørensen, Comparison of the SRK and CPA equations of state for physical properties of water and methanol, Fluid Phase Equilib. 247 (2006) 149–157. doi:10.1016/j.fluid.2006.06.012.

[16] L.E. Zerpa, E.D. Sloan, C. Koh, A. Sum, Hydrate Risk Assessment and Restart-Procedure Optimization of an Offshore Well Using a Transient Hydrate Prediction Model, Oil Gas Facil. 1 (2012) 49–56. doi:10.2118/160578-PA.

[17] P.A. Ferreira, M.F.C. Bezerra, R. Loschiavo, The Internal Corrosion Integrity Strategy on the Development of New Offshore Production Areas in Brazil, in: Offshore Technol. Conf., Offshore Technology Conference, 2013. doi:10.4043/16312-MS.

[18] P. Altoe Ferreira, The Internal Corrosion Integrity Strategy on the Development of New Offshore Production Areas in Brazil, SPE Prod. Facil. 20 (2005) 324–333. doi:10.2118/100155-PA.

[19] A. Chapoy, M. Nazeri, M. Kapateh, R. Burgass, C. Coquelet, B. Tohidi, Effect of impurities on thermophysical properties and phase behaviour of a CO2-rich system in CCS, Int. J. Greenh. Gas Control. 19 (2013) 92–100. doi:10.1016/j.ijggc.2013.08.019.

[20] H. Haghighi, A. Chapoy, R. Burgess, S. Mazloum, B. Tohidi, Phase equilibria for petroleum reservoir fluids containing water and aqueous methanol solutions: Experimental measurements and modelling using the CPA equation of state, Fluid Phase Equilib. 278 (2009) 109–116. doi:10.1016/j.fluid.2009.01.009.

[21] L.-K. Wang, G.-J. Chen, G.-H. Han, X.-Q. Guo, T.-M. Guo, Experimental study on the solubility of natural gas components in water with or without hydrate inhibitor, Fluid Phase Equilib. 207 (2003) 143–154. doi:10.1016/S0378-3812(03)00009-8.

[22] M.H. Kapateh, A. Chapoy, R. Burgass, B. Tohidi, Experimental Measurement and Modeling of the Solubility of Methane in Methanol and Ethanol, J. Chem. Eng. Data. (2015) acs.jced.5b00793. doi:10.1021/acs.jced.5b00793.

[23] M. Wise, A. Chapoy, Carbon dioxide solubility in Triethylene Glycol and aqueous solutions, Fluid Phase Equilib. 419 (2016) 39–49. doi:10.1016/j.fluid.2016.03.007.

[24] E. Brunner, Fluid mixtures at high pressures I. Phase separation and critical phenomena of 10 binary mixtures of (a gas + methanol), J. Chem. Thermodyn. 17 (1985) 671–679. doi:10.1016/0021-9614(85)90121-1.

Chapter 5 – CONCLUSION AND RECOMMENDATION FOR FUTURE WORK

5.1 Introduction

The main goal of this work was to improve thermodynamic models by experimental investigation of thermodynamic gas hydrate inhibitors. Although the main objective of this work was to investigate this issue experimentally, the CPA-SRK72 Equation of State (EoS) was also further optimised using the data from this work and the open literature. This was to further demonstrate the capabilities of this EoS, building on the works of Haghighi et al. [1] and Chapoy et al. [2,3] as well as further optimise this EoS for direct industrial application. These models are intended describe condition for avoiding flow assurance issues in both the natural gas industry as well as contributing to the Carbon Capture and Storage (CCS) industry. Additives, such as methanol and ethanol as well as Mono-Ethylene Glycol (MEG), Diethylene Glycol (DEG) and Triethylene Glycol (TEG) were thoroughly investigated. The summary of this work's achievements in chronological order of presentation are as follows.

1. The author introduced the subject matter as well as its importance in gas transportation and processing in Chapter 1. Hydrates structure and formation conditions were introduced as well as demonstrating the study's goals.
2. An extensive literature review was conducted to define and illustrate the capabilities of the CPA-SRK72 EoS in Chapter 2. The evolution of Equations of State were briefly described together with the need for EoS that are capable of predicting the phase behaviour of systems containing associating components. The EoS parameters used in this work were shown in this chapter allowing the reader to easily implement the results of this work in simulation software.
3. Glycols are commonly used as hydrate inhibitors as well as for the dehydration of gases. An extensive literature review was conducted to extract experimental data measurements for the solubility of CO_2 in glycols and solutions (chapter 3). A number of gaps were spotted in the open literature. This work aimed to investigate the solubility of CO_2 to further understand and assist the development of thermodynamic models.
4. The solubility of CO_2 in pure MEG, DEG and TEG at various pressures and temperatures were measured. The solubility of CO_2 in pure MEG, DEG and

TEG were compared to CPA-SRK72 EoS correlations. The solubility of CO_2 in 90, 60 and 40 wt% MEG, DEG and TEG aqueous solutions at various temperatures and pressures also were measured (Chapter 3). The results were used to regress variable Binary Interaction Parameters (BIPs) optimising the CPA-SRK72 EoS.

5. Methanol and ethanol are commonly used thermodynamic inhibitors. An in-depth literature review regarding the solubility of methane in methanol and ethanol was conducted (Chapter 4). The solubility of methane in pure methanol and ethanol at various pressures and temperatures was investigated. The effect of water on the solubility of methane in methanol and ethanol was also extensively studied. The solubility data in this work was used to optimise the CPA-SRK72 EoS.
6. A number of binary, ternary and quaternary saturation pressure measurements were conducted. Systems containing methane, a light hydrocarbon (C7 – C12), methanol/ethanol and excess water were studied. These measurements were compared to the optimised CPA-SRK72 EoS predictions to validate the model.
7. The vapour content of methanol and ethanol rich methane was also measured in this work. Due to experimental issues, only a limited number of measurements were possible within the timeline of this work. These experimental data were compared with the CPA-SRK72 EoS predictions to determine its performance.

5.2 Thermodynamic Modelling

Thermodynamic models are an essential part of efficient and cost effective chemical and petroleum engineering design. Choosing a suitable EoS for the system being studied is extremely difficult and important. [4,5] In this work the CPA-SRK72 EoS developed by Kontogeorgis et al. [6] was used and further optimised using data from literature and this work. This EoS is a combination of the EoS proposed by Soave [7] and the association term based on SAFT.

Classical EoS, such as SRK and Peng Robinson (PR), have shown significant deviations when predicting the phase behaviour of systems containing associating components. However, their simplicity and relative reliability have made them extremely popular in the industry. CPA-SRK72 combines the simplicity of SRK and the improved prediction capabilities of statistical EoS. It is important to note that this simplicity comes

at the cost of losing the more detailed understanding of molecular behaviour that can be achieved while using statistical mechanics EoS such as SAFT.

This work extensively focused on continuation of the modelling work carried out by Haghighi [1] and Chapoy et al. [2,3]. CPA-SRK72 EoS as well as other EoS can be further optimised using the experimental results. However further understanding of associating molecular interaction is also extremely important. This study maybe further extended to determine the effect of hydrocarbons on interaction between water and alcohols/glycols using statistical mechanics bases EoS as well as molecular modelling simulations.

5.3 Solubility of CO_2 in Glycols and Aqueous Solutions

Glycols are commonly used as thermodynamic hydrate inhibitors (at the well head) as well as in gas dehydration units, making the knowledge of CO_2-glycol phase behaviour essential for CO_2 transportation and processing.

The solubility of CO_2 in glycols has been studied over the years at high temperatures and pressures. As the industry moves towards more extreme conditions, the knowledge of these system phase behaviour at lower temperatures and higher pressures becomes more important. This knowledge is required to be able to effectively predict the phase behaviour of binary and multicomponent systems using thermodynamic models. A wide range of temperatures and pressures were studied in this work. This was to understand the phase behaviour and to be able to correlate the CPA-SRK72 in a wide temperature and pressure range.

The solubility of CO_2 in 90, 60 and 40 wt% glycol solutions also were measured. There were a very limited number of measurement data available in the open literature which were not in complete agreement. This work entailed an extensive study of the effect of water on the solubility of CO_2 in glycols. A small mass of water resulted in a significant drop in CO_2 solubility in glycols. The CPA-SRK72 EoS solubility predictions showed significant deviation from the experimental results when using the BIPs regressed from the solubility of CO_2 in pure glycols. Hence glycol concentration dependant BIPs were developed. This considerably improved the model calculations. However, it is essential to note, to fully validate the model, it is important to compare the calculations to independent experimental results. Three correlations were developed which may be used to calculate BIPs for various glycol concentration.

The deviation of the CPA-SRK72 correlations from the experimental results were significantly reduced in this work. Future work maybe recommended to further optimise

CPA-SRK72 phase behaviour. To validate the model, it is important to use independent experimental data. It is also recommended to measure the vapour content of glycol/water rich CO_2 to determine the solubility of glycol and water-glycol solution in the vapour phase. These data may be used to further optimise the CPA-SRK72 EoS as well as other Equations of state.

5.4 Alcohol Distribution in the Liquid Phase

Methanol and ethanol are two commonly used gas hydrate inhibitors, and thus the knowledge of their phase behaviour together with other components are essential to economic engineering design of transportation and process equipment.

This part of the study focused on performing measurements that would assist in optimising the CPA-SRK72 EoS and other thermodynamic models to predict the inhibitor distribution in reservoir fluids particularly traditional high CH_4 natural gas compositions. Three experiments were setup to achieve this aim.

- Solubility of CH_4 in methanol, ethanol and ethanol water solutions
- Solubility of methanol and ethanol in CH_4
- Saturation pressure measurements for binary, tertiary and quaternary systems containing CH_4 and heavier hydrocarbons.

A literature review was conducted to investigate the previous research in this field. The literature survey showed that numerous studies focused on measuring the solubility of methane in methanol (Hemmaplardh et al. [8], Krichevsky et al. [9], Brunner et al. [10], Hong et al. [11]…). Methanol is the most commonly used alcohol based hydrate inhibitor, however there are moves to minimise its usage due to its toxicity as companies move more towards ‘green chemistry’. Furthermore ethanol is also commonly used in South America as a hydrate inhibitor due to its relative abundance [12–15]. Only a limited number of literature have reported the solubility of methane in ethanol (Suzuki et al. [16], Brunner et al. [17], Ukai et al. [18] and Friend et al. [19])

It is abundantly clear that solubility data for CH_4 in ethanol are scarce and thus this work focused on these solubility measurements and solutions. A number of solubility measurements for methane in methanol and its solutions were also conducted to compare the results from this equipment to the open literature data. The data from this work and the literature was used to tune alcohol concentration dependant methane-alcohol BIPs. These BIPs were then used to develop two correlations which can be used to calculate

alcohol-aqueous solution concentration dependant BIPs between the alcohol and methane.

An saturation pressure study was conducted to determine the inhibitor distribution. Binary, ternary and quaternary systems containing methane, heavier hydrocarbon (C7 – C12), alcohol and water, were investigated. The data from the saturation pressure study was compared to the CPA-SRK72 predictions. The correlations developed in this work was used to calculate concentration dependant BIPs for quaternary systems. This resulted in a significant reduction in the deviation between CPA-SRK72 and the experimental results. This method was chosen to reduce the necessity of more extensive (and expensive) experimental studies.

Alcohol loss, particularly methanol due to its high vapour pressure, results in significant financial losses to the petroleum industry. Thus the knowledge of vapour content of methanol and ethanol rich methane is important. In this study a thorough literature review was conducted showing limitations in the data available in the open literature and their consistency. Substantial effort was placed on demonstrating the reliability of the results in this work. To evaluate the reliability of the calibration, three BOC certified gases were tested, with the results showing very good agreement with the measured values.

In response to the time constraints and technical issues only a limited number of methanol and ethanol rich methane isotherms were investigated. The data showed good agreement with the literature, however the CPA-SRK72 predictions illustrated some shortcomings at higher pressures.

Further experimental studies are recommended to help the understanding of methanol and ethanol phase behaviour in hydrocarbon systems. The solubility of methane can be measured in lower concentrations of alcohol aqueous solutions; however, it is important to note that this is only possible at higher pressures and lower temperatures due to hydrate formation. The solubility of other gaseous hydrocarbons in methanol/ethanol solution measurements can also help to further understand and improve multicomponent EoS phase behaviour predictions.

Saturation pressure measurements can be further utilised in systems with more than one heavy hydrocarbon phase, to investigate the effect of real fluids on inhibitor distribution and phase interactions. This study can be further extended to multicomponent ‘real’ natural gas systems. However, Vapour Liquid Equilibria (VLE) measurements using Gas Chromatography (GC) maybe more efficient for such measurements, albite more rigorous.

The effect of methanol/ethanol on the inhibition characteristics of MEG may also be considered. The addition of a more volatile component may improve the inhibition affect as well as its hydrate dissociation capabilities.

5.5 References

[1] H. Haghighi, PhD Thesis: Phase equilibria modelling of petroleum reservoir fluids containing water, Hydrate Inhibitors and Electrolyte Solutions, (2009).

[2] A. Chapoy, H. Haghighi, R. Burgass, B. Tohidi, On the phase behaviour of the (carbon dioxide+water) systems at low temperatures: Experimental and modelling, J. Chem. Thermodyn. 47 (2012) 6–12. doi:10.1016/j.jct.2011.10.026.

[3] A. Chapoy, R. Burgass, B. Tohidi, I. Alsiyabi, Hydrate and Phase Behavior Modeling in CO 2 -Rich Pipelines, J. Chem. Eng. Data. 60 (2015) 447–453. doi:10.1021/je500834t.

[4] H. Orbey, S.I. Sandler, Modeling Vapor-Liquid Equilibria: Cubic Equations of State and Their Mixing Rules, Volume 1, Cambridge University Press, 1998.

[5] B.E. Poling, J.M. Prausnitz, J.P. O'Connell, The properties of gases and liquids, McGraw-Hill, 2001.

[6] G.M. Kontogeorgis, E.C. Voutsas, I. V. Yakoumis, D.P. Tassios, An Equation of State for Associating Fluids, Ind. Eng. Chem. Res. 35 (1996) 4310–4318. doi:10.1021/ie9600203.

[7] G. Soave, Equilibrium constants from a modified Redlich-Kwong equation of state, Chem. Eng. Sci. 27 (1972) 1197–1203. doi:10.1016/0009-2509(72)80096-4.

[8] B. Hemmaplardh, A.D. King, Solubility of methanol in compressed nitrogen, argon, methane, ethylene, ethane, carbon dioxide, and nitrous oxide. Evidence for association of carbon dioxide with methanol in the gas phase, J. Phys. Chem. 76 (1972) 2170–2175. doi:10.1021/j100659a018.

[9] I. Krichevsky, M. Koroleva, The solubility of methanol in compressed gases, Acta Physicochim. URSS. 15 (1941) 327–342.

[10] E. Brunner, W. Hültenschmidt, G. Schlichthärle, Fluid mixtures at high pressures IV. Isothermal phase equilibria in binary mixtures consisting of (methanol + hydrogen or nitrogen or methane or carbon monoxide or carbon dioxide), J. Chem. Thermodyn. 19 (1987) 273–291. doi:10.1016/0021-9614(87)90135-2.

[11] J.H. Hong, P. V. Malone, M.D. Jett, R. Kobayashi, The measurement and interpretation of the fluid-phase equilibria of a normal fluid in a hydrogen bonding solvent: the methane - methanol system, Fluid Phase Equilib. 38 (1987) 83–96. doi:10.1016/0378-3812(87)90005-7.

[12] C. Lundstrøm, M.L. Michelsen, G.M. Kontogeorgis, K.S. Pedersen, H. Sørensen, Comparison of the SRK and CPA equations of state for physical properties of water and methanol, Fluid Phase Equilib. 247 (2006) 149–157. doi:10.1016/j.fluid.2006.06.012.

[13] L.E. Zerpa, E.D. Sloan, C. Koh, A. Sum, Hydrate Risk Assessment and Restart-Procedure Optimization of an Offshore Well Using a Transient Hydrate Prediction Model, Oil Gas Facil. 1 (2012) 49–56. doi:10.2118/160578-PA.

[14] P.A. Ferreira, M.F.C. Bezerra, R. Loschiavo, The Internal Corrosion Integrity Strategy on the Development of New Offshore Production Areas in Brazil, in: Offshore Technol. Conf., Offshore Technology Conference, 2013. doi:10.4043/16312-MS.

[15] P. Altoe Ferreira, The Internal Corrosion Integrity Strategy on the Development of New Offshore Production Areas in Brazil, SPE Prod. Facil. 20 (2005) 324–333. doi:10.2118/100155-PA.

[16] K. Suzuki, H. Sue, M. Itou, R.L. Smith, H. Inomata, K. Arai, et al., Isothermal vapor-liquid equilibrium data for binary systems at high pressures: carbon dioxide-methanol, carbon dioxide-ethanol, carbon dioxide-1-propanol, methane-ethanol, methane-1-propanol, ethane-ethanol, and ethane-1-propanol systems, J. Chem. Eng. Data. 35 (1990) 63–66. doi:10.1021/je00059a020.

[17] E. Brunner, W. Hültenschmidt, Fluid mixtures at high pressures VIII. Isothermal phase equilibria in the binary mixtures: (ethanol + hydrogen or methane or ethane), J. Chem. Thermodyn. 22 (1990) 73–84. doi:10.1016/0021-9614(90)90033-M.

[18] T. Ukai, D. Kodama, J. Miyazaki, M. Kato, Solubility of Methane in Alcohols and Saturated Density at 280.15 K, J. Chem. Eng. Data. 47 (2002) 1320–1323. doi:10.1021/je020108p.

[19] D.G. Friend, D.J. Frurip, E.W. Lemmon, R.E. Morrison, J.D. Olson, L.C. Wilson, Establishing benchmarks for the Second Industrial Fluids Simulation Challenge, Fluid Phase Equilib. 236 (2005) 15–24. doi:10.1016/j.fluid.2005.04.020.

Appendix A - *UNCERTAINTY OF CO_2 SOLUBILITY IN PURE GLYCOLS*

Appendix A shows the uncertainty calculation formulas used for the solubility of CO_2 in pure glycols.

Equation A.1 solubility of CO_2 in glycol.

$$x_i = \frac{\left[n^v_{CO_2} + n^l_{CO_2}\right] - n^v_{glc}}{\left[n^l_{glc} + n^v_{TEG}\right] + \left[n^v_{CO_2} + n^l_{CO_2}\right]} \tag{A.1}$$

Equation A.2 solubility of CO_2 in glycol with respect to volume

$$x_i = \frac{\left[(\rho_{CO_2} \times v_{CO_2}) + n^l_{CO_2}\right] - n^v_{glc}}{\left[n^l_{glc} + n^v_{glc}\right] + \left[(\rho_{CO_2} \times v_{CO_2}) + n^l_{CO_2}\right]} \tag{A.2}$$

Equation C.3 derivative of the solubility equation with respect to volume

$$\frac{\partial x_i}{\partial v} = \frac{\rho_{CO_2}(2 \times n^v_{glc} + n^l_{glc})}{\left[(\rho_{CO_2} \times v_{CO_2}) + n^l_{CO_2} + n^v_{glc} + n^l_{glc}\right]^2} \tag{A.3}$$

Equation A.4 solubility equation expressed with respect to mass of TEG.

$$x_i = \frac{n^v_{CO_2} + \left[n^l_{frac_{CO_2}} \times \frac{m}{150.17}\right] - n^v_{TEG}}{\left[n^l_{TEG} + n^v_{TEG}\right] + \left[n^v_{CO_2} + \left[n^l_{frac_{CO_2}} \times \frac{m}{150.17}\right]\right]} \tag{A.4}$$

Equation A.5 derivative of the solubility equation with respect to volume

$$\frac{\partial x_i}{\partial m} = \frac{150.17\left[-n^v_{CO_2} + \left(2 \times n^l_{frac_{CO_2}} \times n^v_{TEG}\right) + n^v_{TEG}\right]}{\left[\left(150.17 \times n^v_{CO_2}\right) + \left(n^l_{frac_{CO_2}} \times m\right) + \left(150.17 \times n^v_{TEG}\right) + m\right]^2} \tag{A.5}$$

Equation A.6 solubility of CO_2 in glycol with respect to mole fraction of glycol in the vapour phase

$$x_i = \frac{\left[n^v_{CO_2} + n^l_{CO_2}\right] - \left[n^{frac}_{glc} \times n^v_{CO_2}\right]}{\left[n^l_{glc} + \left[n^{frac}_{glc} \times n^v_{CO_2}\right]\right] + \left[n^v_{CO_2} + n^l_{CO_2}\right]} \tag{A.6}$$

Equation A.7 derivative of the solubility equation with respect to mole fraction of glycol in the vapour phase

$$\frac{\partial x_i}{\partial n_{glc}^{frac}} = \frac{n_{CO_2}^{v}\left[\left(2\times n_{CO_2}^{v}\right)+\left(2\times n_{CO_2}^{l}\right)+n_{glc}^{l}\right]}{\left[\left(n_{CO_2}^{v}\times n_{glc}^{frac}\right)+n_{CO_2}^{v}+n_{CO_2}^{l}+n_{glc}^{l}\right]} \tag{A.7}$$

Equation A.8 the solubility of CO_2 in glycol with respect to mole fraction of CO_2 in the liquid phase

$$x_i = \frac{n_{CO_2}^{v}+\left[n_{CO_2}^{frac}\times n_{glc}^{l}\right]-n_{glc}^{v}}{\left[n_{glc}^{l}+n_{glc}^{v}\right]+\left[n_{CO_2}^{v}+\left[n_{CO_2}^{frac}\times n_{glc}^{l}\right]\right]} \tag{A.8}$$

Equation A.9 derivative of the solubility equation with respect to mole fraction of CO_2 in the liquid phase

$$\frac{\partial x_i}{\partial n_{CO_2}^{frac}} = \frac{n_{glc}^{l}\times\left[n_{glc}^{l}+\left(2\times n_{glc}^{v}\right)\right]}{\left[n_{CO_2}^{v}+\left(n_{glc}^{l}\times n_{CO_2}^{frac}\right)+n_{glc}^{l}+n_{glc}^{v}\right]^2} \tag{A.9}$$

Appendix B – *UNCERTAINTY OF CO_2 SOLUBILITY IN GLYCOLS SOLUTIONS*

Appendix B shows the uncertainty calculation formulas used for the solubility of CO_2 in glycol aqueous solutions.

Equation B.1 used to calculate the solubility of CO_2 in glycol Solutions.

$$x_i = \frac{\left[n^v_{CO_2} + n^l_{CO_2}\right] - \left[n^v_{glc} + n^v_{water}\right]}{\left[n^l_{glc} + n^l_{water} + n^v_{glc} + n^v_{water} + n^v_{CO_2} + n^l_{CO_2}\right]} \tag{B.1}$$

Equation B.2 the solubility equation with respect to volume of the gas measured.

$$x_i = \frac{\left[\left(v_{CO_2} \times \rho_{CO_2}\right) + n^l_{CO_2}\right] - \left[n^v_{glc} + n^v_{water}\right]}{\left[n^l_{glc} + n^l_{water} + n^v_{glc} + n^v_{water}\right] + \left[\left(v_{CO_2} \times \rho_{CO_2}\right) + n^l_{CO_2}\right]} \tag{B.2}$$

Equation B.3 the derivative of the solubility equation with respect to volume

$$\frac{\partial x_i}{\partial v} = \frac{\rho_{CO_2}\left[\left(2 \times n^v_{glc}\right) + \left(2 \times n^v_{water}\right) + n^l_{glc} + n^l_{water}\right]}{\left[\left(v_{CO_2} \times \rho_{CO_2}\right) + n^l_{CO_2} + n^v_{glc} + n^v_{water} + n^l_{glc} + n^l_{water}\right]^2} \tag{B.3}$$

Equation B.4 the solubility equation with respect to the masses measured – MEG.

$$x_i = \frac{n^v_{CO_2}\left[\left(n^l_{frac_{CO_2}} \times \frac{m \times wt\%}{18.01}\right) + \left(n^l_{frac_{CO_2}} \times \frac{m \times wt\%}{62.07}\right) - \left(n^v_{MEG} + n^v_{water}\right)\right]}{\left[\left(\frac{m \times wt\%}{18.01}\right) + \left(\frac{m \times wt\%}{62.07}\right) + n^v_{MEG} + n^v_{water} + n^v_{CO_2} + \left(n^l_{frac_{CO_2}} \times \frac{m \times wt\%}{18.01}\right) + \left(n^l_{frac_{CO_2}} \times \frac{m \times wt\%}{62.07}\right)\right]} \tag{B.4}$$

Equation B.5 the derivative of the solubility equation with respect to mass – 90 wt% MEG.

$$\frac{\partial x_i}{\partial m} = \frac{-0.020 \times n^v_{CO_2} + \left(\left[\left(0.040 \times n^l_{frac_{CO_2}}\right) + 0.020\right] \times n^v_{MEG}\right) + \left(\left[\left(0.040 \times n^l_{frac_{CO_2}}\right) \times 0.020\right] \times n^v_{water}\right)}{\left[n^v_{CO_2} + \left[\left(0.020 \times n^l_{frac_{CO_2}}\right) \times m\right] + n^v_{MEG} + n^v_{water} + \left(0.020m\right)\right]^2} \tag{B.5}$$

Equation B.13B.6 the derivative of the solubility equation with respect to mass – 60 wt% MEG.

$$\frac{\partial x_i}{\partial m} = \frac{-0.032 \times n^v_{CO_2} + \left(\left[\left(0.064 \times n^l_{frac_{CO_2}}\right) + 0.032\right] \times n^v_{MEG}\right) + \left(\left[\left(0.064 \times n^l_{frac_{CO_2}}\right) \times 0.032\right] \times n^v_{water}\right)}{\left[n^v_{CO_2} + \left[\left(0.032 \times n^l_{frac_{CO_2}}\right) \times m\right] + n^v_{MEG} + n^v_{water} + \left(0.032m\right)\right]^2} \tag{B.6}$$

Equation B.7 the derivative of the solubility equation with respect to mass – 40 wt% MEG.

$$\frac{\partial x_i}{\partial m} = \frac{-0.040 \times n^v_{CO_2} + \left(\left[\left(0.079 \times n^l_{frac_{CO_2}}\right) + 0.040\right] \times n^v_{MEG}\right) + \left(\left[\left(0.079 \times n^l_{frac_{CO_2}}\right) \times 0.040\right] \times n^v_{water}\right)}{\left[n^v_{CO_2} + \left[\left(0.040 \times n^l_{frac_{CO_2}}\right) \times m\right] + n^v_{MEG} + n^v_{water} + \left(0.040m\right)\right]^2} \tag{B.7}$$

Equation B.8 the solubility equation with respect to the masses measured – DEG.

$$x_i = \frac{n^v_{CO_2}\left[\left(n^l_{frac_{CO_2}} \times \frac{m \times wt\%}{18.01}\right) + \left(n^l_{frac_{CO_2}} \times \frac{m \times wt\%}{106.12}\right) - \left(n^v_{DEG} + n^v_{water}\right)\right]}{\left[\left(\frac{m \times wt\%}{18.01}\right) + \left(\frac{m \times wt\%}{106.12}\right) + n^v_{DEG} + n^v_{water} + n^v_{CO_2} + \left(n^l_{frac_{CO_2}} \times \frac{m \times wt\%}{18.01}\right) + \left(n^l_{frac_{CO_2}} \times \frac{m \times wt\%}{106.12}\right)\right]} \tag{B.8}$$

Equation B.13B.9 the derivative of the solubility equation with respect to mass – 90 wt% DEG.

$$\frac{\partial x_i}{\partial m} = \frac{-0.014 \times n^v_{CO_2} + \left(\left[\left(0.028 \times n^l_{frac_{CO_2}}\right) + 0.014\right] \times n^v_{DEG}\right) + \left(\left[\left(0.028 \times n^l_{frac_{CO_2}}\right) \times 0.014\right] \times n^v_{water}\right)}{\left[n^v_{CO_2} + \left[\left(0.014 \times n^l_{frac_{CO_2}}\right) \times m\right] + n^v_{DEG} + n^v_{water} + \left(0.014m\right)\right]^2} \tag{B.9}$$

Equation B.10 the derivative of the solubility equation with respect to mass – 60 wt% DEG.

$$\frac{\partial x_i}{\partial m} = \frac{-0.028 \times n^v_{CO_2} + \left(\left[\left(0.056 \times n^l_{frac_{CO_2}}\right) + 0.028\right] \times n^v_{DEG}\right) + \left(\left[\left(0.056 \times n^l_{frac_{CO_2}}\right) \times 0.028\right] \times n^v_{water}\right)}{\left[n^v_{CO_2} + \left[\left(0.028 \times n^l_{frac_{CO_2}}\right) \times m\right] + n^v_{DEG} + n^v_{water} + \left(0.028m\right)\right]^2} \tag{B.10}$$

Equation B.11 the derivative of the solubility equation with respect to mass – 40 wt% DEG.

$$\frac{\partial x_i}{\partial m} = \frac{-0.037 \times n^v_{CO_2} + \left(\left[\left(0.074 \times n^l_{frac_{CO_2}}\right) + 0.037\right] \times n^v_{DEG}\right) + \left(\left[\left(0.074 \times n^l_{frac_{CO_2}}\right) \times 0.037\right] \times n^v_{water}\right)}{\left[n^v_{CO_2} + \left[\left(0.037 \times n^l_{frac_{CO_2}}\right) \times m\right] + n^v_{DEG} + n^v_{water} + \left(0.037m\right)\right]^2} \tag{B.11}$$

Equation B.12 the solubility equation with respect to the masses measured – TEG.

$$x_i = \frac{n^v_{CO_2}\left[\left(n^l_{frac_{CO_2}} \times \frac{m \times wt\%}{18.01}\right) + \left(n^l_{frac_{CO_2}} \times \frac{m \times wt\%}{150.17}\right) - \left(n^v_{TEG} + n^v_{water}\right)\right]}{\left[\left(\frac{m \times wt\%}{18.01}\right) + \left(\frac{m \times wt\%}{150.17}\right) + n^v_{TEG} + n^v_{water} + n^v_{CO_2} + \left(n^l_{frac_{CO_2}} \times \frac{m \times wt\%}{18.01}\right) + \left(n^l_{frac_{CO_2}} \times \frac{m \times wt\%}{150.17}\right)\right]} \tag{B.12}$$

Equation B.13 the derivative of the solubility equation with respect to mass – 90 wt% TEG.

$$\frac{\partial x_i}{\partial m} = \frac{-0.011 \times n^v_{CO_2} + \left(\left[\left(0.023 \times n^l_{frac_{CO_2}}\right) + 0.011\right] \times n^v_{TEG}\right) + \left(\left[\left(0.023 \times n^l_{frac_{CO_2}}\right) \times 0.011\right] \times n^v_{water}\right)}{\left[n^v_{CO_2} + \left[\left(0.011 \times n^l_{frac_{CO_2}}\right) \times m\right] + n^v_{TEG} + n^v_{water} + \left(0.011m\right)\right]^2} \tag{B.13}$$

Equation B.14 the derivative of the solubility equation with respect to mass – 60 wt% TEG.

$$\frac{\partial x_i}{\partial m} = \frac{-0.026 \times n_{CO_2}^{v} + \left(\left[\left(0.052 \times n_{frac_{CO_2}}^{l}\right) + 0.026\right] \times n_{TEG}^{v}\right) + \left(\left[\left(0.052 \times n_{frac_{CO_2}}^{l}\right) \times 0.026\right] \times n_{water}^{v}\right)}{\left[n_{CO_2}^{v} + \left[\left(0.026 \times n_{frac_{CO_2}}^{l}\right) \times m\right] + n_{TEG}^{v} + n_{water}^{v} + \left(0.026m\right)\right]^2} \tag{B.14}$$

Equation B.15 the derivative of the solubility equation with respect to mass – 40 wt% TEG.

$$\frac{\partial x_i}{\partial m} = \frac{-0.036 \times n_{CO_2}^{v} + \left(\left[\left(0.072 \times n_{frac_{CO_2}}^{l}\right) + 0.036\right] \times n_{TEG}^{v}\right) + \left(\left[\left(0.072 \times n_{frac_{CO_2}}^{l}\right) \times 0.036\right] \times n_{water}^{v}\right)}{\left[n_{CO_2}^{v} + \left[\left(0.036 \times n_{frac_{CO_2}}^{l}\right) \times m\right] + n_{TEG}^{v} + n_{water}^{v} + \left(0.036m\right)\right]^2} \tag{B.15}$$

Equation B.16 the solubility equation with respect to the mole glycol in the vapour phase

$$x_i = \frac{n_{CO_2}^{v} + n_{CO_2}^{l} - \left[\left(n_{glc}^{frac} \times n_{CO_2}^{v}\right) + n_{water}^{v}\right]}{\left[n_{glc}^{l} + n_{water}^{l}\right] + \left[\left(n_{glc}^{frac} \times n_{CO_2}^{v}\right) + n_{water}^{v} + n_{CO_2}^{v} + n_{CO_2}^{l}\right]} \tag{B.16}$$

Equation B.16B.17 the derivative of the solubility equation with respect to the mole glycol in the vapour phase.

$$\frac{\partial x_i}{\partial n_{glc}^{frac}} = \frac{n_{CO_2}^{v}\left[\left(n_{CO_2}^{v} \times n_{CO_2}^{l}\right) + n_{CO_2}^{v} + n_{CO_2}^{l} + \left(2 \times n_{water}^{v}\right) + n_{glc}^{l} + n_{water}^{l}\right]}{\left[n_{CO_2}^{v}\left(n_{CO_2}^{l} + n_{glc}^{frac}\right) + n_{water}^{v} + n_{glc}^{l} + n_{water}^{l}\right]^2} \tag{B.17}$$

Equation B.18 the solubility equation with respect to the mole water in the vapour phase.

$$x_i = \frac{n_{CO_2}^{v} + n_{CO_2}^{l} - \left[\left(n_{water}^{frac} \times n_{CO_2}^{v}\right) + n_{glc}^{v}\right]}{\left[n_{glc}^{l} + n_{water}^{l}\right] + \left[\left(n_{water}^{frac} \times n_{CO_2}^{v}\right) + n_{glc}^{v} + n_{CO_2}^{v} + n_{CO_2}^{l}\right]} \tag{B.18}$$

Equation B.19 derivative of the solubility equation with respect to the mole water in the vapour phase.

$$\frac{\partial x_i}{\partial n_{Water}^{frac}} = \frac{n_{CO_2}^{v}\left[\left(n_{CO_2}^{v} \times n_{CO_2}^{l}\right) + n_{CO_2}^{v} + n_{CO_2}^{l} + \left(2 \times n_{glc}^{v}\right) + n_{glc}^{l} + n_{water}^{l}\right]}{\left[n_{CO_2}^{v}\left(n_{CO_2}^{l} + n_{Water}^{frac}\right) + n_{glc}^{v} + n_{glc}^{l} + n_{water}^{l}\right]^2} \tag{B.19}$$

Equation B.20 the solubility equation with respect to the mole of CO_2 in the liquid glycol phase

$$x_i = \frac{n_{CO_2}^{v} + \left(n_{frac}^{CO_2} \times n_{glc}^{l}\right) + n_{CO_2}^{water} - \left(n_{glc}^{v} + n_{water}^{v}\right)}{n_{glc}^{v} + n_{glc}^{l} + n_{water}^{l} + n_{water}^{v} + n_{CO_2}^{v} + n_{CO_2}^{water} + \left(n_{frac}^{CO_2} \times n_{glc}^{l}\right)} \tag{B.20}$$

Equation B.21 the derivative of the solubility equation with respect to the mole CO_2 in the liquid glycol phase

$$\frac{\partial x_i}{\partial n_{CO_2}^{glc}} = \frac{n_{glc}^{l}\left[n_{glc}^{l} + \left(2 \times n_{glc}^{v}\right) + \left(2 \times n_{water}^{v}\right) + n_{water}^{l}\right]}{\left[n_{CO_2}^{v} + \left(n_{frac}^{CO_2} \times n_{glc}^{l}\right) + n_{glc}^{l} + n_{CO_2}^{water} + n_{glc}^{v} + n_{water}^{v} + n_{water}^{l}\right]^2} \tag{B.21}$$

Equation B.22 the solubility equation with respect to the mole of CO_2 in the liquid water phase

$$x_i = \frac{n_{CO_2}^{v} + \left(n_{frac}^{CO_2} \times n_{water}^{l}\right) + n_{CO_2}^{glc} - \left(n_{glc}^{v} + n_{water}^{v}\right)}{n_{glc}^{v} + n_{glc}^{l} + n_{water}^{l} + n_{water}^{v} + n_{CO_2}^{v} + n_{CO_2}^{glc} + \left(n_{frac}^{CO_2} \times n_{water}^{l}\right)} \tag{B.22}$$

Equation B.23 the derivative of the solubility equation with respect to the mole of CO2 in the liquid water phase

$$\frac{\partial x_i}{\partial n_{CO_2}^{H_2O}} = \frac{n_{water}^{l}\left[n_{water}^{l} + \left(2 \times n_{glc}^{v}\right) + \left(2 \times n_{water}^{v}\right) + n_{water}^{l}\right]}{\left[n_{CO_2}^{v} + \left(n_{frac}^{CO_2} \times n_{water}^{l}\right) + n_{water}^{l} + n_{CO_2}^{glc} + n_{glc}^{v} + n_{water}^{v} + n_{water}^{l}\right]^2} \tag{B.23}$$

Equation B.24 combined uncertainty equation

$$u(x_i) = \sqrt{\left(\left(\frac{x_i}{\partial v}^2 \times u_v^{\,2}\right) + \left(\frac{x_i}{\partial m}^2 \times u_m^{\,2}\right) + \left(\frac{\partial x_i}{\partial n_{glc}^{frac}}^2 \times u_{\frac{frac}{glc}}^{\,2}\right) + u_{rep}(\mathrm{x}_i)^2 \ldots \left(\frac{\partial x_i}{\partial n_{Water}^{frac}}^2 \times u_{\frac{frac}{Water}}^{\,2}\right) + \left(\frac{\partial x_i}{\partial n_{CO_2}^{glc}}^2 \times u_{\frac{glc}{CO_2}}^{\,2}\right) + \left(\frac{\partial x_i}{\partial n_{CO_2}^{H_2O}}^2 \times u_{\frac{H_2O}{CO_2}}^{\,2}\right)\right)} \tag{B.24}$$

Standard uncertainty in gas meter volume measurements, u(v) = 0.005 l

Relative standard uncertainty in balance $u_r(m)$ = 0.01 g

$u_r\left(n_{CO_2}^{frac}\right)$ = Relative standard uncertainty in CPA-SRK72 mol fraction calculation of CO_2 in Liquid = 0.05

$u_r\left(n_{glc}^{frac}\right)$ = Relative standard uncertainty in CPA-SRK72 mol fraction calculation of TEG in CO_2 = 0.05

Standard uncertainty of NIST CO_2 density data u(ρ) = 0.00003 (deemed negligible)

Standard uncertainty due to random error (repeatability), = $u_{rep}(x_i)$ = 0.025 [104]

Nomenclature for the uncertainty Equation calculations in this appendix.

x_i Solubility of CO_2 in TEG

$n_{CO_2}^{v}$ Mole of CO_2 in the vapour phase

$n^{l}_{CO_2}$ Mole of CO_2 in the liquid phase

n^{v}_{glc} Mole of glycol in the vapour phase

n^{v}_{water} Mole of water in the vapour phase

n^{l}_{glc} Mole of glycol in the liquid phase

n^{l}_{water} Mole of water in the liquid phase

v_{CO_2} Volume of CO_2

ρ_{CO_2} Density of CO_2

m Mass of glycol/glycol Solution

$n^{l}_{frac_{CO_2}}$ mole fraction of CO2 in glycol calculated using the CPA-SRK72 EoS.

n^{frac}_{glc} mole fraction of glycol in the CO_2 (gas meter) calculated using the CPA-SRK72

n^{frac}_{water} mole fraction of water in the CO_2 (gas meter) calculated using the CPA-SRK72

u_c Cumulative uncertainty [130]

u_v Uncertainty contribution by the gas meter volume as reported by the manufacturer

u_m Uncertainty contribution by the balance as reported by the manufacturer

$u_{\substack{frac \\ glc}}$ Uncertainty contribution by the mole fraction (CPA-SRK72 calculation) of glycol in the vapour phase

$u_{\substack{frac \\ Water}}$ Uncertainty contribution by the mole fraction (CPA-SRK72 calculation) of water in the vapour phase

$u_{\substack{glc \\ CO_2}}$ Uncertainty contribution by the mole fraction (CPA-SRK72 calculation) of CO_2 in glycol

$u_{\substack{H_2O \\ CO_2}}$ Uncertainty contribution by the mole fraction (CPA-SRK72 calculation) of CO_2 in water

Appendix C – UNCERTAINTY OF CH_4 SOLUBILITY IN PURE ALCOHOLS

This section describes the uncertainty analysis calculations undertaken for the solubility of Methane in Alcohols. Table C.1 describes the various parameters used in the equations in this appendix.

Eq. C.1 is used to calculate the solubility of CH_4 in methanol/ethanol.

$$x_i = \frac{\left[n^v_{CH_4} + n^l_{CH_4} \right] - n^v_{EtOH}}{n^l_{EtOH} + n^v_{EtOH} + n^v_{CH_4} + n^l_{CH_4}} \tag{C.1}$$

Eq. C.2 demonstrates the solubility calculation in respect to the volume measured.

$$x_i = \frac{\left[(v_{CH_4} \times \rho_{CH_4}) + n^l_{CH_4} \right] - n^v_{EtOH}}{n^l_{EtOH} + n^v_{EtOH} + (v_{CH_4} \times \rho_{CH_4}) + n^l_{CH_4}} \tag{C.2}$$

Eq. C.3 is the derivative of the solubility equation with respect to volume, v.

$$\frac{\partial x_i}{\partial v} = \frac{\rho_{CH_4}(2 \times n^v_{EtOH} + n^l_{EtOH})}{\left[(v_{CH\,4} \times \rho_{CH_4}) + n^l_{CH_4} + n^v_{EtOH} + n^l_{EtOH} \right]^2} \tag{C.3}$$

Eq. C.4 shows the solubility equation with respect to mass, m – ethanol.

$$x_i = \frac{n^v_{CH_4} + \left(n^l_{frac_{CH_4}} \times \frac{m_{EtOH}}{46} \right) - n^v_{EtOH}}{\frac{m_{EtOH}}{46} + n^v_{EtOH} + n^v_{CH_4} + \left(n^l_{frac_{CH_4}} \times \frac{m_{EtOH}}{46} \right)} \tag{C.4}$$

Eq. C.5 shows the derivative of the solubility equation with respect to mass – ethanol.

$$\frac{\partial x_i}{\partial m} = \frac{46\left(-n^v_{CH_4} + \left[2 \times n^l_{frac_{CH_4}} \times n^v_{EtOH} \right] + n^v_{EtOH} \right)}{\left[\left(46 \times n^v_{CH_4} \right) + \left(n^l_{frac_{CH_4}} \times m \right) + \left(46 \times n^v_{EtOH} \right) + m \right]^2} \tag{C.5}$$

Eq. C.6 shows the solubility equation with respect to the mole fraction of CH_4 in liquid ethanol/methanol at atmospheric pressure.

$$x_i = \frac{n^v_{CH_4} + \left[n^{frac}_{CH_4} \times n^l_{EtOH} \right] - n^v_{EtOH}}{n^l_{EtOH} + n^v_{EtOH} + \left[n^v_{CH_4} + \left[n^{frac}_{CH_4} \times n^l_{EtOH} \right] \right]} \tag{C.6}$$

Eq. C.7 shows the derivative of the equation with respect to the mole fraction of CH_4 in liquid ethanol at atmospheric pressure.

$$\frac{\partial x_i}{\partial n_{CH_4}^{frac}} = \frac{n_{EtOH}^{l}\left(n_{EtOH}^{l} + \left[2 \times n_{EtOH}^{v}\right]\right)}{\left[n_{CH_4}^{v} + \left(n_{EtOH}^{l} \times n_{CH_4}^{frac}\right) + n_{EtOH}^{l} + n_{EtOH}^{v}\right]^2} \tag{C.7}$$

Eq. C.8 shows the solubility equation with respect to the mole fraction of methanol/ethanol in gaseous CH_4 phase at atmospheric pressure.

$$x_i = \frac{n_{CH_4}^{v} + n_{CH_4}^{l} - \left[n_{EtOH}^{frac} \times n_{v}^{CH_4}\right]}{n_{EtOH}^{l} + \left[n_{EtOH}^{frac} \times n_{CH_4}^{v}\right] + n_{CH_4}^{v} + n_{CH_4}^{l}} \tag{C.8}$$

Eq. C.9 shows the derivative of the equation with respect to the mole fraction of methanol/ethanol in gaseous CH_4 phase at atmospheric pressure.

$$\frac{\partial x_i}{\partial n_{EtOH}^{frac}} = \frac{n_{CH_4}^{v}\left(2 \times n_{CH_4}^{v} + 2 \times n_{CH_4}^{l} + n_{EtOH}^{l}\right)}{\left[\left(n_{CH_4}^{v} \times n_{EtOH}^{frac}\right) + n_{CH_4}^{v} + n_{CH_4}^{l} n_{EtOH}^{l}\right]^2} \tag{C.9}$$

Standard uncertainty in gas meter volume measurements, u(v) = 0.0005 liters

Relative standard uncertainty in balance $u_r(m) = 0.005$

$u_r\left(n_{CH_4}^{frac}\right)$ = Relative standard uncertainty in CPA-SRK72 mol fraction calculation (optimized) of CH_4 in Liquid = 0.05

$u_r\left(n_{EtOH}^{frac}\right)$ = Relative standard uncertainty in CPA-SRK72 mol fraction calculation (optimized – limited data) of alcohol in CH_4 = 0.05

Standard uncertainty in NIST CH_4 density $u_r(\rho) = 0.0003$ (deemed negligible)

Standard uncertainty due to random error (repeatability), $u_{rep}(x_i) = 0.025$

Eq. C.10 Cumulative uncertainty equation

$$u(x_i) = \sqrt{\left(\begin{array}{l}\frac{\partial x_i}{\partial v}^2 \times u(v)^2 + \left(\frac{\partial x_i}{\partial m}^2 \times u_r(m)^2\right) + \left(\frac{\partial x_i}{\partial n_{CH_4}^{frac}} \times u_r\left(n_{CH_4}^{frac}\right)\right) + \\ \left(\frac{\partial x_i}{\partial n_{EtOH}^{frac}} \times u_r\left(n_{EtOH}^{frac}\right)\right) + u_{rep}(x_i)^2\end{array}\right)} \tag{C.10}$$

Equation Substitution

Eq. C.11 used to calculate mole of CH_4 in the vapour phase of the flash tank

$$n_{CH_4}^{v} = (v_{CH_4} \times \rho_{CH_4}) \tag{C.11}$$

Eq. C.12 used to calculate the mole of CH_4 in the liquid phase of the flash tank

$$n_{CH_4}^{l} = \left(n_{frac_{CH_4}}^{l} \times \frac{m_{EtOH}}{46} \right) \tag{C.12}$$

Eq. C.13 used to calculate the mole of ethanol/methanol in the vapour phase of the flash tank

$$n_{EtOH}^{v} = \left(n_{EtOH}^{frac} \times n_{v}^{CH_4} \right) \tag{C.13}$$

Eq. C.14 shows the equation used to calculate the mole of ethanol in the liquid phase of the flash tank

$$n_{EtOH}^{l} = \frac{m_{EtOH}}{46} \tag{C.14}$$

Table C.1 Nomenclature

x_i	Solubility of CH_4 in methanol/ethanol (mol/mol)
$n_{CH_4}^{v}$	Mole of CH_4 in the vapour phase
$n_{CH_4}^{l}$	Mole of CH_4 in the liquid phase
n_{EtOH}^{v}	Mole of ethanol/methanol in the vapour phase
n_{EtOH}^{l}	Mole of Ethanol/Methanol in the liquid phase
v_{CH_4}	Volume of CH_4
ρ_{CH_4}	Density of CH_4
m_{EtOH}	Mass of ethanol/methanol
$n_{CH_4}^{frac}$	Mole fraction of CH_4 in the alcohol calculated using the CPA-SRK72 EoS.
n_{EtOH}^{frac}	Mole fraction of Ethanol/methanol in the CH_4 (gas meter) calculated using the CPA-SRK72
$u_r(x_i)$	Cumulative standard uncertainty
$u(v)$	Standard Uncertainty contribution by the gas meter volume as reported by the manufacturer
$u_r(m)$	Relative standard uncertainty contribution by the balance as reported by the manufacturer
$u_r(n_{CH_4}^{frac})$	Standard uncertainty contribution by the mole fraction CPA-SRK72 (optimised) calculation of CH_4 in the liquid phase
$u_r\left(n_{EtOH}^{frac}\right)$	Standard uncertainty contribution by the mole fraction CPA-SRK72 (optimised – limited data)calculation of alcohol in the vapour phase

Appendix D – UNCERTAINTY OF CH_4 SOLUBILITY IN ALCOHOL SOLUTIONS

Eq. D.1 is used to calculate the solubility of CH_4 in the methanol/ethanol solutions.

$$x_i = \frac{\left[n^v_{CH_4} + n^l_{CH_4}\right] - \left[n^v_{EtOH} - n^v_{water}\right]}{n^l_{EtOH} + n^l_{water} + n^v_{EtOH} + n^v_{CH_4} + n^l_{CH_4} + n^v_{water}} \tag{D.1}$$

Eq. D.2 demonstrates the solubility calculation in respect to the volume measured.

$$x_i = \frac{\left[(v_{CH_4} \times \rho_{CH_4}) + n^l_{CH_4}\right] - \left[n^v_{EtOH} - n^v_{water}\right]}{n^l_{EtOH} + n^l_{water} + n^v_{EtOH} + (v_{CH_4} \times \rho_{CH_4}) + n^l_{CH_4} + n^v_{water}} \tag{D.2}$$

Eq. D.3 is the derivative of the solubility equation with respect to volume, v.

$$\frac{\partial x_i}{\partial v} = \frac{\rho_{CH_4}\left[\left(2 \times n^v_{EtOH}\right) + \left(2 \times n^v_{water}\right) + n^l_{EtOH} + n^l_{water}\right]}{\left[(v_{CH4} \times \rho_{CH_4}) + n^l_{CH_4} + n^v_{EtOH} + n^v_{water} + n^l_{EtOH} + n^l_{water}\right]^2} \tag{D.3}$$

Eq. D.4 shows the solubility equation with respect to mass, m – CH_4 in methanol solution.

$$x_i = \frac{n^v_{CH_4} + \left[\left(n^l_{frac_{CH_4}} \times \frac{m}{32.04} \times wt\%\right) + \left(n^l_{frac_{CH_4}} \times \frac{m}{18} \times wt\%\right)\right] - \left[n^v_{MeOH} + n^v_{water}\right]}{n^v_{water} + \left(\frac{m}{32.04} \times wt\%\right) + \left(\frac{m}{18} \times wt\%\right) + n^v_{MeOH} + n^v_{CH_4} + \left[\left(n^l_{frac_{CH_4}} \times \frac{m}{32.04} \times wt\%\right) + \left(n^l_{frac_{CH_4}} \times \frac{m}{18} \times wt\%\right)\right]} \tag{D.4}$$

Eq. D.5 shows the derivative of the solubility equation with respect to mass – 0.7 wt% MeOH.

$$\frac{\partial x_i}{\partial m} = \frac{-0.038 \times n^v_{CH_4} + n^v_{MeOH} \times \left(0.077 \times n^l_{frac_{CH_4}} + 0.038\right) + n^v_{water} \times \left(0.077 \times n^l_{frac_{CH_4}} + 0.038\right)}{\left[n^v_{CH_4} + \left(0.038 \times n^l_{frac_{CH_4}} \times m\right) + n^v_{MeOH} + n^v_{water} + 0.038m\right]^2} \tag{D.5}$$

Eq. D.6 shows the solubility equation with respect to mass, m – CH_4 in ethanol solution.

$$x_i = \frac{n^v_{CH_4} + \left[\left(n^l_{frac_{CH_4}} \times \frac{m}{46} \times wt\%\right) + \left(n^l_{frac_{CH_4}} \times \frac{m}{18} \times wt\%\right)\right] - \left[n^v_{EtOH} + n^v_{water}\right]}{n^v_{water} + \left(\frac{m}{46} \times wt\%\right) + \left(\frac{m}{18} \times wt\%\right) + n^v_{EtOH} + n^v_{CH_4} + \left[\left(n^l_{frac_{CH_4}} \times \frac{m}{46} \times wt\%\right) + \left(n^l_{frac_{CH_4}} \times \frac{m}{18} \times wt\%\right)\right]} \tag{D.6}$$

Eq. D.7 shows the derivative of the solubility equation with respect to mass – 0.7 wt% EtOH.

$$\frac{\partial x_i}{\partial m} = \frac{-0.032 \times n^{v}_{CH_4} + n^{v}_{EtOH} \times \left(0.064 \times n^{l}_{frac_{CH_4}} + 0.032\right) + n^{v}_{water} \times \left(0.064 \times n^{l}_{frac_{CH_4}} + 0.032\right)}{\left[n^{v}_{CH_4} + \left(0.032 \times n^{l}_{frac_{CH_4}} \times m\right) + n^{v}_{EtOH} + n^{v}_{water} + 0.032m\right]^2} \quad \text{(D.7)}$$

Eq. D.8 shows the derivative of the solubility equation with respect to mass – 0.5 wt% EtOH.

$$\frac{\partial x_i}{\partial m} = \frac{-0.039 \times n^{v}_{CH_4} + n^{v}_{EtOH} \times \left(0.077 \times n^{l}_{frac_{CH_4}} + 0.039\right) + n^{v}_{water} \times \left(0.077 \times n^{l}_{frac_{CH_4}} + 0.039\right)}{\left[n^{v}_{CH_4} + \left(0.039 \times n^{l}_{frac_{CH_4}} \times m\right) + n^{v}_{EtOH} + n^{v}_{water} + 0.039m\right]^2} \quad \text{(D.8)}$$

Eq. D.9 shows the solubility equation with respect to the mole fraction of CH_4 in liquid methanol/ethanol at atmospheric pressure.

$$x_i = \frac{n^{v}_{CH_4} + \left[n^{frac}_{CH_4} \times n^{l}_{EtOH}\right] + n^{water}_{CH_4} - \left[n^{v}_{EtOH} + n^{v}_{water}\right]}{\left[n^{l}_{EtOH} + n^{v}_{EtOH} + n^{l}_{water} + n^{v}_{water}\right] + \left[n^{v}_{CH_4} + n^{water}_{CH_4} + \left[n^{frac}_{CH_4} \times n^{l}_{EtOH}\right]\right]} \quad \text{(D.9)}$$

Eq. D.10 shows the derivative of the equation with respect to the mole fraction of CH_4 in liquid methanol/ethanol at atmospheric pressure.

$$\frac{\partial x_i}{\partial n^{EtOH}_{CH_4}} = \frac{n^{l}_{EtOH} \times \left(n^{l}_{EtOH} + \left[2 \times n^{v}_{EtOH}\right] + \left[2 \times n^{v}_{water}\right] + n^{l}_{water}\right)}{\left[n^{v}_{CH_4} + \left(n^{l}_{EtOH} \times n^{frac}_{CH_4}\right) + n^{l}_{EtOH} + n^{water}_{CH_4} + n^{v}_{EtOH} + n^{v}_{water} + n^{l}_{water}\right]^2} \quad \text{(D.10)}$$

Eq. D.11 shows the solubility equation with respect to the mole fraction of CH_4 in liquid methanol/ethanol at atmospheric pressure.

$$x_i = \frac{n^{v}_{CH_4} + \left[n^{frac}_{CH_4} \times n^{l}_{water}\right] + n^{EtOH}_{CH_4} - \left[n^{v}_{EtOH} + n^{v}_{water}\right]}{\left[n^{l}_{EtOH} + n^{v}_{EtOH} + n^{l}_{water} + n^{v}_{water}\right] + \left[n^{v}_{CH_4} + n^{EtOH}_{CH_4} + \left[n^{frac}_{CH_4} \times n^{l}_{water}\right]\right]} \quad \text{(D.11)}$$

Eq. D.12 shows the derivative of the equation with respect to the mole fraction of CH_4 in liquid water at atmospheric pressure.

$$\frac{\partial x_i}{\partial n^{water}_{CH_4}} = \frac{n^{l}_{water} \times \left(n^{l}_{water} + \left[2 \times n^{v}_{EtOH}\right] + \left[2 \times n^{v}_{water}\right] + n^{l}_{water}\right)}{\left[n^{v}_{CH_4} + \left(n^{l}_{water} \times n^{frac}_{CH_4}\right) + n^{l}_{water} + n^{EtOH}_{CH_4} + n^{v}_{EtOH} + n^{v}_{water} + n^{l}_{water}\right]^2} \quad \text{(D.12)}$$

Eq. D.13 shows the solubility equation with respect to the mole fraction of methanol/ethanol in gaseous CH_4 phase at atmospheric pressure.

$$x_i = \frac{n^v_{CH_4} + n^l_{CH_4} - \left[\left[n^{frac}_{EtOH} \times n^{CH_4}_v\right] + n^v_{water}\right]}{\left[n^l_{EtOH} + n^l_{water}\right] + \left[\left[n^{frac}_{EtOH} \times n^v_{CH_4}\right] + n^v_{water}\right] + \left[n^v_{CH_4} + n^l_{CH_4}\right]} \tag{D.13}$$

Eq. D.14 shows the derivative of the equation with respect to the mole fraction of methanol/ethanol in gaseous CH_4 phase at atmospheric pressure.

$$\frac{\partial x_i}{\partial n^{frac}_{EtOH}} = \frac{n^v_{CH_4} \times \left[\left(n^v_{CH_4} \times n^l_{CH_4}\right) + n^v_{CH_4} + n^l_{CH_4} + \left(2 \times n^v_{water}\right) + n^l_{EtOH} + n^l_{water}\right]}{\left[n^v_{CH_4} \times \left(n^l_{CH_4} + n^{frac}_{EtOH}\right) + n^v_{water} + n^l_{EtOH} + n^l_{water}\right]^2} \tag{D.14}$$

Eq. D.15 shows the solubility equation with respect to the mole fraction of ethanol in gaseous CH_4 phase at atmospheric pressure.

$$x_i = \frac{n^v_{CH_4} + n^l_{CH_4} - \left[\left[n^{frac}_{water} \times n^{CH_4}_v\right] + n^v_{EtOH}\right]}{\left[n^l_{EtOH} + n^l_{water}\right] + \left[\left[n^{frac}_{water} \times n^v_{CH_4}\right] + n^v_{EtOH}\right] + \left[n^v_{CH_4} + n^l_{CH_4}\right]} \tag{D.15}$$

Eq. D.16 shows the derivative of the equation with respect to the mole fraction of methanol/ethanol in gaseous CH_4 phase at atmospheric pressure.

$$\frac{\partial x_i}{\partial n^{frac}_{water}} = \frac{n^v_{CH_4} \times \left[\left(n^v_{CH_4} \times n^l_{CH_4}\right) + n^v_{CH_4} + n^l_{CH_4} + \left(2 \times n^v_{EtOH}\right) + n^l_{EtOH} + n^l_{water}\right]}{\left[n^v_{CH_4} \times \left(n^l_{CH_4} + n^{frac}_{water}\right) + n^v_{EtOH} + n^l_{EtOH} + n^l_{water}\right]^2} \tag{D.16}$$

Standard uncertainty in gas meter volume measurements, u(v) = 0.0005 litres

Relative standard uncertainty in balance $u_r(m) = 0.005$

$u_r\left(n^{frac}_{CH_4}\right)$ = Relative standard uncertainty in CPA-SRK72 mol fraction calculation (optimised) of CH_4 in Liquid = 0.05

$u_r\left(n^{frac}_{EtOH}\right)$ = Relative standard uncertainty in CPA-SRK72 mol fraction calculation (optimised – limited data) of alcohol in CH_4 = 0.05

Standard uncertainty in NIST CH_4 density $u_r(\rho) = 0.0003$ (deemed negligible)

Standard uncertainty due to random error (repeatability), $u_{rep}(x_i) = 0.025$

Eq. D.17 Cumulative uncertainty equation

$$u(x_i) = \sqrt{\begin{array}{l} \left(\frac{\partial x_i}{\partial v}\right)^2 \times u(v)^2 + \left(\left(\frac{\partial x_i}{\partial m}\right)^2 \times u_r(m)^2\right) + \left(\left(\frac{\partial x_i}{\partial n_{CH_4}^{EtOH}}\right)^2 \times u_r\left(n_{CH_4}^{EtOH}\right)^2\right) + \ldots \\ \left(\left(\frac{\partial x_i}{\partial n_{CH_4}^{water}}\right)^2 \times u_r\left(n_{CH_4}^{water}\right)^2\right) + \left(\left(\frac{\partial x_i}{\partial n_{EtOH}^{frac}}\right)^2 \times u_r\left(n_{EtOH}^{frac}\right)^2\right) + \ldots \\ \left(\left(\frac{\partial x_i}{\partial n_{water}^{frac}}\right)^2 \times u_r\left(n_{water}^{frac}\right)^2\right) + u_{rep}(x_i)^2 \end{array}} \qquad \text{(D.17)}$$

Appendix E – LINEAR UNCERTAINTY OF VAPOUR CONTENT AND SATURATION PRESSURE MEASUREMENTS

The expanded uncertainties of the methanol/ethanol rich methane were determined by calculating the variances that are associated with the slope and intercept of the calibration linear fits and combined using Pythagorean means.

Ordinary least squares calculations were used in this work. The sum of the squared errors between the line of best fit and the data were calculated and the value was minimised.

(x_i,y_i) represent the experimental data that the line fits.

Eq. E.1 is used to calculate the mean of y_I and Eq. E.2 is the linear model being fitted.

$$\bar{y} \equiv \left(\sum_{i=1}^{n} y_i\right) / n \tag{E.1}$$

$$\hat{y}(x) = \hat{m}x + \hat{b} \tag{E.2}$$

Eq. E.3 is used to determine the total Sum of Squares.

$$SS_T = SS_{yy} \equiv \sum_{i=1}^{n} \left(y_i - \bar{y}\right)^2 \tag{E.3}$$

Eq. E.4 is used to calculate the Error Sum of Squared error between the data and the line of best fit (F.2).

$$SS_E = \sum_{i=1}^{n} \left(y_i - \hat{y}\right)^2 \tag{E.4}$$

Eq. E.5 is used to calculate the Error Sum of Squares, the difference between SS_T and SS_E, which represents the portion of the total sum of squares that can be explained by the linear model.

$$SS_R \equiv SS_T - SS_E \tag{E.5}$$

Eq. E.6 computes the sums of squares for x.

$$SS_{xx} \equiv \sum_{i=1}^{n} \left(x_i - \bar{x}\right)^2 \tag{E.6}$$

Eq. E.7 is used to calculate the cross product sums of squares for xy.

$$SS_{xy} \equiv \sum_{i=1}^{n} \left(x_i - \bar{x}\right)\left(y_i - \bar{y}\right) \tag{E.7}$$

Where:

$$\bar{x} \equiv \left(\sum_{i=1}^{n} x_i\right) / n \tag{E.8}$$

Eq. E.9 is used to calculate the slope of the ordinary least squares line of best fit.

$$\hat{m} = \frac{n\sum_{i=1}^{n} x_i y_i - \left(\sum_{i=1}^{n} x_i\right)\left(\sum_{i=1}^{n} y_i\right)}{n\sum_{i=1}^{n} {x_i}^2 - \left(\sum_{i=1}^{n} x_i\right)^2} = \frac{SS_{xy}}{SS_{xx}} \tag{E.9}$$

Eq. 2.11 is used to calculate the intercept of the ordinary least squares line of best fit.

$$\hat{b} = \frac{\left(\sum_{i=1}^{n} x_i\right)^2 \left(\sum_{i=1}^{n} y_i\right) - \left(\sum_{i=1}^{n} x_i y_i\right)\left(\sum_{i=1}^{n} x_i\right)}{n\sum_{i=1}^{n} {x_i}^2 - \left(\sum_{i=1}^{n} x_i\right)^2} = \bar{y} - \hat{m}\bar{x} \tag{E.10}$$

Eq. E.11 is used to calculate the standard deviation of y(x) through the square root of the variance $s_{y,x}^2$ of y(x). The variance is defined as the error sum of squares divided by the degrees of freedom, where n represents the degrees of freedom.

$$s_{y,x}^2 = \left(\frac{1}{n-2}\right)\sum_{i=1}^{n}\left(y_i - \hat{y}\right)^2 = \frac{SS_E}{n-2} \tag{E.11}$$

The square root of s_m^2 can be used to calculate the variance of $\hat{m}$, as shown in eq. E.12.

$$s_m^2 = \frac{s_{y,x}^2}{SS_{xx}} \tag{E.12}$$

The square root of s_b^2 can be used to calculate the variance of $\hat{b}$, as shown in eq. E.13.

$$s_b^2 = \frac{s_{y,x}^2 \sum_{i=1}^{n} {x_i}^2}{nSS_{xx}} = s_{y,x}^2\left(\frac{1}{n} + \frac{\bar{x}^2}{SS_{xx}}\right) \tag{E.13}$$

Eq. E.11 – E.13 may be derived from the propagation of error calculations based on eq. F.9 and F.10 as demonstrated.

For a linear function y of p variables x_i, the linear function f may be demonstrated as follows:

$$y = f\left(x_1, x_2, ...x_p\right) = c_1x_1 + c_2x_2 + c_3x_3 + ...c_px_p = \sum_{i=1}^{p} c_i x_i \tag{E.14}$$

Variance of linear function f:

$$\partial_f^2 = \sum_{i=1}^{p} c_i^2 \partial_i^2 + 2\sum_{i<j}^{p}\ \sum_{i=2}^{p} c_i c_j \operatorname{cov}\left(x_i, x_j\right) \tag{E.15}$$

Where $\operatorname{cov}\left(x_i, x_j\right)$ is the covariance of the variables x_i and x_j.

Using a generalised nonlinear function (eq. E.16), the equation for the variance of the function f maybe shown as:

$$y = f\left(x_1, x_2, \ldots x_p\right) \tag{E.16}$$

Variance of nonlinear function f:

$$\partial_f^2 = \sum_{i=1}^{p}\left(\frac{\partial f}{\partial x_i}\right)^2 \partial_{x_i}^2 + \sum_{i<j}^{p}\sum_{j=2}^{p} 2\left(\frac{\partial f}{\partial x_i}\right)\left(\frac{\partial f}{\partial x_j}\right)\mathrm{cov}\left(x_i, x_j\right) \tag{E.17}$$

The variance of a linear function (eq. E.15) by solving the general variance equation (eq. E.17) with eq. E.14. Eq. E.12 and eq. E.13 can be obtained by the evaluation of eq. E.17 using eq. E.9 and eq. E.11 for $\hat{m}$ and $\hat{b}$ respectively.

To determine the 95% confidence intervals around the calculated $\hat{m}$ and $\hat{b}$, a t-distribution function together with n-2 degrees of freedom were used. [131]

The confidence deviation, Cd, is calculated using eq. E.18.

$$Cd\left(x_\circ\right) = t_{2,\alpha,n-2} \times u(x_\circ) \tag{E.18}$$

Where t-distribution is:

$$t_{2,\alpha,n-2} \tag{E.19}$$

The confidence interval is calculated using eq. E.20.

$$\mathrm{Ci}\left(x_\circ\right) = x_\circ \pm Cd\left(x_\circ\right) \tag{E.20}$$

R^2 coefficient of determination – fraction of the variability of the y_i.

$$R^2 = \frac{SS_R}{SS_T} = \frac{SS_T - SS_E}{SS_T} \tag{E.21}$$

Standard uncertainty:

$$u(x_\circ) = \frac{SE_{xy}}{\hat{m}} \times \sqrt{\left\{\frac{1}{k} + \frac{1}{n} + \frac{\left(y_\circ - \bar{y}\right)^2}{\hat{m}^2 \times s^2 \times \left(n-1\right)}\right\}} \tag{E.22}$$

Expanded uncertainty:

$$U(x) = \sqrt{u(x_i)^2 + u(x_j)^2} \tag{E.23}$$